Exploring New Catalysts for Photocatalytic Carbon Dioxide Reduction Using Homogeneous Transition Metal Complexes

By

Yasmeen Hameed

A thesis submitted to the

Faculty of Graduate and Postdoctoral Studies

University of Ottawa

In partial fulfillment of the requirements

For the degree of

Doctor of Philosophy in Chemistry

Department of Chemistry and Biomolecular Science

Faculty of Science

University of Ottawa

uOttawa

L'Université canadienne
Canada's university

Abstract

The increase of the carbon dioxide concentration in the atmosphere provides a strong impetus to discover new catalysts that are able to reduce CO_2. The reduction processes of this greenhouse gas CO_2 have recently received enormous efforts in the research area. The objective of this thesis was the photocatalytic reduction of CO_2 that is known as an artificial photosynthesis using visible light, and the objective of the thesis was to study the ability and efficiency of different new molecular catalysts towards CO_2 reduction. The goals of the thesis are to design and characterize new catalysts that have high efficiency for the catalytic reduction of CO_2.

After a brief introduction in Chapter 1 about the photocatalytic reduction of CO_2, a different catalyst is presented in each chapter with their characterization and examination for the photocatalytic reduction of CO_2. In addition, these presented catalysts were also examined for the electrocatalytic reduction of CO_2, but they show a good catalytic behavior in the photocatalytic reduction of CO_2. The catalytic mechanisms were also suggested for each catalyst and tried to be confirmed by many different experiments. observed to be highly influenced by CO_2 concentration.

These newly discovered catalysts are based on transition metal complexes that are able to be good catalysts for the photocatalytic CO_2 reduction. These new transition metal complexes have been synthesized, characterized and examined for their catalytic reactivity for CO_2 reduction. As presented in Chapter 2, new manganese and rhenium ccomplexes bearing a phosphino-amino-pyridine ligand were synthesized, characterized and showed their photocatalytic ability for CO_2 reduction. In addition, Chapter 3 presents new Ru catalysts supported by an unprecedented ligand array and documented their photocatalytic

ability towards CO_2 reduction. Moreover, Chapter 4 focuses on new Zn(II) complexes that are novel catalysts in the photocatalytic CO_2 reduction area. Furthermore, Chapter 5 presents a new environment for Re photocatalyst that has the switch in product to formic acid compare to all other reported Re photocatalysts. On the other hand, Chapter 6 shows new dimers and monomers for a series of earth-abundant transition metal dibromide complexes supported by a neutral SNS ligand framework and reveals their applications in the catalysis. Finally, Chapter 7 presents a brief conclusion and a number of future directions.

The attempts to explore and discover the new catalysts for CO_2 reduction were exciting, successfully and resulted in the discovery of new catalysts. These catalysts show their good ability to reduce carbon dioxide (CO_2) to more valuable products such as carbon monoxide (CO) and formic acid (HCOOH).

Acknowledgements

In the name of Allah, the Most Gracious and the Most Merciful

First and foremost, I thank my God Allah for facilitating and helping me to complete this thesis despite all the difficulties and obstacles that I faced in my life during my study times.

Fundamental and important, I would like to express my genuine gratitude to my amazing supervisor Prof. Darrin Richeson. All of the results presented in this thesis and all of the other unseen work would certainly never have completed without the wonderful supervision and continuous effort of my supervisor. He spent an enormous time and effort on guiding and supporting me throughout my Ph.D. project. I am thankfully for his guidance and help, and I am also very thankfully for showing me the way to improve my skills and knowledge. He has kept me motivated and on-task during good and bad times, and he has believed in my ability to finish and achieve this thesis during my difficult times. All the words of thanks and appreciation will not be enough to thank him for being a great supervisor. I am honored to work under his great supervision, and I am proud to be a part of his group.

Great thanks to every member in Richeson group, (the previous and current members), especially Dr. Titel Jurca who is the person I cannot forget his wonderful support when I needed it at my hard time. In addition, many thanks to Dr. Bulat, Dr. Jeff and Dr. Camilo for the help in the X-ray structure determination, Dr. Sharon for all of her help in the Mass spectra and GC analysis, Dr. Glenn for the NMR help, and Dr. Wendy for all of her help in the electrochemistry data. Moreover, great thanks to Prof. Sandro

Gambarotta and Prof. Abdelhamid Sayri for their efforts that contributed to increase my knowledge during the courses of my research.

I would extend my thanks to the graduate studies and chemistry departments of the University of Ottawa for giving me the opportunity to study and develop my academic skills. Very special thanks go to the Ministry of Education in Saudi Arabia and Saudi cultural bureau in Canada for their supporting and helping in all respects, and very special and great thanks to my great king who gave me the scholarship and to give me this great opportunity to come to Canada and learn.

Significant and essential, I would like to express my gratitude and thanks to my great and awesome parents Abdullah and Najihah for their great and amazing love, care, patience, and support that have been essential for my continuous strive to achieve this beautiful dream successfully. My parents are a blessing from God Allah. I really cannot describe them in words; they are a piece of paradise. I would also like to send my warm gratitude to my wonderful brothers and sisters; Ahmed, Mohammad, Yasir, Anod, Shahad, Jawaher. I am very grateful for having them beside me, and I would be never forgetting their support and assistance that they provided over the years. My beautiful family gives me constant support from far away, and they are always with me in my heart. Special gratitude and thanks go to my beautiful and beloved grandmother Saoud for her continued support, and I hope that her soul will rest in peace and may God Allah give her eternal rest. I will never have forgotten her. In addition, I would like also to thank all my friends especially Mei and Zynab who shared with me my beautiful and difficult times and help me to pass some of the difficult days. Last but not least, I would like to express my special thanks to my sincere love, my life, my man, my best friend forever, my son Hesham who joined me in this long and exciting journey in Canada.

Table of Contents

Chapter 1 Introduction:

Chapter 2 Breaking the α–Diimine Hold on Group 7 Catalysts and Switching Selectivity: Photocatalytic CO_2 Reduction with Manganese Complexes Bearing a Phosphinoaminopyridine Ligand:

Chapter 3 Visible light photocatalytic reduction of CO_2 to formic acid with a Ru catalyst supported by an unprecedented ligand array:

Chapter 4 Photocatalytic Reduction of CO_2 to formic acid with an Unconventional Zn(II) Catalyst:

Chapter 5 Turning on the Formation of Formic Acid from CO_2 with an Integrated Re Photocatalyst/Sensitizer:

Chapter 6 **Dimers, Monomers and Pentacoordination in a Series of Earth-Abundant Transition Metal Dibromido Complexes Supported by a Neutral SNS Ligand Framework and their Applications in the Catalysis:**

Chapter 7 **Conclusion and Future Study:**

List of Figures

List of Scheme

List of Table

List of Abbreviations

DFT	Density Functional Theory
GC	Gas Chromatograph
GC-TCD	Gas Chromatograph with Thermal-conductivity detector.
HOMO	Highest occupied molecular orbital
LUMO	Lowest unoccupied molecular orbital
SOMO	Singly Occupied Molecular Orbital
MS-EI	Mass spectrometry with electronic impact
NMR	Nuclear Magnetic Resonance
UV	Ultraviolet
XRD	X-ray diffraction
SC-XRD	Single crystal X-ray diffraction
CV	Cyclic Voltammetry
M	Molar (mol)
V	Volt
LV	Linear Voltammetry
SCE	Standard Calomel Electrode
SHE	Standard Hydrogen Electrode
t	Time, s
XRD	X-ray Diffraction
E°	potentials
pH	potential of Hydrogen

Chapter 1: Photo-Catalytic Carbon Dioxide Reduction Using Homogeneous Transition Metal Complexes

1.1. Introduction

The two critical worldwide challenges that are facing the humanity are the energy shortage and environmental pollution. The main energy source currently used all over the world is fossil fuels, which are rapidly consumed to supply increasing energy demands. The release of energy from the combustion of fossil fuels results in generation of carbon dioxide (CO_2), which is a major greenhouse gas. The level of atmospheric carbon dioxide has significantly increased since the beginning of industrial revolution and continues due to human activities. The central reason for this is attributed to fossil fuel combustion. The contribution of this extra carbon dioxide towards global warming has resulted in the search for different solutions to reduce the carbon dioxide. The reduction of the atmospheric CO_2 level to produce more valuable products has become an important research area in the recent decades. However, there is a critical challenge in this area of CO_2 reduction, and that is the low thermodynamic energy value of the carbon dioxide. This means that this effort requires a large energy contribution to convert CO_2 to other valuable products, and that leads to a high cost of production. To address this challenge, there is a huge effort to develop innovative new catalysis systems that are able to increase the potential of transforming CO_2.[1]

Carbon dioxide (CO_2) can be reduced via electrochemical or photochemical approaches, and this thesis focuses mainly on efforts for successful photocatalytic CO_2 reduction. A central goal of this thesis is the discovery of new catalysts coupled with an exploration of photochemical parameters for CO_2 reduction. This introduction will begin with a presentation of some of the basic principles for the photo-catalytic CO_2 reduction and provide some literature precedent for known CO_2 reduction photo-catalysts. This provides context for the results presented in the subsequent Chapters. At the end of this thesis, a brief conclusion about these results in photochemical CO_2 reduction and possible directions for the future development of this photo-catalytic field are presented.

1.2. Thermodynamics of CO_2 Reduction

The reduction of CO_2 is a very challenging reaction and the thermodynamic requirements for this reduction should be considered. The reduction of CO_2 by the direct one electron reduction to form the radical $CO_2^{\bullet-}$ is unfavourable process because it requires a high energy as shown by the large reduction potential of -2.14 V vs SCE. There are other more favourable pathways that employ proton-assisted multiple-electron transfer (MET), which are summarized in Table 1.1. These proton coupled electron transfer reactions require much less energy than the one electron reduction reaction, so the reduction potential of most of these proton-assisted multiple-electron transfers becomes less negative when the number of electrons is increased, as shown in Table 1.1.[2]

Table 1.1. The CO_2 reduction potentials for various CO_2 reduction reactions.[2]

Reaction	E°(V) vs SCE[a]
$CO_2 + 2H^+ + 2e^- \rightarrow HCO_2H$	- 0.85
$CO_2 + 2H^+ + 2e^- \rightarrow CO + H_2O$	- 0.77
$CO_2 + 4H^+ + 4e^- \rightarrow C + 2H_2O$	- 0.44
$CO_2 + 4H^+ + 4e^- \rightarrow HCHO + H_2O$	- 0.72
$CO_2 + 6H^+ + 6e^- \rightarrow CH_3OH + H_2O$	- 0.62
$CO_2 + 8H^+ + 8e^- \rightarrow CH_4 + 2H_2O$	- 0.48

[a] $E^{\circ\prime}$ potentials are reported at pH 7.

These proton coupled electron transfer reductions are thermodynamically more favourable, but also require a catalyst. The catalysts for these reactions play an important role because they are needed to overcome kinetic limitations. Transition metal compounds can be used at homogeneous systems that can be influenced by the supporting ligands on the complex. These catalysts are able to promote the multiple-electron transfer reactivity of the reduction reaction. A number of different transition metal complexes have been explored for CO_2 reduction applications. These transition metal complexes consist of two main parts the central metal and the organic-based ligands that surround the metal center. Two major areas that have been explored employed macrocyclic ligands or bipyridine ligands and these two classes of catalysts will be briefly explained in the following section.[2]

In this thesis, the primary goals are to explore photocatalytic behaviours for CO_2 reduction. Certainly, the electrochemical features of potential catalysts are important and have direct implication on their reactivity. As a result, some electrochemical analysis and investigates were employed in these studies.

1.3. Common Terms in The Photo-Catalytic Reduction

There are some common terms that are commonly used in the photo-catalytic system to describe important information of the catalytic CO_2 reduction processes. These important terms should be clearly defined in order to understand and characterize these photo-catalytic reactions. These terms include the catalytic selectivity, the photochemical quantum yield, and turnover number.[2]

1.3.1. The Catalytic Selectivity (CS)

This term is used to define the product selectivity for the catalytic reduction of CO_2. There are two features of selectivity that can be addressed. The first is the selectivity for a particular reduction product. In this thesis the observed reduction products are carbon monoxide (CO) and formic acid/formate (HCOOH, $HCOO^-$). The second is selectivity of the reducing equivalents. Because any catalyst that is able to reduce CO_2 to other valuable products such as carbon monoxide or formate may also able to reduce protons to hydrogen. The reduction potentials of these products for the half-cell reactions at pH 7 in aqueous solution versus the normal hydrogen electrode (E°') are shown in the following table (1.2).[3]

Although there are several possible products from CO_2 reduction as was explained, this thesis focuses on two main products from this reaction, carbon monoxide and the formic acid. In addition, hydrogen is a common by-product of the photocatalytic CO_2 reduction. It also plays an important role in the global energy system because there is a big requirement for a renewable fuel to replace current energy sources. Since hydrogen is a perfect secondary energy, it can be a solution to many problems such as the environmental emissions and energy security. Therefore, hydrogen can be an alternative fuel and an energy carrier for the future energy supply, and this is one form of harnessing renewable energy.[4,5] Moreover, hydrogen can be produced from water that is abundant, and this way of hydrogen production from water was tried with some catalysts that did not show a good catalytic behavior towards CO_2 reduction. Some of these catalysts as will be shown in the thesis were able to reduce water and produce hydrogen, and they showed a good catalytic performance in water reduction and hydrogen production.

Table 1.2. The standard reduction potentials for half-cell reactions.[3]

Reaction	E°(V) vs SHE[a]
$2H^+ + 2e^- \longrightarrow H_2$	- 0.41 V
$CO_2 + 2H^+ + 2e^- \longrightarrow CO + H_2O$	- 0.52 V
$CO_2 + 2H^+ + 2e^- \longrightarrow HCO_2H$	- 0.61 V

[a] $E^{\circ\prime}$ potentials are reported at pH 7.

Catalytic selectivity values also give information about the overall efficiency of CO_2 reduction system. Selectivity in terms of C products such as CO or formate, or selectivity in terms of the reducing equivalents this would compare carbon products to H_2. This term is defined as the ratio of the moles of products from CO_2 reduction to the moles of H_2 that is also from the CO_2 reduction reaction.[2] The definition of this catalytic selectivity is described in equation 1.

$$CS = \frac{[\text{CO2 reduction products}]}{[\text{H2}]} \tag{1}$$

This parameter is important because it is commonly used to quantify the efficiency of catalytic CO_2 reduction processes.[2]

1.3.2. The Photochemical Quantum Yield (ϕ)

The photochemical quantum yield is a common parameter that is used in photochemical systems to describe the efficiency of the catalytic CO_2 reduction system. The photochemical quantum yield is defined as the molar ratio of CO_2 reduction products to the incident photons.[2] The definition of this photochemical quantum yield is shown in equation 2.

$$\phi = \frac{[\text{CO2 reduction products}]}{[\text{incident photons}]} \qquad (2)$$

This parameter is very important because it normalizes results using different light sources. To determine the photochemical quantum yield (Φ) of a photochemical reaction, the number of photons absorbed by the system during a given period must be measured. The incident photon flux can be measured using chemical or physical means such as the actinometry that is able to measure the number of photons in a beam integrally or per unit time.[6]

1.3.3. The Turnover Number (TN)

The turnover number is used to describe the activity of the catalyst, which indicates to the lifetime of the catalyst because it is the number of the reduction processes that occur per catalyst cycle over the catalyst's lifetime. This turnover number is defined as the as the molar ratio of CO_2 reduction products to the catalyst, and the definition of this turnover number is explained in equation 3.[2]

$$TN = \frac{[\text{CO2 reduction products}]}{[\text{catalyst}]} \qquad (3)$$

The turnover number is an important parameter because a fundamental feature of any catalyst and it indicates to the activity of the catalyst.

1.4. Photocatalytic Reduction of CO_2

Photocatalytic reduction of CO_2 by using the energy of sunlight combined with homogeneous transition metals as catalysts is an attractive process to address the both energy and environmental issues of carbon dioxide emissions. Transforming CO_2 to more valuable products such as CO and CH_4 in the gas phase or as alcohols, aldehydes and carboxylic acids in the liquid phase is a tremendous challenge due to the need of control the CO_2 reduction pathways for the products.[7]

Several important components require attention and consideration in order to carry out photocatalytic CO_2 reduction. First, the two main components for the photocatalytic CO_2 reduction are derived from the word photocatalysis, that consists of the terms photo and catalysis. The photo part means the use of light, which provides the primary essential energy input for the reaction, and the catalysis part refers to the chemical conversion of the reactants and change to the reaction rate without any change to the catalyst species. These concepts lead to the two main components for this reaction, the photosensitizer and the catalyst. The photosensitizer is responsible for the light absorption to generate an excited state photosensitizer that can use the absorbed energy for the reaction. Perhaps the most common species that has been used in this regard is the Ru(II) complex, $[Ru(bpy)_3]^{2+}$. The success of this photosensitizer is due to its unique combination of chemical stability, redox properties, and long lifetime of the excited state. The catalyst component is the central exploration and discovery target in this thesis.

The next most obvious components that need consideration are the so-called sacrificial electron donor and the reaction solvent. In general, a sacrificial electron donor is required to provide the electrons needed in the reduction reaction and this species most commonly interacts with the excited state photosensitizer to undergo an electron transfer quenching of this species. There are a variety of different quenchers that have been used as the sacrificial electron donor in CO_2 photoreduction systems. Examples include triethanolamine (TEOA), triethylamine (TEA), 1-benzyl-1,4-dihydronicotinamide (BNAH), ascorbic acid (H_2A), and sodium ascorbate (NaA). In terms of solvent, a variety have been employed in successful photoreactions. These include dimethylformamide (DMF), acetonitrile (ACN), dimethylacetamide (DMA), and methanol (MeOH) which have all been used for photocatalytic CO_2 reduction reactions.[8,9]

In summary, the photocatalytic CO_2 reduction system will generally consist of a catalyst, photosensitizer, sacrificial electron donor reagents, and solvent. This reaction mixture will then be subject to irradiation from a light source which can be characterized by emission wavelength and photon flux/intensity.

In order to have a clearer understanding about these photocatalytic reactions and to have a better idea about the operation of these photocatalytic systems a general mechanism of the photocatalytic reaction is useful. Therefore, the basic mechanisms of the known photocatalytic CO_2 reduction reaction will be described in the following sections.

1.4.1. Basic Mechanism of Photocatalytic Reaction

In general, the photocatalytic processes of many different reactions follow the same basic steps, which will be discussed here. These photochemical processes that are the beginning of the photocatalytic process can be expressed by the following equations:

$$\mathrm{PS} + h\nu \rightarrow \mathrm{PS(S1)}^*$$

$$\mathrm{PS}^*\mathrm{(S1)} \rightarrow \mathrm{PS(T1)}^*$$

$$\mathrm{PS(T1)}^* + \mathrm{A} \rightarrow \mathrm{PS} + \mathrm{A}^*$$

Where is PS is the photosensitizer, PS* is the excited species, A is the acceptor substrate molecule, and A* is the excited acceptor molecule.

The process begins when the photosensitizer (PS), when exposed to light, absorbs a photon. The photosensitizer will be transferred from the ground state (S0) to the first excited singlet state (S1). The singlet-excited state (S1) can then undergo intersystem crossing (ISC) to produces the triplet-excited state (T1), which is a longer-lived state. In the next step, the energy will be transferred from the triplet state (T1) of the photosensitizer molecule to a substrate molecule (Acceptor = A). This produces A and a chemical change can result.[14,10,11]

A Jablonski diagram can be used to summarize the photochemical processes, as shown Figure 1.1. The Jablonski diagram is used to show the molecular electronic states and energy levels, and to explain the possible photophysical and photochemical processes. A Jablonski diagram represents the electronic energy levels and the vibrational energy levels of the photosensitizer. The electrons in the electronic ground state are paired (+1/2, -1/2), and this electronic singlet ground state is represented as S0. In the absorption of photons and the excitation step, one of the paired electrons in the electronic singlet ground state will be excited, and the electronic excited state will be classified in two different electronic excited states depending on the different spin directions of the electrons. In the excitation, if the electron maintains its spin orientation and the spin multiplicity will equal to one ($M = 2S + 1 = 1$), the excited state will be excited singlet state (S1), and this singlet-singlet transition is the allowed transition. The emission of light from this singlet-excited state to the singlet ground state is called fluorescence. On the other hand, spin orientation of the electron can changes resulting in a spin multiplicity equal to three ($M = 2S + 1 = 3$), and this excited state is an excited triplet state (T1). The flip of spin going from S1 to T1 is called intersystem crossing (ISC). The emission of a photon from the excited triplet state to return the molecule to the singlet ground state is called phosphorescence.[9–12]

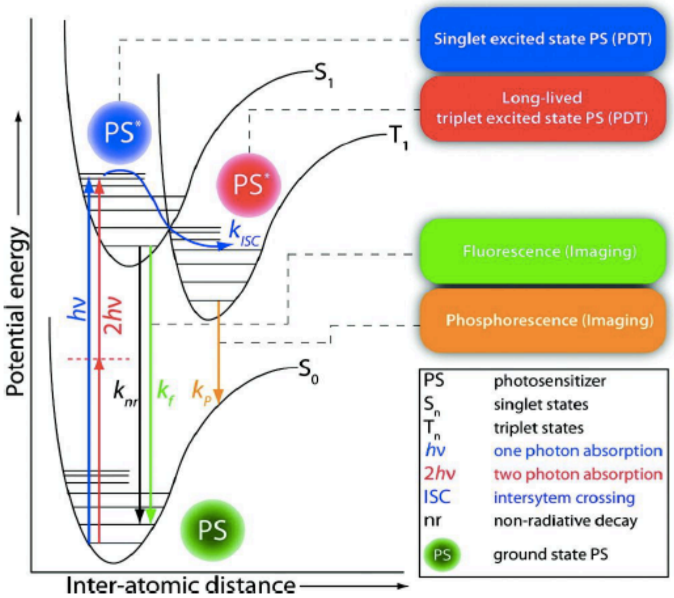

Figure 1.1. The Perrin-Jablonski energy diagram for a photosensitizer (PS) molecule.[12] Produced from reference number 12 with permission by the Chemical Reviews.

In general, the triplet-excited states (T1) is longer lived than the first excited singlet state (S1), being in microsecond to millisecond range, while the singlet states lifetime is in the nanoseconds range. Thus, the fluorescence, which is the short-lived, has the lifetime of 10^{-9}-10^{-6}s while the lifetime of the phosphorescence is 10^{-4}-10^{-2}s. Finally, there is another radiation-less deactivation pathway that can occur between states of the same spin, it is called the internal conversion (IC). This involved vibrational relaxation, which is allowed the molecule in the higher excited vibrational state to return to the lower vibrational state by the energy transfer.[9–12]

1.5. Types of Catalysts for Photocatalytic Reduction of CO_2

As outlined above, a homogeneous photocatalytic system consists of a photosenstitizer and a catalyst. The relationship between these two components can be categorized in two ways that are generally identified as Type I and Type II systems. Type I systems consist of two separate components that are the photosensitizer and the catalyst, and they are mixed in the solution to make the photoreduction system. On the other hand, in Type II systems the two components are in a single molecular unit that functions as both the light absorber (photosensitizer) and the catalyst. These two types are explained with more details in the next section.

1.5.1. Type I Photocatalyst System

Type I catalysis consists of the two separate components with one acting as a photosensitizer (PS) and the other as a catalyst (Cat). In the light irradiation, the photosensitizer, such as tris(bipyridine)ruthenium (II) $[Ru(bpy)_3]^{2+}$, absorbs the light, and then it is promoted to an excited electronic state (as shown in equation 1). The excited state of the photosensitizer is reductively quenched by a sacrificial electron donor (D), which is commonly an amine such as triethanoamine (TEOA) or triethylamine (TEA), to form the reduced photosensitizer (PS^-) and the oxidized sacrificial donor ($D^{\cdot+}$) (as shown in equation 2). This reduced photosensitizer (PS^-) will transfer the electron to the catalyst (Cat) to produce the reduced catalyst (Cat^-) that will react with CO_2 to reduce it and produce the desired products (as shown in equation 3 and 4).[2,13]

$$\mathrm{PS} + h\nu \rightarrow \mathrm{PS}^* \tag{1}$$

$$\mathrm{PS}^* + \mathrm{D} \rightarrow \mathrm{PS}^- + \mathrm{D}^{\bullet+} \tag{2}$$

$$\mathrm{PS}^- + \mathrm{Cat} \rightarrow \mathrm{PS} + \mathrm{Cat}^- \tag{3}$$

$$\mathrm{Cat}^- + \mathrm{CO_2} \rightarrow\rightarrow \mathrm{Cat} + \mathrm{Products} \tag{4}$$

An example of a Type I catalysis system uses transition metal complexes such as cobalt or nickel tetraaza-macrocylic compounds as the catalyst for CO_2 reduction in combination with photosensitizer (e.g. $[Ru(bpy)_3]^{2+}$) and a sacrificial electron donor. These tetraaza-macrocylic ligands of the homogeneous catalysts cobalt and nickel complexes are shown in Scheme 1.1. Tinnemans et al. was the first group that investigated the CO_2 reduction by using these transition-metal tetraaza-macrocyclic compounds as catalyst with $[Ru(bpy)_3]^{2+}$ photosensitizer. The main products of this CO_2 reduction were carbon monoxide and formate, and there were many studies that carried out to suggest the proposed pathways of the mechanisms for the formation of these products.[2,13]

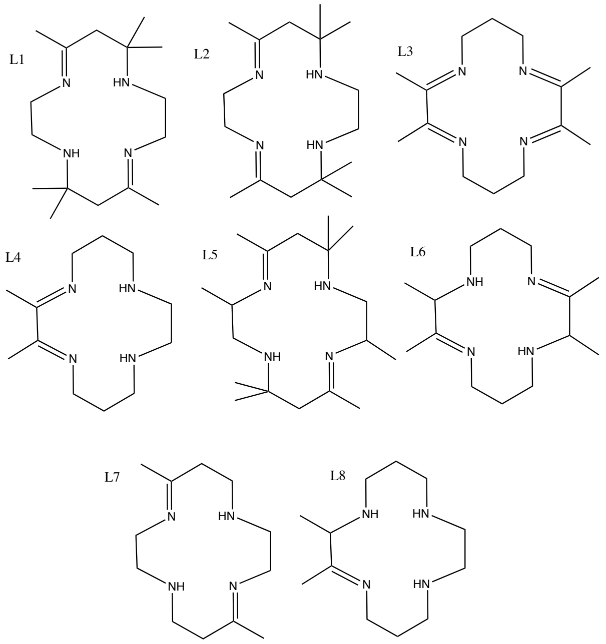

Scheme 1.1. The tetraaza-macrocyclic ligands of Cobalt(II) and Nickel(II).[2] Reproduced from reference number 2 with permission by the Accounts of Chemical Research.

There were many studies undertaken in Type I catalysis for CO_2 reduction to increase the efficiency of the CO_2 reduction reactions, and that was by increasing the selectivity and the turnover number of the products. Therefore, one technique to increase the efficiency of the reactions is the use of supramolecular complexes, which are considered as a part of the first type Type I, and they form from the covalent attachment of a photosensitizer and a catalyst. The idea of these supramolecular complexes is the covalent attachment between the photosensitizer and the catalyst can transfer the electron more efficiently because the electron should be able to be transferred easier and faster between the photosensitizer and the catalyst during the photocatalytic reaction.[2] These supramolecular complexes will be discussed with more details below in the next section.

1.5.1.2. Supramolecular Complexes

Supramolecular complexes are the covalent attachment of the redox photosensitizer and the transition metal complex that is the catalyst. The purpose of these supramolecular complexes is to increase the efficiency of excited-state electron that will be transferred between the photosensitizer (the donor moiety) and the catalyst (the acceptor moiety) during the photocatalytic process. There are two classes of compounds that have been investigated as supramolecular complexes for CO_2 reduction. Both of these classes of compounds have employed the attachment of ruthenium polypyridine complexes as the photosensitizer to be linked to both Ni and Re catalysts. The ruthenium polypyridyl photosensitizer linkage to a nickel cyclam catalyst is attributed to Kimura who designed and synthesized this type of the supramolecular complex. While the ruthenium polypyridyl photosensitizer linkage to $Re(bpy)(CO)_3X$ catalyst is attributed to Ishitani who designed and synthesized this type of the supramolecular complex. Both classes of these supramolecular catalysts have proved their ability to increase the stability and the turnover number of these supramolecular catalysts towards the CO_2 reduction reaction. The structure of some examples of these supramolecular complexes that utilized by Ishitani and Kimura are shown in Scheme 1.2.[14, 15–18]

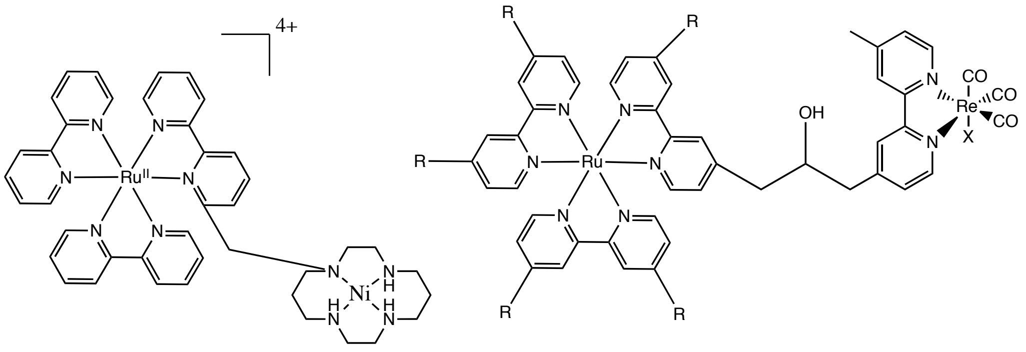

Scheme 1.2. The structure of some of these supramolecular complexes that used by Ishitani and Kimura.[2] Reproduced from reference number 2 with permission by the Accounts of Chemical Research.

These supramolecular complexes, which are binuclear complexes, have achieved success in increasing the efficiency of the homogeneous photocatalyst CO_2 reduction compared to the Type I complexes. Ishitani et al. have prepared some examples of these supramolecular complexes and showed the effect of these supramolecular complexes for the photocatalytic CO_2 reduction systems. He reported a series of Ru(II)-Re(I) binuclear complexes linked by bridging ligands, and some of these Ru(II)-Re(I) binuclear complexes such as the bimetallic complex $[(dmb)_2Ru(bpyC_3bpy)Re\text{-}\ (CO)_3Cl]^{2+}$ (d_2Ru-Re) and $[Ru\{bpyC_3bpyRe(CO)_3Cl\}_3]^{2+}$ ($RuRe_3$). These Ru(II)-Re(I) supramolecular complexes are presented in Scheme 1.3, and the evidence for their successful effect is also shown in Table 1.3.[17]

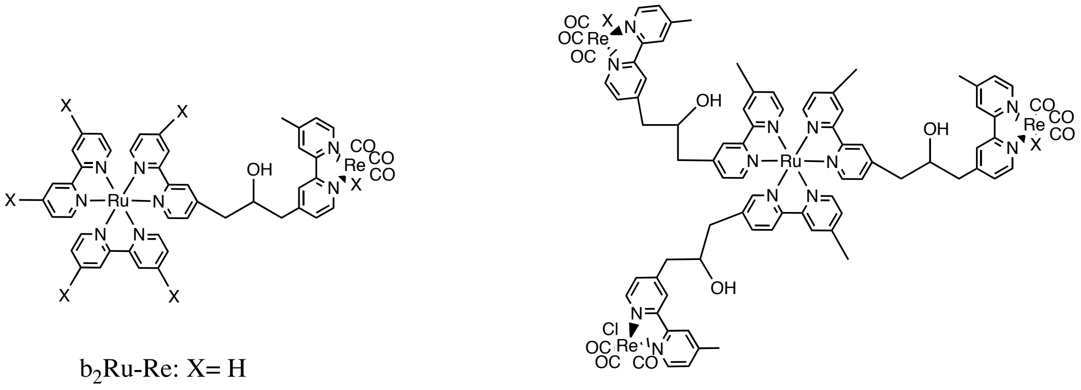

b_2Ru-Re: X= H
d_2Ru-re: X=CH_3

Ru-Re_3

Scheme 1.3. The structure of some of the Ru(II)-Re(I) supramolecular complexes utilized by Ishitani.[17] Reproduced from reference number 17 with permission by the Inorganic Chemistry.

Table 1.3. The turnover number of the CO product formed from these types of supramolecular complexes.[17]

Compound	TN_{CO}[a]
mixed Ru and Re (1:1)[b]	101
$[(dmb)_2Ru(bpyC_3bpy)Re\text{-}(CO)_3Cl]^{2+}$ (d_2Ru-Re)	170
$[Ru\{bpyC_3bpyRe(CO)_3Cl\}_3]^{2+}$ ($RuRe_3$)	240

[a] TN_{CO} is the turnover number for the production of CO after 16 h of irradiation; and the concentration of the complex is 0.05 mM. [b] Mixed solution of $[Ru(dmb)_3]^{2+}$ and $[(dmb)Re(CO)_3Cl]$.

Type I catalysts systems and the supramolecular complexes have confirmed the ability of CO_2 reduction in the homogeneous catalytic reactions. However, this type had suffered from a disadvantage that is the low stability of the catalyst, and this drawback made a big challenge to apply this laboratory scale to practical applications. Even though the supramolecular complexes that are the modified systems of the type I catalysts have shown better activity than the type I catalysts, the synthesis of these complicated supramolecular complexes is not easy.[2]

1.5.2. Type II Photocatalyst System

Type II catalysis consist of one single transition metal complex that acts as both the photosensitizer and the catalyst, and this photocatalyst can be represented as PScat. As described in Type I catalysis, after the photocatalyst PScat absorbs the light to be excited, the excited state of the photocatalyst PScat will be reduced by the reductive quenching (D) to form the active state of the catalyst that is able to react directly with CO_2 and reduce CO_2 to more valuable products. These general photocatalytic processes of this type II catalysis are shown in the below equations (5, 6, and 7).[2,19]

$$\text{PScat} + h\nu \rightarrow \text{PScat}^{*} \quad (5)$$

$$\text{PScat}^{*} + \text{D} \rightarrow \text{PScat}^{-} + \text{D}^{\bullet +} \quad (6)$$

$$\text{PScat}^{-} + \text{CO}_2 \rightarrow \rightarrow \text{PScat} + \text{Products} \quad (7)$$

Type II catalysis systems have been reported for metalloporphyrins or the related metallo-macrocycles and the rhenium complexes $\text{Re}^{\text{I}}(\text{bpy})(\text{CO})_3\text{X}$ (where X= Cl- or Br). In addition, all of these Type II complexes can be used as a catalysts for Type I catalysis system with an appropriate photosensitizer.[2,19] The metalloporphyrins and related metallo-macrocycles catalysts have very low yields due to the short lifetimes of the excited states of the active catalysts.[20,21,22] Some examples of these metalloporphyrins and related metallo-macrocycles complexes are shown in Scheme 1.4.[2] In contrast, in the early 1980's the pioneering discovery that *fac*-$[\text{Re}^{\text{I}}(\text{bipy})(\text{CO})_3\text{Cl}]$ (bipy = 2,2'-bipyridine), represented in Scheme 1.5, was an effective photocatalysts for CO_2 reduction initiated investigations of the bpy framework in this field. These $\text{Re}^{\text{I}}(\text{bipy})(\text{CO})_3\text{X}$ complexes show the highest quantum efficiencies of the catalysts for their ability to reduce CO_2 selectively to CO. The mechanism of these complexes will be discussed here.[2,19]

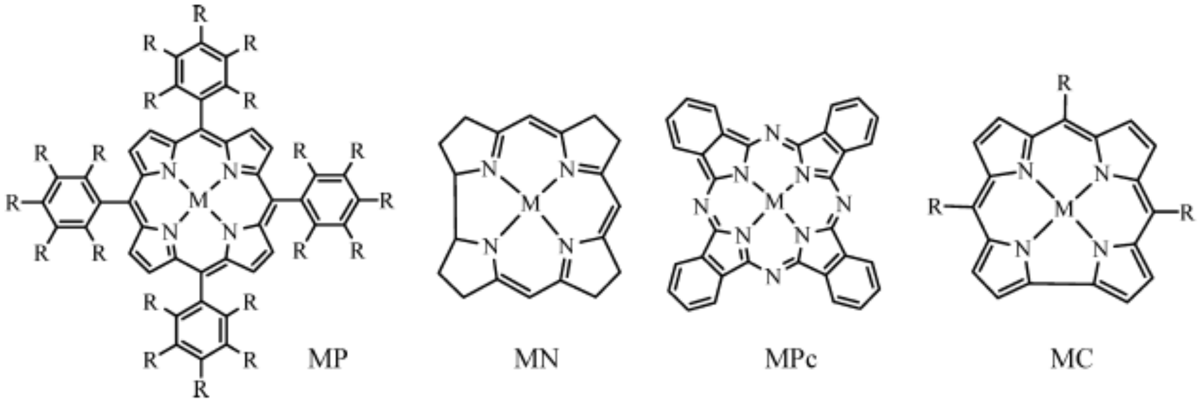

Scheme 1.4. The structure of the metal porphyrin derivates and related metallo-macrocycles. metalloporphyrin (MP), metallocorrin (MN),) metallophthalocyanine (MPc), and metallocorrole (MC, where R = C_6F_5 or 2,6 -$\text{C}_6\text{H}_3\text{Cl}_2$).[2] Produced from reference number 2 with permission by the Accounts of Chemical Research.

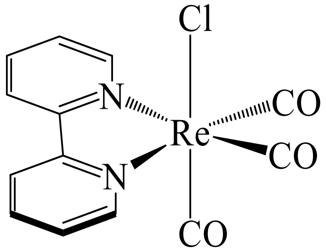

Scheme 1.5. The structure of [Re^{I} (bipy)$(CO)_3Cl$] complex.[23] Reproduced from reference number 23 with permission by Helvetica Chimica Acta.

When the complex $Re^{I}(bpy)(CO)_3X$ absorbs a visible photon, it will be promoted to the MLCT excited state with essentially a Re^{II} metal center and an excited electron located on the bpy ligand. The excited state of the $[Re^{II}(bpy\bullet)^{-}(CO)_3X]$ complex will be reductively quenched to form the $[Re^{I}(bpy\bullet)(CO)_3X]^{-}$ complex. The next step in the proposed action of the reduced complex $[Re^{I}(bpy\bullet)(CO)_3X]^{-}$ is the release of the halide ligand which is replaced to form the solvent (S) complex $[Re^{I}(bpy\bullet)(CO)_3S]$. Protonation of this complex will form the rhenium-hydride bond complex $[Re^{I}(CO)_3(bpy)H]$. This rhenium-hydride complex can react with CO_2 to allow the CO_2 insertion and produce the formate product. Formate production is represented by red line in the scheme 1.6. Another proposed route for this CO_2 reaction is the CO production route that also drives through the solvent compound $[Re^{I}(bpy\bullet)(CO)_3S]$. This solvent compound can be protonated and then can be followed by CO_2 insertion to form the metal carboxylate intermediate that can undergo acid-promoted hydrolysis to produce CO as the main product and H_2O as the secondary product. In addition, it was suggested for this proposed route that the $Re(bpy)(CO)_3(COOH)$ compound can undergo proton-promoted dehydroxylation to form the $Re(bpy)(CO)_4^{+}$ compound that can release CO and react with X to regenerate the initial compound $Re^{I}(bpy)(CO)_3X$. Furthermore, Ishitani et al. have suggested a last route for the CO_2 reduction proposed mechanism that is the possibility for the formation of a binuclear intermediate. In the presence of CO_2, the CO_2-bridged Re dimer $[Re(bpy)(CO)_3]_2(CO_2)$ can react with CO_2 to release CO and to yield $Re(bpy)(CO)_3OCO_2Re(bpy)(CO)_3$. In addition, the protonation of $Re(bpy)(CO)_3OCO_2Re(bpy)(CO)_3$ and the addition of the halide X^- can form HCO_3^-. All of these proposed routes of the proposed mechanism for the CO_2 reduction reactions are show below in the Scheme 1.6.[2,19]

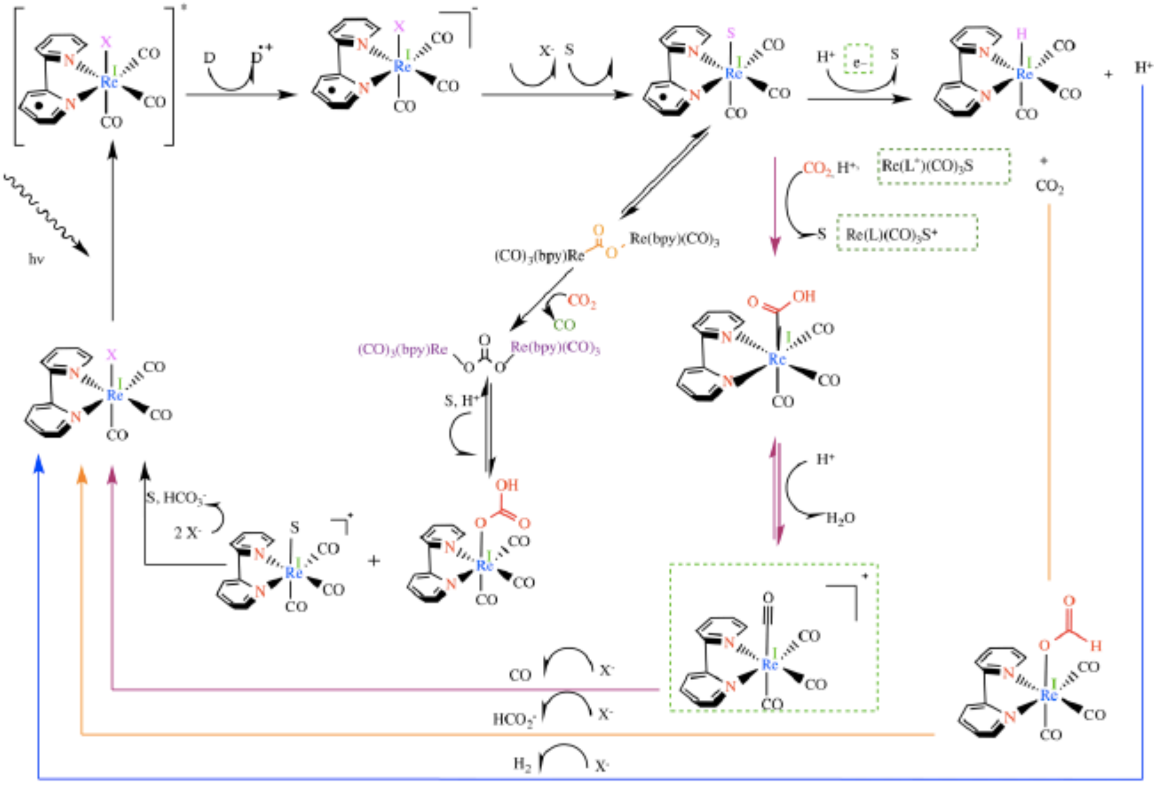

Scheme 1.6. The proposed mechanism of $Re^I (CO)_3 (bpy)X$ complexes.[2] Produced from reference number 2 with permission by the Accounts of Chemical Research.

In 2011, the Mn(I) analogues were investigated. In order to replace the rare metals for the photocatalytic CO_2 reduction system, more abundant metals were explored for the same photocatalytic CO_2 reduction system. This Mn(I) analogues was discovered as a good electrocatalyst in 2011, and it was reported as a good photocatalyst in 2014. In photocatalytic CO_2 reactions, fac-$Mn(bpy)(CO)_3Br$ (bpy = 2,20-bipyridine) was reported as an efficient catalyst for CO_2 reduction. This Mn(I) complex has shown good activity towards CO_2 reduction, and it has shown good selectivity of CO_2 reduction.[24,25] The structure of the Mn catalyst is shown below in Scheme 1.7.

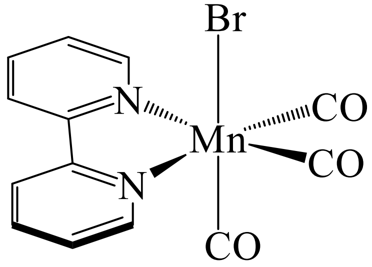

Scheme 1.7. The structure of fac-Mn(bpy)$(CO)_3$Br complex.[24] Reproduced from reference number 24 with permission by the Chem. Commun.

1.6. Components for The Photocatalytic CO_2 Reduction Systems

As it was mentioned before, the photocatalytic reactions require many important components that are the photosensitizer (PS), the catalyst (Cat), the electron donor (D), and the solvent (S). These components will be explained briefly below.

1.6.1. Redox photosensitizer (PS)

A redox photosensitizer (PS) that absorbs the light should be able to facilitate the electron transfer from the electron donor to the catalyst. In the photosensitized reduction reactions, two types of electron transfer reactions can be envisioned and these involve either reductive quenching of the PS or oxidative quenching of the PS. Reductive quenching is the more commonly encountered processes with photocatalytic reduction of CO_2 and in this process the excited state of the photosensitizer (PS*) is reductively quenched by the electron donor (D) to form the one electron reduced species (OERS) of the photosensitizer ($PS^{\bullet-}$). In contrast, for oxidative quenching the excited state of the photosensitizer (PS*) is oxidatively quenched by the catalyst (Cat) to form a reduced catalyst (Cat^-) and the one-electron-oxidized species (OEOS) of the photosensitizer ($PS^{\bullet+}$).[26,27] Both reductive quenching and oxidative quenching processes are represented by energy diagrams in Scheme 1.8.

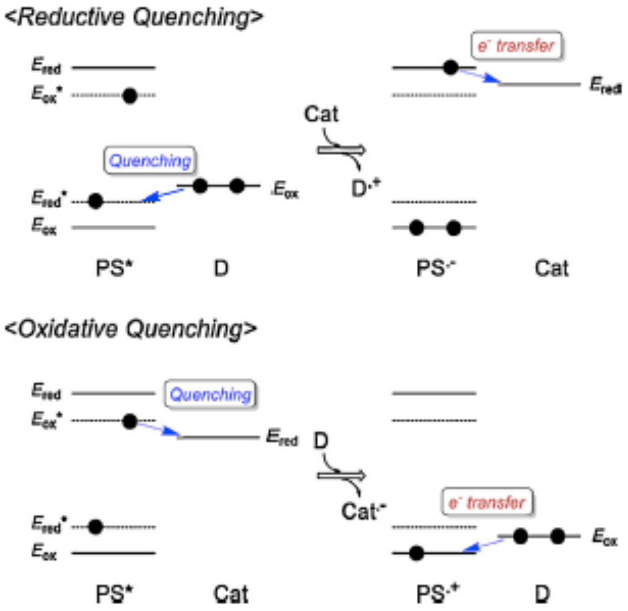

Scheme 1.8. The energy diagrams of the reductive quenching process and the oxidative quenching process.[26] Produced from reference number 26 with permission by the Elsevier.

Photosensitizers are compounds that are able to absorb light at specific wavelength and transform it into a useful energy. There are some properties that have to be present in these photosensitizers to have the ideal photosensitizers.[26,27] These properties include:

1. Have a strong absorbance at longer wavelengths than the other components like the catalyst and the donor, preferably above 600 nm (600-850 nm).[26,27]
2. Have a long lifetime of the reactive excited state.[26,27]
3. Have a high stability of the form the one electron reduced species.[26,27]
4. Have a strong oxidation power of the excited state.[26,27]

For homogeneous applications, there are several different photosensitizers that can be used in these photocatalytic reactions. The tris(2,2′-bipyridine) ruthenium(II) complex, which belongs to the family of polypyridine Ru(II) complexes, has been one of the most commonly used photosensitizers in the photocatalytic CO_2 reduction. This photosensitizer has a great interest due to its unique combination of the redox properties, the chemical stability, the excited state reactivity, and excited state lifetime.[9,28,29] The structure of this tris(2,2′-bipyridine) ruthenium(II) photosensitizer is shown below in the Scheme 1.9.

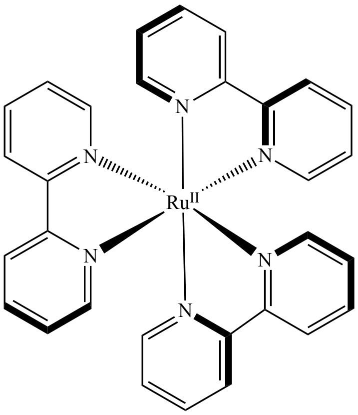

Scheme 1.9. The structure of $[Ru(bpy)_3]^{2+}$ complex.[29] Reproduced from reference number 29 with permission by the Chemical Reviews.

1.6.2. Catalyst (Cat)

There are a variety of known catalysts that in conjunction with electrons from the photosensitizer can catalytically reduce CO_2 molecule to produce CO or HCOOH (discussed in the above in Section 1.2). These types of the photocatalysts for CO_2 reduction that are the two component systems, which contain the photosensitizer and the catalyst, and the supramolecular photocatalysts, which the photosensitizer and catalyst are connected to each other by a bridging ligand, are very well known area.[2,26,28,30] Polypyridine ligands, which have a minimum of two conjugated pyridine motifs, have been used widely in these catalysts that are used for CO_2 reduction. These polypyridine ligands have the ability to stabilize the reduced metal and to accept the reducing equivalents. The bipyridine (bpy), terpyridine (tpy), phenanthroline (phen), and quaterpyridine (qtpy) ligands are some examples of these polypyridine ligands that are used in the photocatalysts CO_2 reduction. Examples of the polypyridine ligands are shown in Scheme 1.10, and the abbreviations of these polypyridine ligands are given in Table 1.4.[28]

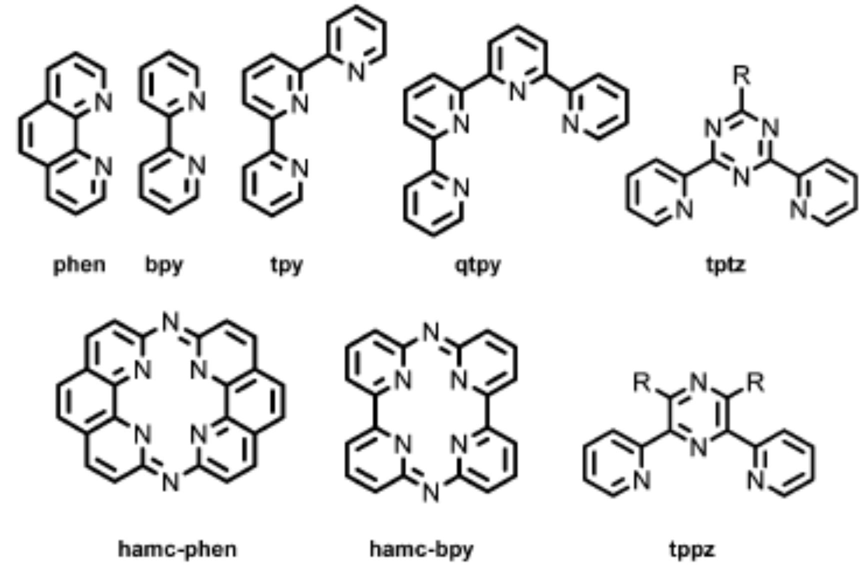

Scheme 1.10. The structure and abbreviation of the most common polypyridyl ligands.[28] Produced from reference number 28 with permission by Chemical Society Reviews.

Table 1.4. The Abbreviations of the most common polypyridyl ligands.[28]

Abbreviations	Name
phen	1,10-phenanthroline
bpy	2,2′-bipyridine
tpy	2,2′:6′,2″-terpyridine
qtpy	2,2′:6′,2″:6″,2‴- quaterpyridine
tptz	2,4,6-tri(pyridine-2-yl)-1,3,5-triazine
hamc-phen	diaza-1,3(2,9)-diphenanthrolinacyclobutaphane
hamc-bpy	diaza-1,2,4,5(2,6)- tetrapyridinacyclo-hexaphane
tppz	2,3,5,6-tetra(pyridine-2-yl)pyrazine.

These abbreviations of the most common polypyridyl ligands are used in scheme 1.10.

There are several important factors that should be considered when attempting to design the catalysts with effective reactivity. They include high activity, high stability, high efficiency, and high selectivity, and these parameters were explained in section 1.2 common terms in the photo-catalytic reduction.[2,28]

The Re(I) complexes [$\mathrm{Re^{I}(bpy)(CO)_3(X)}$] (X= Cl, or Br) were the first photo-catalysts for CO_2 reduction reported by Lehn and coworkers which are able to reduce CO_2 to CO.[19,26] In addition, this Re(I) complex has the ability to work as both the catalyst and also as the photosensitizer for CO_2 making a Type II system.[26,31,32] The catalytic ability of this complex has undergone extensive investigation, which have lead to increase of the catalytic ability and the efficiency of this Re(I) complex. For example, one approach was to change the halo ligand, X^-, to explore the role of this group in the catalysis. These substituents are such as CN^-, PPh_3, and {$P(OEt)_3$}. Another approach was to add substituents on the bipyridine ligands. The substituents that have been used on the bipyridine ligands include H, CH_3, COOH, or CN. Four different Re(I) complexes with different substituents in the bipyridine ligand $\mathrm{Re(bpy\text{-}R)(CO)_3Cl}$ (R = H, CH_3, CN, or COOH) are documented to show the photocatalytic ability to reduce CO_2 to CO. The highest molar absorption coefficient between them was achieved with COOH group.[26,28,33,34] The chemical structure of $\mathrm{Re(bpy\text{-}R)\ (CO)_3Cl}$ complexes are shown below in Scheme 1.11.[34]

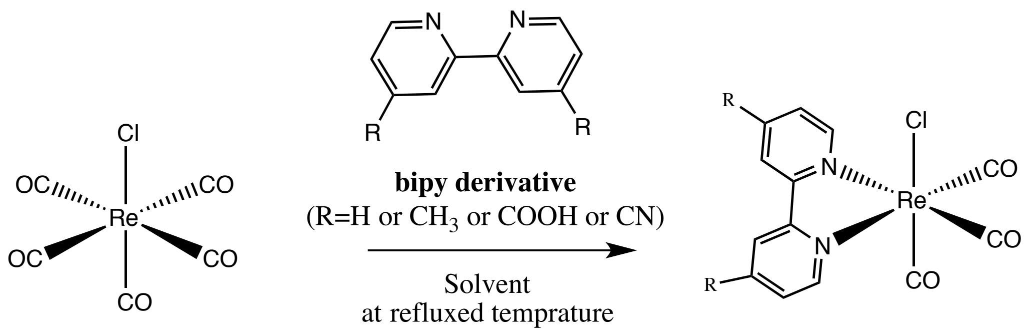

$Re(CO)_5Cl$

Re (bipy-R)

Scheme 1.11. The structure of $Re(bpy-R)(CO)_3Cl$ complexes.[34] Reproduced from reference number 34 with permission by the American Journal of Applied Chemistry.

A more dramatic modification was to change the Re center to Mn in order to investigate and the ability to use a more abundant metal center. This catalyst was mentioned before, and it behaves differently under photo catalysis versus electro catalysis. This *fac*-$Mn(bpy)(CO)_3Br$ catalyst was able to reduce the CO_2 to formate in the photocatalytic systems, and it was able to reduce the CO_2 to CO in the electrochemical reduction.[24–26,28,35,36]

1.6.3. Electron Donor (D)

The catalytic cycles of these photocatalytic CO_2 reduction are activated by the reductive quenching process, and in this reductive quenching process the electron will be injected into the excited state of the photosensitizer (PS*) from the electron donor (D). Following the reductive quenching process, the one-electron-reduced species (OERS) of PS ($PS^{\bullet-}$) and the one-electron-oxidized species (OEOS) of the D ($D^{\bullet+}$) will be formed. There are many different electron donors that can be used in the photocatalytic system, but there are some points that have to be consider in the selection of these electron donors. For example, the stability of the oxidized electron donor ($D^{\bullet+}$) is one of the important points that should be considered because it has a large effect on the overall efficiency of the photocatalytic system due to the back-electron transfer that can happen from the reduced excited state of the photosensitizer ($PS^{\bullet -}$) to the oxidized electron donor ($D^{\bullet +}$). Another point that should be also considered in the choosing the electron donor is the reactivity of the oxidized donor and byproducts. These species can react with the intermediates in the photocatalytic process. These considerations are very important in the selecting the electron donors. There are some electron donors that have been widely used in most of the photocatalytic systems for CO_2 reduction. These include triethanolamine (TEOA), triethylamine (TEA), 1-benzyl-1,4-dihydronicotinamide (BNAH), ascorbic acid (H_2A), and sodium ascorbate (NaA).[26,28] Some structures of these electron donors are shown below in Scheme 1.12. The reactivity of the these electron donors are shown in the reported literature.[26]

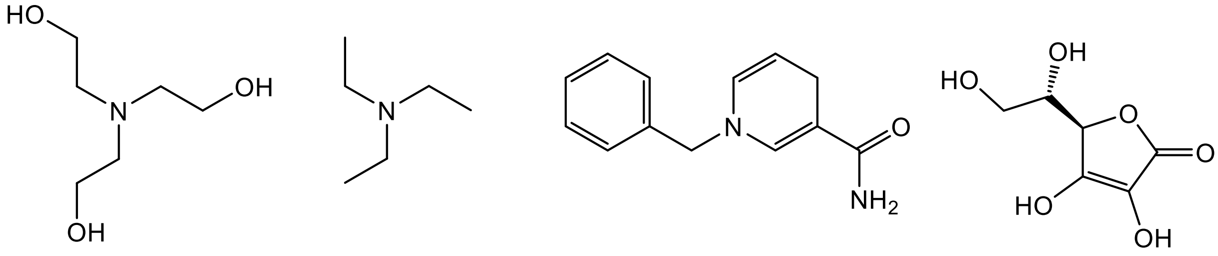

TEOA **TEA** **BNAH** **$ASCH_2$**

Scheme 1.12. The structures of some electron donors complexes.[26,28] Reproduced from reference number 26 with permission by the Elsevier.

1.6.4. Solvent (S)

There are some commonly employed organic solvents that are used in most of the photocatalytic systems for CO_2 reduction. These solvents include dimethylformamide (DMF), acetonitrile (ACN), dimethylacetamide (DMA), and methanol (MeOH).[8,9,26,28]

1.7. General Experimental Techniques

The following sections cover the commonly employed techniques in this field. There are also some details specific to the experimental techniques that will be used in the following chapters.

1.7.1. Photocatalytic CO_2 Reduction Systems Experimental Environment

1.7.1.1. Experimental Details

In a typical photocatalytic experiment used in this thesis, a 20 mL glass vial with a magnetic stirrer bar was charged with 4mL of a solvent mixture, such as N,N-dimethylformamide (N,N- DMF) or acetonitrile (MeCN), that contained the catalyst, the photosensitizer ($[Ru(bpy)_3](PF_6)_2$), and the electron donor (e.g. triethanolamine (TEOA), trimethylamine (TEA) or 1-benzyl-1,4-dihydronicotinamide (BNAH)). The vial was then sealed and removed from the nitrogen filled glovebox. The solution was purged with CO_2 for 15 minutes followed by irradiation using a 405 nm LED light (radiant flux at 700 mA of 1050 mW) for 24 hours. The light intensity was measured to be $3.4x10^{-8}$ moles photons s^{-1} using a $Ru(bpy)_3^{2+}$/1,9-diphenylanthracene (DPA) actinometer as described in the reported literature)[6] Some photographs of the irradiation apparatus that were used for the photocatalytic experiments of this thesis are shown below in Scheme 1.13.

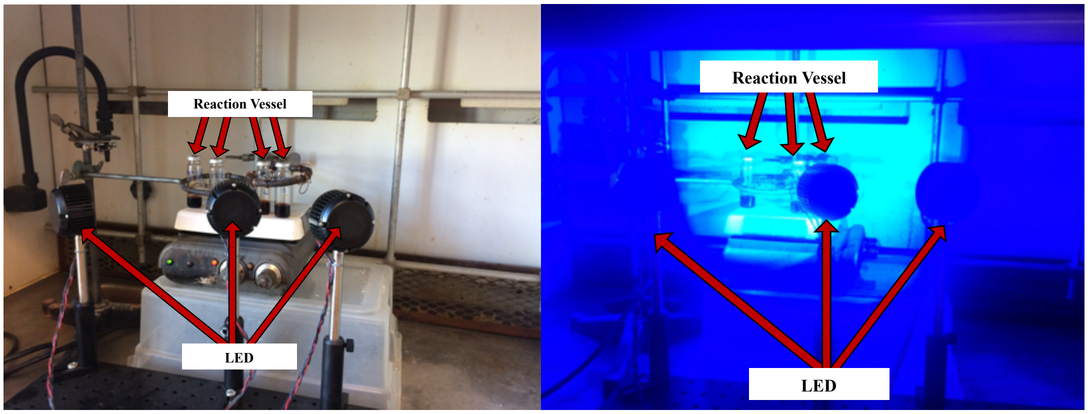

Scheme 1.13. The photographs of the irradiation apparatus used for the photocatalytic experiments before and during the light irradiation.

1.7.1.2. Experimental Results

The gaseous products of reduction, CO and H_2, were measured using an Agilent 7820A gas chromatograph (GC) with an Agilent select permanent gases column and equipped with a thermal conductivity detector (TCD). The gas chromatography (GC) is a technique that is used to detect and quantify the volatile compounds in the gas phase, and the thermal conductivity detector (TCD) is a commonly detector that is used in gas chromatography to give the integration of the peak. In general, the chromatographic data is shown as a graph of detector response versus the retention time, and it gives a spectrum of peaks for the sample that will be injected to represent the substance analytes that are present in the sample eluting from the column at different times. Retention time can be used to identify analytes, and the area under a peak is proportional to the amount of the analyte present. The concentration of the analyte in the original sample can be determined by calculating the area of the peak using a calibration curve that can be created by determining the response for a series of concentrations of analyte. A calibration curve for carbon monoxide and hydrogen was prepared, and the amount of the carbon monoxide and hydrogen were determined using the integrated values for the carbon monoxide and hydrogen (17.409, 5.393 min) and the calibration curve.

The liquid products from the photocatalytic reactions were analyzed using ^{1}H NMR and ^{13}C when appropriate. A calibration curve for formic acid was prepared in D_2O containing dimethyl sulfone as an internal standard. An aliquot (100 μL) was removed from the irradiated samples and was mixed in an NMR tube with D_2O containing a known amount of dimethyl sulfone (400 μL). The sample was mixed well and the ^{1}H NMR spectra were collected. Using the integrated values for the formic acid ($\delta \approx 8.1$ ppm) and a calibration curve, the amount of formic acid was determined.[37]

1.7.2. Photocatalytic $^{13}CO_2$ Reduction Systems Experimental Environment

In order to definitively confirm that the products were derived from photocatalytic CO_2 reduction, in some cases photocatalytic reduction was carried out under a $^{13}CO_2$ atmosphere employing the same condition as outlined above. Analysis of these results used high resolution mass spectrometry for analysis of ^{13}CO and $H^{13}COOH$. These measurements were performed using a Kratos Concept 1S HiRes Electron Impact Magnetic Sector Mass Spectrometer using an inlet system in the John L. Holmes Mass Spectrometry Center at the University of Ottawa.

1.7.3. Actinometer Experiment

The flux of photons from the experimental arrangement was measured using an actinometery experiment described in the literature.[6] The light intensity was measured to be 3.4×10^{-8}moles photons s^{-1} using a $Ru(bpy)_3^{2+}$/1,9-diphenylanthracene (DPA) actinometer. Data from the experimental measurement is shown below and as shown in Figure 1.2.

Details for the method of carrying out this experiment are as follows:

1) The experiment was performed in a dark room and used the same reaction vessel as the photochemistry experiment. A solution of $Ru(bpy)_3(PF_6)_2$ (0.19 mM) and DPA (0.10 mM) in acetonitrile was prepared.

2) A UV-Vis spectrum of the $Ru(bpy)_3(PF_6)_2$ and DPA solution before irradiation was measured. This was used as the "time zero" spectrum and the absorbance at 372 nm was used as the intial absorbance (AINITIAL).

3) The sample was placed in the photochemical system and irradiated for a set period of time (6 minutes).

4) A new UV-Vis Spectrum of the irradiated sample was recorded and the absorbance at

372 nm was measured and used as the final absorbance (AFINAL).

5) Using the volume of the irradiated sample (5 mL) and the reported molar extinction coefficient (ε) for DPA of 11,100 $M^{-1}cm^{-1}$, the number of moles of DPA consumed during the irradiation can be determined using the following equation (1).

$$\#\text{ of moles DPA consumed} = \left(\frac{AINITIAL-AFINAL}{\varepsilon 372\ nm\ \iota}\right) \times \mathrm{V} \qquad (1)$$

$$\#\text{ of moles DPA consumed} = \left(\frac{0.913946927-0.368025571}{11{,}100\ \mathrm{M-1cm-1}\ \times 1\ \mathrm{cm}}\right) \times 0.005\ \mathrm{L}$$

$$\#\text{ of moles DPA consumed} = 0.00000025\ \text{mole} = 2.5 \times 10^{-7}\ \text{mole}$$

Where AINITIAL and AFINAL are the absorbance of the solution at 372 nm before and after irradiation, respectively; $\varepsilon_{372\ \mathrm{nm}}$ is the extinction coefficient of DPA at 372 nm in acetonitrile, l is the path length of the cuvette (10 mm = 1 cm), and V is the volume of the sample for which the absorption was measured (5 mL = 0.005 L).

6) Since the quantum yield (Φ) for this actinometer system is known to be 0.019, the number of moles of photons absorbed by the sample per unit time can be determined by using the number of moles DPA consumed and by applying equation (2).

$$\frac{Nh\nu}{t} = \frac{moles\ of\ DPA\ consumed}{\Phi\ \mathrm{t}} \qquad (2)$$

$$\frac{Nh\nu}{t} = \frac{2.5 \times 10{-}7\ \text{mole}}{0.019 \times 360\ \text{second}}$$

$$\frac{Nh\nu}{t} = 3.7 \times 10^{-8}\ \text{mole/second}$$

where Φ is the quantum yield of DPA consumption, and t is the irradiation time in seconds.

7) To determine the Φ for the reaction of interest, the sample of interest must be irradiated using the same geometry employed for the actinometer, and when the irradiation is complete then the number of moles of product formed or substrate consumed per unit time must be determined using an appropiate analytical technique. This one the equation (3) can be applied to determine the Φ of the reaction.

$$\Phi = \frac{\#\ of\ moles\ consumed\ or\ produced}{t} \times \left(\frac{Nhv}{t}\right)^{-1} \qquad (3)$$

$$\Phi = \frac{2.5 \times 10-7\ \text{mole}}{360\ \text{second}} \times (3.7\ \times\ 10-8\ \text{mole/second})^{-1}$$

$\Phi = 0.01876864$

Where t is the time of irradiation and $\left(\frac{Nhv}{t}\right)^{-1}$ is the reciprocal of the number of photons absorbed by the sample per unit time.

In order to ensure the accuracy of this measurement, this experiment was repeated with different position of the reaction vessel as shown in the picture in Scheme 1.14.

Repeating the same experiment and same calculation but with different position of the reaction vessel in the photochemical process and take the average between them:

$$\#\ \text{of moles DPA consumed} = \left(\frac{AINITIAL-AFINAL}{\varepsilon 372\ nm\ \iota}\right) \times \text{V} \qquad (1)$$

$$\#\ \text{of moles DPA consumed} = \left(\frac{0.874016881-0.407077521}{11{,}100\ \text{M}-1\text{cm}-1\ \times 1\ \text{cm}}\right) \times 0.005\ \text{L}$$

$\#$ of moles DPA consumed = 0.00000021 mole = 2.1×10^{-7} mole

$$\frac{Nhv}{t} = \frac{moles\ of\ DPA\ consumed}{\Phi\ \text{t}} \qquad (2)$$

$$\frac{Nhv}{t} = \frac{2.1 \times 10-7\ \text{mole}}{0.019 \times 360\ \text{second}}$$

$$\frac{Nhv}{t} = 3.07 \times 10^{-8}\ \text{mole/second} = = 3.1 \times 10^{-8}\ \text{mole/second}$$

$$\Phi = \frac{\#\ of\ moles\ consumed\ or\ produced}{t} \times \left(\frac{Nhv}{t}\right)^{-1} \qquad (3)$$

$$\Phi = \frac{2.1 \times 10-7\ \text{mole}}{360\ \text{second}} \times (3.1\ \times\ 10-8\ \text{mole/second})^{-1}$$

$\Phi = 0.0190009771987$

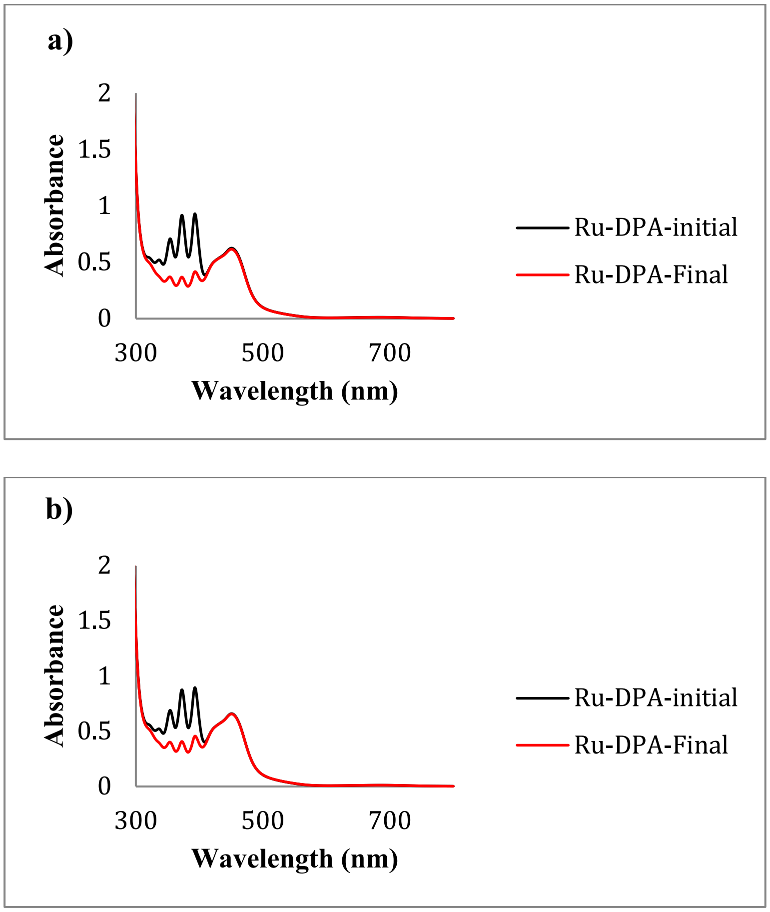

Figure 1.2. Absorption spectra of a typical actinometry experiment performed with $Ru(bpy)_3(PF_6)_2$ (0.19 mM) and DPA (0.10 mM) in acetonitrile and irradiated with a 405 nm light. $A_{INITIAL}$ is before irradiation and A_{FINAL} is after 6 minutes of irradiation. In this case of a and b, the actinometer experiment was performed in different position of light.

1.7.4. Emission-Quenching Experiments

Since the photochemical process involves the transfer of energy from the excited state photosensitizer (**PS***) to another agent, commonly the electron donor, emission quenching experiments using the sacrificial electron donor and catalyst molecules was carried out in a similar manner to a procedure in the literature.[38] A solution of the photosensitizer $Ru(bpy)_3(PF6)_2$ (0.1 mM) in anhydrous acetonitrile were prepared and mixed with different concentrations of the quencher. For example, using the sacrificial electron donors, TEOA or TEA, the concentration was varied from 0.375 mM to 1.875 mM as shown in Figures 1.3 and 1.4 respectively. The steady-state emission spectrum (excitation wavelength 450 nm) of each solution was recorded, and the intensity of the luminescence for the ^{3}MLCT excited state of the photosensitizer (452 nm) was recorded. Quenching rate constants k_q for both quenchers were calculated from the linear Stern-Volmer plots as shown in Figure 1.5. The Stern-Volmer equation is is expressed by the shown below equation.

$$\frac{I^0{}_f}{I_f} = 1 + \kappa_q\, \mathcal{T}_0 \cdot [Q]$$

Where $I^0{}_f$ is the intensity or the rate of fluorescence without a quencher, I_f is the intensity or the rate of the fluorescence with a quencher, κ_q is the quencher rate coefficient, $\mathcal{T}_0$ is the lifetime of the emissive excited state without a quencher present and $[Q]$ is the concentration of the quencher.

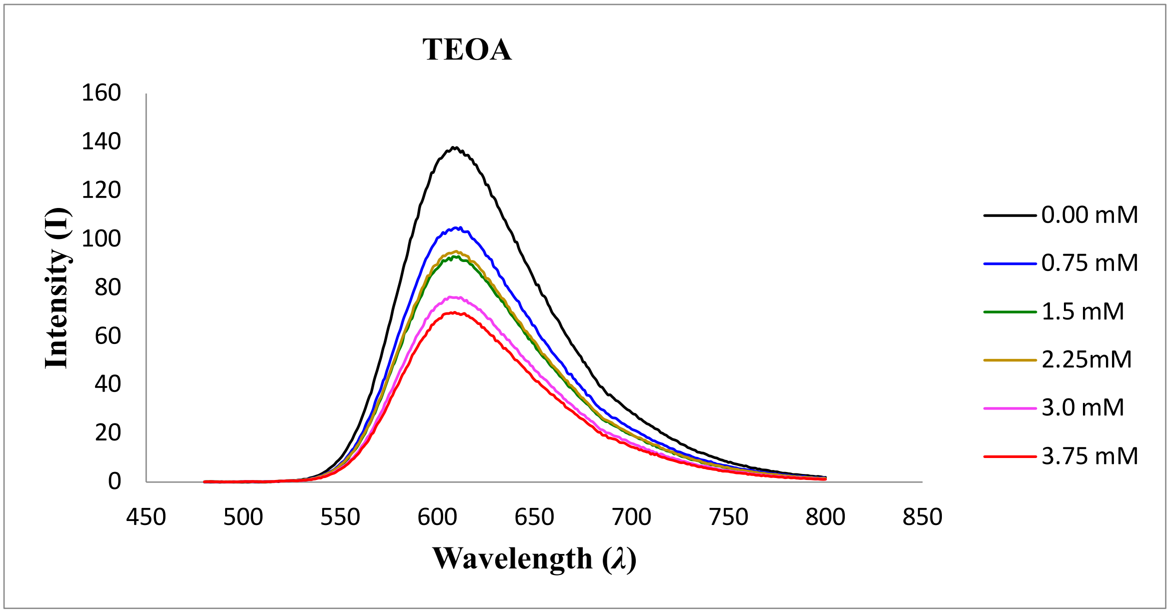

Figure 1.3. Spectra demonstrating the quenching of the emission from the photosensitizer $Ru(bpy)_3(PF_6)_2$ with various concentrations (0-3.75 mM) TEOA.

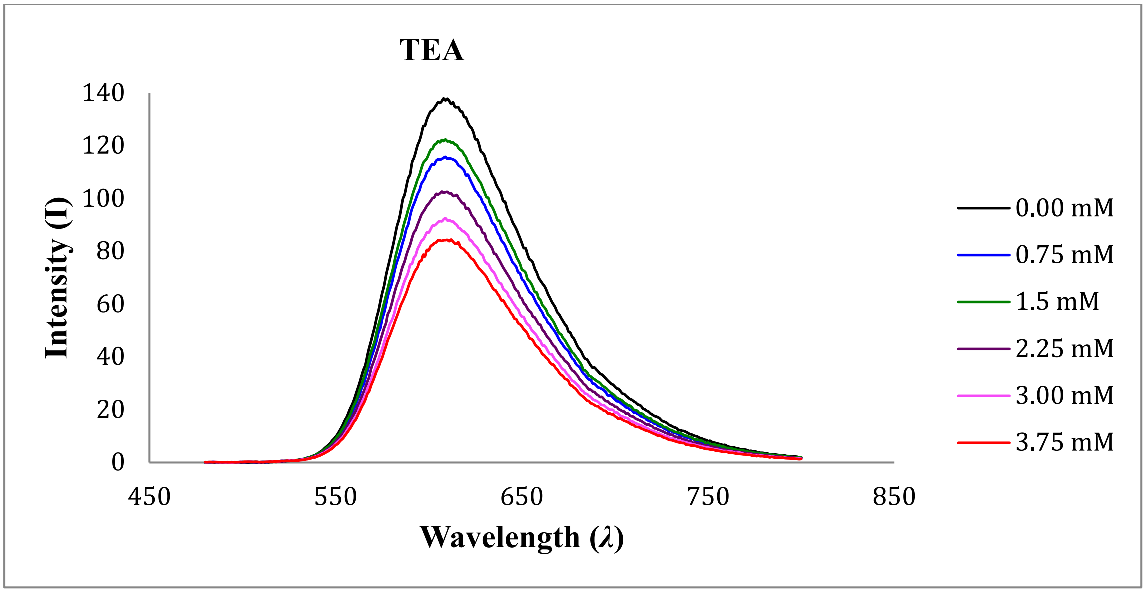

Figure 1.4. Spectra demonstrating the quenching of the emission from the photosensitizer $Ru(bpy)_3(PF_6)_2$ with various concentrations (0-3.75 mM) trimethylamine (TEA).

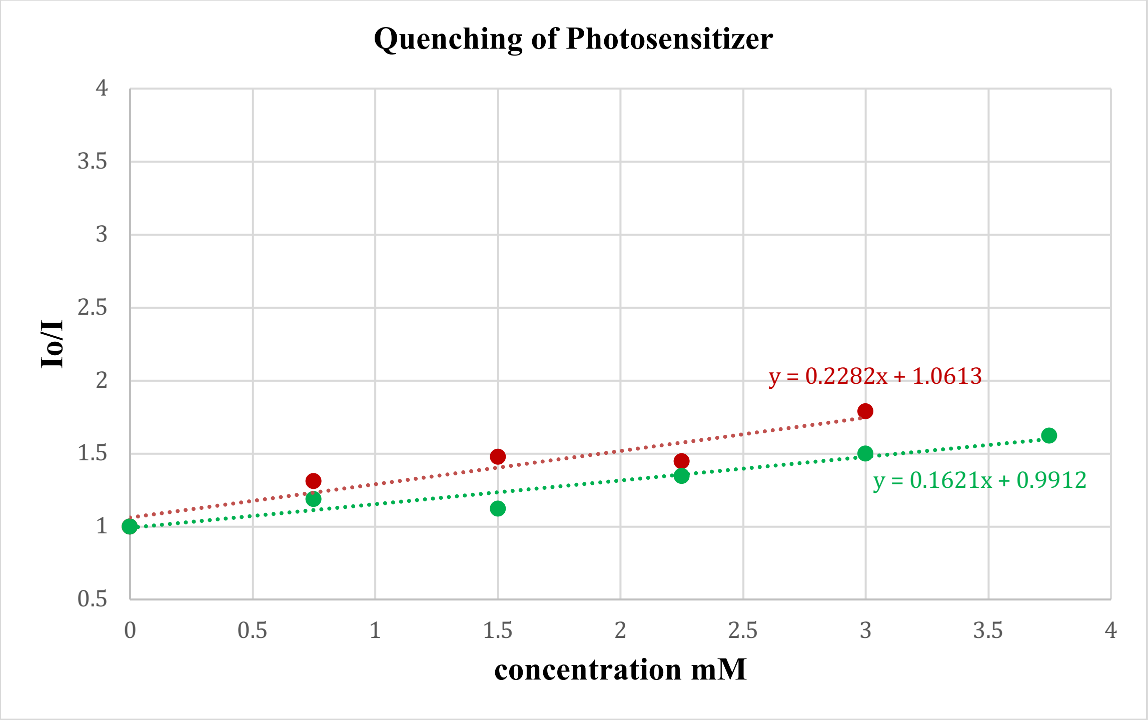

Figure 1.5. Stern-Volmer plot for quenching of the emission of the photosensitizer $Ru(bpy)_3(PF_6)_2$ with various concentrations of TEOA (red) TEA (green). Linear equations are shown.

1.7.5. Electrocatalytic Reduction of CO_2

Electrochemical characterization is an excellent and direct method to investigate and explore the reactions that are involving electron transfers, and the cyclic voltammetry (CV) is a powerful electrochemical technique usually used to probe the reduction and oxidation processes of the complexes in electrocatalytic system. Furthermore, exploration of electrocatalytic reduction processes provides an ally to the photocatalysis reduction that is at the heart of this thesis. The reduction potentials for some reduction reactions of CO_2 are presented in Table 1.1. Electrochemical investigations can be used as characterization and as a means to probe reduction mechanism by providing useful kinetic and mechanistic information about the reduction and oxidation processes of the catalysts. Such measurements can also reveal possible electrocatalytic processes. In general, molecular electrochemistry has been a fundamental technique for revealing catalysts in electroreduction CO_2. For a basic introduction about electrochemistry and to understand more about the requirements tools of the electrochemistry and cyclic voltammetry the reader is referred to the literature.[39]

For the experimental conditions in this thesis, all cyclic voltammetry experiments have been carried out in a three neck round bottom flask, and the solution of the sample should be prepared in a glove box under N_2 atmosphere and sealed before removing from the glove box for the measurement. The cyclic voltammetry was performed using a VersaSTAT 3 (Princeton Applied Research) potentiostat, and a conventional three electrode system was employed. A glassy carbon electrode (diameter = 0.2 cm) was used as the working electrode, a Pt wire as the auxiliary electrode, and an Ag wire was used as pseudo-reference electrode. For bulk electrocatalytic reduction experiments, a glassy carbon rod (diameter = 0.4 cm; length 2 cm) was used as the working electrode, a Pt gauze as the auxiliary electrode, and an Ag wire was used as pseudo-reference electrode. The ferrocene/ferrocenium couple was used as the reference potential was added to the analysis mixture after purging CO_2 and measured before and after water addition. Dried acetonitrile was purchased from Sigma-Aldrich and stored on molecular sieves in a glove-box. Tetrabutylammonium hexafluorophosphate has been used as the supporting electrolyte, and it was crystallized two times from dried methanol and dried in vacuum at 90 °C for 24 h before use and stored in glove box. The electrolyte solution, 0.1 M $(n\text{-Bu})_4N(PF_6)$ in CH_3CN, was saturated with N_2 or CO_2 by purging with N_2 or CO_2 (purity. 99.8%, BOC gases) for 15 min prior to each experiment. The concentration of catalyst was 1 mM (15 mL acetonitrile) in each experiment. Evolved carbon monoxide and hydrogen gasses was measured using an Agilent 7820A gas chromatograph (GC) equipped with a thermal conductivity detector (TCD) analyzer using an Agilent select permanent gases column.[40]

1.7.6. X-ray Crystallography

In general, crystals were mounted on thin glass fibers using paraffin oil. Prior to data collection, crystals were cooled to 200.15 °K. Data were collected on a Bruker AXS SMART single crystal diffractometer equipped with a sealed Mo tube source (wavelength 0.71073 Å) APEX II CCD detector. Raw data collection and processing were performed with APEX II software package from BRUKER AXS.[41] Initial unit cell parameters were determined from 60 data frames with 0.3° ω scan each collected at the different sections of the Ewald sphere. Semi-empirical absorption corrections based on equivalent reflections were applied.[42] Systematic absences in the diffraction data-set and unit-cell parameters were consistent with the assigned space group. The structures were solved by direct methods, completed with difference Fourier synthesis, and refined with full-matrix least-squares procedures based on F^2. All hydrogen atoms positions were calculated based on the geometry of the related non-hydrogen atoms. All hydrogen atoms were treated as idealized contributions during the refinement. All scattering factors are contained in several versions of the SHELXTL program library, with the latest version used being v.6.12.[43]

1.8. Thesis Outline (Summary of Content for the body of the thesis)

The increasing in the rate of the CO_2 production provides a strong impetus to discover new catalysts that are able to reduce CO_2. The history and background of the photocatalytic CO_2 reduction that were described in this introduction show that this area is a rich and active research area. In this thesis, the focus will be on homogeneous molecular catalysts for the photocatalytic CO_2 reduction, and the research objective of the thesis will be to discover and explore new catalysts for the photocatalytic reduction of CO_2 to produce more valuable products such as CO and HCOOH. This approach to discovery has employed many different ligand geometries with a range of metal centers in order to discover new molecular catalysts that have the ability for the CO_2 reduction. This dissertation is constructed with eight chapters, and a brief summary description of these chapters follow.

1.8.1. Chapter 1 “Introduction”

This chapter gives a brief introduction of the photochemistry and the photocatalytic CO_2 reduction. The general backgrounds and the overview of the whole photocatalytic CO_2 reduction system were explained in this chapter. In addition, this chapter gives an overview of the experimental techniques and environments that were used in the research of this thesis.

1.8.2. Chapter 2 “Photocatalytic CO_2 Reduction with Manganese Complexes Bearing a κ^2- PN Ligand.”

In this chapter, new catalysts were explored for the photocatalytic CO_2 reduction. New group 7 compounds built on Mn(I) and Re(I) with PN-H and PN-Me ligands architectures were discovered for the CO_2 photoreduction.[37] Furthermore Mn-PN-Me and Mn-PNP-Me complexes were revealed to be good catalysts for electrocatalytic CO_2 reduction.[40] Group 7 compounds have an established history in this area, but there are a limited range of ligands for photo- and electrocatalysts for CO_2 reduction. Specifically, the common supporting ligands have been limited 2,2’-bipyridine and related species to give compounds of the general formulae, $[M(bpy)(CO)_3X]$ (M= Re or Mn, X= Cl or Br). These species remain as the benchmark compounds in this field. The goal in this chapter was to explore a significant modification of these catalysts by removing the α-diimine ligand and replacing it with a bi-dentate “PN” ligand.

1.8.3. Chapter 3 “Visible light photocatalytic reduction of CO_2 to formic acid with a Ru catalyst supported by an unprecedented ligand array”

In this chapter the PNP ligand, that is the extended type of the PN ligand, was explored as a supporting ligand for photocatalysis. This tridentate PNP ligand has a different geometry than the previous reported bidentate PN ligand. The goal of this tridentate PNP ligand was to investigate other pyridine-centered ligand that has the ability to develop distinctive metal coordination geometries and novel reactivity for the reduction catalysis. The tridentate ligand was used to prepare some unique Ru(II) complexes which demonstrated excellent ability towards the CO_2 photoreduction. Ruthenium was selected due to the established ability of its 2,2’-bipyridine complexes as effective photocatalyst for CO_2 reduction. Replacement of this ligand limitation by employing the Ru-PNP complexes not only revealed new photocatalysts but opened this area to investigation with new metal architectures.

1.8.4. Chapter 4 “Photocatalytic reduction of CO_2 to formic acid with Zn catalysts supported by different ligand arrays”

This chapter introduces a new distinctive metal coordination geometry that has novel reactivity towards the photocatalytic CO_2 reduction. Photochemical carbon dioxide reduction using the redox inactive Zn(II) complex of bipyridine (bpy) ligand. In addition, different bidentate ligands displaying extended π-bonding architectures, such as the 1,10-phenanthroline-5,6-dione (phendione) and the 11,12-dimethyldipyrido[3,2-a:2',3'-c]phenazine (dppz) ligands, gave similar or improved photocatalytic reactivity. These new Zn photocatalysts show the novel reactivity towards the photocatalytic CO_2 reduction, and they have the ability to reduce CO_2 to HCOOH.

1.8.5. Chapter 5 “Photocatalytic reduction of CO_2 to formic acid using a Rhenium(I) Bisbipyridine Dicarbonyl Complex”

This chapter describes a new geometry for the photocatalyst with a Re(I) complex. The use of two bpy ligands yielded the species $Re(bpy)_2(CO)_2$. This complex is already reported in the literature[44], but their activity for CO_2 reduction has not been explored. The goal was to explore new compounds that show the novel ability to reduce CO_2 to other valuable products.

1.8.6. Chapter 6 “Dimers, Monomers and Pentacoordination in a Series of Earth-Abundant Transition Metal Dibromide Complexes Supported by a Neutral SNS Ligand Framework and their Applications in the Catalysis”

In this chapter a new ligand and broader scan of metal complexes are presented. New pyridine-centered ligands were explored and examined their reactivity for CO_2

reduction. The SNS ligands provide a neutral pincer ligand array reminiscent of PNP ligands due to the replacement of the P with S. A series of first row metal complexes were synthesized with this SNS ligand and characterized, and the activity of these catalysts were studied for CO_2 reduction.[45] These first-row metals Mn/Fe/Co/Ni/Cu/Zn-SNS-Br_2 complexes do not show the desired results. However, they show a good activity towards the hydrogen production from water in the photocatalytic process.

1.8.7. Chapter 7 "Conclusion and Future Work"

This chapter provides a general conclusion about the photochemistry and the photocatalytic CO_2 reduction, and it also gives an overview about the recommendations for the future works and directions for this photocatalytic research.

1.9. Conclusion

The approach to utilization CO_2 is an interesting topic with a broad scope that has attracted many scientists and investigators to overcome the challenges of transforming CO_2 to more valuable products as CO and HCOOH. Polypyridine–metal complexes are the largest class of the molecular catalysts for the electro- and photo-catalytic CO_2 reduction. In this thesis, the research objectives and main goals are to explore new catalysts for photocatalytic reduction of CO_2 to produce CO or HCOOH. Therefore, there are different approaches with different ligand geometries that will be presented and discussed in this thesis in order to investigate and explore new catalysts for CO_2 reduction.

1.10. References

1 J. Wu, Y. Huang, W. Ye and Y. Li, *Adv. Sci.*, 2017, **4**, 1700194.

2 A. J. Morris, G. J. Meyer and E. Fujita, *Acc. Chem. Res.*, 2009, **42**, 1983–1994.

3 J.-M. Lehn and R. Ziessel, *Proc. Natl. Acad. Sci.*, 1982, **79**, 701–704.

4 S. Dunn, *Int. J. Hydrogen Energy*, 2002, **27**, 235–264.

5 L. J. Guo, L. Zhao, D. W. Jing, Y. J. Lu, H. H. Yang, B. F. Bai, X. M. Zhang, L. J. Ma and X. M. Wu, *Energy*, 2009, **34**, 1073–1090.

6 S. P. Pitre, C. D. McTiernan, W. Vine, R. DiPucchio, M. Grenier and J. C. Scaiano, *Sci. Rep.*, 2015, **5**, 16397.

7 J. Hong, W. Zhang, J. Ren and R. Xu, *Anal. methods*, 2013, **5**, 1086–1097.

8 S. Nahar, M. Zain, A. Kadhum, H. Hasan and M. Hasan, *Materials (Basel).*, 2017, **10**, 629.

9 A. Juris, V. Balzani, F. Barigelletti, S. Campagna, P. l Belser and A. Von Zelewsky, *Coord. Chem. Rev.*, 1988, **84**, 85–277.

10 R. Reithmeier, C. Bruckmeier and B. Rieger, *Catalysts*, 2012, **2**, 544–571.

11 A. H. Dwivedi and U. C. Pande, *Sci. Revs. Chem. Commn*, 2012, **2**, 41–452.

12 J. P. Celli, B. Q. Spring, I. Rizvi, C. L. Evans, K. S. Samkoe, S. Verma, B. W. Pogue and T. Hasan, *Chem. Rev.*, 2010, **110**, 2795–2838.

13 A. H. A. Tinnemans, T. P. M. Koster, D. Thewissen and A. Mackor, *Recl. des Trav. Chim. des Pays-Bas*, 1984, **103**, 288–295.

14 E. Kimura, S. Wada, M. Shionoya, T. Takahashi and Y. Litaka, *J. Chem. Soc. Chem. Commun.*, 1990, 397–398.

15 E. Kimura, X. Bu, M. Shionoya, S. Wada and S. Maruyama, *Inorg. Chem.*, 1992, **31**, 4542–4546.

16 E. Kimura, S. Wada, M. Shionoya and Y. Okazaki, *Inorg. Chem.*, 1994, **33**, 770–778.

17 B. Gholamkhass, H. Mametsuka, K. Koike, T. Tanabe, M. Furue and O. Ishitani, *Inorg. Chem.*, 2005, **44**, 2326–2336.

18 S. Sato, K. Koike, H. Inoue and O. Ishitani, *Photochem. Photobiol. Sci.*, 2007, **6**, 454–461.

19 J. Hawecker, J.-M. Lehn and R. Ziessel, *J. Chem. Soc. Chem. Commun.*, 1983, 536–538.

20 J. Grodkowski, P. Neta, E. Fujita, A. Mahammed, L. Simkhovich and Z. Gross, *J. Phys. Chem. A*, 2002, **106**, 4772–4778.

21 J. Grodkowski, T. Dhanasekaran, P. Neta, P. Hambright, B. S. Brunschwig, K. Shinozaki and E. Fujita, *J. Phys. Chem. A*, 2000, **104**, 11332–11339.

22 J. Grodkowski and P. Neta, *J. Phys. Chem. A*, 2000, **104**, 1848–1853.

23 J. Hawecker, J. Lehn and R. Ziessel, *Helv. Chim. Acta*, 1986, **69**, 1990–2012.

24 H. Takeda, H. Koizumi, K. Okamoto and O. Ishitani, *Chem. Commun.*, 2014, **50**, 1491–1493.

25 M. Bourrez, F. Molton, S. Chardon-Noblat and A. Deronzier, *Angew. Chemie Int. Ed.*, 2011, **50**, 9903–9906.

26 Y. Yamazaki, H. Takeda and O. Ishitani, *J. Photochem. Photobiol. C Photochem. Rev.*, 2015, **25**, 106–137.

27 G. J. Kavarnos and N. J. Turro, *Chem. Rev.*, 1986, **86**, 401–449.

28 N. Elgrishi, M. B. Chambers, X. Wang and M. Fontecave, *Chem. Soc. Rev.*, 2017, **46**, 761–796.

29 C. K. Prier, D. A. Rankic and D. W. C. MacMillan, *Chem. Rev.*, 2013, **113**, 5322–

5363.

30 G. Sahara and O. Ishitani, *Inorg. Chem.*, 2015, **54**, 5096–5104.

31 C. Kutal, M. A. Weber, G. Ferraudi and D. Geiger, *Organometallics*, 1985, **4**, 2161–2166.

32 K. Kalyanasundaram, *J. Chem. Soc. Faraday Trans. 2 Mol. Chem. Phys.*, 1986, **82**, 2401–2415.

33 H. Hori, F. P. A. Johnson, K. Koike, O. Ishitani and T. Ibusuki, *J. Photochem. Photobiol. A Chem.*, 1996, **96**, 171–174.

34 Y. Ono, J. Nakamura, M. Hayashi and K. I. Takahashi, *Am. J. Appl. Chem*, 2014, **2**, 74.

35 M. Bourrez, M. Orio, F. Molton, H. Vezin, C. Duboc, A. Deronzier and S. Chardon-Noblat, *Angew. Chemie Int. Ed.*, 2014, **53**, 240–243.

36 M. D. Sampson, A. D. Nguyen, K. A. Grice, C. E. Moore, A. L. Rheingold and C. P. Kubiak, *J. Am. Chem. Soc.*, 2014, **136**, 5460–5471.

37 Y. Hameed, B. Gabidullin and D. Richeson, *Inorg. Chem.*, 2018, **57**, 13092–13096.

38 A. Rosas-Hernández, C. Steinlechner, H. Junge and M. Beller, *Green Chem.*, 2017, **19**, 2356–2360.

39 N. Elgrishi, K. J. Rountree, B. D. McCarthy, E. S. Rountree, T. T. Eisenhart and J. L. Dempsey, *J. Chem. Educ.*, 2017, **95**, 197–206.

40 G. K. Rao, W. Pell, I. Korobkov and D. Richeson, *Chem. Commun.*, 2016, **52**, 8010–8013.

41 A. Mallick, S. Saha, P. Pachfule, S. Roy and R. Banerjee, *J. Mater. Chem.*, 2010, **20**, 9073–9080.

42 R. H. Blessing, *Acta Crystallogr. Sect. A*, 1995, 33–38.

43 G. M. Sheldrick, *Acta Crystallogr. Sect. A*, 2008, 112–122.

44 J. L. Smithback, J. B. Helms, E. Schutte, S. M. Woessner and B. P. Sullivan, *Inorg. Chem.*, 2006, **45**, 2163–2174.

45 Y. Hameed, S. Ouanounou, B. Gabidullin, I. Korobkov and D. Richeson, *Polyhedron*, 2018, **154**, 252–258.

Chapter 2: Breaking the α–Diimine Hold on Group 7 Catalysts and Switching Selectivity: Photocatalytic CO_2 Reduction with Manganese Complexes Bearing a Phosphinoaminopyridine Ligand

The work in this chapter formed a significant component of the following publication:

(Y. Hameed, B. Gabidullin, and D. S Richeson, *Inorg. Chem,* 2018, 57 (21), 13092–13096. DOI: 10.1021/acs.inorgchem.8b02719.)

In this chapter, the fundamental challenge of reducing CO_2 into more valuable energy containing compounds is addressed by efforts to reveal new catalysts for this process. By removing the long standing limitation of α-dimmine ligation, that is dominant in catalytic complexes in this area, new visible light, CO_2 reducing photocatalysts based on Mn and Re supported by phosphinoaminopyridine ligands, have been identified. These catalysts, $[M\{\kappa^2\text{-}(Ph_2P)NH(NC_5H_4)\}(CO)_3Br]$, displayed excellent product selectivity and when the metal center was changed, while maintaining identical ligand environments, gave a dramatic product switch from CO with M = Mn to HCO_2H with M = Re. The catalyst systems were explored with variation of the ligand, electron donor, solvent, and photosensitizer. The products were definitively traced using $^{13}CO_2$ as a substrate. Both the Mn and Re complexes quench the excited state photosensitizer $Ru(bpy)_3^{2+*}$ suggesting oxidative quenching as the entry into the catalytic cycle. This project was conceptualized by Y. Hameed and D. Richeson. The major contribution to the synthesis and characterization of the complexes and the catalytic behavior of the complexes were done by Y. Hameed. The crystallography was carried out by B. Gabidullin., and the DFT calculations of these complexes were carried out by D. Richeson.

2.1. Introduction

The catalytic reduction of carbon dioxide, the end product of fuel combustion and cellular respiration, represents a fundamental challenge due to the inherent stability of this simple, pervasive compound. Success in this endeavor would represent a paradigm shift to viewing CO_2 as a feedstock rather than as a waste product. The practical reduction of CO_2 into chemically valuable products hinges on the identification of an appropriate energy source and catalysts that can convert energy input into chemical transformation.[1–3] For eons, light has provided the limitless energy for plants to carry out selective and efficient CO_2 reduction. Reports that $[ReX(bipy)(CO)_3]$ (bipy = 2,2'-bipyridine, X = halide) complexes were selective photocatalysts for reduction of CO_2 to CO using triethanol amine (TEOA) as an electron donor, demonstrated the potential of metal complexes as catalysts for this transformation and remain a benchmark more than 30 years later.[4,5] While second and third row metal complexes have been shown to function as photocatalysts for CO_2 reduction, it is widely recognized that earth-abundant, first-row transition metal complexes must be the focus of designing economically viable, environmentally responsible and sustainable catalysts.[6–8] The determination to discover photocatalysts for CO_2 reduction has recently revealed first-row transition metal catalyst complexes that have been built around Fe,[9–12] Co,[13–20] Ni,[21–27] and Cu.[28,29] Group 7 complexes, headed by Mn, have continued to hold a central position in these efforts after $MnX(bipy)(CO)_3$ was demonstrated to electrocatalytically reduce CO_2[30] and subsequently shown to be, in the presence of a $Ru(bipy)_3^{2+}$ photosensitizer and electron donor (TEOA), capable of photocatalytically reducing CO_2 with selectivity for formic acid (89%, TON =157).[31] A cooperative chemical system is required in all of these cases, consisting of a photosensitizer (PS) an electron donor (ED) and the catalyst (CAT) species. Success to date has been a central challenge in catalysis, stimulating new catalyst design and revealing routes to new products and selectivities. Recent pertinent examples include the use of Ni complexes with mixed pyridine/carbene ligands[25] or mixed pyridine/thioether ligands[27] for selective visible-light driven CO_2 reduction catalysis.

With the key objectives of developing distinctive metal coordination geometries and novel reactivity, including reduction catalysis, we investigated the application of the bidentate *N*-(diphenylphosphino)-2-aminopyridine ligands ($\{Ph_2PNR\}NC_5H_4$; R = H, CH_3) with Mn(I) and Re(I) to yield unprecedented complexes, competent in photocatalytic reduction of CO_2. Ligand selection was based on an interrogation of the role of ligand on catalyst performance. First, replacement of one of the py moieties with a more basic phosphine donor targeted modulation of the electron density on the catalytic metal center. Second, modification of the amino substituent of the 2-aminopyridine group probes the importance of this group on catalyst execution. Finally, this ligand frame lacks the π-conjugation of the bipy scaffold, allowing interrogation of the criticality of this ligand feature. In fact, these complexes displayed not only uncommon selectivity for either CO or HCOOH that contrasts with the current photocatalytic reduction literature, but a distinctive switch in this selectivity depending on the identity of the metal center.

2.2. The synthesis and Characterization of the Complexes

2.2.1. Experimental Procedures

Reagents and analytical grade solvents were purchased from Strem Chemicals or Sigma Aldrich and used without further purification. The^1H, $^{13}C\{^1H\}$ and $^{31}P\{^1H\}$ NMR spectra were recorded at 400, 100 and 162 MHz respectively with chemical shifts reported in ppm using the residual protons of the NMR solvent as internal standards. The synthesis of "PN^{H}N" (2,6-$\{Ph_2PNH\}NC_5H_4$) and "PN^{Me}N" (2,6-$\{Ph_2PNH]CH_3\}NC_5H_4$) ligands was based on the procedures described in the literature.[38,39]

Synthesis of [Mn{κ^2-(Ph$_2$P)NH(NC$_5$H$_4$)}(CO)$_3$Br] (**1**): This synthesis is modified from the literature.[40] In a glove box, a solution of 2-(diphenylphosphinoamino)pyridine (0.138 g, 0.5 mmol) was prepared in 15 mL of tetrahydrofuran. $Mn(CO)_5Br$ (0.137 g, 0.5 mmol) was added via stirring to the THF solution of ligand. The flask was wrapped with aluminum foil, removed from the glovebox and connected to a Schlenk line via a reflux condenser. The reaction mixture was heated to 100°C under N_2 and stirred for an additional 3 h. Then, the solution was cooled to room temperature and the volume was reduced to ~3 mL and 50 mL of hexane was added to get the complex **1** as a yellow solid. Single crystals of **1** were grown by slow diffusion of hexane to the solution of 1 in THF. Yield 0.229 g (93%). The single crystal X-ray structure of **1** was independently obtained and analyzed and confirmed the identity of **1** was consistent with the literature (Figure 2.1).[40]

Synthesis of [Mn{κ^2-(Ph$_2$P)NMe(NC$_5$H$_4$)}(CO)$_3$Br] (**2**): This complex was synthesized according to the literature procedure.[39]

Synthesis of [Mn{[κ^2-(Ph$_2$P)NH(NC$_5$H$_4$)}(CO)$_3$(OTf)] (**3**): A solution of complex **1** (0.203 g, 0.5 mmol) was prepared in a 1:1 toluene:dichloromethane mixture and this was added to a solution of silver trifluoromethanesulfonate (0.128 g, 0.5 mmol). The reaction flask was wrapped with Al foil and the mixture was stirred for additional 2 h at room temperature under N_2. The precipitate of AgBr was removed by filtration through a syringe filter in the glove box. The solvent was removed to give a yellow solid of **3**. Single crystals of this complex were grown by slow diffusion of hexane into a concentrated solution of the complex in dichloromethane and the results of X-ray analysis are represented in Figure 2.3. Yield 0.198 g (70%). ^{1}H NMR (400 MHz, DMSO-d_6, 25°C): δ = 6.85 (s, 1H), 7.04-7.93 (m, 14H). ^{13}C{1H} NMR (400 MHz, DMSO-d_6, 25 ºC): 67.41, 112.78, 116.11, 117.57, 128.56, 129.25, 129.41, 129.55, 129.66, 129.81, 130.58, 130.75, 130.95, 131.49, 131.64, 131.94, 132.16, 140.44, 141.75, 151.51, 153.86. ^{31}P{^{1}H} NMR (400 MHz, DMSO-d_6, 25°C): δ = 114.8.

Synthesis of [Re{κ^2-(Ph$_2$P)NH(NC$_5$H$_4$)}(CO)$_3$Br] (**4**): This synthesis is modified from the literature.[41] In a glove box, 2-(diphenylphosphinoamino)pyridine (0.138 g, 0.5 mmol) was added to a solution of Re(CO)$_5$Br (0.203 g, 0.5 mmol) in anhydrous toluene (15 mL). The flask was removed from the glovebox and connected to a Schlenk line via a reflux condenser. The reaction mixture was stirred at 100 °C overnight under N_2, then cooled to room temperature and toluene was evaporated under vacuum. The crude residue was dissolved in dichloromethane (1 mL) and then pentane (5 mL) was added to afford the complex **4** as a white solid. Single crystals suitable for X-Ray diffraction studies were grown by slow diffusion of pentane into a solution of **4** in CH_2Cl_2 at room temperature. Yield 0.264 g (85%). The single crystal X-ray structure of **4** was independently obtained and analyzed and confirmed the identity of **4** was consistent with the literature (Figure 2.3.).[42]

X-ray Crystallography: As it was mentioned in section 1.7.6. X-ray Crystallography of Chapter 1, the crystals were mounted on thin glass fibers using paraffin oil. All hydrogen atoms positions were calculated based on the geometry of the related non-hydrogen atoms, and all hydrogen atoms were treated as idealized contributions during the refinement.

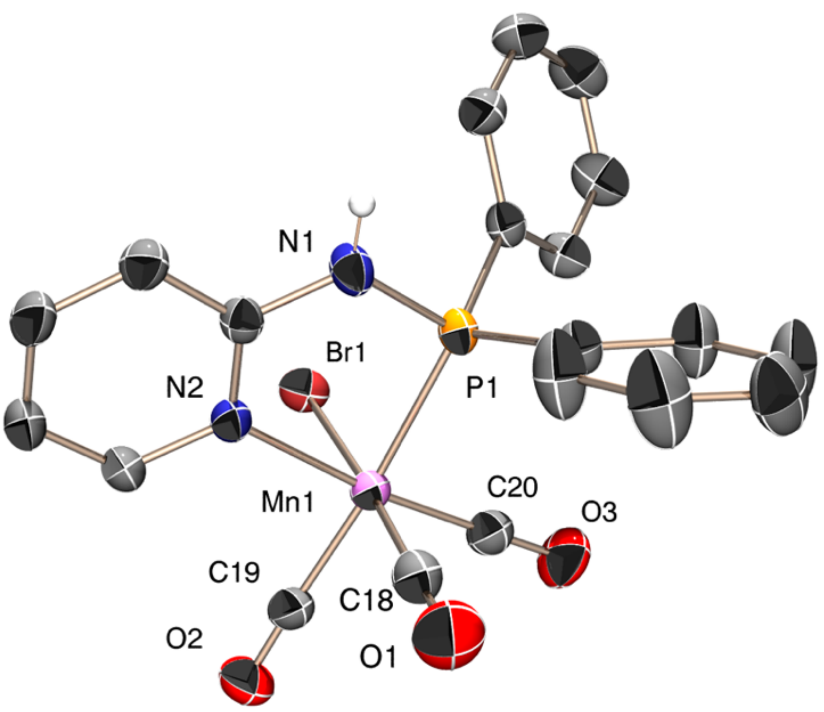

Figure 2.1. Structural representation [Mn{κ^2-(Ph$_2$P)NH(NC$_5$H$_4$)}(CO)$_3$Br] (**1**) obtained from X-ray analysis. Hydrogen atoms are omitted for clarity. Thermal ellipsoids are shown at 60% probability. This structure has been previously reported.[40]

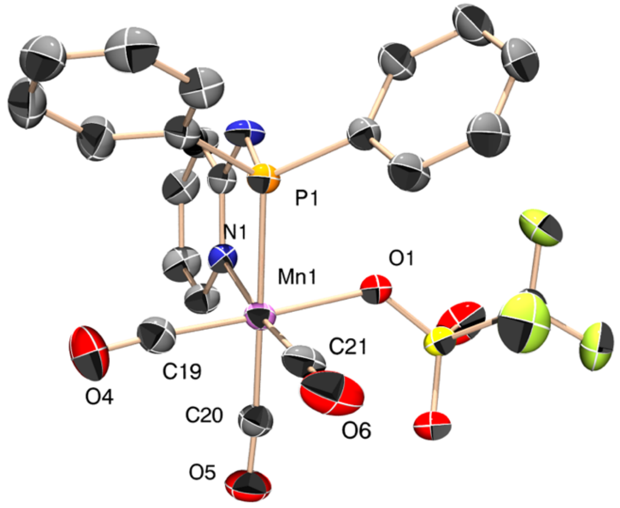

Figure 2.2. Structural representation [Mn{κ^2-(Ph$_2$P)NH(NC$_5$H$_4$)}(CO)$_3$OTf] (**3**) obtained from X-ray analysis. Hydrogen atoms are omitted for clarity. Thermal ellipsoids are shown at 60% probability.

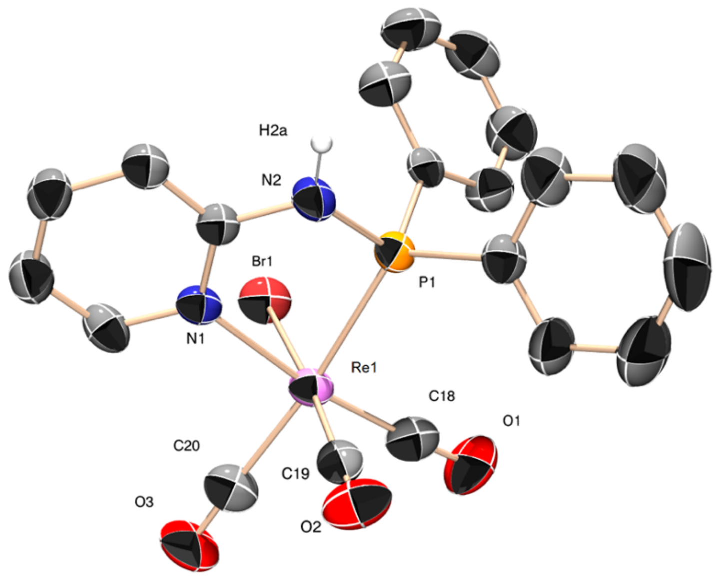

Figure 2.3. Structural representation [Re{κ^2-(Ph$_2$P)NH(NC$_5$H$_4$)}(CO)$_3$Br] (**4**) obtained from X-ray analysis. Hydrogen atoms are omitted for clarity. Thermal ellipsoids are shown at 60% probability. This structure has been previously reported.[41]

2.2.2. General Procedures.

The direct reaction of $Mn(CO)_5Br$ with two different *N*-(diphenylphosphino)-2-aminopyridines yielded the complexes $[Mn\{\kappa^2\text{-}(Ph_2P)NR(NC_5H_4)\}(CO)_3Br]$ (R = H, **1**; R = Me, **2**), obtained in yields of 93% and 78%, respectively.[39,40] Confirmation of the identities of **1** and **2** was provided by matching of the spectroscopic data with the literature and our independent single crystal X-ray analyses (Figures 2.1). As represented schematically in Figure 2.4, these complexes exhibited a *fac*-tricarbonyl coordination geometry that is supported by a bidentate PN ligand. The sixth coordination site of these pseudo-octahedral compounds was completed by a bromo ligand. In complex **1** the Br ligand was exchanged with triflate by reaction with AgOTf to yield **3**, which was fully characterized through NMR spectroscopy and single crystal X-ray analysis (Figure 2.2).

The structural parameters for **1-3** are analogous, displaying similar $Mn\text{-}N_{py}$ and Mn-P distances and the $N_{py}\text{-}Mn\text{-}P$ bite angles.[39,40] Similarly, the analogous Re complex, $[Re\{\kappa^2\text{-}(Ph_2P)NH(NC_5H_4)\}(CO)_3Br]$ (**4**) was prepared and spectroscopic and structural analyses (see Figure 2.4.) were completely consistent with this recently reported complex.[41]

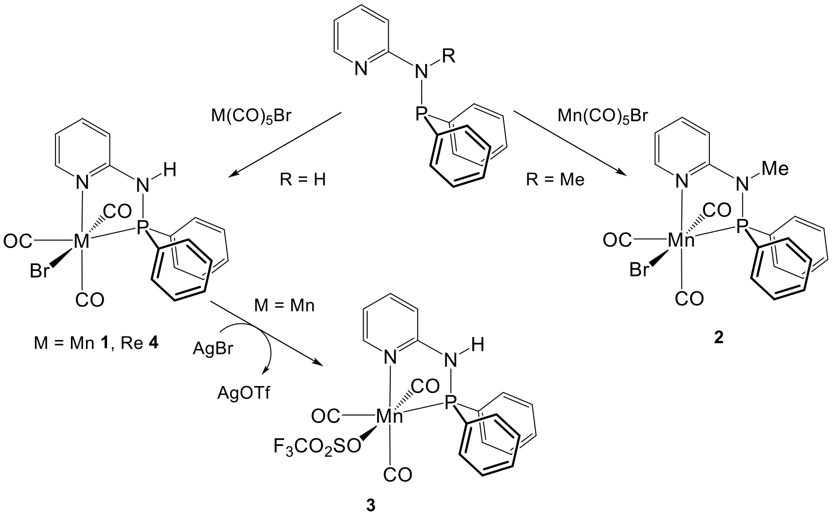

Figure 2.4. Synthetic scheme for the preparation of phosphinoaminopyridine PN ligated Mn and Re complexes.

2.3. Photocatalytic CO_2 Reduction Results

The photocatalytic reduction of carbon dioxide was carried out in a glass reactor at room temperature using [Mn{κ^2-(Ph_2P)NH(NC_5H_4)}$(CO)_3$Br] (**1**) combined with [Ru(bpy)$_3$](PF_6)$_2$ (PS) and TEOA (ED) under a CO_2 atmosphere in 4 mL of DMF. The reaction mixture was irradiated with 405 nm visible light from an LED (1050 mW, 700mA, 3.4×10^{-8} mol photons/sec). The gaseous product from this reaction was identified as CO and quantified by gas chromatography (GC) thus confirming that under these conditions, **1** was a visible-light photoredox catalyst for selective production of CO with no other detected by-products (Table 2.1, Figure 2.5). The molar ratio of CO produced to catalyst **1** defined the turnover number for CO (TON_{CO}) and with 0.1 mM **1** and 1 mM Ru(bpy)$_3^{2+}$ the TON_{CO} of 55 was obtained (Table 2.1). The time profile for CO production is shown in Figure 2.5. (blue) and demonstrated that **1** was well-behaved for over 96 hr of irradiation with >99% selectivity for CO formation (the data for the Figure 2.5 are shown in Table 2.2). These observations are in contrast to the few reported homogeneous α-diimine Mn-based CO_2 reducing photocatalysts, which display excellent selectivity for formic acid[31,34,37] or an 80/20 ratio of CO/formate (Table 2.3.).[35]

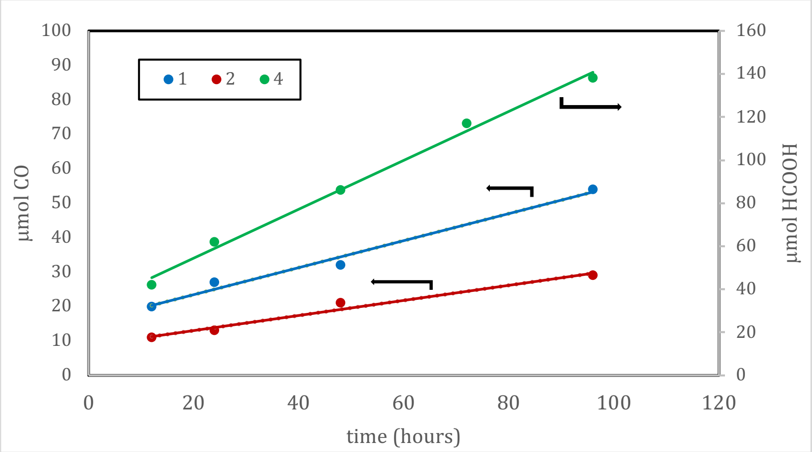

Figure 2.5. Time profile for producing CO (left y axis) with catalyst **1** (blue) and **2** (red) and for producing HCOOH (right y axis) with catalyst **4** (green). (Data from Table 2.2).

Table 2.1. Photocatalytic experiments with complexes **1**, **2**, **3** and **4**. In DMF (4mL) with $Ru(bpy)_3(PF_6)_2$ (**Rubpy**) or 1,2,4-trihydroxyanthraquinone (**Pur**) as photosensitizer (**PS**) and TEOA as the electon donor (ED). Turn-over number (TON) = (moles of product)/(moles of catalyst). Irradiation with 405 nm light for 24 h.

Catalyst	**PS**	**[Catalyst] (mM)**	**[PS] (mM)**	**CO (µmol)**	**TON (CO)**
1	**Rubpy**	0.1	0.1	14	35
	Rubpy	0.1	1	22	55
	Rubpy	0.05	0.05	4	20
	Rubpy	1	1	27	6.8
	Pur	1	1	14	3.5
2	**Rubpy**	0.1	0.1	5	13
	Rubpy	0.1	1	11	28
	Rubpy	0.05	0.05	3	15
	Rubpy	1	1	13	3.3
	Pur	1	1	12	2.8
3	**Rubpy**	1	1	14	3.5
				HCOOH (µmol)	**TON (HCOOH)**
4	**Rubpy**	0.1	0.1	59	148
	Rubpy	0.1	1	137	343
	Rubpy	0.05	0.05	48	240
	Pur	0.1	1	42	105

Table 2.2. Time profiles for the photocatalytic reduction of CO_2 to yield CO for catalysts $[Mn\{\kappa^2\text{-}(Ph_2P)NH(NC_5H_4)\}(CO)_3Br]$ **(1)**, $[Mn\{\kappa^2\text{-}(Ph_2P)NMe(NC_5H_4)\}(CO)_3Br]$ (**2**), and $[Re\{\kappa^2\text{-}(Ph_2P)NH(NC_5H_4)\}(CO)_3Br]$ (**4**). Solutions of catalyst (1mM) and $Ru(bpy)_3(PF_6)_2$ (**Rubpy**) (1mM) and TEOA as the electon donor (ED) in DMF (4mL) irradiated with 405 nm LED lamp.

Time (h)	**CO (µmol)** with **1**	**CO (µmol)** with **2**	**HCOOH (µmol)**
12	20	11	107
24	27	13	123
48	30	23	133
72	32	25	173
96	54	29	190

Table 2.3. Comparison of the performance parameters for photocatalysts $Mn(bpy)(CO)_3Br$ (I)[43], $Mn(bpy)CO_3CN$ (II)[34] and $Mn(phen)CO_3Br$ (III)[35] with complexes **1**, **2** and **4**.

CAT	H_2 (µmol)	TON_{H_2}/(ϕ%)	CO (µmol)	TON_{CO}/(ϕ%)	HCOOH (µmol)	TON_{HCOOH} /(ϕ%)
I[a]	1.6	14/(0.14)	2.4	12/(0.12)	31.4	149/(1.7)
II[b]	14.2	1.6/(0.01)	3.2	7.1/(0.05)	254	127/(1.9)
III[c]	-	-	800	64	200	16
1[d]	-	-	20	55/(0.75)	-	-
2[d]	-	-	11	28/(0.37)	-	-
4[d]	-	-	-	-	137	343/(4.7)

[a] PS = $[Ru(bpy)_3]^{2+}$; ED = BNAH, 4.3 x 10^{-8} mol photons/s[43] [b] PS = $[Ru(dmb)_3]^{2+}$; ED = BNAH, 2.51x10^{-7} mol photons/s[34] [c] PS = Zn(tetraphenylporphyrin), ED = TEA, no photon flux was provided[35] [d] 24h, 0.1mM CAT, PS = $[Ru(bpy)_3]^{2+}$ (1mM); ED = TEOA, 3.4 x 10^{-8} mol photons/sec.

Several control experiments established the need and roles of the different components of this catalyst system in the formation of CO. Reactions run in the absence of **1** but otherwise identical conditions produced no observed CO. The complete photocatalytic reaction process was carried out under an N_2 atmosphere and showed that no CO was generated, demonstrating that CO originated from CO_2 rather than the decomposition of **1**, the PS or the ED. Variation of electron donor was explored by employing TEOA, BNAH (N-benzyl-1,4-dihydridonicotinamide), triethylamine, or sodium ascorbate as the ED, and catalyst **1** displayed the highest activity for reduction of CO_2 to CO with TEOA (Table 2.4). Furthermore, while both DMF and CH_3CN are capable of supporting the catalytic activity of **1**, in general DMF gave superior catalyst activity. Definitive confirmation that the CO arose from CO_2 was provided by an isotope tracing experiment. Carrying out the photolysis reaction with **1**, $Ru(bpy)_3^{2+}$, and TEOA under a $^{13}CO_2$ atmosphere resulted in generation of ^{13}CO (Figure 2.6). This is further powerful evidence that that **1** catalyzes CO_2 reduction to CO selectively.

Table 2.4. Effect of solvent and electron donor on the photocatalytic reduction of CO_2 with the [Mn{κ^2-(Ph_2P)NH(NC_5H_4)}$(CO)_3$Br] (**1**). Irradiation with 405 nm light conducted on a DMF or acetonitrile (4mL) solution under a CO_2 atmosphere for 24 h. Electron donors used were triethanol amine (TEOA), N-benzyl-1,4-dihydridonicotinamide (BNAH), triethylamine (NEt_3), or sodium ascorbate (NaAsc).

[1] (mM)	[Ru(bpy)$_3^{2+}$] (mM)	Solvent	Electron donor	CO (µmol)
1	1	DMF	TEOA	27
1	1	DMF	BNAH	17
1	1	DMF	NEt_3	12
1	1	DMF	NaAsc	12
1	1	CH_3CN	TEOA	18
1	1	CH_3CN	BNAH	15
1	1	CH_3CN	NEt_3	18
1	1	CH_3CN	NaAsc	17

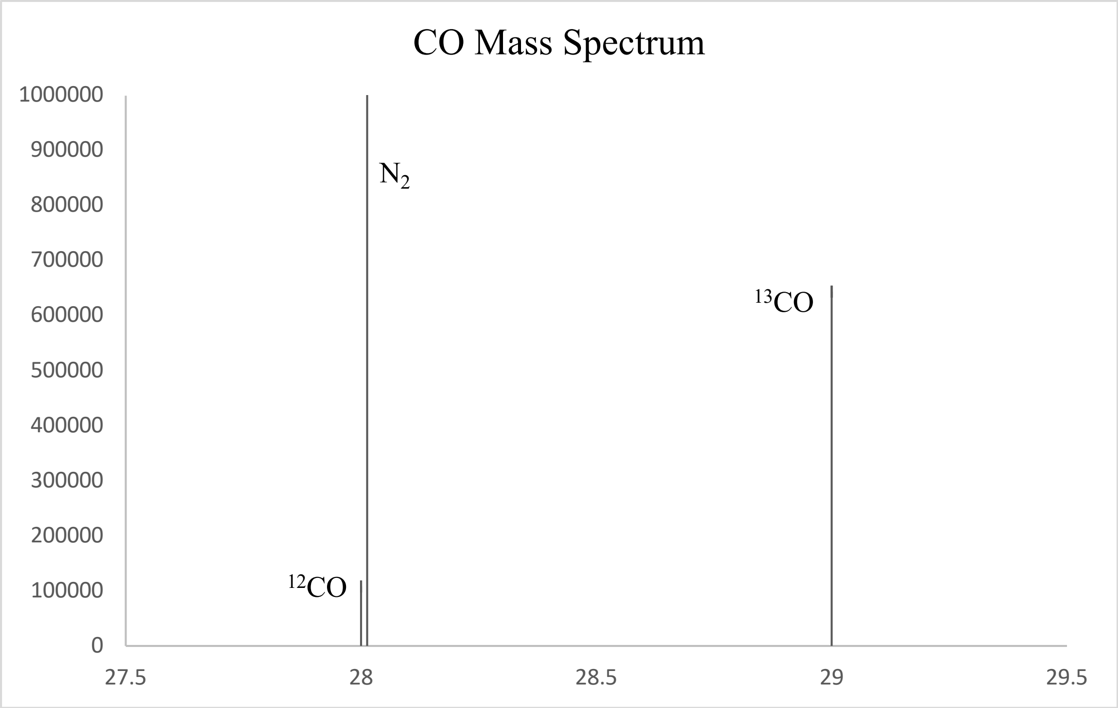

Figure 2.6. High resolution MS of the head space of a photocatalytic reduction experiment in DMF using $^{13}CO_2$ with complex **1,** $Ru(bpy)_3(PF_6)_2$ (**Rubpy**) as photosensitizer and TEOA as the electon donor. Mass peaks for ^{13}CO, N_2 and $^{12}CO_2$ are indicated.

Complexes **2** and **3** provided analogues of **1** with variation to the ligand and the coordinated anion, respectively. In the case of **2**, where the N–H group has been replaced with N–Me, successful photocatalytic reduction was observed albeit with lower TON_{CO}

(Table 2.1). The time profile for catalyst **2** (Figure 2.5) reflects this lower activity compared to **1**. Similarly, replacement of bromide in **1** by triflate to yield **3**, led to reduction in the catalyst activity (Table 2.1).

Encouraged by these results we also attempted to employ an alternative, non-noble metal photosensitizer.[7] First-row transition metal sensitizers have been explored for photocatalytic CO_2 reduction[29,44,35] We were attracted to the use of available organic photosensitizers with complex **1**. The use of p-terphenyl as a photosensitizer has been reported but required UV light (< 400 nm).[14,16,45,46] An effective iron porphyrin catalyst in combination with 9-cyanoanthracene as PS reduced CO_2 to CO with 100% selectivity.[10] Recently, the commercial anthroquinone dye, purpurin (1,2,4-trihydroxyanthroquinone), was reported as a versatile photosensitizer for photocatalytic CO_2 reduction with both Fe and Co catalysts.[12] Use of purpurin (**Pur**) as PS with **1** and **2** did produce photocatalytic CO_2 reduction but with much reduced activity (Table 2.1).

The unique photocatalytic abilities of **1** and **2** compared to reported molecular Mn catalysts, which all possess α-diimine ligands, are provided in Table 2.1. These results further emphasize the contrasting selectivity of complexes **1** and **2** for CO production compared to reported complexes and the critical imperative for exploring ligand variation in these reactions.

Having access to the Re analogue of complex **1** (Figure 2.1) allows a comparison of the photocatalytic activities of **1** and **4**. Surprisingly, when complex **4** was combined with $Ru(bpy)_3^{2+}$ and TEOA in DMF and the system was irradiated with a 405 nm LED under a CO_2 atmosphere, no gaseous products were observed. Examination of the solution revealed formation of formic acid. With 0.1 mM **4** and 1 mM PS a TON_{HCOOH} (moles HCOOH/moles **4**) of 343 was obtained (Tables 2.1 and 2.3). The HCOOH production profile is shown in Figure 2 (green) and demonstrated that **4** was well-behaved and selective over > 96 hr of irradiation. Like **1**, a variety of reaction parameters were explored with **4** (Tables 2.1, 2.2 and 2.5). The catalytic performance of **4** was quite sensitive to the identity of the ED (Table 2.5) with TEOA being superior. A ^{13}C tracer experiment was carried out for the photolysis reaction with **4**, $Ru(bpy)_3^{2+}$, and TEOA under a $^{13}CO_2$ atmosphere. HRMS analysis of the reaction head-space clearly documented selective formation of $H^{13}COOH$ (Figure 2.7). These results are conclusive evidence that the formic acid observed in these experiments arose from CO_2 reduction. They further highlight this unusual switch in product selectivity by replacing Mn with Re in this complex and significantly contrast with the reported selectivity of Re α-dimmine species which selectively yield CO as the product of CO_2 photoreduction.[6,37]

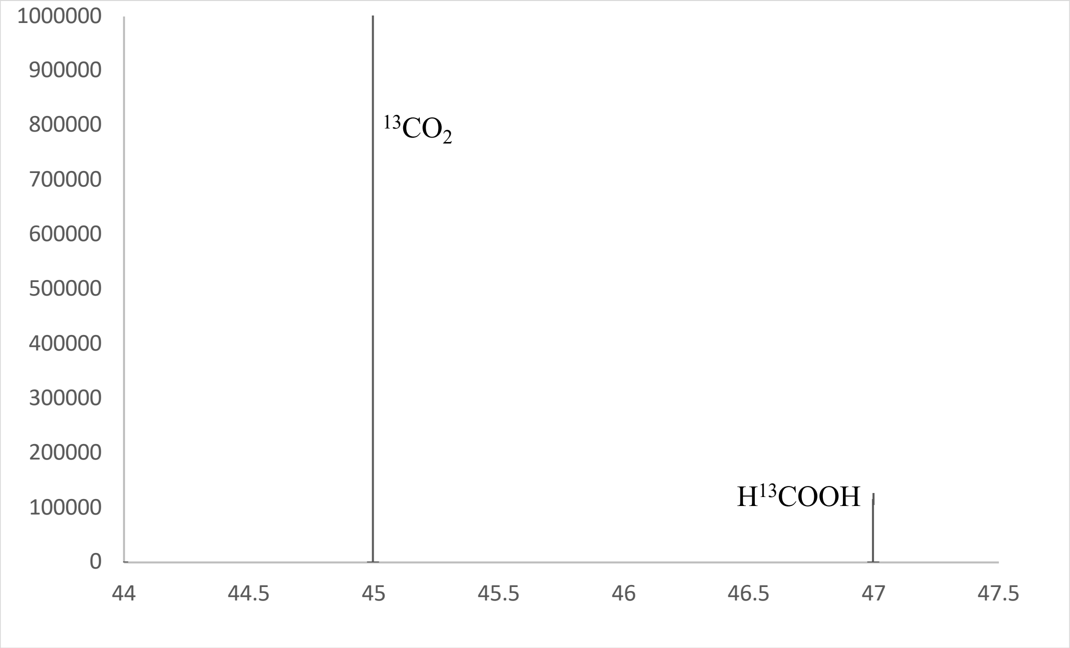

Figure 2.7. High resolution MS of the head space of a photocatalytic reduction experiment in DMF using $^{13}CO_2$ with complex **4,** $Ru(bpy)_3(PF_6)_2$ (**Rubpy**) as photosensitizer and TEOA as the electon donor. Mass peaks for $H^{13}CO_2H$, $^{13}CO_2$ are indicated.

Table 2.5. Effect of electron donor and solvent on the photocatalytic CO_2 reduction with the [Re{κ^2-(Ph_2P)NH(NC_5H_4)}$(CO)_3$Br] (**4**). Irradiation with 405 nm light conducted on a DMF or acetonitrile (4mL) solution under a CO_2 atmosphere for 24 h. Electron donors used were triethanol amine (TEOA), N-benzyl-1,4-dihydridonicotinamide (BNAH), triethylamine (NEt_3), or sodium ascorbate (NaAsc).

[4] (mM)	**[Ru(bpy)$_3^{2+}$] (mM)**	**Solvent**	**Electron donor**	**HCOOH (μmol)**
1	1	DMF	TEOA	123
1	1	DMF	BNAH	-
1	1	DMF	NEt_3	75
1	1	DMF	NaAsc	-
1	1	CH_3CN	TEOA	73
1	1	CH_3CN	BNAH	-
1	1	CH_3CN	NEt_3	-
1	1	CH_3CN	NaAsc	-

Several experiments were explored in order to interrogate mechanistic features for the photocatalytic activity of **1** and **4**. Since catalysis is initiated with light absorption by the Ru(bpy)$_3^{2+}$ (PS) the quenching of the excited state PS* was examined. As mentioned in section 1.7.4. Emission-Quenching Experiment in Chapter 1, the emission-spectra were obtained for the quencher TEOA and TEA. The quenching rate constants kq were calculated from the linear Stern-Volmer plots for both the quenchers and the complexes as shown in Figure 2.8. Both complexes **1** and **4** were effective in quenching the PS* excited state and in fact are more efficient than either TEOA or TEA (Figures 2.9, and 2.10). This observation suggests one possible entry into the catalytic cycle through the oxidative quenching proposed as will be shown later in Figure 2.20. Similar oxidative quenching of PS* by metal complexes has been previously reported.[17–19,26]

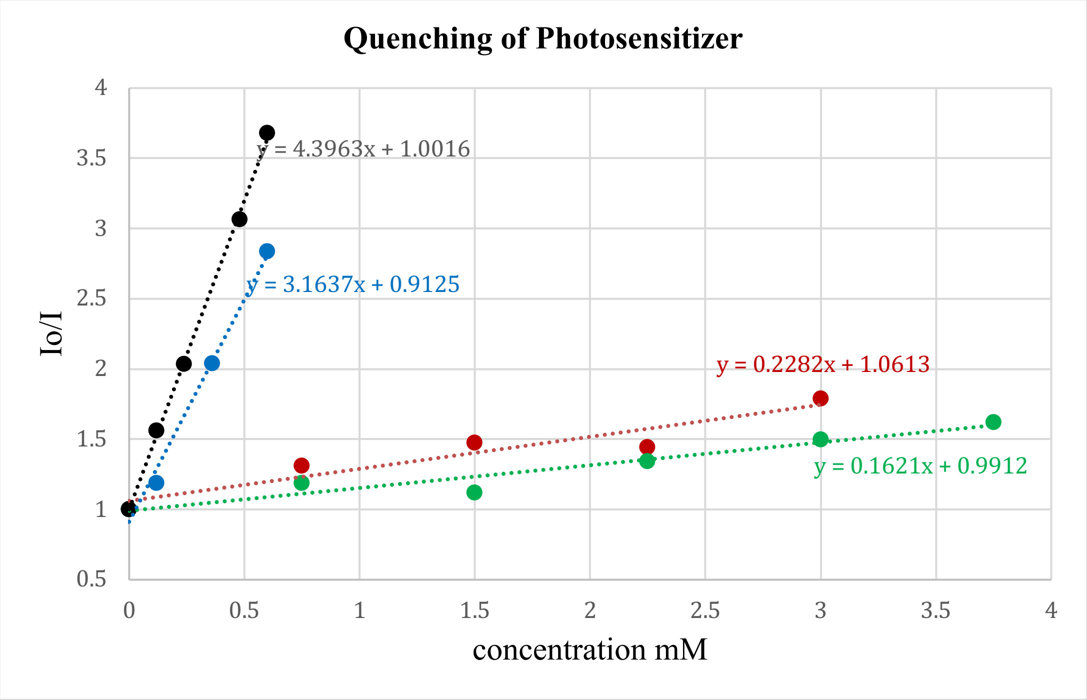

Figure 2.8. Stern-Volmer plot for quenching of the emission of the photosensitizer Ru(bpy)$_3$(PF$_6$)$_2$ with various concentrations of TEOA (red) TEA (green) complex **1** (blue) and complex **4** (black). Linear equations are shown.

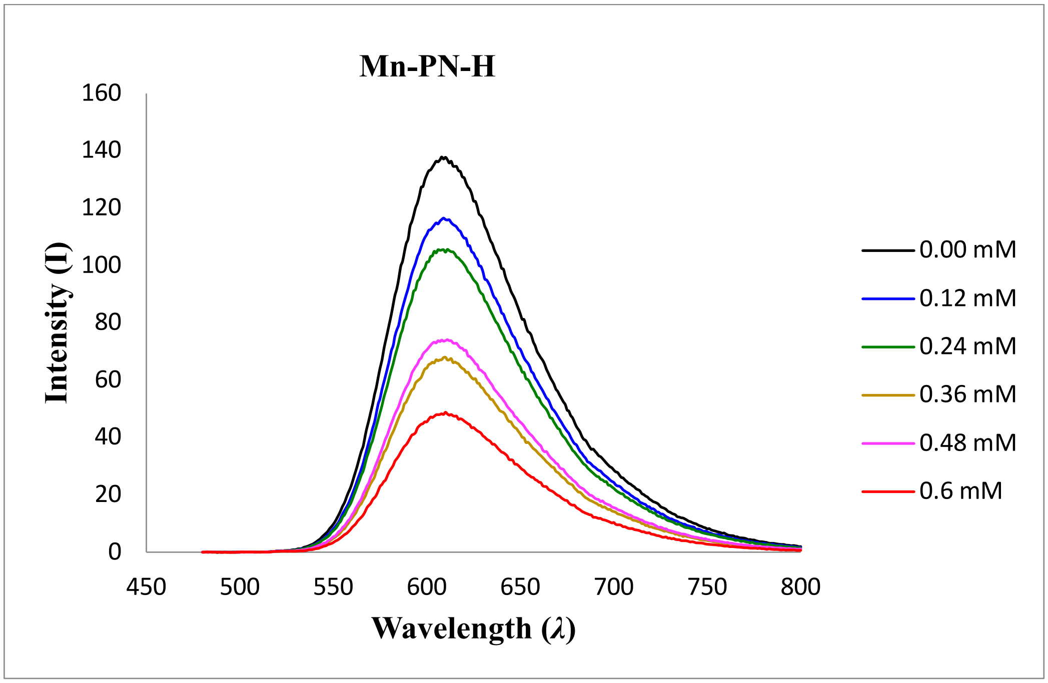

Figure 2.9. Spectra demonstrating the quenching of the emission from the photosensitizer Ru(bpy)$_3$(PF$_6$)$_2$ with various concentrations (0-0.6mM) complex **1**.

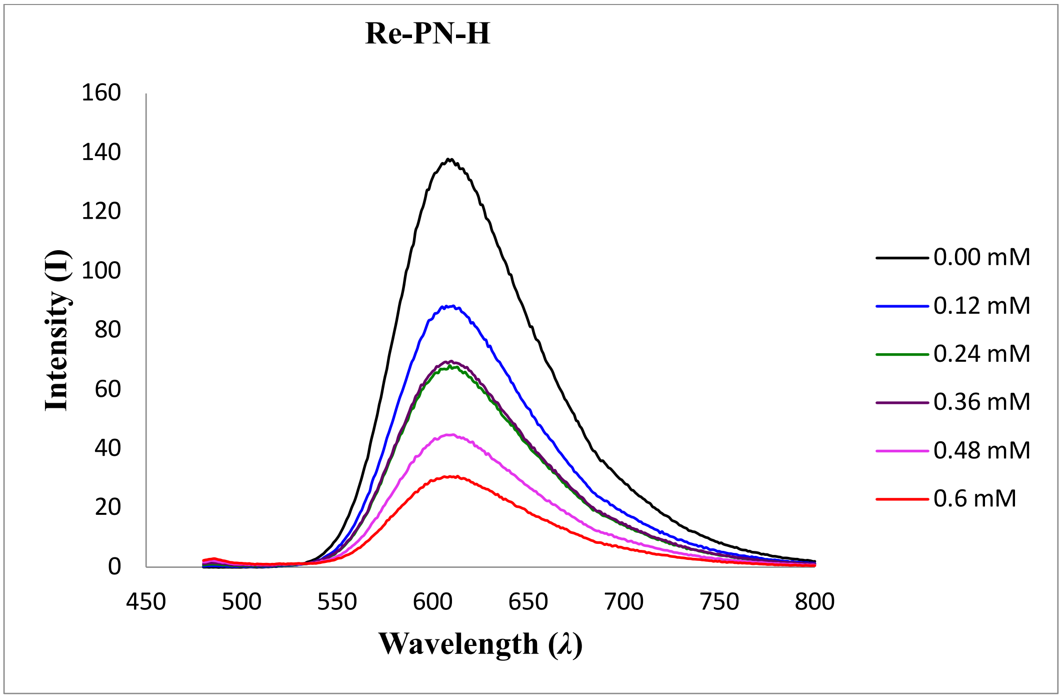

Figure 2.10. Spectra demonstrating the quenching of the emission from the photosensitizer $Ru(bpy)_3(PF_6)_2$ with various concentrations (0-0.6 mM) **4**.

In order to probe the nature of the reduced complex, $[Mn\{\kappa^2\text{-}(Ph_2P)NH(NC_5H_4)\}(CO)_3Br]^-$ (1^-), was then examined through a DFT computational investigation. Beginning with the optimized structure of 1 (Figure 2.11, 2.12, and Table 2.6), the reduced species 1^- was optimized (B3LYP, mixed TZVP/DZVP basis set). During the optimization, a Br^- anion dissociated to yield a distorted square pyramidal complex $[Mn\{\kappa^2\text{-}(Ph_2P)NH(NC_5H_4)\}(CO)_3]$ (A) with the SOMO electron density in this species localized in an MO that is a combination of d_z^2 and pyridyl π^* in character (Figures 2.14. and Table 2.6). Similar species have been proposed and observed with reduction of *fac*-$MnX(bipyR_2)(CO)_3$[30,47,48,49] and these commonly dimerize via formation of a M-M bond to yield $[Mn(\kappa^2\text{-}bpyR_2)(CO)_3]_2$, which in some cases can be a component of the CO_2 reduction catalysis cycle.[34,48,49] The analogous DFT optimization for the single electron reduction of 2 to yield 2^-. In this case the SOMO density was distributed on the PN ligand framework and not on the metal center (Figure 2.14).

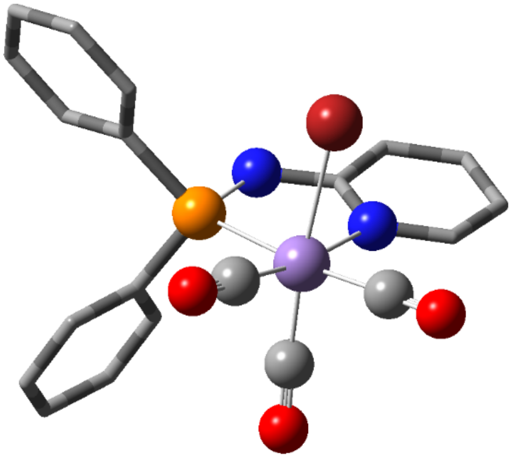

Figure 2.11. A ball and stick structural representation for the computationally optimized $[Mn\{\kappa^2\text{-}(Ph_2P)NH(NC_5H_4)\}(CO)_3Br]$ compound **1**. DFT calculations used the B3LYP functional and the mixed TZVP/DZVP basis set. Hydrogen atoms are not shown for clarity. Some carbon atoms have been removed for clarity.

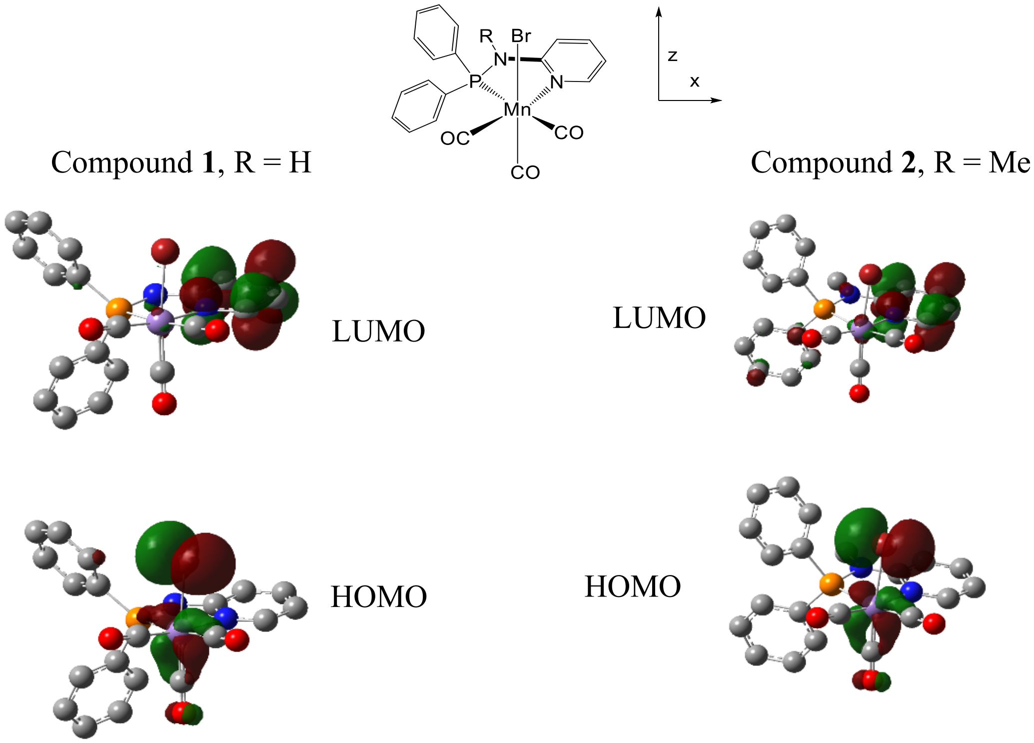
Compound **1**, R = H

Compound **2**, R = Me

Figure 2.12. Representations of the HOMO and LUMO for the computationally optimized $[Mn\{\kappa^2\text{-}(Ph_2P)NH(NC_5H_4)\}(CO)_3Br]$ compound 1 and $[Mn\{\kappa^2\text{-}(Ph_2P)NMe(NC_5H_4)\}(CO)_3Br]$ compound 2. DFT calculations used the B3LYP functional and the mixed TZVP/DZVP basis set. Hydrogen atoms are not shown for clarity. In both compounds the LUMO is centered in the pyridyl π^* orbital. (Isovalues = 0.03).

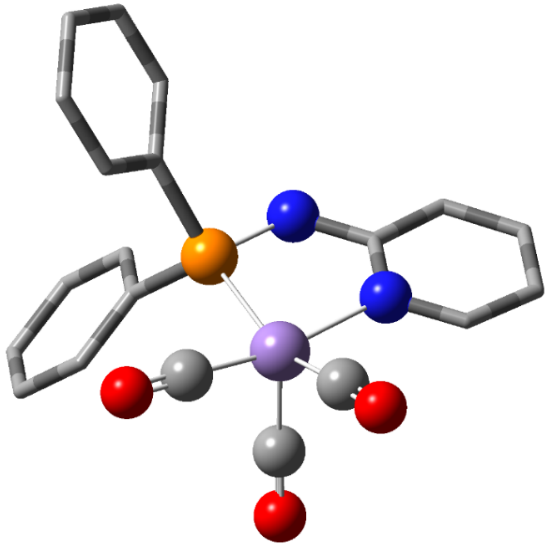

Figure 2.13. A ball and stick structural representation for the computationally optimized product from single electron reduction of **1,** [Mn{κ^2-(Ph$_2$P)NH(NC$_5$H$_4$)}(CO)$_3$] **A**. During the optimization, the Br$^-$ spontaneously dissociated from the complex to yield five-coordinate, distorted square-base pyramidal [Mn{κ^2-(Ph$_2$P)NH(NC$_5$H$_4$)}(CO)$_3$] (**A**) as shown. DFT calculations used the B3LYP functional and the mixed TZVP/DZVP basis set. Hydrogen atoms are not shown for clarity. Some carbon atoms have been removed for clarity.

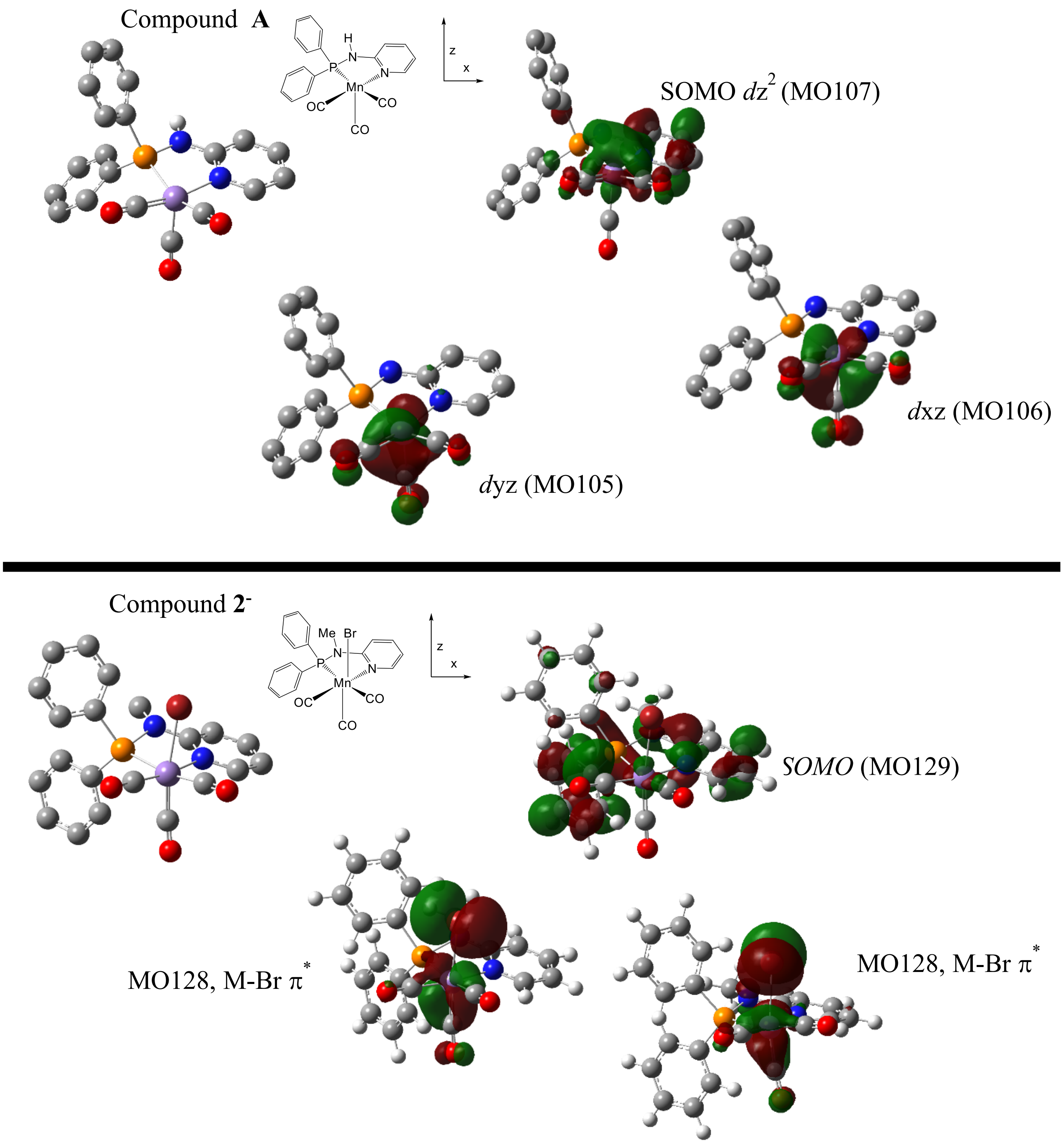

Figure 2.14. Representations of the SOMO and next two MO's for the computationally optimized singly reduced compounds [Mn{κ^2-(Ph_2P)NH(NC_5H_4)}$(CO)_3$] (**A**) and [Mn{κ^2-(Ph_2P)NMe(NC_5H_4)}$(CO)_3Br]^-$ (**2**$^-$). DFT calculations used the B3LYP functional and the mixed TZVP/DZVP basis set. Hydrogen atoms are not shown for clarity. (Isovalues = 0.03).

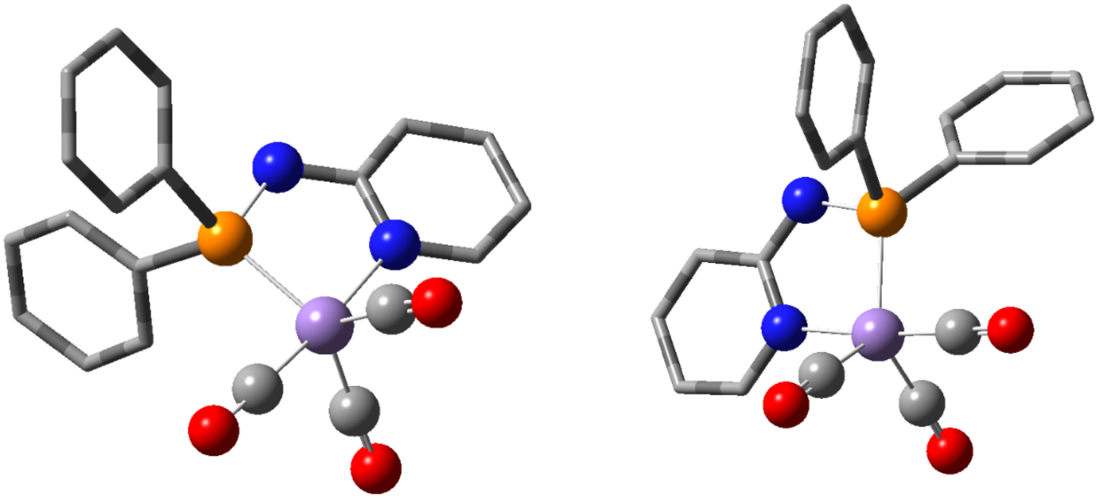

Figure 2.15. Two views of a ball and stick structural representation for the computationally optimized product from the two electron reduction of compound **1**, [Mn{κ^2-(Ph$_2$P)NH(NC$_5$H$_4$)}(CO)$_3$]$^-$ (**B**). DFT calculations used the B3LYP functional and the mixed TZVP/DZVP basis set. Hydrogen atoms are not shown for clarity. Some carbon atoms have been removed for clarity.

Table 2.6. A comparison of metal–ligand distances and angles from the experimental single crystal X-ray analysis and from the computationally optimized structures for [Mn{κ^2-(Ph$_2$P)NH(NC$_5$H$_4$)}(CO)$_3$Br (**1**) and and the single electron reduction product [Mn{κ^2-(Ph$_2$P)NH(NC$_5$H$_4$)}(CO)$_3$] (**A**) and the double reduction product [Mn{κ^2-(Ph$_2$P)NH(NC$_5$H$_4$)}(CO)$_3$]$^-$ (**B**).

Bond/cmpd	[Mn{κ^2-PNN}(CO)$_3$Br] **(1)** Exp[a]	[Mn{κ^2-PNN}(CO)$_3$Br] (**1**) Computed	[Mn{κ^2-PNN}(CO)$_3$] (**A**) Computed	[Mn{κ^2-PNN}(CO)$_3$]$^-$ (**B**) Computed
M-N$_{py}$	2.0886(14)	2.15680	2.13037	2.11023
M-P	2.2844(5)	2.34932	2.33650	2.22122
M-Br axial	2.5212(4)	2.58491	-	-
M-CO (trans P)	1.837(2),	1.84316	1.82931	1.82120, 1.82544[b]
M-CO (trans Npy)	1.8043(19)	1.82375	1.81721	1.79698
M-CO (trans Br)	1.810(2)	1.81055		
P-Mn-N$_{py}$	81.15(4)	80.671	81.168	80.078

[a] From this work.

[b] the two CO ligands are symmetrically arranged around the M-P axis in this pseudo-trigonal bipyramidal complex

Interestingly, the cathodic scan in the cyclic voltammetry of **1** under N_2 displayed two irreversible reductions at -1.72 V and -2.20 V versus Fc/Fc^+ (Figure 2.16). These features are reminiscent of the cyclic voltammograms of $MnX(bipyR_2)(CO)_3$ complexes.[30,47] On the basis of these computational and experimental observations, the effect of addition of bromide anion on catalyst TON was measured for both **1** and **4** by addition of NEt_4Br to active systems (Table 2.7). In both cases an increased TON was observed and supports a preliminary proposal of retention of Br^- as the catalyst receives the second electron necessary for the reduction of CO_2 to either CO or HCO_2H.

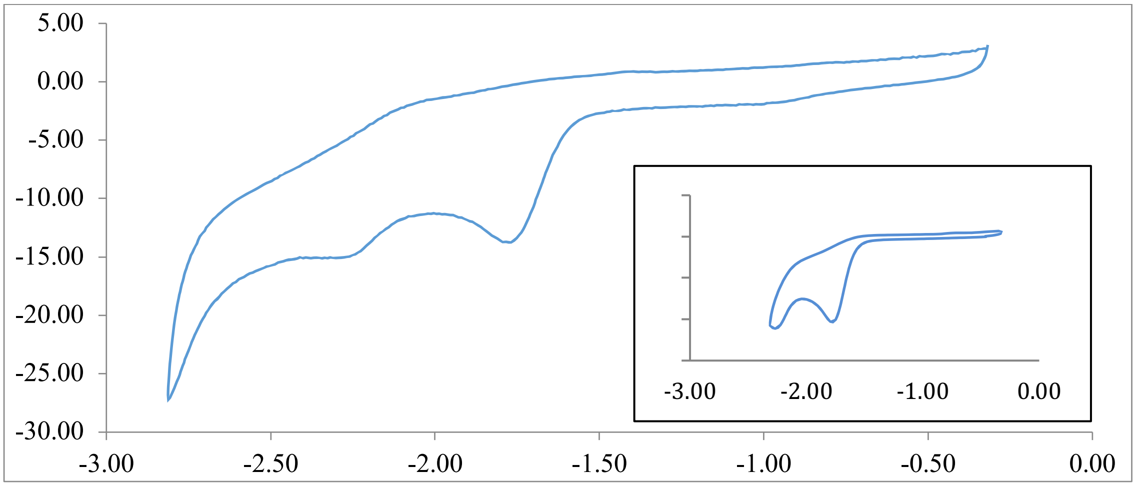

Figure 2.16. Cyclic voltammograms of 1.0 mM $[Mn\{\kappa^2\text{-}(Ph_2P)NH(NC_5H_4)\}(CO)_3Br]$under N_2 in CH_3CN with 0.1 M $(n\text{-}Bu)_4NPF_6$ supporting electrolyte at 100 mV/s. Reductions appear at -1.72 V and -2.20 V vs Fc^+/Fc. The inset shows the scan of only the first reduction.

Table 2.7. Comparison of photocatalytic experiments using complexes **1** or **4** with added tetrethylamonium bromide during reaction. Photocatalytic experiments in DMF (4mL) under a CO_2 atmosphere with $Ru(bpy)_3(PF_6)_2$ photosensitizer (1mM) and TEOA as the electon donor. Irradiation with 405 nm light for 24 h.

Added Br⁻ source? NEt_4Br	**Catalyst (1 mM)**	**Product**	
		CO (μmol)	
No	**1**	27	
Yes	**1**	35	
			HCOOH (μmol)
No	**4**		123
Yes	**4**	11	176

The electrocatalytic behavior of these complexes was next explored. As explained in section 1.7.5. Electrocatalytic Reduction of CO_2 of Chapter 1, the electrochemical experiments for these complexes were carried out in a single compartment cell in CH_3CN and tetrabutylammoniumhexafluorophosphate, $[(n\text{-}Bu)_4N]PF_6$ (TBAHFP) as the supporting electrolyte. These electrochemical experiments were performed under N_2 and CO_2 atmosphere and also in the presence of H_2O. These following figures are shown the electrocatalytic CO_2 reduction behavior of these complexes.

The catalytic behavior of Mn-PN-H complex under N_2 as discussed before in Figure 2.16 show two irreversible reductions at -1.72 V and -2.20 V versus Fc/Fc^+. In the presence of the CO_2 atmosphere, there is a small enhancement of the second reduction peak, and this second reduction peak showed a big enhancement of the current after adding H_2O as shown in Figure 2.17. This enhancement of the current indicates that the catalyst was able to reduce CO_2 in the electrocatalytic process. Bulk electrolysis experiments should be carried out in order to figure out the products of this electrocatalytic CO_2 reduction. This bulk electrolysis experiment will be done in the same condition using the acetonitrile solvent and the supporting electrolyte ($(n\text{-}Bu)_4NPF_6$). On the other hand, the cyclic voltammetry of Re-PN-H complex under N_2 displayed two irreversible reduction peaks at -1.04 V and -2.07 V versus Fc/Fc^+ (as shown in Figure 2.18). Carrying out this same measurement with a solution saturated with an atmosphere of CO_2 produced a great enhancement of the reduction current indicating to the electrocatalytic CO_2 reduction as shown in Figure 2.19. In addition, there is also obvious enhancement in the presence of H_2O. More experiments such as the bulk electrolysis should be done in order to know and measure the evolved products.

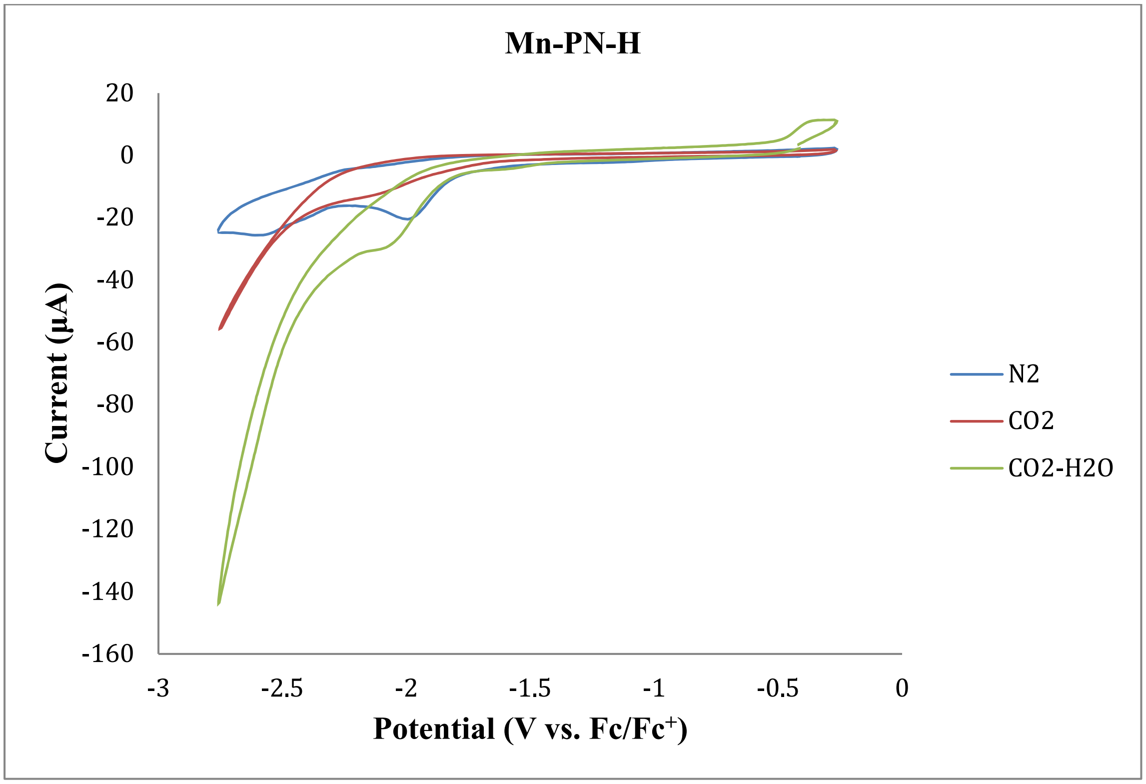

Figure 2.17. Cyclic voltammograms of 1.0 mM [Mn(PN-H)(CO)$_3$]Br under N_2 (blue), CO_2 (red) and CO_2/5% H_2O (green) in CH_3CN with 0.1 M (n-Bu)$_4$NPF$_6$ supporting electrolyte at 100 mV/s.

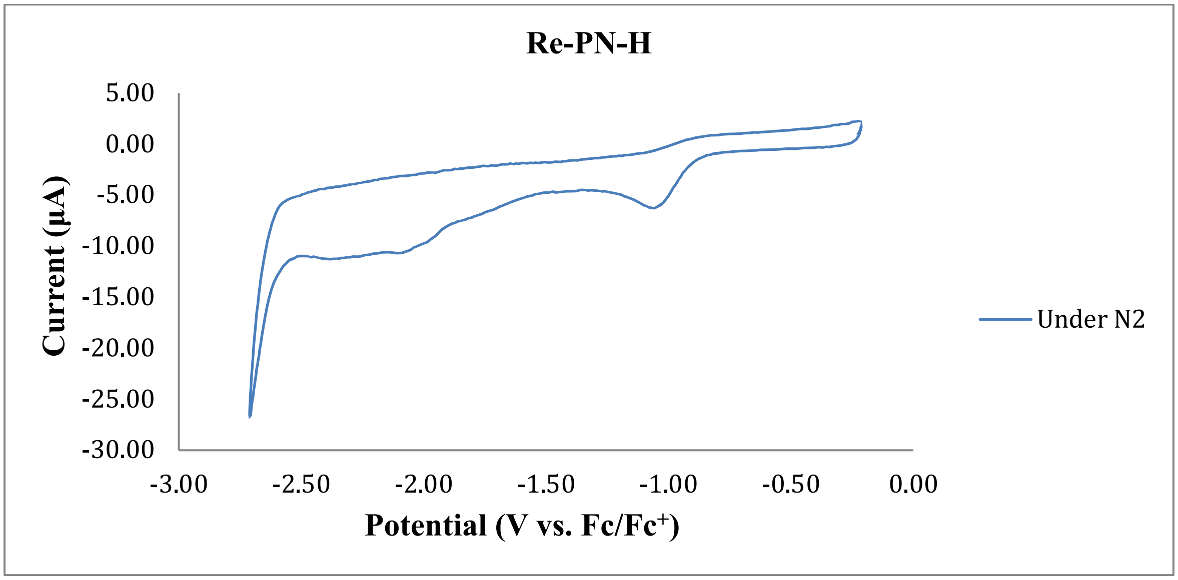

Figure 2.18. Cyclic voltammograms of 1.0 mM [Re(PN-H)(CO)$_3$]Br under N_2 in CH_3CN with 0.1 M (n-Bu)$_4$NPF$_6$ supporting electrolyte at 100 mV/s.

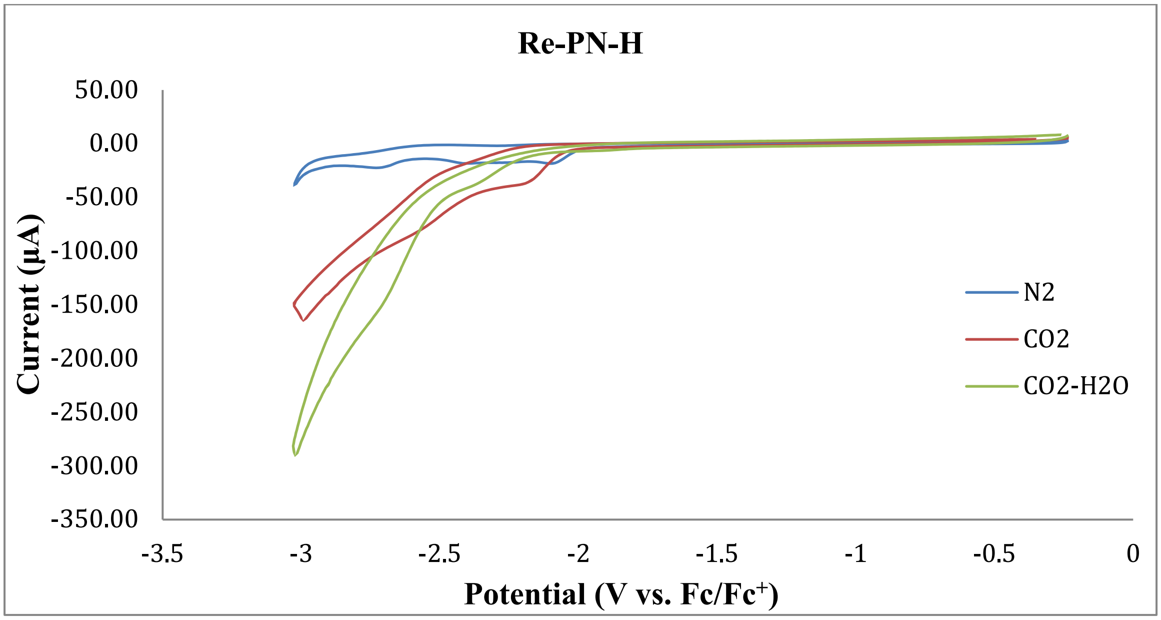

Figure 2.19. Cyclic voltammograms of 1.0 mM [Re(PN-H)(CO)$_3$]Br under N_2 (blue), CO_2 (red) and CO_2/5% H_2O (green) in CH_3CN with 0.1 M (n-Bu)$_4$NPF$_6$ supporting electrolyte at 50 mV/s.

IR spectro-electrochemistry (IR SEC) is a good technique that can be used to study the electrochemical reactions for binuclear metal carbonyl compounds. The solution of the experiment was prepared under an atmosphere of nitrogen before injection into the SEC cell. The solution contains 0.001 M of the catalyst (Mn-PN-H) and 0.1 M of the supporting electrolyte ((n-Bu)$_4$NPF$_6$) in acetonitrile. The IR spectrum was obtained for the solution under N_2 before starting the electrochemistry, and then it was obtained again at a potential of -1.7 V under N_2 atmosphere. For the IR spectrum that was obtained before applying to the potential at which the redox reaction happens, the IR bands of the three carbonyl groups are shown as presenting in the black spectrum in Figure 2.20. For the IR spectrum that was taken after the electrocatalytic system occurs at the potential of the redox reaction, the IR bands of the five carbonyl groups that are indicating to the formation of the Mn dimer [Mn$_2$(CO)$_6$(PN)$_2$] were appeared in the spectrum (as shown in the red spectrum in Figure 2.20). The IR v(CO) bands of the [Mn(Br)(CO)$_3$(PN)] under N_2 are 1920, 1950, and 2030 nm while the IR v(CO) bands of the $[Mn_2(CO)_6(PN)_2]$ are 1860, 1890, 1920, 1970, and 2000 nm. In Figure 2.20, the IR spectra show the two pathways of the corresponding mononuclear and binuclear metal carbonyl compounds. A Similar experiment was done with the known *fac*- $[Mn(Cl)(CO)_3(bpy)]$, and it showed same behaviour to give $[Mn_2(CO)_6(bpy)_2]$ as shown in the reported literature.[50]

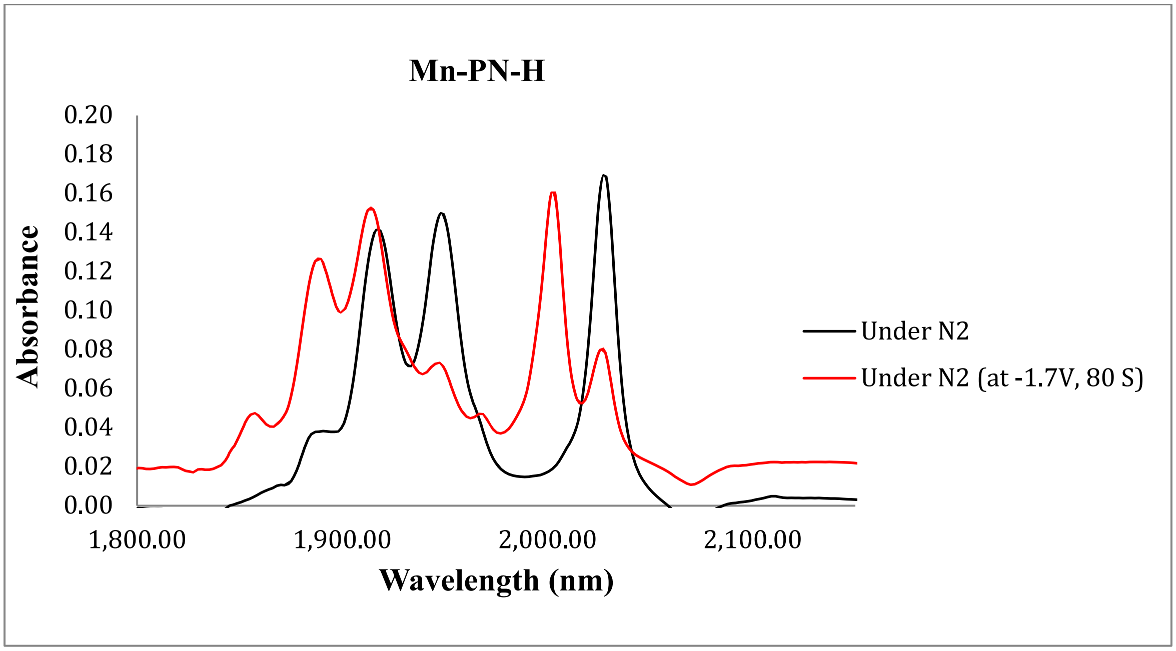

Figure 2.20. Electrochemistry of $[Mn(PN\text{-}H)(CO)_3Br]$ (1) monitored by IR spectroscopy in the v(CO) region. Conditions of IR-SEC: under N_2 in CH_3CN with 0.1 M $(n\text{-}Bu)_4NPF_6$ supporting electrolyte.

After the investigation of the mechanistic features through these experiments for the photocatalytic activity of these catalysts **1** and **4**, the results of suggest the catalytic cycle that is presented in Figure 2.21.

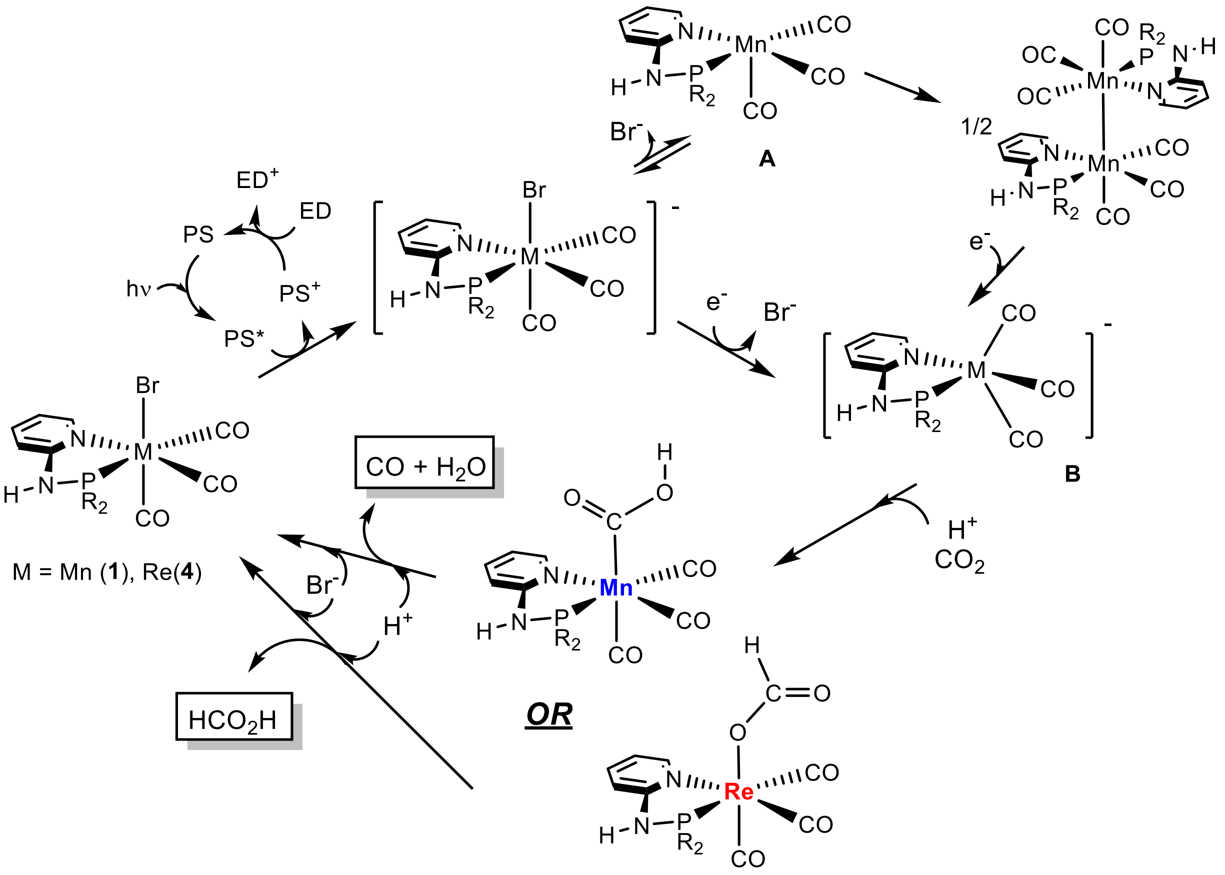

Figure 2.21. Proposed mechanism for the photocatalytic reduction of CO_2 using complexes $[Mn\{\kappa^2\text{-}(Ph_2P)NH(NC_5H_4)\}(CO)_3Br]$ (**1**) or $[Re\{\kappa^2\text{-}(Ph_2P)NH(NC_5H_4)\}(CO)_3Br]$ (**4**).

2.4. Conclusion

Our search for new catalysts that can photocatalytically reduce CO_2 led to four new group 7 complexes that are active in this respect. Importantly these catalysts display ligand arrays that are completely different from conventional reported catalysts of group 7. Their general performance parameters (e.g. TON, ϕ) are comparable to more conventional catalysts with some striking differences. The switch in product selectivity observed for the reduction of CO_2 by **1** compared to **4** indicated that the coordination between CO_2 and the metal plays an important role in the cycle. In the case of **1**, CO_2 likely binds to the metal through the carbon center, and protonation of the oxygen center leads to a metallocarboxylic acid species which subsequently undergoes protonation and cleavage of a C–O bond to furnish water and a CO molecule. Complex **4** appears to evolve into an O bonded formate complex by protonation of the carbon center to ultimately yield formic acid as the reduction product. These results parallel the recently reported switching between CO and formate when the metal in identical ligand environments was changed from Co to Fe.[20] The detailed sequencing of this catalytic process remains to be more precisely determined.

Breaking with the historic hold of α-dimmine ligands on photocatalyst for CO_2 reduction has yielded new Mn and Re-based complexes with remarkable selectivities and good efficiency. We continue to explore ligand variation and probe the mechanistic features of these transformations.

2.5. References

1 J. L. Inglis, B. J. MacLean, M. T. Pryce and J. G. Vos, *Coord. Chem. Rev.*, 2012, **256**, 2571–2600.

2 C. Costentin, M. Robert and J.-M. Savéant, *Chem. Soc. Rev.*, 2013, **42**, 2423–36.

3 J. Schneider, H. Jia, J. T. Muckerman and E. Fujita, *Chem. Soc. Rev.*, 2012, **41**, 2036.

4 J. Hawecker, J. Lehn and R. Ziessel, *Helv. Chim. Acta*, 1986, **69**, 1990–2012.

5 J. Hawecker, J.-M. Lehn and R. Ziessel, *J. Chem. Soc. Chem. Commun.*, 1984, **984**, 328.

6 Y. Yamazaki, H. Takeda and O. Ishitani, *J. Photochem. Photobiol. C Photochem. Rev.*, 2015, **25**, 106–137.

7 A. Rosas-Hernández, C. Steinlechner, H. Junge and M. Beller, *Top. Curr. Chem.*, 2018, **376**, 1–25.

8 J. Bonin, A. Maurin and M. Robert, *Coord. Chem. Rev.*, 2017, **334**, 184–198.

9 C. Constentin, S. Drouet, M. Robert and J.-M. Saveant, *Science*, 2012, **338**, 90–94.

10 J. Bonin, M. Robert and M. Routier, *J. Am. Chem. Soc.*, 2014, **136**, 16768–16771.

11 H. Rao, J. Bonin and M. Robert, *Chem. Commun.*, 2017, **53**, 2830–2833.

12 Z. Guo, S. Cheng, C. Cometto, E. Anxolabéhère-Mallart, S.-M. Ng, C.-C. Ko, G. Liu, L. Chen, M. Robert and T.-C. Lau, *J. Am. Chem. Soc.*, 2016, **138**, 9413–9416.

13 B. Fisher and R. Eisenberg, *J. Am. Chem. Soc.*, 1980, **102**, 7361–7363.

14 T. Ogata, Y. Yamamoto, Y. Wada, K. Murakoshi, M. Kusaba, N. Nakashima, A. Ishida, S. Takamuku and S. Yanagida, *J. Phys. Chem.*, 1995, **99**, 11916–11922.

15 E. Fujita, D. J. Szalda, C. Creutz and N. Sutin, *J. Am. Chem. Soc.*, 1988, **110**, 4870–4871.

16 S. Matsuoka, K. Yamamoto, T. Ogata, M. Kusaba, N. Nakashima, E. Fujita and S. Yanagida, *J. Am. Chem. Soc.*, 1993, **115**, 601–609.

17 Y. Yao, Y. Gao, L. Ye, H. Chen and L. Sun, *J. Energy Chem.*, 2018, **27**, 502–506.

18 T. Ouyang, C. Hou, J. W. Wang, W. J. Liu, D. C. Zhong, Z. F. Ke and T. B. Lu, *Inorg. Chem.*, 2017, **56**, 7307–7311.

19 S. L.-F. Chan, T. L. Lam, C. Yang, S.-C. Yan and N. M. Cheng, *Chem. Commun.*, 2015, **51**, 7799–801.

20 L. Chen, Z. Guo, X. G. Wei, C. Gallenkamp, J. Bonin, E. Anxolabéhère-Mallart, K. C. Lau, T. C. Lau and M. Robert, *J. Am. Chem. Soc.*, 2015, **137**, 10918–10921.

21 J.-P. Collin, A. Jouaiti and J.-P. Sauvage, *Inorg. Chem.*, 1988, **27**, 1986–1990.

22 M. Beley, J. P. Collin, R. Ruppert and J. P. Sauvage, *J. Am. Chem. Soc.*, 1986, **108**, 7461–7.

23 M. Beley, J.-P. Collin, R. Ruppert and J.-P. Sauvage, *J. Chem. Soc. Chem. Commun.*, 1984, **2**, 1315.

24 J. D. Froehlich and C. P. Kubiak, *Inorg. Chem.*, 2012, **51**, 3932–4.

25 V. S. Thoi and C. J. Chang, *Chem. Commun.*, 2011, **47**, 6578–6580.

26 V. S. Thoi, N. Kornienko, C. G. Margarit, P. Yang and C. J. Chang, *J. Am. Chem. Soc.*, 2013, **135**, 14413–14424.

27 D. Hong, Y. Tsukakoshi, H. Kotani, T. Ishizuka and T. Kojima, *J. Am. Chem. Soc.*, 2017, **139**, 6538–6541.

28 Z. Guo, F. Yu, Y. Yang, C.-F. Leung, S.-M. Ng, C.-C. Ko, C. Cometto, T.-C. Lau and M. Robert, *ChemSusChem*, 2017, **10**, 4009–4013.

29 A. Rosas-Hernández, C. Steinlechner, H. Junge and M. Beller, *Green Chem.*, 2017, **19**, 2356–2360.

30 M. Bourrez, F. Molton, S. Chardon-Noblat and A. Deronzier, *Angew. Chem. Int. Ed. Engl.*, 2011, **50**, 9903–9906.

31 H. Takeda, H. Koizumi, K. Okamoto and O. Ishitani, *Chem. Commun.*, 2014, **50**, 1491–3.

32 F. Franco, M. F. Pinto, B. Royo and J. Lloret-fillol, *Angew. Chemie Int. Ed.*, 2018, **57**, 4603–4606.

33 D. C. Grills, M. Z. Ertem, M. Mckinnon, K. T. Ngo and J. Rochford, *Coord. Chem. Rev.*, 2018, **374**, 173–217.

34 P. L. Cheung, C. W. Machan, A. Y. S. Malkhasian, J. Agarwal and C. P. Kubiak, *Inorg. Chem.*, 2016, **55**, 3192–3198.

35 J. X. Zhang, C. Y. Hu, W. Wang, H. Wang and Z. Y. Bian, *Appl. Catal. A Gen.*, 2016, **522**, 145–151.

36 H. Fei, M. D. Sampson, Y. Lee, C. P. Kubiak and S. M. Cohen, *Inorg. Chem.*, 2015, **54**, 6821–6828.

37 J. Rohacova and O. Ishitani, *Chem. Sci.*, 2016, **7**, 6728–6739.

38 S. M. Aucott, A. M. Z. Slawin and J. D. Woollins, *J. Chem. Soc. Dalt. Trans.*, 2000, 2559–2575.

39 G. K. Rao, W. Pell, I. Korobkov and D. Richeson, *Chem. Commun.*, 2016, **52**, 8010–8013.

40 D. Wei, A. Bruneau-Voisine, T. Chauvin, V. Dorcet, T. Roisnel, D. A. Valyaev, N. Lugan and J. B. Sortais, *Adv. Synth. Catal.*, 2018, **360**, 676–681.

41 P. Mella, J. C. Palma, M. Cepeda-Plaza, P. Aguirre, J. Manzur, G. Günther, N. Pizarro and A. Vega, *Polyhedron*, 2016, **111**, 64–70.

42 P. Mella, J. Carlos, M. Cepeda-Plaza, P. Aguirre, J. Manzur, G. Günther, N. Pizarro

and A. Vega, *Polyhedron*, 2016, **111**, 64–70.

43 H. Takeda, H. Koizumi, K. Okamoto and O. Ishitani, *Chem. Commun.*, 2014, **50**, 1491–3.

44 H. Takeda, K. Ohashi, A. Sekine and O. Ishitani, *J. Am. Chem. Soc.*, 2016, **138**, 4354–4357.

45 T. Dhanasekaran, J. Grodkowski, P. Neta, P. Hambright and E. Fujita, *J. Phys. Chem. A*, 1999, **103**, 7742–7748.

46 J. Grodkowski, P. Neta, E. Fujita, A. Mahammed, L. Simkhovich and Z. Gross, *J. Phys. Chem. A*, 2002, **106**, 4772–4778.

47 J. M. Smieja, M. D. Sampson, K. A. Grice, E. E. Benson, J. D. Froehlich and C. P. Kubiak, *Inorg. Chem.*, 2013, **52**, 2484–2491.

48 M. D. Sampson, A. D. Nguyen, K. A. Grice, C. E. Moore, A. L. Rheingold and C. P. Kubiak, *J. Am. Chem. Soc.*, 2014, **136**, 5460–5471.

49 M. Bourrez, M. Orio, F. Molton, H. Vezin, C. Duboc, A. Deronzier and S. Chardon-Noblat, *Angew. Chemie - Int. Ed.*, 2014, **53**, 240–243.

50 F. Hartl, B. D. Rossenaar, G. J. Stor and D. J. Stufkens, *Recl. des Trav. Chim. des Pays-Bas*, 1995, **114**, 565–570.

Chapter 3: Visible light photocatalytic reduction of CO_2 to formic acid with a Ru catalyst supported by an unprecedented ligand array

The work in this chapter formed a significant component of the submitted publication:

(Y. Hameed, G. Rao, J. Ovens, B. Gabidullin and D. Richeson, *ACS Catalysis*, 2019.)

This chapter reports on Ru(II) complexes with a unique tridentate neutral pincer coordination geometry that are able to photocatalytic reduce CO_2 to HCOOH. Visible light photocatalytic CO_2 reduction using N,N′-bis(diphenylphosphino)-2,6-diamino)pyridine ligand supported Ru(II), an unprecedented molecular architecture for this reaction, breaks the domination of α-diimine ligands after more than three decades. These competent catalysts transform CO_2 to formic acid with high selectivity, turnover numbers as high as 11,600 and excellent quantum yields. A proposed mechanism, with combined electron transfer and catalytic cycle, successfully modeled the experimental rate of formic acid production. The initial concept of this project arose from work of G Rao and D. Richeson with contributions from Y. Hameed. Subsequent experimental design was conceived by Y. Hameed and D, Richeson. The synthesis of the first Ru(II) complex was a contribution from G. Rao, and the crystallography was carried out by both J. Ovens and B. Gabidullin. The DFT calacualtions were done by D. Richeson. The synthesis of the second Ru(II) complex was done by Y. Hameed, and all of the characterization and the catalytic exploration for the complexes have been done by Y. Hameed.

3.1. Introduction

Designing and assembling catalysts that can utilize the energy of visible light to overcome the barriers to reduce CO_2 is an important fundamental and technological challenge. Success in this endeavor requires overcoming the inherent stability and low thermodynamic value of CO_2 and would transform this ubiquitous compound from a waste product into a feedstock. For example, photocatalytic formation of formic acid, a two-electron reduction product of CO_2, would result in formation of a commodity chemical and a liquid fuel. Furthermore, formic acid has been identified and explored as a potential carrier of dihydrogen.[1,2]

Homogeneous catalysts for CO_2 reduction, under both electrochemical and photochemical conditions, have been discovered.[3–6] Photocatalysis is a particularly appealing approach as it relies on an essentially limitless and clean solar energy source. Photocatalytic systems consist of integrated components that include a photosensitizer (**PS**), for harvesting the energy of the light, an electron donor (**ED**), that provides the electrons for the reduction, and a catalyst (**CAT**) that is a site for the transformation of CO_2. Since their discovery in 1985[7] all of the reported molecular photocatalyts of Ru(II) display α-diimine supporting ligands and these species fall into two broad groups. One class are bis(α-diimine) species represented by *cis*-$[Ru(N^\wedge N)_2(CO)_2]^{2+}$ [8–11] and the other are mono(α-diimine) catalysts, *cis,trans*-$Ru(N^\wedge N)(CO)_2Cl_2$.[12–14] Although a variety of substituents on the α-diimine ligands has been productively explored to improve catalyst performance, given the maturity of this field, a broader variation of molecular architecture is required to offer new insights and stimulate new concepts. Ligand variation and discovery are a central challenge in catalysis and expanding Ru-based photocatalysts beyond the restrictions of α-diimine support is certainly warranted. Support for this approach comes from the very recent report for successful use of a phosphine-substituted Ru(II) terpyridine complex, *trans*-$[Ru(tpy)(8\text{-quinolyl(diphenyl)phosphine})(MeCN)]^{2+}$, as a Ru photocatalyst that can function both as a photosensitizer and catalyst for CO_2 reduction.[15,16]

Recently, pincer ligand supported catalysts of Fe, Co, Ru and Ir have been shown to have excellent activity and selectivity for hydrogenation of CO_2.[17–23] Furthermore, the potential of pincer complexes as efficient electrocatalysts for CO_2 reduction under mild conditions has recently been demonstrated for Mn,[24] Ru[25] and Ir[26,27] complexes. Interestingly, the Ru complex remains in the α-diimine (i.e. bpy) class of catalysts.

With the objectives of discovering new environments for photocatalytic CO_2 reduction and revealing insight into mechanistic aspects of this transformation we targeted the preparation of new N,N′-bis(diphenylphosphino)-2,6-diamino)pyridine, "PN_3P", pincer complexes of Ru(II). The "PN_3P" notation is used in order to differentiate these ligand scaffolds from, related di(phosphinomethyl)pyridine, 2,6-$\{R_2PCH_2\}_2(NC_5H_3)$ ("PNP"), ligands. The new Ru(II) complexes, $[Ru\{\kappa^3\text{-}2,6\text{-}\{Ph_2PNR\}_2(NC_5H_3)\}(CO)_2Cl^+]Cl^-$ (R = H, Me), are, to our knowledge, the first Ru-based photocatalysts for CO_2 reduction that do not possess α-diimine ligation as well as use a pincer ligand framework.

3.2. Synthesis and Characterization of the Complexes

3.2.1. Experimental Procedures

Reagents and analytical grade solvents were purchased from Strem Chemicals or Sigma Aldrich and used without further purification. The ^1H, $^{13}C\{^1H\}$ and $^{31}P\{^1H\}$ NMR spectra were recorded at 400, 100 and 162 MHz respectively with chemical shifts reported in ppm using the residual protons of the NMR solvent as internal standards. The synthesis of "PN^HP" (2,6-$\{Ph_2PNH\}_2NC_5H_3$) and "$PN^{Me}P$" (2,6-$\{Ph_2PNMe\}_2NC_5H_3$) ligands was based on the procedures described in the literature.[24,34] The photochemical techniques that will be used in this chapter are already described in section 1.7.1 of Chapter 1 and the electrochemical techniques are also described in section 1.7.5 of Chapter 1.

Synthesis and Characterization of $[Ru(\kappa^3\text{-}\{2,6\text{-}(Ph_2PNMe)_2NC_5H_3\})(CO)_2Cl]^+Cl^-$ (1^+Cl^-):

In a glove box, a solution of ligand N,N′-bis(diphenylphosphino)-2,6-di(methylamino)pyridine (0.200 g, 0.4 mmol) was prepared in 10 mL of toluene. To this solution was added $[Ru(CO)_3Cl_2]_2$ (0.100 g, 0.2 mmol). The flask was removed from the glovebox and connected to a Schlenk line via a reflux condenser. The reaction mixture was stirred and heated to 100 °C under N_2 for 16h. The solution was cooled to room temperature. The reaction mixture was filtered, and the precipitate was washed with hexane to give complex (**1^+Cl^-**). Yield 0.245 g (89%). Single crystals of this complex were grown by slow diffusion of hexane into the solution of the complex in dichloromethane. ^{1}H NMR (300 MHz, $CDCl_3$, 25°C): δ = 3.31 (s, 6H, CH_3), 7.06 (d, 2H, J = 11.2), 7.51−7.63 (m, 16H), 7.82-7.89 (m, 4H), 8.18 (t, 1H, J = 12.8). ^{13}C NMR (75 MHz, $CDCl_3$, 25 ºC): δ = 37.51, 103.9, 125.1, 129.0, 130.0, 130.4, 130.9, 132.6, 133.0, 133.4, 144.4, 159.8, 187.9, 193.3. $^{31}P\{^1H\}$ NMR (122 MHz, $CDCl_3$, 25°C): δ = 97.7. Elemental analysis calcd (%) for $C_{33}H_{29}Cl_2N_3O_2P_2Ru$ C 54.03, H 3.99, N 5.73, found C 54.53, H 3.61, N 5.73.

Synthesis and Characterization of $[Ru(\kappa^3\text{-}\{2,6\text{-}(Ph_2PNH)_2NC_5H_3\})(CO)_2Cl]^+Cl^-$ (2^+Cl^-):

In a glove box, a solution of ligand N,N′-bis(diphenylphosphino)-2,6-di(amino)pyridine (0.190 g, 0.4 mmol) was prepared in 10 mL of toluene. To this solution was added $[Ru(CO)_3Cl_2]_2$ (0.100 g, 0.2 mmol). The flask was removed from the glovebox and connected to a Schlenk line via a reflux condenser. The reaction mixture was stirred and heated to 100 °C under N_2 for 16h. The solution was cooled to room temperature. The reaction mixture was filtered, and the precipitate was washed with hexane to give complex (2^+Cl^-). Yield 0.261 g (93%). Single crystals of this complex were grown by slow diffusion of hexane into the solution of complex made in dichloromethane. ^{1}H NMR (300 MHz, $CDCl_3$, 25°C): $\delta = 7.22-7.11$ (m, 8H), 7.47-7.32 (m, 8H), 7.81-7.74 (m, 5H), 8.03-7.94 (m, 4H). ^{13}C NMR (75 MHz, $CDCl_3$, 25 ºC): δ = 128.6, 129.1, 129.3, 129.8, 130.9, 132.1, 132.3, 132.6, 134.6, 159.7, 159.8, 187.9, 193.3. $^{31}P\{^1H\}$ NMR (122 MHz, $CDCl_3$, 25°C): δ = 80.5. Elemental analysis calcd (%) for $C_{31}H_{25}Cl_2N_3O_2P_2Ru$ C 52.78, H 3.57, N 5.96, found C 52.69, H 3.65, N 6.24.

3.2.2. General Procedures of the $[Ru\{\kappa^3\text{-}2,6\text{-}\{Ph_2PNR\}_2(NC_5H_3)\}(CO)_2Cl^+]Cl^-$ Complexes

The direct addition of N,N′-bis(diphenylphosphino)-2,6-di(methylamino)pyridine to $[Ru(CO)_3Cl_2]_2$ in toluene followed by heating to 100 °C under N_2 for 16h led to the new cationic Ru complex $[Ru\{\kappa^3\text{-}2,6\text{-}(Ph_2PNMe)_2NC_5H_3\}(CO)_2Cl]^+Cl^-$ (**1^+Cl^-**) as a colorless solid with a yield of 89%. Replacing the starting ligand with N,N′-bis(diphenylphosphino)-2,6-diaminopyridine and following a similar procedure produced the analogous complex, $[Ru\{\kappa^3\text{-}2,6\text{-}(Ph_2PNH)_2NC_5H_3\}(CO)_2Cl]^+Cl^-$ (**2^+Cl^-**) with a yield of 93%. Spectroscopic data and a single crystal x-ray analysis of **1^+Cl^-** definitively confirmed the identity of this species. As shown in Figure 3.1, the **1^+** cation exhibited a distorted octahedral environment for the Ru(II) center comprised of a tridentate, *mer*-PN_3P ligand, a CO ligand oriented *trans* to the pyridyl function, and axially aligned CO and Cl ligands.

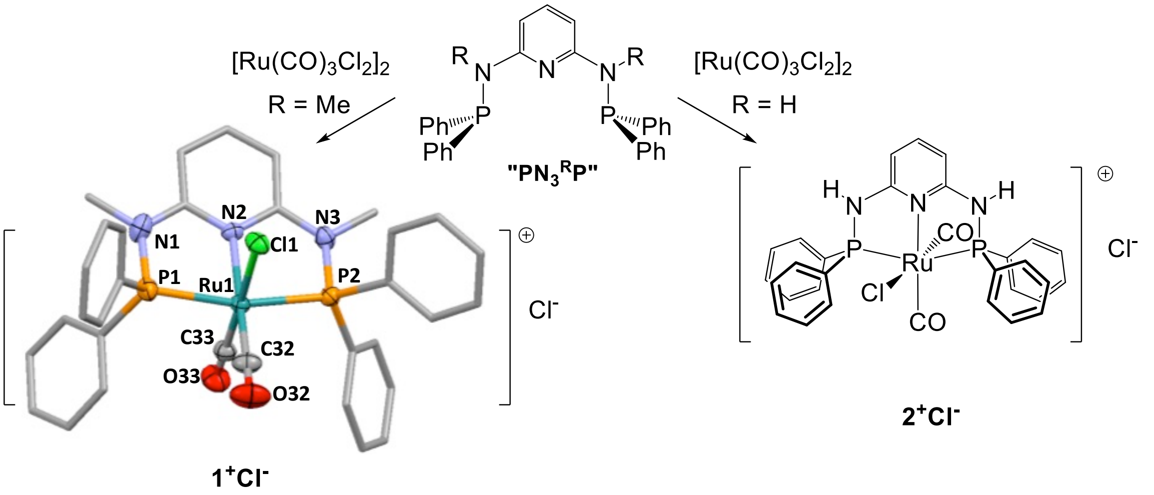

Figure 3.1. Reaction scheme for the preparation of complexes $\mathbf{1^+Cl^-}$ and $\mathbf{2^+Cl^-}$ and a representation of the single crystal X-ray structure of $\mathbf{1^+}$. Selected bond distances (Å): Ru-N2 2.092(3), Ru-P1 2.3289 (12), Ru-P2 2.3456(11), Ru-C33 1.890(4), Ru-C32 1.913(5), Ru-Cl1 2.4037(10).

There are only two reported crystal structures for PN_3P ligated Ru(II) complexes which, although not direct analogues to $\mathbf{1^+}$, do serve for comparison. The first is a Ru(II) hydride $[RuH\{\kappa^3\text{-}2,6\text{-}({}^tBu_2PNH)_2NC_5H_3\}(CO)_2]^+Cl^-(HCO_2H)$[28] (**I**) which displayed a distorted square-pyramidal geometry around the ruthenium center with the PN_3P and CO ligands forming the basal plane and the hydride located in the apical position. The corresponding metal-ligand metrical parameters of this complex are similar to those of $\mathbf{1^+}$. The second complex had the formula *cis*-Ru(PN_3P-BIPOL)(PPh_3)Cl_2 $2CH_2Cl_2$[29](**II**) (PN_3P-BIPOL = N,N′-bis(dibenzo[d,f][1,3,2]dioxaphosphepine)-2,6-diaminopyridine). This complex displayed Ru in a distorted octahedral geometry with a *mer*-tridentate ligand, a PPh_3 ligand, *cis* to the pyridine nitrogen center, and two *cis* Cl atoms. Again, the metal-ligand metrical parameters are similar to those in $\mathbf{1^+}$ showing slightly shorter Ru-P bond distances that are likely due to the fact that, in contract to $\mathbf{1^+}$ and **I**, **II** does not possess strong π-accepting ligands (i.e. CO).

3.3. Photocatalytic CO_2 Reduction Results

The photocatalytic reduction of carbon dioxide was carried out in a glass reactor at room temperature using 1mM $[Ru\{\kappa^3\text{-}2,6\text{-}\{Ph_2PNMe\}_2(NC_5H_3)\}(CO)_2Cl^+]Cl^-$ (**1^+Cl^-**) as the catalyst along with $[Ru(bpy)_3](PF_6)_2$ (**PS**) (1mM) and TEOA (**ED**) under a CO_2 atmosphere in 4 mL of DMF. The reaction mixture was irradiated with visible light from an LED (1050 mW at 700mA, 3.4 x 10^{-8} mol photons/sec) at 405 nm. After 24 hr, the ^1H NMR spectrum of the reaction solution revealed that the only product was HCO_2H, which was quantified by NMR analysis thus confirming that the Ru complex **1^+Cl^-** was a photoredox catalyst for selective reduction of CO_2 to formic acid. No CO(g) was observed in the analysis of this reaction giving further evidence of the selectivity for formic acid. Analysis of the reaction headspace did reveal that the sole gas phase product was H_2, which was quantified by gas chromatography (GC) (Table 3.1, Table 3.2). The necessity of the components in this photoreaction was confirmed through several control experiments involving the omission of catalyst, **PS**, and **ED** (Table 3.2). Successful formation of formic acid required all of these components.

Table 3.1. Photocatalytic experiments with complexes **[Ru(κ^3-{2,6-(Ph$_2$PNMe)$_2$NC$_5$H$_3$})(CO)$_2$Cl]$^+$Cl$^-$ (1$^+$Cl$^-$)** and **[Ru(κ^3-{2,6-(Ph$_2$PNH)$_2$NC$_5$H$_3$})(CO)$_2$Cl]$^+$Cl$^-$ (2$^+$Cl$^-$)**. In DMF (4mL) with Ru(bpy)$_3$(PF$_6$)$_2$ as photosensitizer (**PS**) and TEOA as the electon donor (**ED**). Turn-over number (TON) = (moles of product)/(moles of catalyst). Irradiation with 405 nm light for 24 h.[a]

Catalyst (μM)	**[PS] (μM)**	**H$_2$ (μmol)**	**TON$_{H2}$**	**ϕ_{H2}[b] (%)**	**HCOOH (μmol)**	**TON$_{HCOOH}$**	**ϕ_{HCOOH}[b] (%)**
1$^+$Cl$^-$							
25	1000	22	220	0.75	152	1520	5.2
50	1000	26	130	0.89	179	895	6.1
500	1000	28	14	0.95	324	162	11
1000	1000	53	13.3	1.8	362	90.5	12
2000	1000	148	18.5	5.7	330	41.3	11
2$^+$Cl$^-$							
25	1000	32	320	1.1	194	1940	6.6
50	1000	24	120	0.82	180	900	5.5
500	1000	28	14	0.95	141	70.5	4.3
1000	1000	48	12	1.6	178	44.5	5.4
2000	1000	74	9.25	2.5	332	41.5	5.1

[a] 4mL DMF, **PS** = Ru(bpy)$_3$(PF$_6$)$_2$ 1mM, **ED** = TEOA. Irradiation with 405 nm light for 24 h. [b] photon flux = 3.4 x 10^{-8} photons/sec.

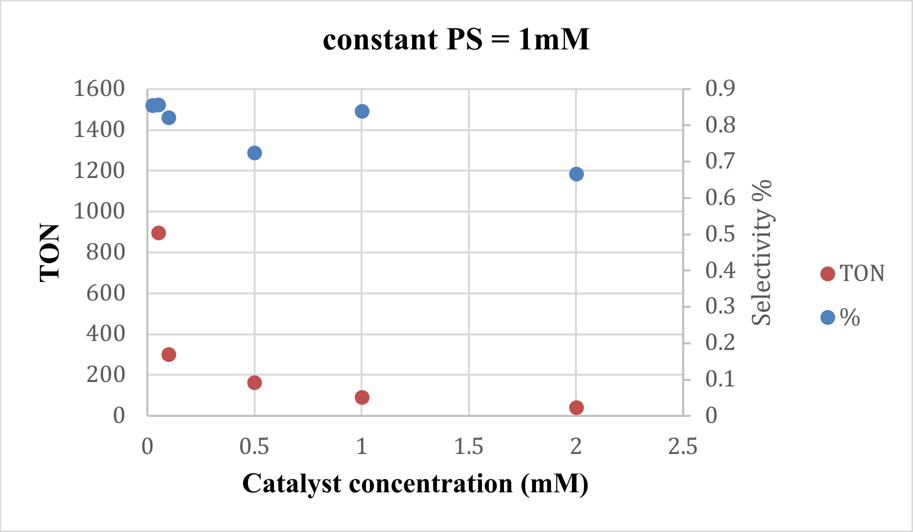

Figure 3.2. Trends with different concentrations of the catalyst versus TON and selectivity.

As shown in Table 3.2 and Figure 3.3, various concentrations of the photosensitizer were been done and the best effect of **[PS]** in terms of TON and selectivity was with 1 mM of PS, and that is the reason for keeping the concentration of the **PS** is constant with 1000 μmol of [PS] in Table 3.1.

Table 3.2. Photocatalytic experiments with complexes **[Ru(κ^3-{2,6-(Ph$_2$PNMe)$_2$NC$_5$H$_3$})(CO)$_2$Cl]$^+$Cl$^-$ (1$^+$Cl$^-$)** with different concentations of **[PS]**. In DMF (4mL) with Ru(bpy)$_3$(PF$_6$)$_2$ as photosensitizer (**PS**) and TEOA as the electon donor (**ED**). Turn-over number (TON) = (moles of product)/(moles of catalyst). Irradiation with 405 nm light for 24 h.[a]

Catalyst	[Catalyst] (mM)	[PS] (mM)	H_2 (μmol)	TON$_{H2}$	HCOOH (μmol)	TON HCOOH	Selectivity[a] for HCOOH (%)
1$^+$Cl$^-$	-	1	-	-	5	-	-
	1	-	6	-	2	-	-
	0.025	0.025	-	-	38	380	100
	0.05	0.05	-	-	42	210	100
	0.1	0.1	23	57.5	145	363	86.3
	0.5	0.5	72	36	277	139	79.4
	2	2	89	11.1	286	35.8	76.3
	1	**1**	**53**	**13.3**	**362**	**90.5**	**87.2**
	1	0.1	30	7.5	135	33.8	81.8
	1	0.5	83	20.8	188	47	69.4
	1	2	77	19.3	324	81	80.8

[a] selectivity is calculated as μmol HCOOH/(μmol HCOOH + μmol H_2) x 100

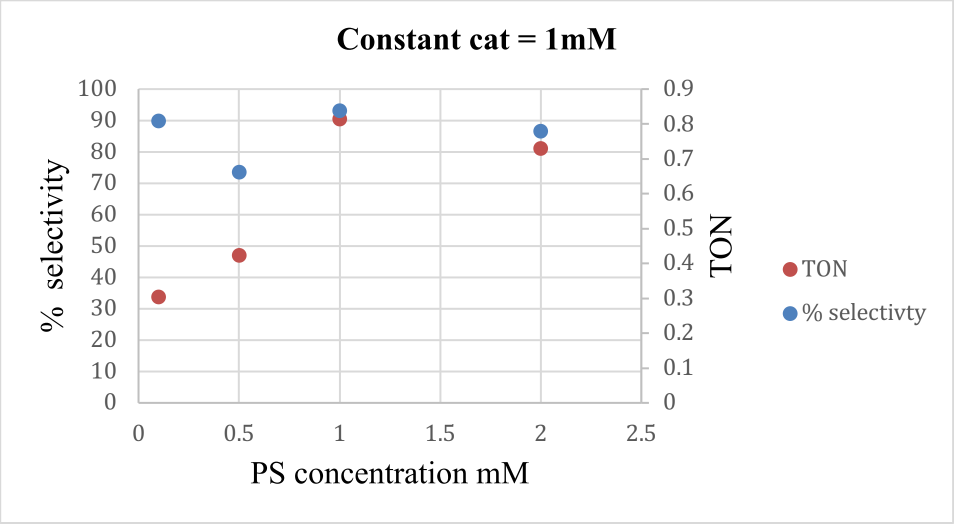

Figure 3.3. Trends with different concentrations of the photosensitizer versus TON and selectivity.

The effects of solvent and of various electron donors was also examined. For example, the DMF reaction solvent could be replaced by acetonitrile but the photocatalytic activity of this system for reduction of CO_2 was diminished (Table 3.3). Importantly, attempts to use other **ED** such as BNAH, ascorbic acid, sodium ascorbate, and trimethylamine gave poor results as shown in Table 3.4.

Table 3.3. A comparison of the photocatalytic experiments with complexes $\mathbf{1^+Cl^-}$ and $\mathbf{2^+Cl^-}$ in CH_3CN and DMF. Experiments carried out in 4mL of solvent with $Ru(bpy)_3(PF_6)_2$ as photosensitizer (**PS**), TEOA as the electon donor (**ED**) and irradiation at 405 nm for 24 h.

Catalyst	[Catalyst] (mM)	[PS] (mM)	Solvent	H_2 (µmol)	TON_{H2}	HCOOH (µmol)	TON_{HCOOH}
$\mathbf{1^+Cl^-}$	1	1	DMF	53	13.3	362	90.5
	1	1	CH_3CN	37	9.25	150	38
$\mathbf{2^+Cl^-}$	1	1	DMF	48	12	178	45.5
	1	1	CH_3CN	30	7.5	131	32.8

Table 3.4. Photocatalytic results for complex **1**$^+$ using different electron donors.[a]

Complex 1 (mM)	**Ru(bpy)$_3$.2PF$_6$ (mM)**	**Solvent**	**Electron donor**	**H$_2$ (µmol)**	**HCOOH^c (µmol)**
-	1	DMF	TEOA^b	0	5
1	-	DMF	TEOA^b	6	2
1	1	DMF	TEOA^b	53	362
1	1	DMF	TEOA+*BNAH*	23	131
1	1	DMF	BNAH^e	0	0
1	1	DMF	NEt$_3$^{b}	6	65
1	1	DMF	Ascorbic acid^d	0	0
1	1	DMF	Sodium ascorbate^d	0	0
1	-	CH$_3$CN	TEOA^b	0	0
1	1	CH$_3$CN	TEOA^b	37	150
1	1	CH$_3$CN	TEOA+*BNAH*	10	46
1	1	CH$_3$CN	BNAH^e	0	0
1	1	CH$_3$CN	NEt$_3$^{b}	4	44
1	1	CH$_3$CN	Ascorbic acid^d	0	0
1	1	CH$_3$CN	Sodium ascorbate^d	0	0

^{a}Irradiation with 405 nm light conducted on a solution containing the catalyst **Ru-PNP-Me complex [1]** and [Ru(bpy)$_3$]$^{2+}$ complex as a photosensitizer under an CO$_2$ atmosphere for 24 h. ^{b}TEOA (1 mL). DMF (4 mL) or Acetonitrile (4 mL) was used as solvent. ^{c}corrected for background formation under N$_2$ ^{d}Ascorbic acid / Sodium ascorbate (1 g). ^{e}BNAH (0.2 g).

In addition, the time profile for the formic acid (HCOOH) and the hydrogen (H$_2$) productions are shown in Figure 3.4. and Table 3.5. The time profile demonstrated that the catalyst (**1**$^+$**Cl**$^-$) was well-behaved for over 72 hr.

Table 3.5. Time profile data for the photocatalytic reduction of CO$_2$ to yield HCOOH and H$_2$ for catalysts **1**$^+$**Cl**$^-$. [catalyst] =1mM, [Ru(bpy)$_3$(PF$_6$)$_2$] = 1mM and TEOA as the electon donor (**ED**) in DMF (4mL) irradiated with 405 nm LED lamp.

Time (h)	**H$_2$ (µmol)**	**TON$_{H2}$**	**HCOOH (µmol)/TON**	**TON$_{HCOOH}$**
24	53	13.25	304	76
48	116	29	368	92
72	143	35.75	444	111

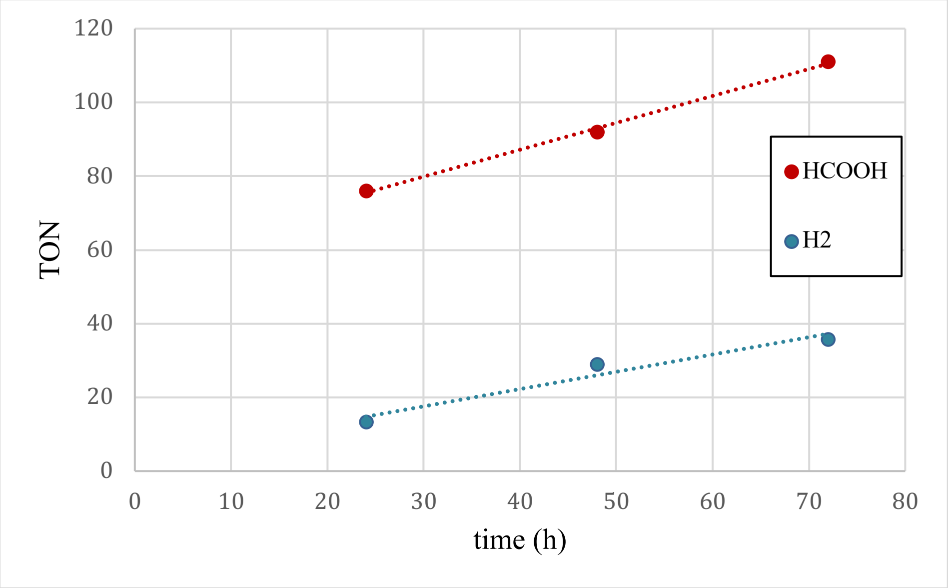

Figure 3.4. Time profile for product formation in the photocatalytic reduction of CO_2 to yield HCOOH and H_2 for catalyst **1^+Cl^-**. (Data from Table 3.5).

Additional critical details of these reactions were provided by carrying out the reduction of $^{13}CO_2$ employing **1^+Cl^-**. Under these photocatalytic conditions, formation of $H^{13}COOH$ was clearly documented by analysis of the reaction headspace to high-resolution mass spectrometry (Figure 3.5) as well as analysis of the liquid phase by ^{13}C and ^{1}H NMR (Figures 3.6, 3.7). All three measurements documented conversion of $^{13}CO_2$ to $H^{13}COOH$. All of these data support that the Ru complexes are entirely new frameworks for photocatalysts for CO_2 reduction.

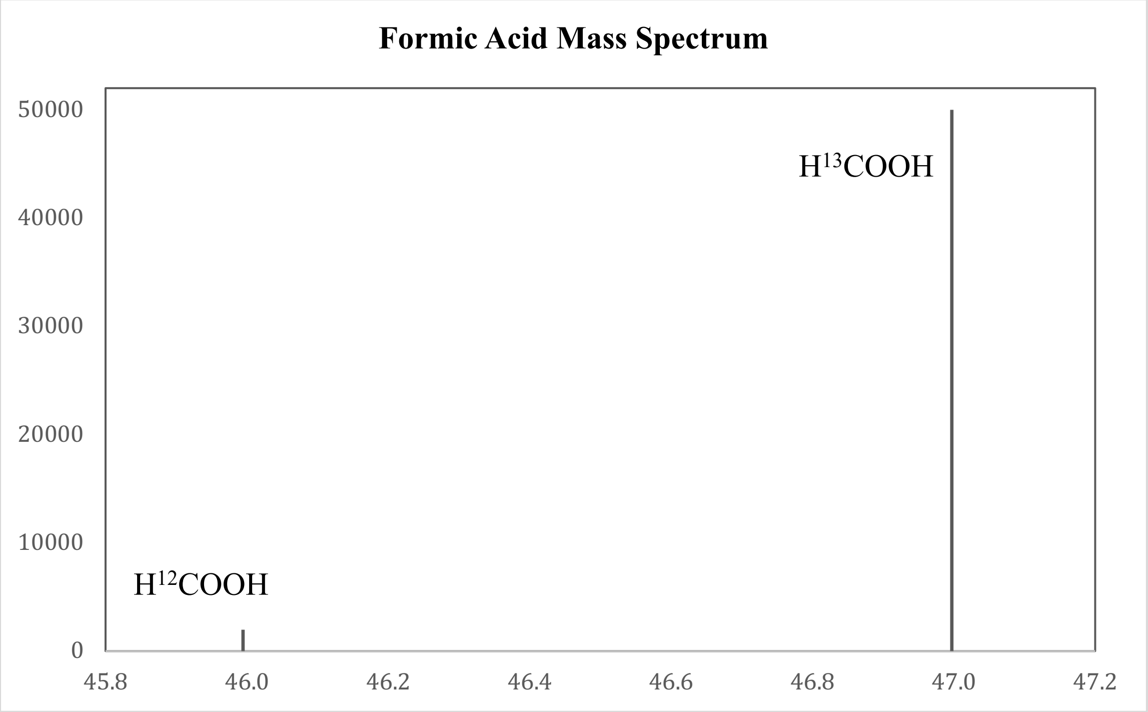

Figure 3.5. High resolution mass spectrum from the head-space of the photocatalytic reduction of $^{13}CO_2$ using **1^+Cl^-** as the catalyst.

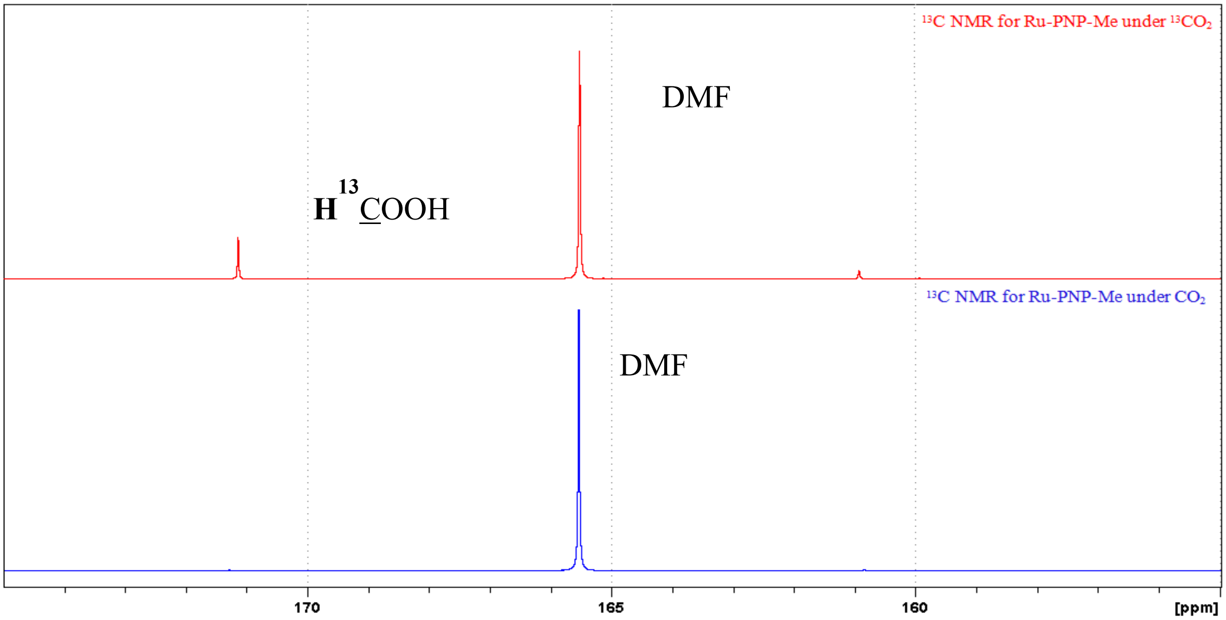

Figure 3.6. ^{13}C NMR spectra in D_2O for the photocatalytic reduction of $^{13}CO_2$ (top) to produce formic acid **1^+Cl^-** as the catalyst. For comparison, a reaction using unlabeled CO_2 (bottom) is shown.

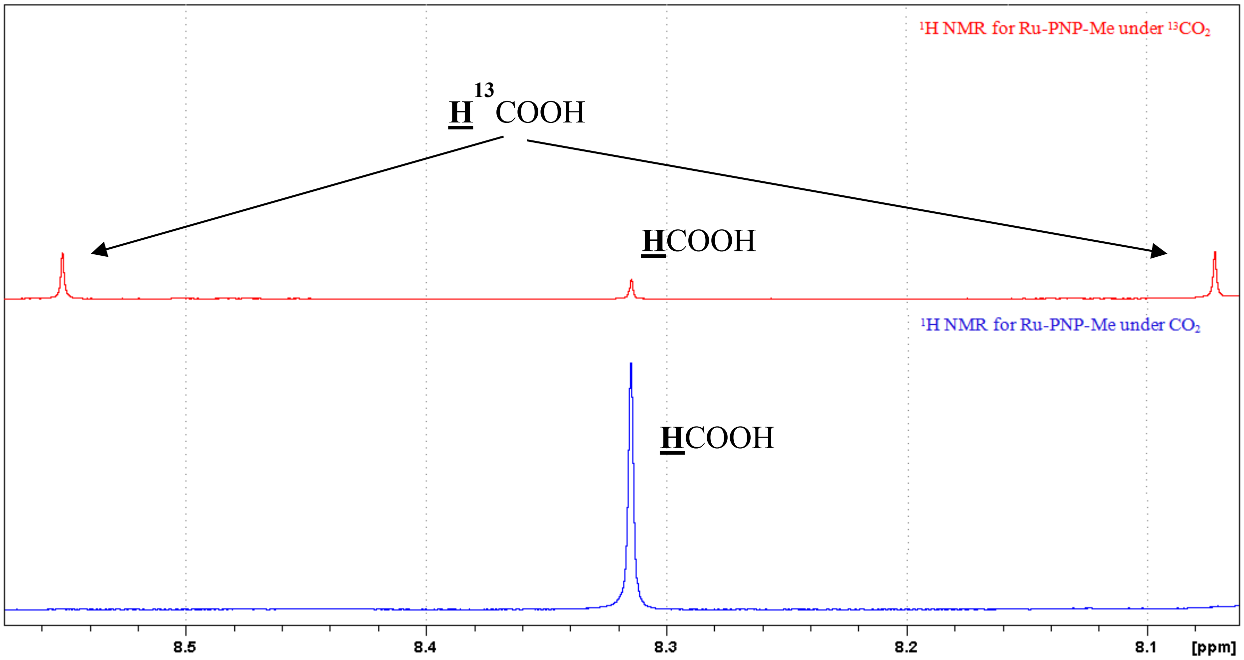

Figure 3.7. ^{1}H NMR spectra for the formyl HOOC-**H** proton of formic acid obtained from photocatalytic reduction of $^{13}CO_2$ using **1⁺Cl⁻** as the catalyst (top). For comparison, a reaction using unlabeled CO_2 is shown (bottom).

Product selectivity for the conversion of CO_2 is excellent, however the selectivity with regard to the reducing equivalents used in this reaction is diminished due to the appearance of H_2 (Table 3.1 and Table 3.2). Taking into account the H_2 the selectivity of the reduction reaction is >88% over a concentration range of 2.5-1000μmolar [**1^+Cl^-**] and constant [**PS**] (Table 3.2).

The generality of the proficiency of this catalyst architecture to photocatalytic reduction of CO_2 was substantiated by the success application of **2^+Cl^-** to this transformation. Perhaps not surprisingly, these initial data indicate very similar performance but with **2^+Cl^-** giving slightly lower quantum yields and selectivity of the reduction products (Table 3.1, Table 3.2).

The molar ratio of HCOOH produced to catalyst **1^+Cl^-** defined the turnover number for formic acid (TON_{HCOOH}) and through variation of the [**1^+Cl^-**] with a constant 1mM concentration of **PS**, the $\text{TON}_{\text{HCOOH}}$ ranged from 41 up to 11600 (Table 3.2). The TON values for H_2 production are lower and paralleled these values. When the [$\mathbf{1^+Cl^-}$] was varied the TON_{H2} was 10-14% of the values for $\text{TON}_{\text{HCOOH}}$. The time profile for the photocatalytic performance of $\mathbf{1^+Cl^-}$ is shown in Figure 3.4 and demonstrated that $\mathbf{1^+Cl^-}$ was well-behaved for over 72 hr of irradiation.

Photocatalytic systems consist of an electron transfer cycle coupled with a catalysis cycle.[12,14,30] The electron transfer cycle is the process that supplies electrons to the catalyst from the reduced photosensitizer (**PS**$^-$) (Figure 3.8).

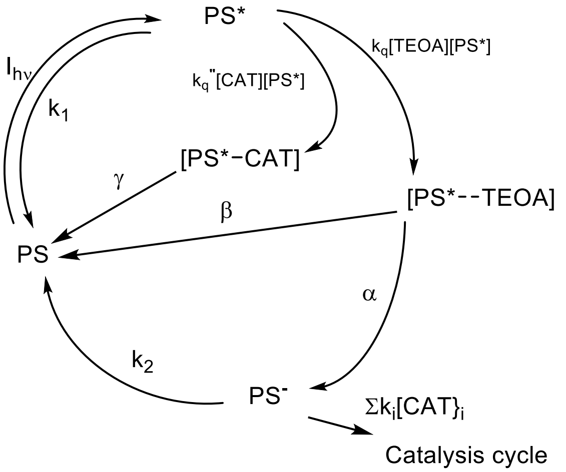

Figure 3.8. The electron transfer cycle used in modeling.[12] In this Figure the following terms apply:

$I_{h\nu}$ is the rate of incident photons,
k_1 is the sum of the radiative and non-radiative rate constants for relaxation of PS*,
k_q is the quenching rate constant of PS* by TEOA,
α is the cage escape efficiency after the electron transfer from TEOA to PS*,
β is the fraction of back-electron transfer in the solvent cage,
k_q'' is the quenching rate constant of PS* by CAT,
γ is the cage escape efficiency quenching of PS* by CAT,
k_2 is the quenching rate constant of PS$^-$,
k_i is the electron transfer rate constant from the PS$^-$ of the form of the catalyst
$[\text{CAT}]_i$ is the concentration of the form of the catalyst.

Coupled to the electron transfer cycle shown in Figure 3.7, is the catalytic cycle shown in Figure 3.9. This reaction path represents the steps where, in this case, a Ru complex catalytically reduces CO_2 using these supplied electrons. Beginning with the starting cationic complex, all of the Ru species in this mechanism were computationally optimized through DFT with the B3LYP functional and def2TZVP basis set to help guide the proposed reactions (Figures 3.10-3.14).

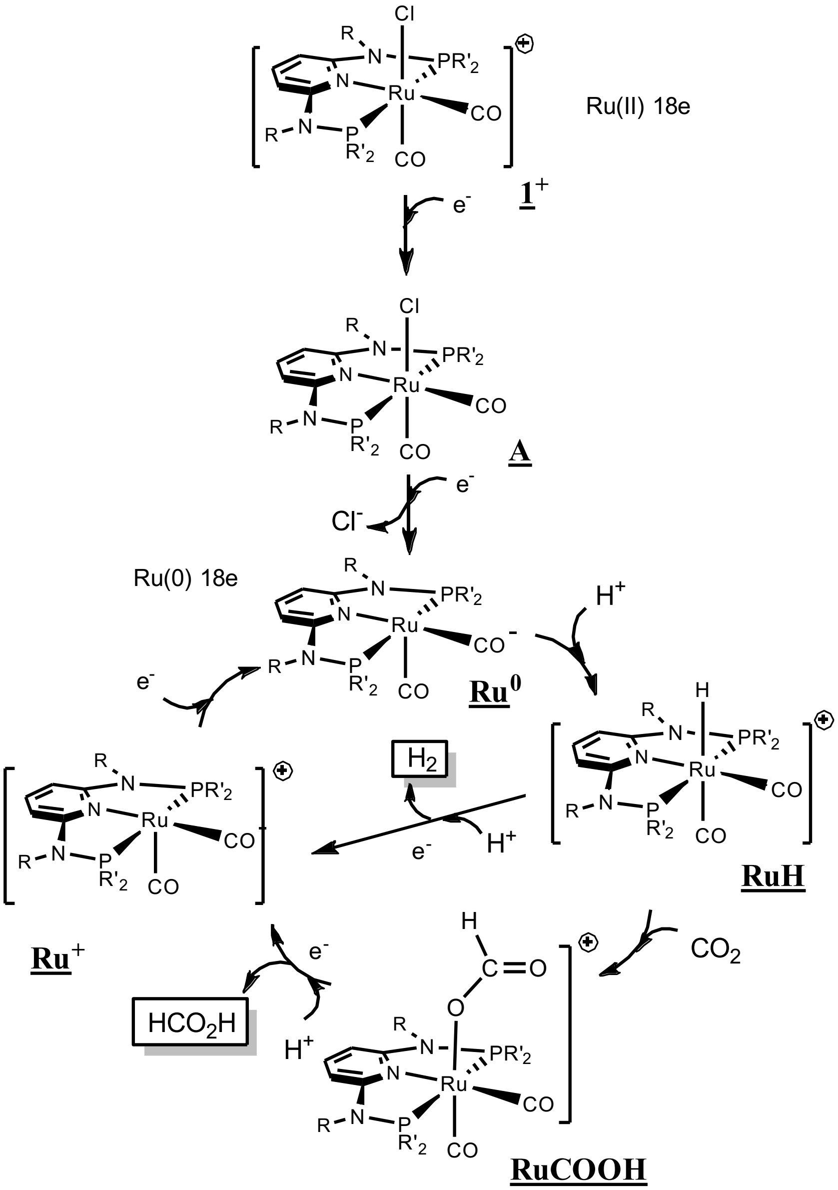

Figure 3.9. Proposed mechanism for photocatalytic reduction of CO_2 to formic acid beginning with $[Ru(\kappa^3\text{-}\{2,6\text{-}(Ph_2PNMe)_2NC_5H_3\})(CO)_2Cl]^+$ **(1^+)**.

Entry into the catalysis cycle comes from the reduction of **A** (Figure 3.9), which during optimization, spontaneously dissociated a Cl^- anion to yield a distorted square pyramidal complex labelled **$\underline{Ru^0}$**. Visualization of the HOMO of this complex shows that the electron density is localized in a $d_z{}^2$ type orbital with some contributions from the CO ligands (Figures 3.15). Protonation of this electron pair yielded the hydride complex, **RuH**. Generally, the route to successful transformation of CO_2 to formate is envisioned to proceed through a transition metal hydride intermediate that can insert CO_2 leading to a metallacarboxylic acid complex.[31,32] The insertion of CO_2 into the Ru-H complex yielded the metallacarboxylic acid species **RuCOOH**, which through reduction and proton transfer releases formic acid and generates a Ru(I) complex **Ru^+**. The catalytic cycle closes with return to **Ru**^{0} via reduction from **PS^-**. This proposed catalytic cycle also provides a path for the formation of H_2. In principle, as shown in Figure 3.9, this can occur via protonation of the hydride intermediate, RuH, or combination of two of these metal–hydrides. This process short cuts the catalytic cycle for formic acid production. In practice, protonation of the hydride intermediate is a reaction that is difficult to avoid, and this implies that choice of reaction medium (specifically the pKa of any protons available) will influence H_2 formation.

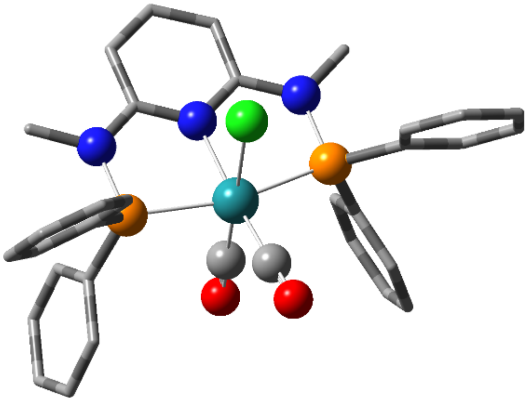

Figure 3.10. A ball and stick structural representation for the computationally optimized $[Ru(\kappa^3\text{-}\{2,6\text{-}(Ph_2PNMe)_2NC_5H_3\})(CO)_2Cl]^+Cl^-$ (**1^+Cl^-**). DFT calculations used the B3LYP functional and the def2TZVP basis set. Hydrogen atoms are not shown for clarity.

Table 3.6. A comparison of selected metal–ligand distances from the experimental single crystal X-ray analysis and from the computationally optimized structure for $[Ru(\kappa^3\text{-}\{2,6\text{-}(Ph_2PNMe)_2NC_5H_3\})(CO)_2Cl]^+Cl^-$ (**1^+Cl^-**).

Bond	Experiment (Å)	Computed (def2TZVP) (Å)
Ru-Npy	2.092	2.13276
Ru-P	2.329, 2.406	2.38705, 2.38707
Ru-CO (trans Cl)	1.890	1.88771
Ru-CO (trans py)	1.913	1.90811
Ru-Cl	2.404	2.45344

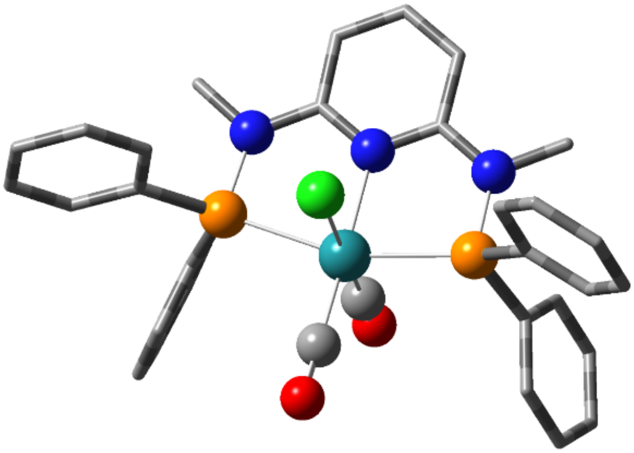

Figure 3.11. A ball and stick structural representation for the computationally optimized product from single electron reduction of **1**$^+$, [Ru(κ^3-{2,6-(Ph_2PNMe)$_2NC_5H_3$})(CO)$_2$Cl], **A**. DFT calculations used the B3LYP functional and the def2TZVP basis set. Hydrogen atoms are not shown for clarity.

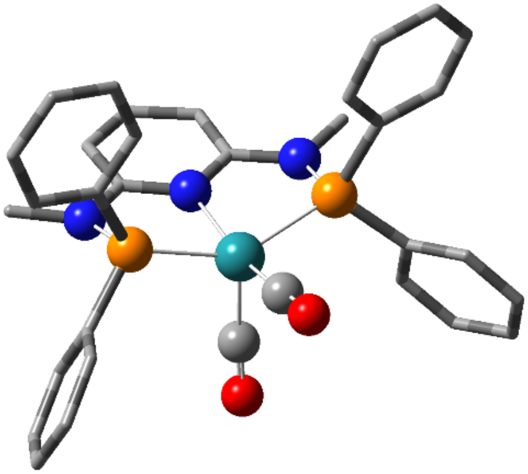

Figure 3.12. A ball and stick structural representation for the computationally optimized [Ru(κ^3-{2,6-(Ph_2PNMe)$_2NC_5H_3$})(CO)$_2$], **Ru^0**. DFT calculations used the B3LYP functional and the def2TZVP basis set. Hydrogen atoms are not shown for clarity. During the optimization, the Cl$^-$ spontaneously dissociated from the complex to yield five-coordinate, distorted square-base pyramidal [Ru(κ^3-{2,6-(Ph_2PNMe)$_2NC_5H_3$})(CO)$_2$] (**Ru^0**) as shown.

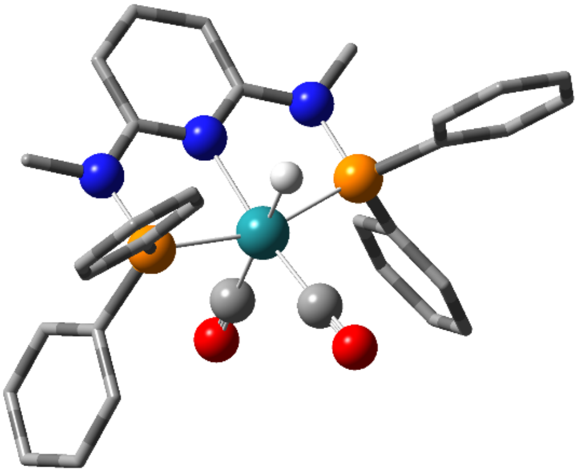

Figure 3.13. A ball and stick structural representation for the computationally optimized [Ru(κ^3-{2,6-(Ph$_2$PNMe)$_2$NC$_5$H$_3$})(CO)$_2$H]$^+$, **<u>RuH</u>**, obtained from protonation of **Ru^0**. DFT calculations used the B3LYP functional and the def2TZVP basis set. Hydrogen atoms are not shown for clarity.

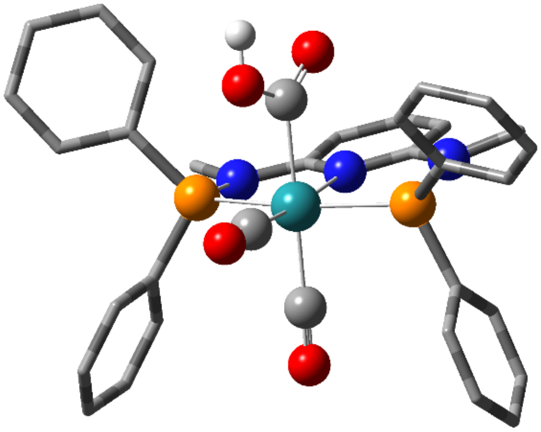

Figure 3.14. A ball and stick structural representation for the computationally optimized metallaformic acid proposed complex [Ru(κ^3-{2,6-(Ph$_2$PNMe)$_2$NC$_5$H$_3$})(CO)$_2$(COOH)]$^+$ **RuCOOH**. This complex arises from the insertion of CO$_2$ into M-H complex, **RuH**. DFT calculations used the B3LYP functional and the def2TZVP basis set. Hydrogen atoms are not shown for clarity.

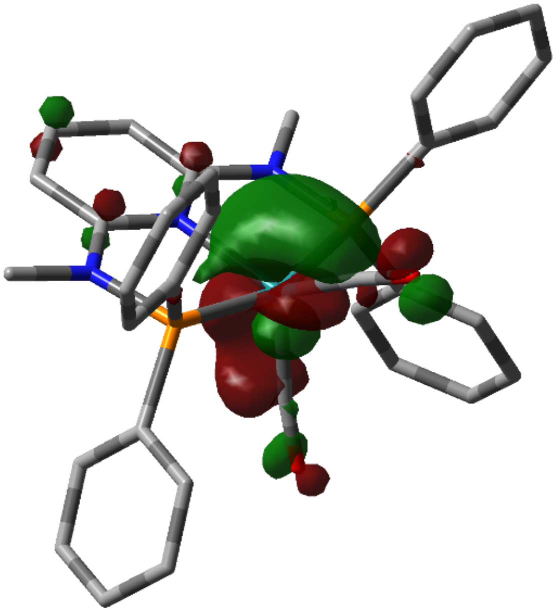

Figure 3.15. Representation of the HOMO (isovalue 0.05) for the computationally optimized [Ru(κ^3-{2,6-(Ph$_2$PNMe)$_2$NC$_5$H$_3$})(CO)$_2$], **Ru^0**. DFT calculations used the B3LYP functional and the def2TZVP basis set. Hydrogen atoms are not shown, and the structure is represented in tube form for clarity.

The rate of formation of formic acid from the proposed mechanism is given by eqn 1:

$$\frac{d[HCOOH]}{dt} = k_3[RuCOOH][PS^-] \qquad (1)$$

The electron transfer cycle provides the electrons for the catalysis cycle through the formation of [PS$^-$] as shown in Figure 3.8.

A key step in every photocatalytic process is quenching and electron transfer involving the excited PS. The quenching of Ru(bpy)$_3^{2+}$ was examined using the two catalysts **1$^+$Cl$^-$** and **2$^+$Cl$^-$**. The spectra of these quenching experiments for both catalysts are shown below in Figure 3.16.and 3.17. Since the electron transfer cycle is initiated with light absorption by PS (Ru(bpy)$_3^{2+}$) the quenching of the excited state PS* was examined. The known quenching by TEOA was confirmed (as was shown before in Chapter 1).

Similarly we determined that both complexes **1^+Cl^-** and **2^+Cl^-** were actually even more effective (≈10x) at quenching the PS* excited state (Figures 3.18) but this is most likely a loss channel for the photocatalytic system.[33]

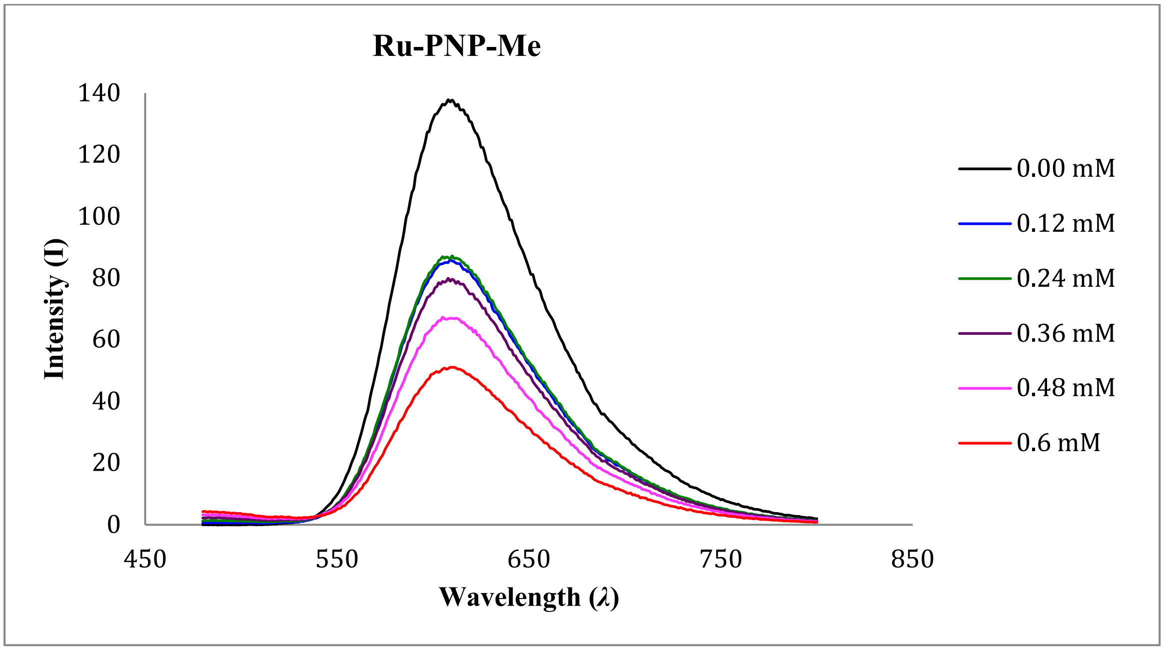

Figure 3.16. Emission-spectra from the quenching experiments with complex (**1^+Cl^-**).

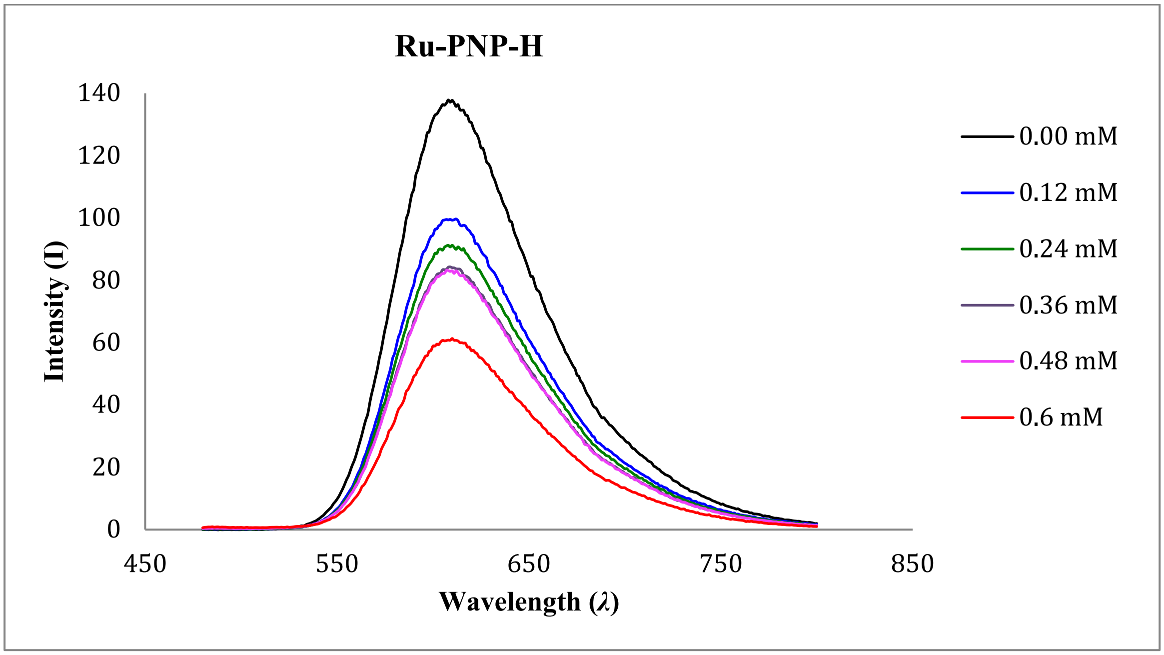

Figure 3.17. Emission-spectra from the quenching experiments with complex (**2^+Cl^-**).

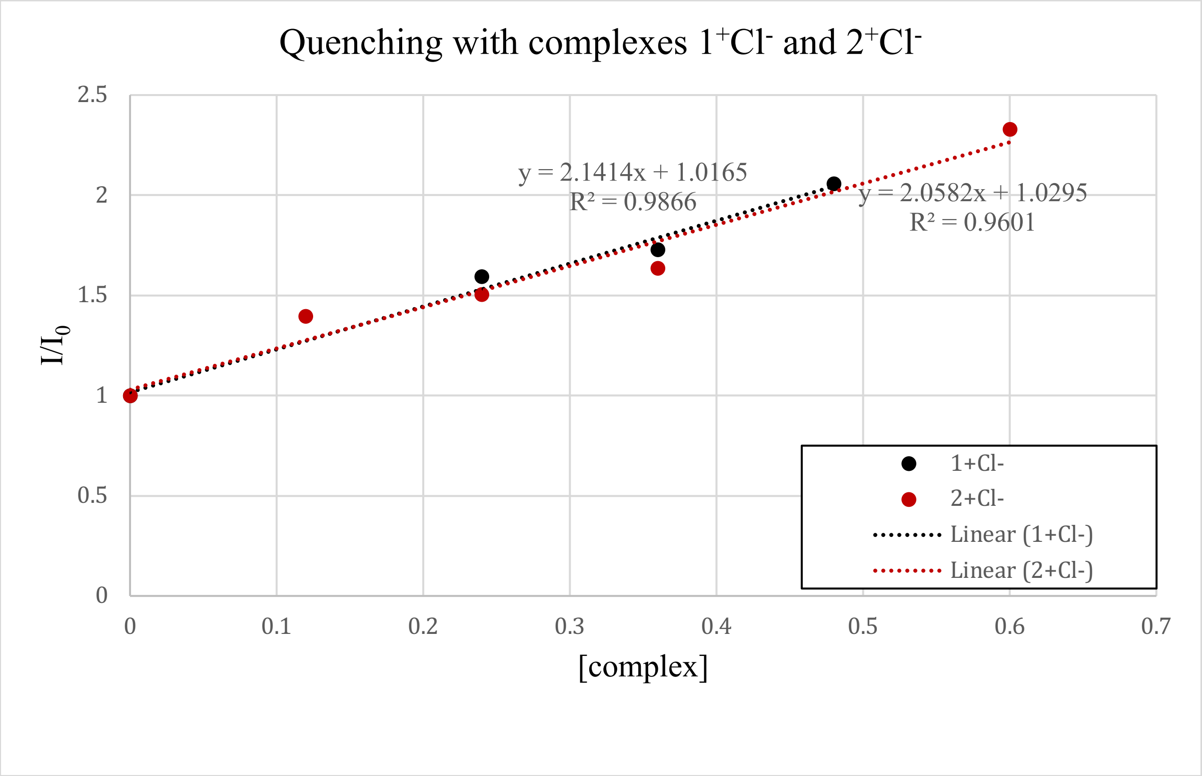

Figure 3.18. Stern-Volmer plot for quenching of the emission of the photosensitizer $Ru(bpy)_3(PF_6)_2$ with various concentrations of complex **1**$^+$**Cl**$^-$ (black) and complex **2**$^+$**Cl**$^-$ (red).

Using the electron transfer cycle in Figure 3.8 and the catalytic cycle in Figure 3.9 the reaction rate could be modeled. Our model for the electron transfer cycle (Figure 3.8) includes PS and quenching from both the ED (TEOA) and the Ru starting materials **1**$^+$**Cl**$^-$ and **2**$^+$**Cl**$^-$ (CAT). The source of electrons for the catalytic cycle is represented by the reduced photosensitzer, [PS$^-$] and given by eqn 2 where the rate constants are defined in the scheme (Figure 3.8).[12,30] The interplay of the electron transfer and catalysis cycles is clearly demonstrated with eqn 1 and 2.

Based on the electron transfer cycle shown in Figure 3.8 and using the steady state approximation, the rates of change in [PS] and [PS*] are given by:

$$\frac{d[PS]}{dt} = -I_{hv} + k_1[PS^*] + \beta k_q[TEOA]PS^*] + \gamma k_q''[CAT][PS^*] + \sum_i k_i[CAT]_i\,[PS^-] + k_2[PS^-] = 0 \tag{3.1}$$

$$\frac{d[PS^*]}{dt} = I_{hv} - k_1[PS^*] - (\alpha + \beta)k_q[TEOA]PS^*] - \gamma k_q''[CAT][PS^*] = 0 \tag{3.2}$$

Combining (3.1) and (3.2) yields

$$(\alpha)k_q[TEOA][PS^*] + \sum_i k_i[CAT]_i\,[PS^-] + k_2[PS^-] = 0$$

and

$$\frac{(\alpha)k_q[TEOA]}{\sum_i k_i[CAT]_i + k_2}[PS^*] = [PS^-] \tag{3.3}$$

From (3.2)

$$\frac{I_{hv}}{k_1 + \alpha k_q[TEOA] + \gamma k_q''[CAT]} = [PS^*] \tag{3.4}$$

Combining 3.3 and 3.4 gives:

$$[\mathbf{PS}^-] = \frac{\frac{\alpha k_q[TEOA]I_{hv}}{(k_1 + \alpha k_q[TEOA] + \gamma k_q''[CAT]}}{k_2 + \sum_i k_i[CAT]_i} \tag{2}$$

According to the Catalysis Cycle shown in the proposed mechanism (Figure 3.9), contribution of the electron transfer from PS$^-$ (i.e. $[Ru(bpy)_3]^+$) to the catalyst is expressed as equation (3.5):

$$\sum_i k_i[CAT]_i = k_3[\boldsymbol{RuCOOH}] + k_4[\boldsymbol{Ru}^+] \tag{3.5}$$

Using the steady state approximation for the [Ru$^+$]:

$$\sum_i k_i[CAT]_i = k_3[RuCOOH] + \frac{k_3}{k_4}[RuCOOH]$$

Using the proposed mechanism, the rate of formation of product formic acid is given by:

$$\frac{d[HCOOH]}{dt} = k_3[RuCOOH][PS^-] \tag{3.6}$$

Which is the same as eqn 1 shown above.

When combined with 3.5, this can be expressed by:

$$= \ k_3[RuCOOH](\frac{\frac{\alpha k_q[TEOA]I_{h\nu}}{(k_1+\alpha k_q[TEOA]+\gamma k_q^{''}[CAT]}}{k_2+(k_3+\frac{k_3}{k_4})[RuCOOH]}$$

Rearrangement of this give the following expression for the rate of formic acid formation:

$$\frac{d[HCOOH]}{dt} = \ k_3 \frac{\frac{\alpha k_q[TEOA]I_{h\nu}}{(k_1+\alpha k_q[TEOA]+\gamma k_q^{''}[CAT]}[RuCOOH]}{k_2+(k_3+\frac{k_3}{k_4})[RuCOOH]} \qquad (3.7)$$

The concentration of [RuCOOH] will be related to the initial concentration of complex **1^+Cl^-** by [RuCOOH] = ω $[1^+Cl^-]_{initial.}$ ω is a proportionality constant.

Collecting the term, equation 3.7 can be more simply written as

$$\frac{d[HCOOH]}{dt} = \ \frac{a[RuCOOH]}{b+c[RuCOOH]} \qquad \textbf{(3)}$$

With the following definitions:

$$a = \ k_3 \frac{\alpha k_q[TEOA]I_{h\nu}}{(k + \alpha k_q[TEOA] + \gamma k_q^{''}[CAT]}$$

$$b = \ k_b$$

$$c = \ k_3 + \frac{k_3}{k_4}$$

A graph for the rate of formic acid formation *vs*. μmol 1^+ is presented in Figure 3.19 along with the curve fitting results using equation 3 with parameter values of a = 2.8×10^{-3}, b = 0.068, and c = 2.8×10^{-3}. The proposed model reproduces the experimental observations.

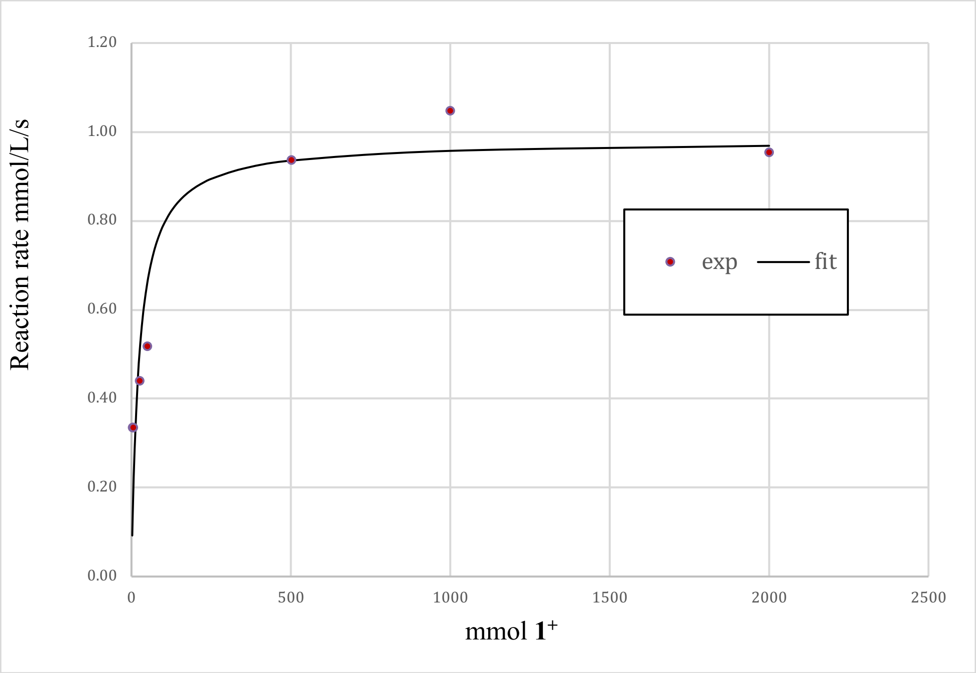

Figure 3.19. A plot of reaction rate for the formation of formic acid versus concentration of catalyst $[Ru(\kappa^3\text{-}\{2,6\text{-}(Ph_2PNMe)_2NC_5H_3\})(CO)_2Cl]^+Cl^-$ (1^+Cl^-) (red points) with constant 1mM PS. The black curve represents the fitted values using the model described in the text.

As expected, the catalyst reaction rates increase as the [cat] is increased but this increase is limited as the electron supply becomes rate determining. With low concentrations of 1^+, it is possible for the catalyst to accept two electrons smoothly from the PS^-. In this region the electron transfer cycle experiences less loss due to quenching by [CAT] and can operate at a sufficient rate to supply electrons to the catalysis cycle. On the other hand, in the high concentration regime, the electron transfer cycle cannot supply sufficient [PS^-] to the ruthenium catalyst and accordingly a more significant portion 1^+ remains unreacted and the catalysis cycle is less efficient.

3.4. Electrocatalytic CO_2 Reduction Results

In order to investigate more about the catalytic behavior of the catalysts, the electrochemistry has been also obtained. The electrochemical experiments were carried out in a single compartment cell wrapped with aluminum foil using a VersaSTAT 3 (Princeton Applied Research) potentiostat. Samples were prepared in a glovebox, sealed, removed from the glovebox and connected to a Schlenk line and maintained under a nitrogen atmosphere. A conventional three electrode system was employed consisting of a glassy carbon working electrode (diameter = 0.3 cm), a Pt wire as the auxiliary electrode, and an Ag wire as a pseudo-reference electrode. Ferrocene was added as a reference compound and potentials were referred to the redox potential of ferrocene (Fc)/ferrocenium ion (Fc^+) as an internal standard. Dried acetonitrile was purchased from Sigma Aldrich and stored on molecular sieves in glove-box. Tetrabutylammoniumhexafluorophosphate, $[(n\text{-}Bu)_4N]PF_6$ (TBAHFP), the supporting electrolyte, was crystallized two times with methanol, dried in vacuum at 90 °C for 24 h before use and stored in a glovebox. The electrolyte solution, 0.1 M $[(n\text{-}Bu)_4N]PF_6$ in CH_3CN, was saturated with N_2 by purging with N_2 for 10 min prior to each experiment. The typical concentration of catalyst was 1 mM (15 mL acetonitrile) in each experiment. The cyclic voltammetry studies were also performed under CO_2 atmosphere and in the presence of the proton source such as H_2O. The following figures give the electrocatalytic behavior of the two Ru catalysts.

The cyclic voltammetry of $\mathbf{1^+Cl^-}$ complex that was obtained showed two reduction peaks. The first reduction was observed at -1.64 V under N_2 as presented in Figure 3.20 and the second reduction at -2.70 V versus Fc/Fc^+. Carrying out this same measurement with a solution saturated with an atmosphere of CO_2 produced an enhancement of the reduction current indicating to an electrocatalytic CO_2 reduction as shown in Figure 3.21.

In addition, the same behavior of the enhancement of the current was also observed with the addition and presence of H_2O as shown in Figure 3.22. Moreover, the cyclic voltammetry of **2⁺Cl⁻** complex under N_2 displayed two irreversible reduction peaks at -1.52 V and -1.78 V versus Fc/Fc$^+$ (as shown in Figure 3.23). Carrying out this same measurement under CO_2 atmosphere, a large enhancement of the reduction current was appeared indicating an electrocatalytic CO_2 reduction as shown in Figure 3.24. This enhancement disappeared with the addition of H_2O as shown in Figure 3.25. Bulk electrolysis should be done in order to understand more about the catalytic behavior of these catalysts and to figure out the products of this electrocatalytic CO_2 reduction. This bulk electrolysis experiment could be carried out in the same condition using the acetonitrile solvent and the supporting electrolyte ($(n\text{-}Bu)_4NPF_6$).

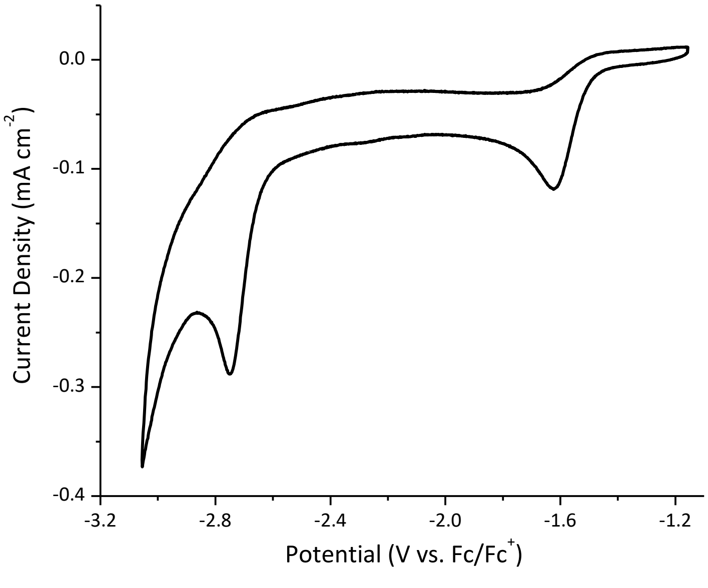

Figure 3.20. Cyclic voltammogram of 1.0 mM [Ru(κ^3-{2,6-$(Ph_2PNMe)_2NC_5H_3$})$(CO)_2Cl$]$^+$Cl$^-$ (**1⁺Cl⁻**) under N_2 in CH_3CN with 0.1 M $(n\text{-}Bu)_4NPF_6$ supporting electrolyte at 50 mV/s.

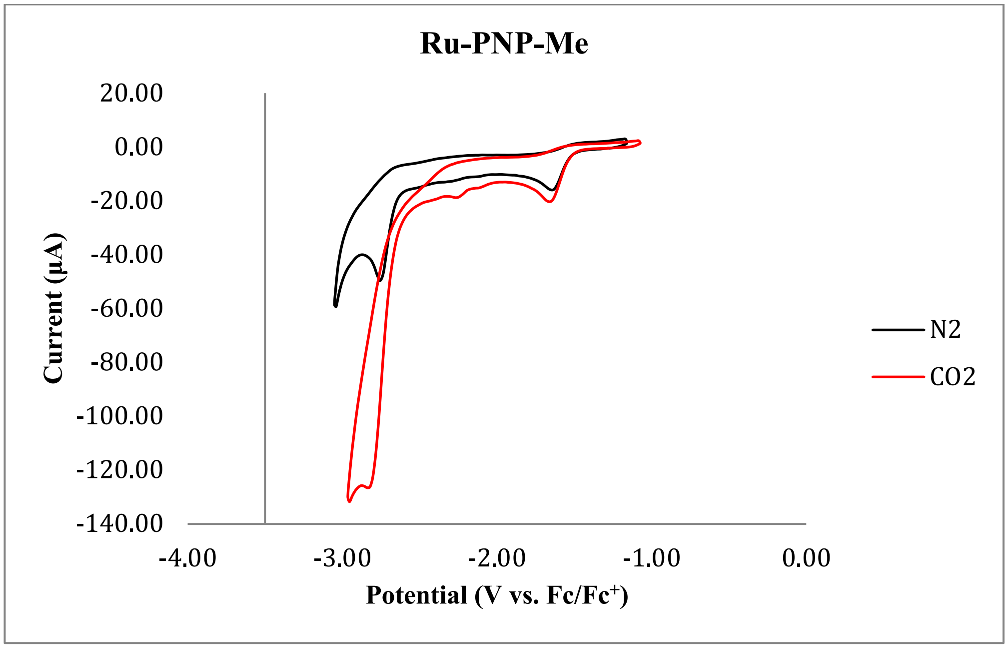

Figure 3.21. Cyclic voltammograms of Ru(PN$_3$P-Me)(CO)$_2$Cl (**1$^+$Cl$^-$**) under N$_2$ (black), and CO$_2$ (red) in CH$_3$CN with 0.1M (n-Bu)$_4$NPF$_6$ supporting electrolyte at 100 mV/s.

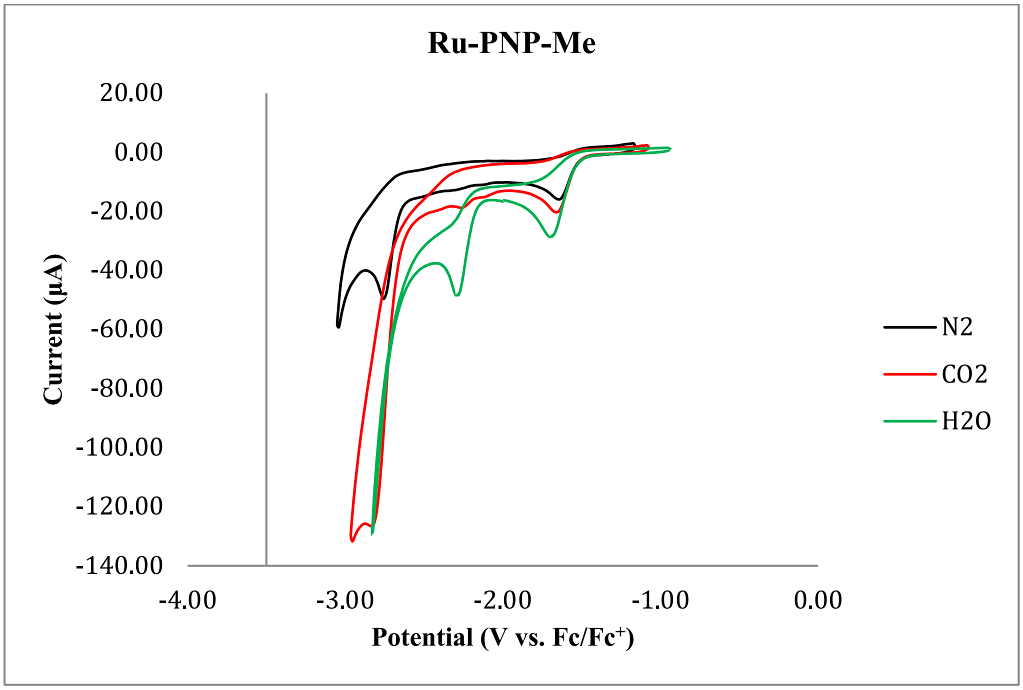

Figure 3.22. Cyclic voltammograms of Ru(PN$_3$P-Me)(CO)$_2$Cl (**1$^+$Cl$^-$**) under N$_2$ (black), CO$_2$ (red) and CO$_2$/Water (blue) in CH$_3$CN with 0.1M (n-Bu)$_4$NPF$_6$ supporting electrolyte at 100 mV/s.

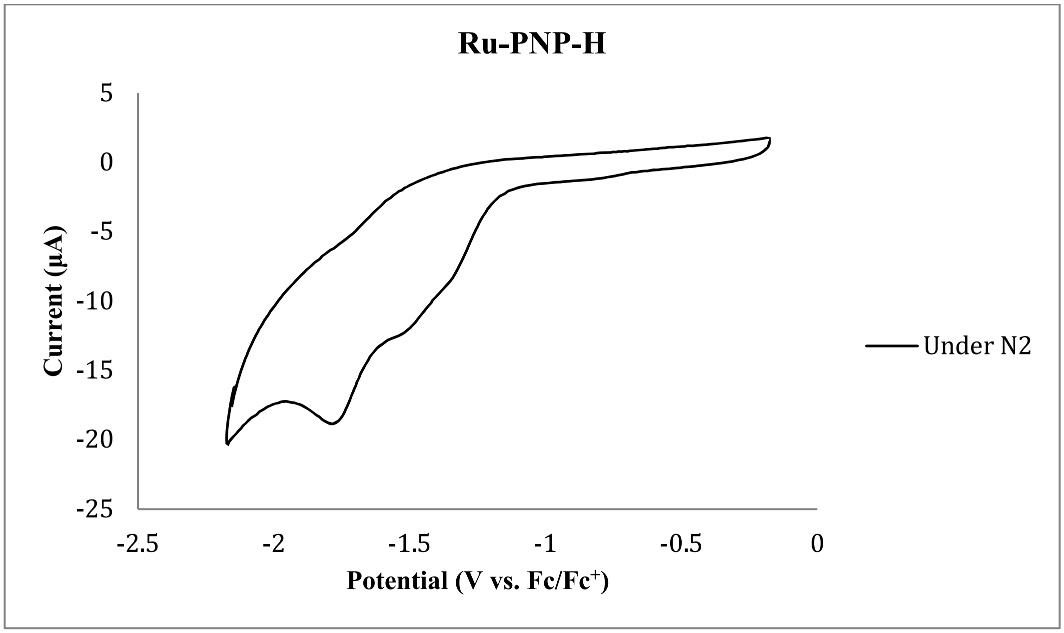

Figure 3.23. Cyclic voltammograms of Ru(PN$_3$P-H)(CO)$_2$Cl (**2**) under N$_2$ (blue) in CH$_3$CN with 0.1M (n-Bu)$_4$NPF$_6$ supporting electrolyte at 100 mV/s.

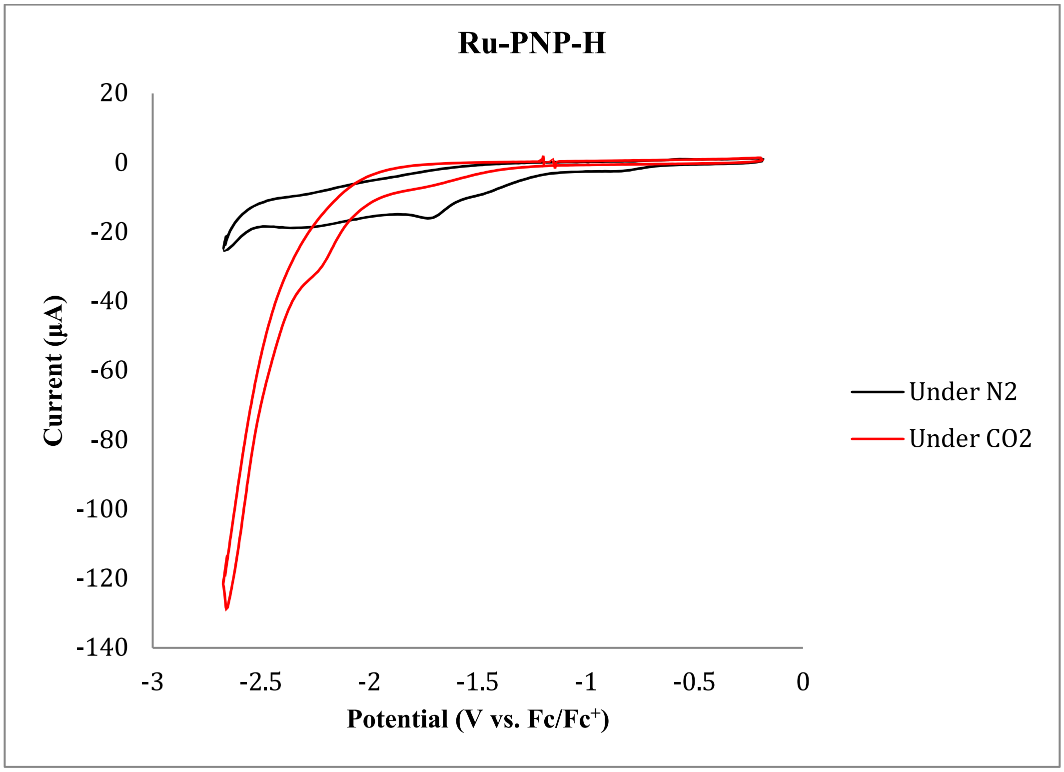

Figure 3.24. Cyclic voltammograms of Ru(PN$_3$P-H)(CO)$_2$Cl (**2**) under N$_2$ (blue) and CO$_2$ (red) in CH$_3$CN with 0.1M (n-Bu)$_4$NPF$_6$ supporting electrolyte at 100 mV/s.

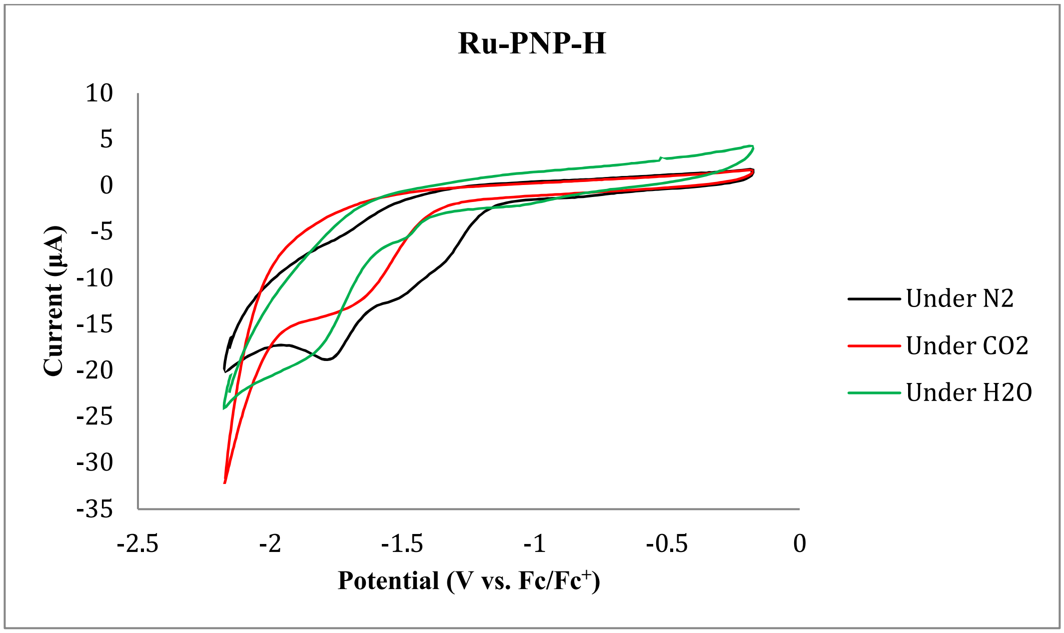

Figure 3.25. Cyclic voltammograms of Ru(PN$_3$P-H)(CO)$_2$Cl (**2**) under N$_2$ (blue), CO$_2$ (red) and CO$_2$/Water (green) in CH$_3$CN with 0.1M (n-Bu)$_4$NPF$_6$ supporting electrolyte at 100 mV/s.

3.5. Conclusion

After more than 30 years since the first reports of photocatalytic CO$_2$ reduction using Ru complexes,[7–9] we have now demonstrated effective catalytic photoreduction using an unprecedented molecular architecture for a Ru metal catalyst. These newly prepared pincer complexes have been documented as competent catalysts for the conversion of CO$_2$ to formic acid with high selectivities. Furthermore, they displayed competitive formic acid turnover numbers, as high as 11,600, and quantum yields in the range of 4-12%. Our proposed mechanism, combining an electron transfer cycle with a catalytic cycle successfully modeled the experimental rate of formic acid production. These findings will stimulate new efforts in the design and construction of more effective metal complexes in this field. Our ongoing efforts are exploring ligand tuning, and variations to solvent, electron donor and photosensitizer in an effort to increase selectivity and discover improved photocatalysts.

3.6. Future Directions

In order to investigate more and explore new catalyst systems, the PN-R bidentate ligands with the two different substations (R = H and Me) were also synthesized with the Ru metal and characterized. Both Ru-PN-H and Ru-PN-Me were examined for the electrocatalytic and photocatalytic CO_2 reduction. The Ru-PN-Me show less activity than the Ru-PNP-Me tridentate complexes. More experiments should be done for this exploration of Ru-PN-H and Ru-PN-Me.

The direct synthesis of these complexes is shown in Figure 3.26 that is the direct addition of diphenylphosphino-2-amino-pyridine to $[Ru(CO)_3Cl_2]_2$ in toluene followed by heating to 100 °C under N_2 for 16h led to the new cationic Ru complex $[Ru\{\kappa^2\text{-}2\text{-}(Ph_2PNMe)NC_5H_4\}(CO)_2(Cl)_2]$ (3) as a colorless solid with a yield of 85%. Replacing the starting ligand with diphenylphosphino-2-diamino-pyridine and following a similar procedure produced the analogous complex, $[Ru\{\kappa^2\text{-}2\text{-}(Ph_2PNH)NC_5H_4\}(CO)_2(Cl)_2]$(4) with a yield of 95%. Spectroscopic data and a single crystal x-ray analysis of 3 definitively confirmed the identity of this species.

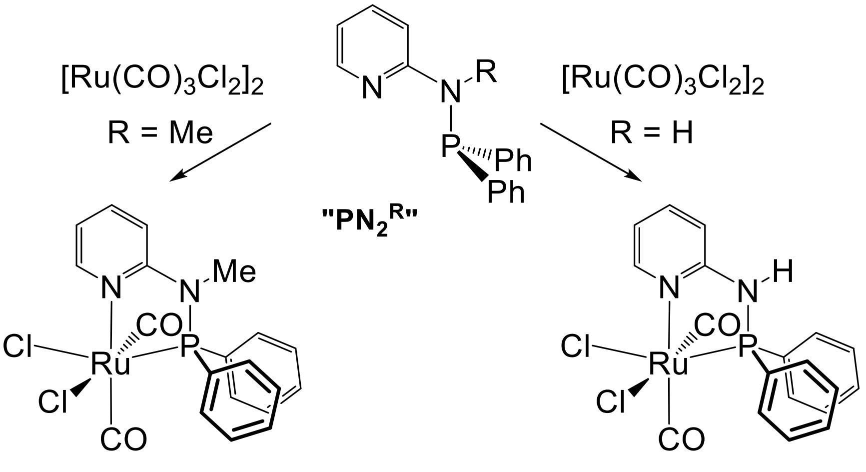

Figure 3.26. The reaction scheme for the preparation of complexes 3 and 4.

The photocatalytic results for the photocatalytic CO_2 reduction are shown in Table 3.7, and the best result was with DMF and TEOA. The Ru-PN-Me and Ru-PN-H complexes worked very well towards the photocatalytic CO_2 reduction, but they are not selective like the Ru-PNP-Me and Ru-PNP-Me. In the photocatalytic CO_2 reduction, more experiments should be done for these bi-dentate complexes in order to investigate more about the mechanism.

Table 3.7. The photocatalytic results for Ru-PN-Me (3) and Ru-PN-H (4).

Catalyst (mM)	**PS (mM)**	**Solvent**	**Electron Donors**	**H_2 (µmol)**	**CO (µmol)**	**HCOOH (µmol)**
3 (1)	1	DMF	TEOA	35	14	234
3 (1)	1	DMF	NEt_3	-	-	-
3 (1)	1	DMF	BNAH	-	-	-
3 (1)	1	CH_3CN	TEOA	31	11	67
3 (1)	1	CH_3CN	NEt_3	-	-	-
3 (1)	1	CH_3CN	BNAH	-	-	-
4 (1)	1	DMF	TEOA	26	18	323
4 (1)	1	DMF	NEt_3	-	-	-
4 (1)	1	DMF	BNAH	-	-	-
4 (1)	1	CH_3CN	TEOA	11	12	143
4 (1)	1	CH_3CN	NEt_3	-	-	-
4 (1)	1	CH_3CN	BNAH	-	-	-

3.7. References

1 K. Sordakis, C. Tang, L. K. Vogt, H. Junge, P. J. Dyson, M. Beller and G. Laurenczy, *Chem. Rev.*, 2018, **118**, 372–433.

2 H. Zhong, M. Iguchi, M. Chatterjee, Y. Himeda, Q. Xu and H. Kawanami, *Adv. Sustain. Syst.*, 2018, **1700161**, 1700161.

3 Y. Yamazaki, H. Takeda and O. Ishitani, *J. Photochem. Photobiol. C Photochem. Rev.*, 2015, **25**, 106–137.

4 N. Elgrishi, M. B. Chambers, X. Wang and M. Fontecave, *Chem. Soc. Rev.*, 2017, **46**, 761–796.

5 J. Bonin, A. Maurin and M. Robert, *Coord. Chem. Rev.*, 2017, **334**, 184–198.

6 H. Takeda, C. Cometto, O. Ishitani and M. Robert, *ACS Catal.*, 2017, **7**, 70–88.

7 J. Hawecker, J. M. Lehn and R. Ziessel, *J. Chem. Soc. Chem. Commun.*, 1985, **20**, 56–58.

8 H. Ishida, T. Terada, K. Tanaka and T. Tanaka, *Inorg. Chem.*, 1990, **29**, 905–911.

9 J. M. Lehn and R. Ziessel, *J. Organomet. Chem.*, 1990, **382**, 157–173.

10 P. Voyame, K. E. Toghill, M. A. Méndez and H. H. Girault, *Inorg. Chem.*, 2013, **52**, 10949–10957.

11 Y. Kuramochi, M. Kamiya and H. Ishida, *Inorg. Chem.*, 2014, **53**, 3326–3332.

12 Y. Kuramochi, J. Itabashi, K. Fukaya, A. Enomoto, M. Yoshida and H. Ishida, *Chem. Sci.*, 2015, **6**, 3063–3074.

13 K. Sekizawa, K. Maeda, K. Domen, K. Koike and O. Ishitani, *J. Am. Chem. Soc.*, 2013, **135**, 4596–4599.

14 Y. Kuramochi, O. Ishitani and H. Ishida, *Coord. Chem. Rev.*, 2018, **373**, 333–356.

15 S. K. Lee, M. Kondo, M. Okamura, T. Enomoto, G. Nakamura and S. Masaoka, *J.*

Am. Chem. Soc., 2018, **140**, 16899–16903.

16 S. K. Lee, M. Kondo, G. Nakamura and S. Masaoka, *Chem. Commun.*, 2018, **54**, 6915–6918.

17 T. Zell and D. Milstein, *Acc. Chem. Res.*, 2015, **48**, 1979–1994.

18 X. Yang, *ACS Catal.*, 2011, **1**, 849–854.

19 G. A. Filonenko, M. P. Conley, C. Copéret, M. Lutz, E. J. M. Hensen and E. A. Pidko, *ACS Catal.*, 2013, **3**, 2522–2526.

20 G. A. Filonenko, E. J. M. Hensen and E. A. Pidko, *Catal. Sci. Technol.*, 2014, **4**, 3474–3485.

21 N. M. Rezayee, C. A. Huff and M. S. Sanford, *J. Am. Chem. Soc.*, 2015, **137**, 1028–1031.

22 C. A. Huff and M. S. Sanford, *J. Am. Chem. Soc.*, 2011, **133**, 18122–18125.

23 R. Tanaka, M. Yamashita and K. Nozaki, *J. Am. Chem. Soc.*, 2009, 14168–14169.

24 G. K. Rao, W. Pell, I. Korobkov and D. Richeson, *Chem. Commun.*, 2016, **52**, 8010–8013.

25 S. Min, S. Rasul, H. Li, D. C. Grills, K. Takanabe, L. J. Li and K. W. Huang, *Chempluschem*, 2016, **81**, 166–171.

26 P. Kang, T. J. Meyer and M. Brookhart, *Chem. Sci.*, 2013, **4**, 3497–3502.

27 P. Kang, S. Zhang, T. J. Meyer and M. Brookhart, *Angew. Chemie - Int. Ed.*, 2014, **53**, 8709–8713.

28 L. P. He, T. Chen, D. X. Xue, M. Eddaoudi and K. W. Huang, *J. Organomet. Chem.*, 2012, **700**, 202–206.

29 D. Benito-Garagorri, E. Becker, J. Wiedermann, W. Lackner, M. Pollak, K. Mereiter, J. Kisala and K. Kirchner, *Organometallics*, 2006, **25**, 1900–1913.

30 Y. Kuramochi, J. Itabashi, M. Toyama and H. Ishida, *ChemPhotoChem*, 2018, **2**, 314–322.

31 A. Taheri and L. A. Berben, *Chem. Commun.*, 2016, 1768–1777.

32 J. R. Pugh, M. R. M. Bruce, B. P. Sullivan and T. J. Meyer, *Inorg. Chem.*, 1991, **30**, 86–91.

33 A. Neubauer, G. Grell, A. Friedrich, S. I. Bokarev, P. Schwarzbach, F. Gartner, A.-E. Sukus, H. Junge, M. Beller, O. Kuhn and S. Lochbrunner, *J. Phys. Chem. Lett.*, 2014, **5**, 1355–1360.

34 S. M. Aucott, A. M. Z. Slawin and J. D. Woollins, *J. Chem. Soc. Dalt. Trans.*, 2000, 2559–2575.

Chapter 4: Photocatalytic Reduction of CO_2 to formic acid with an Unconventional Zn(II) Catalyst

The work in this chapter formed a significant component, and the manuscript is in the perpetration to be published soon:

(Y. Hameed, G. Rao, A. Sharif, B. Gabidullin, and D. S Richeson, 2019)

In this chapter, three divalent Zn(II) complexes have been successfully synthesized, characterized and examined towards CO_2 reduction. These novel and unprecedented Zn(II) complexes show a novel ability for the photocatalytic CO_2 reduction. This project was conceptualized by Y. Hameed and D. Richeson. The major contribution to the synthesis and characterization of the complexes and the catalytic behavior of the complexes were done by Y. Hameed. G. Rao and A. Sharif helped with initial investigations of the Zn(II) complex [Zn(bpy)$(Br)_2$]. The crystallography was carried out by B. Gabidullin., and the DFT calculations of these complexes were carried out by D. Richeson.

4.1. Introduction

Society is currently facing momentous challenges from the increasing emissions of greenhouse gases and depleting resources for C1 feedstocks. Due to these pressures, there is increasing drive to discover chemical transformations of CO_2. This ubiquitous and thermodynamically stable species requires catalysts to activate it for reactions and chemical reduction. Reduction of CO_2 into valuable compounds provides new opportunities for use of this common oxidation product. Photocatalytic routes are particularly interesting as well as fundamentally appealing because one can envision using the limitless and sustainable supply of sunlight as the energy source to power these transformations.

A broad assortment of homogeneous transition-metal complexes (e.g., Mn-, Fe-, Co-, Ni-, Cu-, Ru-, and Re-based complexes), have been explored for catalyzing photoreduction of CO_2 under both electrochemical and photochemical conditions.[1–6] Both from a sustainability point and due to the low toxicity of first row transition metals, catalyst built on these metal centers are critical.

Among the 3d metals, perhaps not surprising, Zn is nearly absent from the metals that have been used for CO_2 reduction. This is likely because Zn is normally not viewed as a redox active center. However, Zn does have some important documented roles in catalyzed reactions. For example, Zn has an key role in the catalytic preparation of polycarbonates and cyclic carbonates.[78] These reactions involves the capture of CO_2 and rely on the Lewis acidity of Zn(II). Zinc bromide was used as a catalyst in a recently reported conversion of CO_2 to CO with the parallel oxidation of phosphine.[9] Complexes of Zn have been used to catalyze hydrogenation and hydrosilylations. In these reduction reactions rely on the formation and reactivity of a Zn-H moiety as a key step of the mechanism.[10]

Related and more pertinent to our goals is the hydrosilylation of CO_2 using [tris(2-pyridylthio)methyl]zinc hydride, [κ^3-Tptm]ZnH, **A** (Scheme 4.1)**.**[11] This catalyst is capable of performing hydrosilylation of aldehydes, ketones, and carbon dioxide. Specifically, [κ^3-Tptm]ZnH (**A**) catalyzes the formation of triethoxysilyl formate via hydrosilylation of carbon dioxide with triethoxysilane.[11]

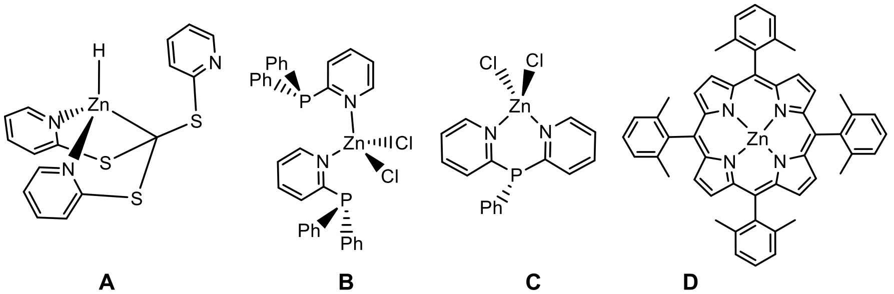

A B C D

Scheme 4.1. The reported Zn catalysts for the reduction of CO_2.

There are only two reports of electrocatalysis for CO_2 reduction using Zn(II). A heterogenized Zn porphyrin complex **D** that had been deposited on a carbon fiber and subsequently used for electrocatalytic reduction in a mixed H_2O:DMF solvent.[12] The Zn cation is reported to be crucial for activity, however, it appeard that the oxidation state of the metal remains fixed throughout the catalytic cycle. The authors argue that the reactivity of the noninnocent redox-active ligands can, reversibly store reducing equivalents and facilitate catalytic conversion of CO_2.

The other electrochemical reduction involved pyridylphosphine ligated Zn(II) centers. The two related complexes **B** and **C** were reported but only compound **B** was active in electrocatalytic reduction of CO_2.[13] Cyclic voltammetry of this complex under Ar showed an irreversible one-electron reduction at −2.03 V vs Fc^+/Fc. Current enhancement of this reduction was observed when the CV was repeated under a CO_2 atmosphere, indicating electrocatalysis. When electrolysis was carried out with **B** under CO_2 and an applied potential of -1.8V (vs Fc^+/Fc), CO formation was observed. However, no quantification of this reduction was reported. A proposed mechanism suggested that the free phosphorus centers participated in a nucleophilic attack at the carbon of CO_2, forming an adduct, with the Zn-atom behaving solely as a Lewis acid. The greater rigidity and less flexible chelating ligand for **C** was suggested to hinder CO_2 access to the lone pair of the phosphorus atom and given as the reason that this complex did not react with CO_2.

Importantly, there are no reports of Zn as a center for photocatalysis.[5] This prompted our initial consideration of investigating the potential of using Zn in this regard. Furthermore, when selecting the ligand scaffold to support this target, the polypyridyl scaffold was selected due to its prevalence in the field, its ability to directly participate in electron transfer (as a reservoir), and the fact that there are established Zn complexes of bpy-type ligands.

Our first targets for investigating the potential of Zn complexes for photocatalytic CO_2 reduction were the α-diimine species shown in Scheme 4.2. These species represented relatively straightforward targets with complex **1** representing a more conventional bpy complex and complexes **2** and **3** displaying modified π-frameworks. As expected, the direct reaction of $ZnBr_2$ with a stoichiometric quantity of the appropriate diimine ligand produced these new complexes in 76-78% yield. These complexes were not particularly soluble in most organic solvents, requiring polar solvents (e.g. CH_2Cl_2 or DMF) for isolation and purification. In addition, solution NMR spectroscopy required use of DMSO-d_6. Both ^{1}H and ^{13}C NMR spectra were consistent with the symmetrical structures anticipated for complexes **1-3**. We were fortunate to obtain single crystals of **1** and definitive structural confirmation was provided by single crystal x-ray analysis of this complex. The results are shown in Figure 4.1 which established complex **1** as the anticipated tetrahedral Zn(II) dibromide species with a bidentate bpy ligand. The bond distances and angles were unremarkable.

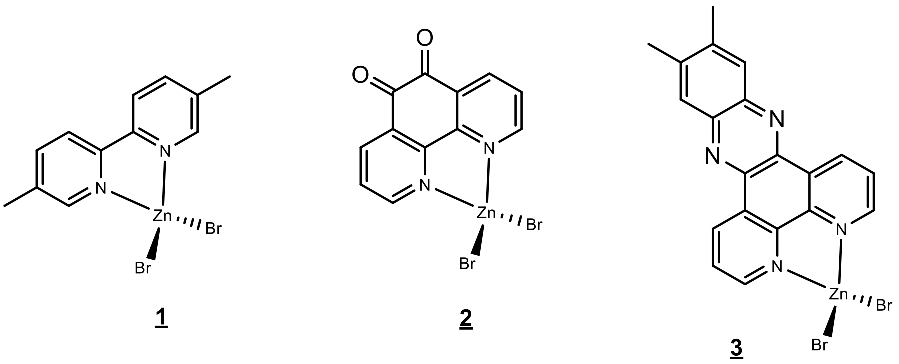

Scheme 4.2. Complexes synthesized and employed in photocatalytic CO_2 reduction [Zn(κ^2-Me_2bpy)Br_2] **1** [Zn(κ^2-phendione)Br_2] **2,** [Zn(κ^2-dppz)Br_2] **3.**

4.2. Experimental Details

4.2.1. Synthetic methods and Characterization

Synthesis of 5,5′-dimethyl-2,2′-bipyridine-dibromide zinc complex [Zn(κ^2-Me$_2$bpy)Br$_2$] 1: In a glove box, a solution of ligand 5,5′-dimethyl-2,2′-bipyridine (0.552 g, 3 mmol) was prepared in 10 mL of toluene. Then, $ZnBr_2$ (0.675 g, 3 mmol) was added to the solution of ligand. The reaction mixture was allowed to stir at room temperature for overnight (16h). The white product was formed, and 10 mL hexane was added. The precipitate was filtered off and washed with hexane to give the zinc complex. Single crystals of this complex were grown by slow diffusion of hexane into the solution of complex made in dichloromethane. Yield 0.959 g (78%); ^{1}H NMR (300 MHz, DMSO-d$_6$, 25°C): δ = 2.34 (s, 6H, CH_3), 8.03 (d, 2H), 8.27 (s, 2H), 8.45 (d, 2H). ^{13}C NMR (75 MHz, DMSO-d$_6$, 25 ºC): δ = 18.40, 122.1, 137.2, 141.9, 146.7, 148.4.

Synthesis of 1,10-Phenanthroline-5,6-dione-dibromide zinc complex [Zn(κ^2-phendione)(Br)$_2$] (2): In a round bottom flask, a solution of phendione ligand (0.210 g, 1 mmol) was prepared in 30 mL of ethanol, and zinc bromide $ZnBr_2$ (0.225 g, 1 mmol) was dissolved in 30 mL of ethanol and added to the solution of the ligand in the flask and capped. The reaction mixture was heated to 40 ºC and stirred for a period of 20 hours. The resulting fine yellow powder is collected by suction filtration and washed with ethanol and ether, Crystals of this complex were grown by slow diffusion of acetone into the solution of complex made in dimethylformamide. Yield 0.33 g (76%); ^{1}H NMR (300 MHz, DMSO-d$_6$, 25°C): δ = 7.88 (d, 2H, CH_3), 8.61 (d, 2H), 8.89 (dd, 2H). ^{13}C NMR (75 MHz, DMSO-d$_6$, 25 ºC): δ = 175.9, 152.5, 151.1, 138.2, 130.7, 127.7.

Synthesis of 1,12-Dimethyldipyrido[3,2-a:2',3'-c]phenazine-dibromide zinc complex [Zn(κ^2-dppz)(Br)$_2$] (3): In a round bottom flask, a solution of dppz ligand (0.310g, 1mmol) was prepared in 30 mL of ethanol, and zinc bromide $ZnBr_2$ (0.225 g, 1 mmol) was dissolved in 30 mL of ethanol and added to the solution of the ligand in the flask and capped. The reaction mixture was heated to 40 ^{o}C and stirred for a period of 20 hours. The resulting fine light-yellow powder is collected by suction filtration and washed with ethanol and ether. Crystals of this complex were grown by slow diffusion of acetone into the solution of complex made in dimethylformamide. Yield 0.41 g (77%); ^{1}H NMR (300 MHz, DMSO-d$_6$, 25°C): δ = 2.57 (s, 6H), 8.16 (m, 4H), 9.09 (dd, 2H), 9.67 (2H, d). ^{13}C NMR (75 MHz, DMSO-d$_6$, 25 ºC): δ = 153.2, 150.9, 141.6, 134.5, 132.3, 129.2, 127.7, 127.1, 125.0, 122.8.

4.2.2. X-ray Analysis

There were more details about the X-ray analysis described in section 1.7.6 of the introduction chapter (Chapter 1). Single crystals of this complex **1** were grown by slow diffusion of hexane into the solution of complex made in dichloromethane. The structural features of **1** were determined by single crystal X-ray analysis as shown in Figure 4.2.

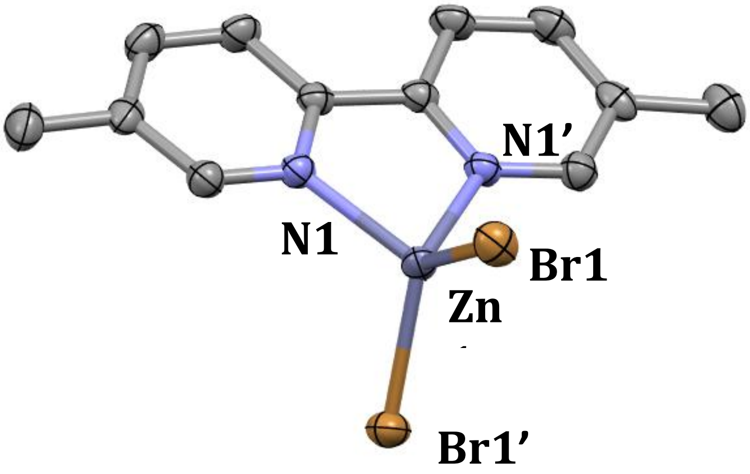

Figure 4.1. Structural representation for the compound **[Zn(κ^2-Me$_2$bpy)Br$_2$] 1** obtained from X-ray analysis. Hydrogen atoms are omitted for clarity.

4.2.3. UV Spectra

The compounds are colorless, so they cannot function as visible light photocatalysts in the absence of photosensitizer. As shown in Figure 4.2, the UV-via spectra of the catalysts were obtained in CH_3CN, and they just show the ligand absorption that is below 400 nm.

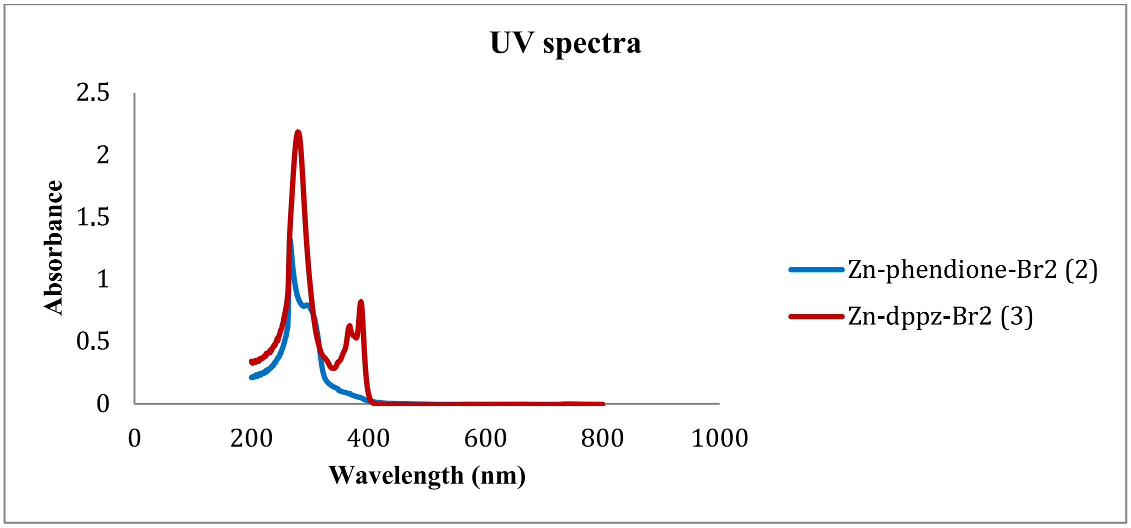

Figure 4.2. UV spectrum of the both complexes Zn-phendione-Br_2 (2) and Zn-dppz-Br_2 (3).

4.2.4. Photocatalytic Experiments

The photoreaction procedure for these experiments is described in section 1.7.1 of the introduction chapter (Chapter 1).

4.3. Photocatalytic CO_2 Reduction

With complexes **1-3** in hand, an exploration of the photocatalytic ability of these Zn α-diimine complexes was initiated. The general mechanism for photoreduction involves excitation by photon absorption, electron transfer to a metal-centered catalyst, which can react with either protons or CO_2 to begin the catalytic cycle. Photon absorption can occur directly to the catalyst species but more commonly a photosensitizer is required. Complexes **1-3** are white or very slightly colored which indicates that they do not strongly absorb visible light. As a result, we chose to use Ru(bpy)$_3^{2+}$ as the photosensitizer (**PS**). Dimethylacetamide (DMA) was selected as the reaction solvent due to its ability to solubilize these compounds and its stability. Importantly, DMA is useful as a solvent for CO_2 reduction because it does not yield formate in the event of hydrolysis.[14] Reaction mixtures were prepared with equimolar (1000μmol) **PS** and one of the Zn species **1-3** along with TEOA as the electron donor (**ED**) and the atmosphere over these solutions was exchanged for CO_2. The mixtures were subjected to irradiation with a blue LED (λ = 405 nm, $3.4x10^{-8}$moles photons s^{-1}) for 24 hours. After irradiation, the reaction headspace was examined by GC and H_2 was the only gas phase produce that was observed. Solution NMR analysis confirmed formation of formic acid as the only product obtained (Figures 4.3-4.5). The following figures show the NMR spectra after carrying out the photolysis under either an N_2 or CO_2 atmosphere. They provide clear documentation for the formation of formic acid from CO_2.

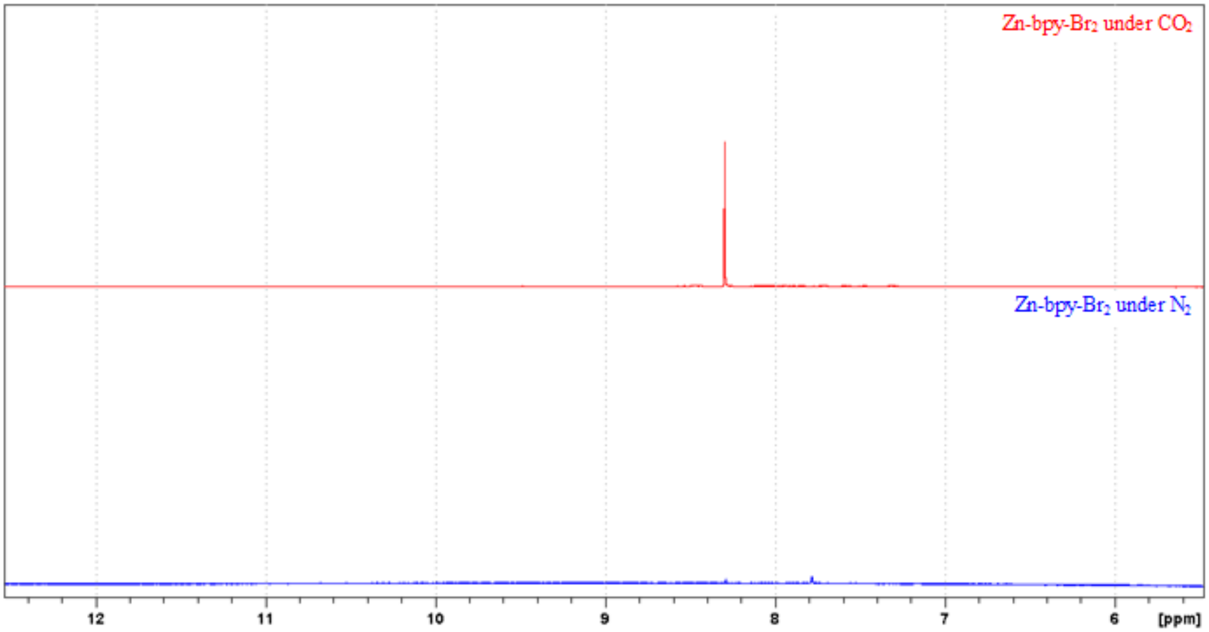

Figure 4.3. ^{1}H NMR spectra for the formyl HOOC-**<u>H</u>** proton of formic acid obtained from photocatalytic reduction of CO_2 using catalyst **1** (top, red). For comparison, an analogous reaction carried out in an N_2 atmosphere in the absence of CO_2 is shown (bottom, blue).

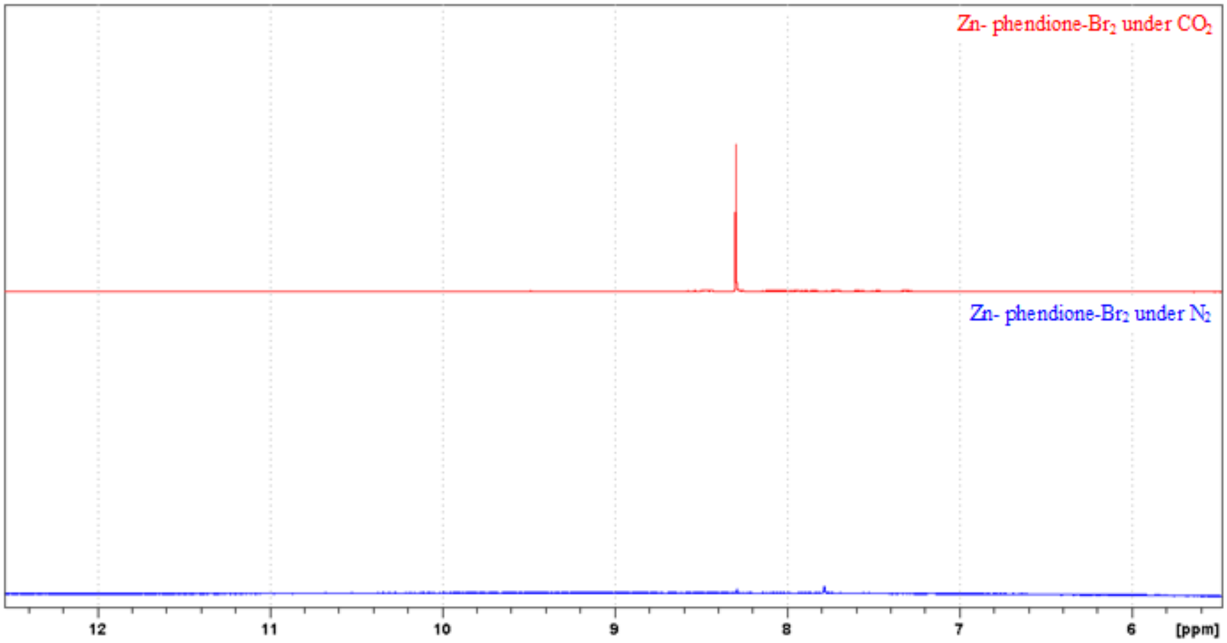

Figure 4.4. ^{1}H NMR spectra for the formyl HOOC-**<u>H</u>** proton of formic acid obtained from photocatalytic reduction of CO$_2$ using catalyst **2** (top red). For comparison, an analogous reaction carried out in an N$_2$ atmosphere in the absence of CO$_2$ is shown (bottom, blue).

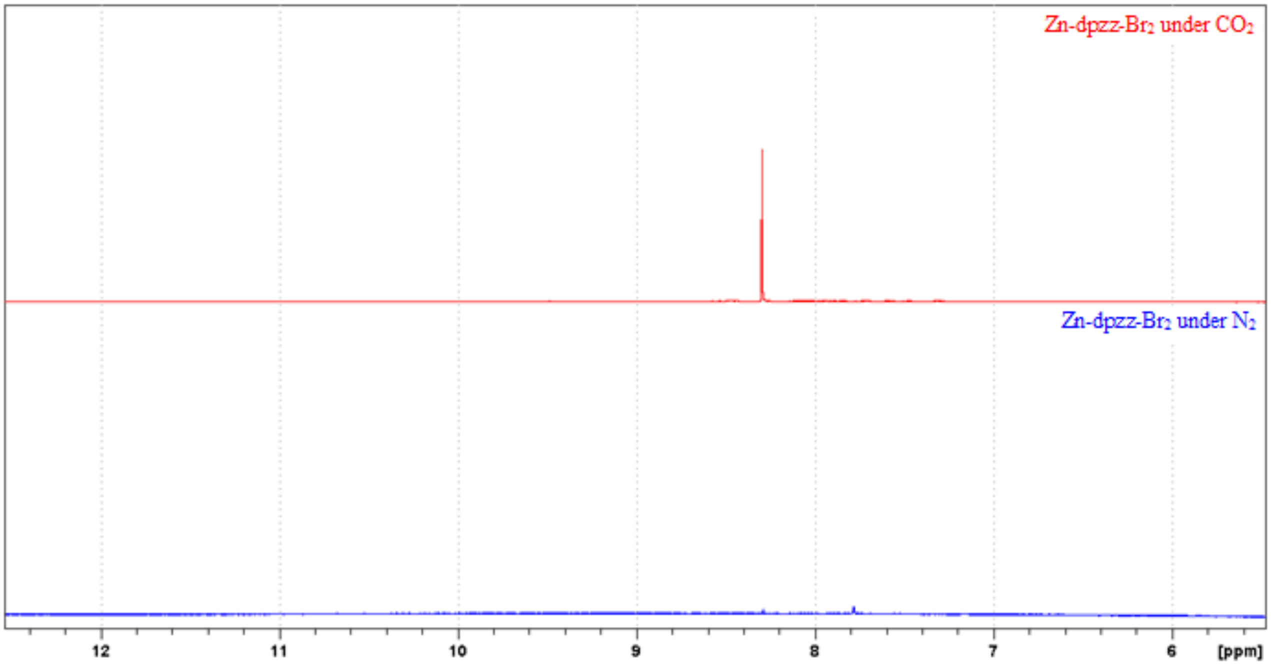

Figure 4.5. ^{1}H NMR spectra for the formyl HOOC-**<u>H</u>** proton of formic acid obtained from photocatalytic reduction of CO$_2$ using catalyst **3** (top red). For comparison, an analogous reaction carried out in an N$_2$ atmosphere in the absence of CO$_2$ is shown (bottom, blue).

As part of the examination of the reaction conditions, the solvent was varied to include both dimethylformamide (DMF) and acetonitrile (MeCN), which are commonly used as solvents in CO_2 reduction chemistry. Slightly lower TON's were obtained with DMF (Table 4.1) and no formation of H_2 or HCO_2H was observed with MeCN. Several alternatives to TEOA as the electron donor were examined and trimethylamine (TEA),1-benzyl-1,4-dihydronicotinamide (BNAH), sodium ascorbate, and ascorbic acid did not yield any indications of successful CO_2 photoreduction with catalysts **1-3**.

Table 4.1. Photocatalytic experiments with **$[Zn(\kappa^2\text{-}Me_2bpy)Br_2]$ 1** , **$[Zn(\kappa^2\text{-}phendione)(Br)_2]$ 2** and **$[Zn(\kappa^2\text{-}dppz)(Br)_2]$ 3**. In DMA (4mL) with $Ru(bpy)_3(PF_6)_2$ (1mM) as photosensitizer (**PS**) and TEOA as the electon donor (**ED**) under **a CO_2** atmosphere. Turn-over number (TON) = (moles of product)/(moles of catalyst). Irradiation with 405 nm light for 24 h.

Complex (mM)	**Solvent**	**H_2 (μmol)**	**TON_{H2}**	**HCOOH (μmol)**	**TON_{HCOOH}**
$[Zn(\kappa^2\text{-}Me_2bpy)Br_2]$ **1**	DMA	35	8.75	119	29.75
$[Zn(\kappa^2\text{-}phendione)(Br)_2]$ **2**	DMA	8	2	80	20
$[Zn(\kappa^2\text{-}dppz)(Br)_2]$ **3**	DMA	19	4.75	146	36.5
$[Zn(\kappa^2\text{-}Me_2bpy)Br_2]$ **1**	DMF	21	5.3	58	14.5
$[Zn(\kappa^2\text{-}phendione)(Br)_2]$ **2**	DMF	5	1.3	98	24.5
$[Zn(\kappa^2\text{-}dppz)(Br)_2]$ **3**	DMF	6	1.5	125	31.3

Several control experiments were also carried out to establish the nature of these catalyst systems. For example, when an identical set of experimental conditions was employed with an atmosphere of N_2 rather than CO_2. While some H_2 was observed, no CO_2 reduction products were observed as shown in Table 4.2. The necessity of catalysts **1-3** was demonstrated by performing analogous irradiation experiments in the absence of the Zn complexes but in the presence of 1mM of the respective ligands (Table 4.3). No products of CO_2 reduction and no H_2 were observed.

Table 4.2. Photocatalytic experiments with **[Zn(κ^2-Me$_2$bpy)Br$_2$] 1**, **[Zn(κ^2-phendione)(Br)$_2$] 2** and **[Zn(κ^2-dppz)(Br)$_2$] 3**. In DMA (4mL) with Ru(bpy)$_3$(PF$_6$)$_2$ as photosensitizer (**PS**) and TEOA as the electon donor (**ED**) under an **N$_2$** atmosphere. Turn-over number (TON) = (moles of product)/(moles of catalyst). Irradiation with 405 nm light for 24 h.

Complex (mM)	Solvent	Electron donor	H$_2$ (µmol)	HCOOH (µmol)
[Zn(κ^2-Me$_2$bpy)Br$_2$] 1	DMA	TEOA	18	-
[Zn(κ^2-phendione)(Br)$_2$] 2	DMA	TEOA	10	-
[Zn(κ^2-dppz)(Br)$_2$] 3	DMA	TEOA	5	-

Table 4.3. Photocatalytic experiments with ligand (1mM) in DMF (4mL) with Ru(bpy)$_3$(PF$_6$)$_2$ as photosensitizer (**PS**) and TEOA as the electon donor (**ED**) under a **CO$_2$** atmosphere. Irradiation with 405 nm light for 24 h.

Ligand	Electron donor	H$_2$ (µmol)	HCOOH (µmol)
5,5'-Me$_2$bpy	TEOA	-	-
phendione	TEOA	-	-
dppz	TEOA	-	-

Zn metal is known to be catalytically active for electrochemical CO$_2$ reduction to CO,[15] A common method to try to eliminate the possibility that metallic particles are the source of catalysis is a test using elemental Hg. To perform this test, a drop of Hg is added to the reaction mixture and the catalytic reaction is carried out. The Hg should react with metal particles and if they are the source of catalysis, should eliminate or reduce formation of the product. If metallic particles are not important for the reaction, there should be little or no effect on the product amount. The catalytic activity of these reactions was maintained as shown in Table 4.4 thus indicating that metallic Zn particles are not a likely source for our photocatalysis results.

Table 4.4. Photocatalytic experiments with ligand (1mM) in DMA (4mL) with Ru(bpy)$_3$(PF$_6$)$_2$ as photosensitizer (**PS**) and TEOA as the electron donor (**ED**) with drops of Hg under a **CO$_2$** atmosphere. Irradiation with 405 nm light for 24 h.

Complex (mM)	Ru(bpy)$_3$.2PF$_6$ (mM)	H$_2$ (µmol)	TON$_{H2}$	HCOOH (µmol)	TON$_{HCOOH}$
Zn-bpy-Br$_2$ (1)	1	40	10	150	37.5
Zn- phendione -Br$_2$ (2)	1	14	3.25	119	29.75
Zn-dppz-Br$_2$ (3)	1	15	3.75	70	17.5

All of these experiments confirmed that these Zn catalysts are active towards the CO_2 reduction, and they are able efficiently to reduce CO_2 to HCOOH. The photocatalytic CO_2 reduction ability of these catalysts were performed with different catalyst concentrations as shown in Table 4.5. Even though with the small concentrations of the catalysts, the catalysts are still active and able to reduce CO_2 to HCOOH efficiently. Moreover, the turnover number is increased with the decrees of the catalyst as shown in Table 4.5. In addition, the rate of the reaction for these three catalysts did not change a lot with the different concentrations as presenting in the Table 4.5.

Table 4.5. Photocatalytic experiments with varying concentrations of complexes **[Zn(κ^2-Me$_2$bpy)Br$_2$] 1 , [Zn(κ^2-phendione)(Br)$_2$] 2** and **[Zn(κ^2-dppz)(Br)$_2$] 3**. In DMA (4mL) with $Ru(bpy)_3(PF_6)_2$ (1mM) as photosensitizer (**PS**) and TEOA as the electon donor (**ED**) under a CO_2 atmosphere. Turn-over number (TON) = (moles of product)/(moles of catalyst). Irradiation with 405 nm light for 24 h.

Catalyst	(mM)	H_2 (µmol)	TON_{H2}	HCO_2H (µmol)	TON_{HCOOH}	Rate HCO_2H formation (µmol/hr)
1						
	0.1	15	37.5	119	298	5.0
	0.2	26	32.5	171	214	7.1
	0.5	26	13	166	83	6.9
	1	35	8.75	112	28	4.7
2						
	0.1	13	32.5	145	363	6.0
	0.2	10	12.5	150	188	6.3
	0.5	15	7.5	159	79.5	6.6
	1	8	2	84	21	3.5
3						
	0.1	13	32.5	133	333	5.5
	0.2	20	25	170	213	7.1
	0.5	19	9.5	116	58	4.8
	1	19	4.75	146	36.5	6.1

4.4. The Photocatalytic Mechanism

Two considerations were initially taken into account when proposing the mechanism for these catalytic reactions. First, the initial reduction of the complex was interrogated using DFT optimizations (B3LYP, def2TZVP). Second, the likelihood that a Zn-H should be one of the intermediates in the catalytic reaction. This second feature is based on the observations that: (i) literature reports for the formation of formic acid are dominated by a step involving CO_2 insertion into a M-H function; (ii) the reported reduction of CO_2 using catalyst **A** (Scheme 4.1); and (iii) observed H_2 formation is likely due to protonation of a M-H moiety. On this basis, a proposed mechanism for this photocatalytic process of the CO_2 reduction is given in Scheme 4.3.

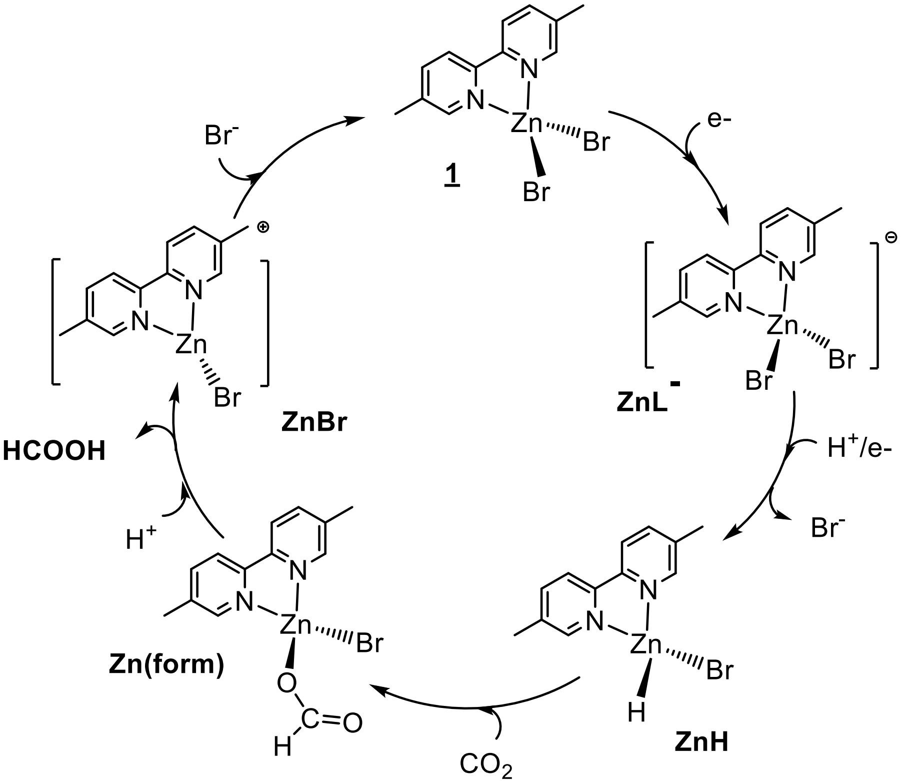

Scheme 4.3. The proposed mechanism for the photocatalytic CO_2 reduction process of these Zn(II) catalysts.

The first step of this mechanism is the reduction of the starting Zn complex **1**. The electrons are delivered from the electron transfer cycle that involves the excited photosensitizer (PS*) and the electron donor, TEOA. This cycle was previously presented and discussed in Chapter 3, Section 3.3. This step was investigated by first carrying out a DFT optimization of the starting material using the B3LYP functional and the def2TZVP basis set. The results are shown in Figure 4.6 and a comparison of the computed and experimental structures is given in Table 4.6. The optimization was then repeated for the singly reduced species **ZnL**$^-$ with the resultant struchture shown in Figure 4.7 and parameters in Table 4.6. The most notable structural changes that occurred during this reduction were a slight lengthening in the Zn-Br bonds and slightly shorter Zn-N distances. The symmetry of the complex did not change in any obvious way. As expected, the SOMO is bpy ligand centered in a π^* orbital and is represented in Figure 4.8. The next step in the proposed mechanism is the replacement of a bromide group with a hydrogen to yield **ZnH** and the DFT optimized structure is depicted in Figure 4.9.

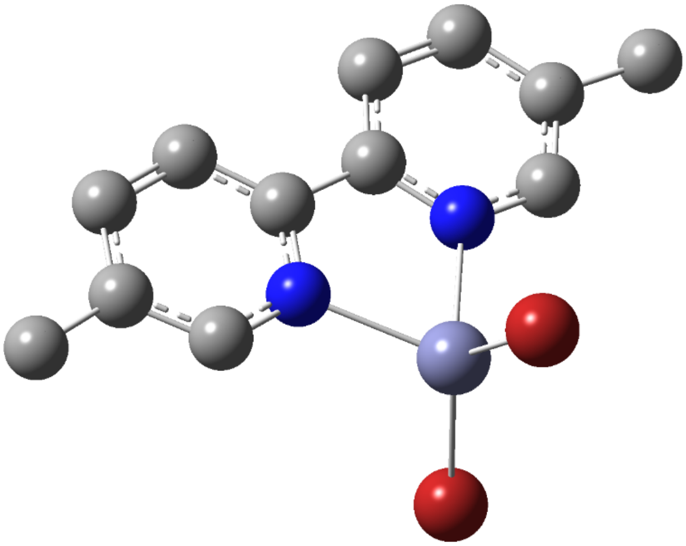

Figure 4.6. A ball and stick structural representation for the computationally optimized **[Zn(κ^2-2,2'-bpy)Br$_2$ 1**. DFT calculations used the B3LYP functional and the def2TZVP basis set. Hydrogen atoms are not shown for clarity.

Table 4.6. Selected metrical parameters from the experimental single crystal X-ray analysis for **[Zn(κ^2-2,2’-bpy)Br$_2$] 1**, the computationally optimized structure for **1**, the optimized structure of the single electron reduction product, **ZnL$^-$**,and optimized **[Zn(κ^2-dppz)Br$_2$] 3**.

Compound	**Zn-Br**	**Zn-N**	**Br-Zn-Br**	**Br-Zn-N**
experimental **1**	2.3458(3)	2.0518(15)	117.457(17)	111.39(4)
optimized **1**	2.35989	2.15279	130.630	109.1
ZnL$^-$	2.42385	2.07858	117.723	113.273
optimized **3**	2.35708	2.16589	131.568	108.717

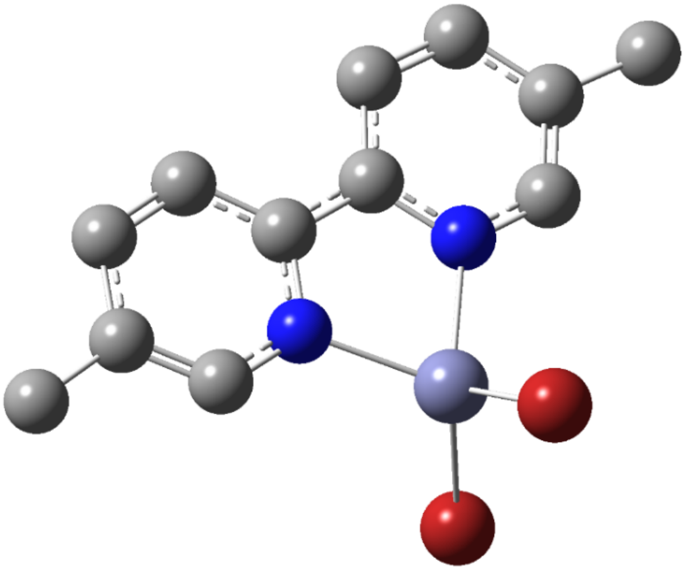

Figure 4.7. A ball and stick structural representation for the computationally optimized anion complex **[Zn(κ^2-2,2’-bpy)Br$_2$]$^-$** , **“ZnL$^-$”**. DFT calculations used the B3LYP functional and the def2TZVP basis set. Hydrogen atoms are not shown for clarity.

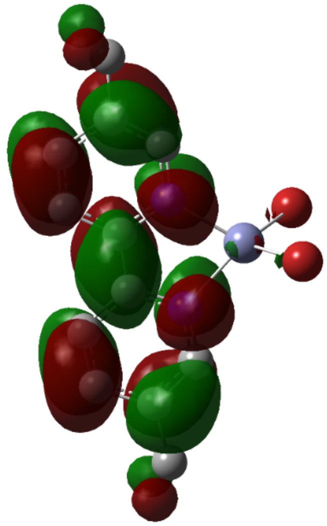

Figure 4.8. Representation of the SOMO (isovalue 0.05) for the computationally optimized anion complex **[Zn(κ^2-2,2'-bpy)Br$_2$]$^-$** , **"ZnL$^-$"**. DFT calculations used the B3LYP functional and the def2TZVP basis set. Hydrogen atoms are not shown for clarity.

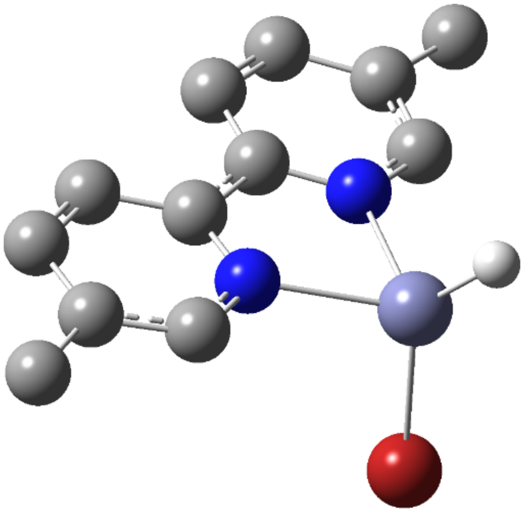

Figure 4.9. A ball and stick structural representation for the computationally optimized hydride complex **[Zn(κ^2-2,2'-bpy)Br(H)] "ZnH"**. DFT calculations used the B3LYP functional and the def2TZVP basis set. Hydrogen atoms are not shown for clarity.

The next two steps in the proposed cycle are the insertion of CO_2 into the Zn-H moiety to yield a formate complex, [Zn(κ^2-2,2'-bpy)Br(OCHO)], and the loss of formic acid to produce a cationic complex [Zn(κ^2-2,2'-bpy)Br]$^+$. Both of these proposed species were successfully modeled by DFT (B3LYP, def2TZVP) with the resultant structures depicted as **Zn(form)** and **ZnBr** in Figures 4.10 and 4.11 respectively. Support for these computed results requires additional evidence and future efforts will be targeted on synthesis and/or spectroscopic observation of these species.

Finally, to complete the computational investigations, the proposed structure of **[Zn(κ^2-dppz)Br$_2$] 3** was performed. The structure that was obtained is shown in Figure 4.12 and some selected structural parameters are given in Table 4.6. Not surprisingly, the structural parameters closely mirror those of the optimized structure **1**.

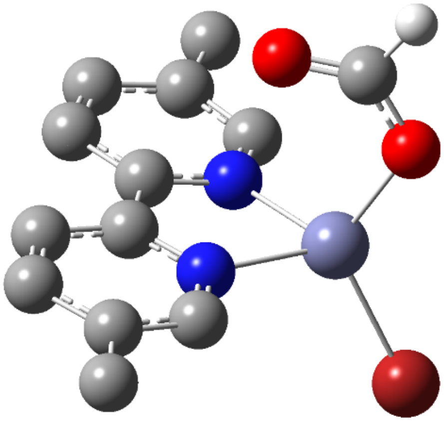

Figure 4.10. A ball and stick structural representation for the computationally optimized hydride complex **[Zn(κ^2-2,2'-bpy)Br(OCHO)]**, **"Zn(form)"**. DFT calculations used the B3LYP functional and the def2TZVP basis set. Hydrogen atoms are not shown for clarity.

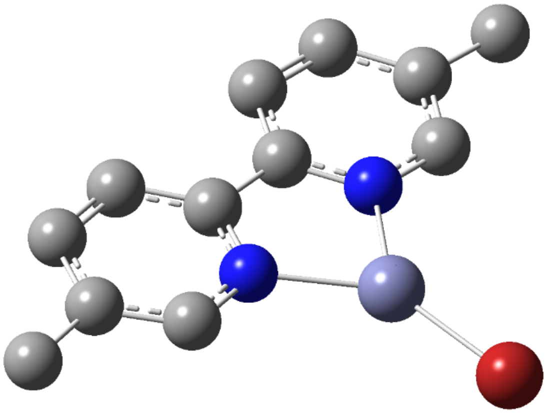

Figure 4.11. A ball and stick structural representation for the computationally optimized cation complex **[Zn(κ^2-2,2'-bpy)Br]$^+$ ZnBr**. DFT calculations used the B3LYP functional and the def2TZVP basis set. Hydrogen atoms are not shown for clarity.

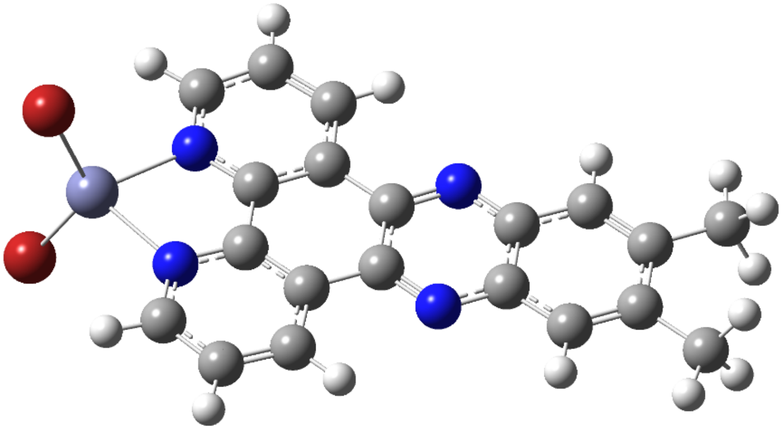

Figure 4.12. A ball and stick structural representation for the computationally optimized complex **[Zn(κ^2-dppz)Br$_2$] 3**. DFT calculations used the B3LYP functional and the def2TZVP basis set.

4.5. Emission-Quenching Experiments

The emission spectra for the three catalysts were obtained according to similar method that explained section 1.7.4 of Chapter 1 and the emission-spectra for the both electron donors TEOA and TEA were also obtained as shown in Chapter 1. The purpose of obtaining the quenching spectra here is to see if there are any possible mechanistic implications for these Zn catalysts. The results of these studies is shown in Figures 4.13-4.15. It is quite clear that the Zn complexes 1-3 quench the excited Ru(bpy)$_3^{2+}$. The implications of these results on the mechanism for CO_2 reduction will be a component of the future study of this transformation.

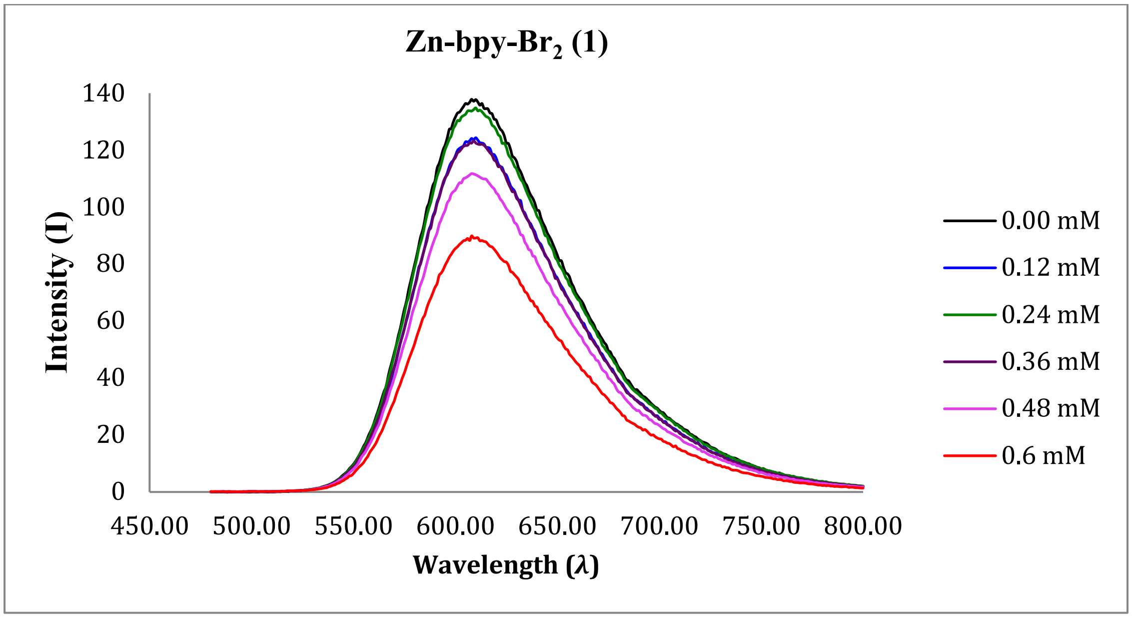

Figure 4.13. Emission-spectra from the quenching experiments with complex Zn-bpy-Br$_2$ (1).

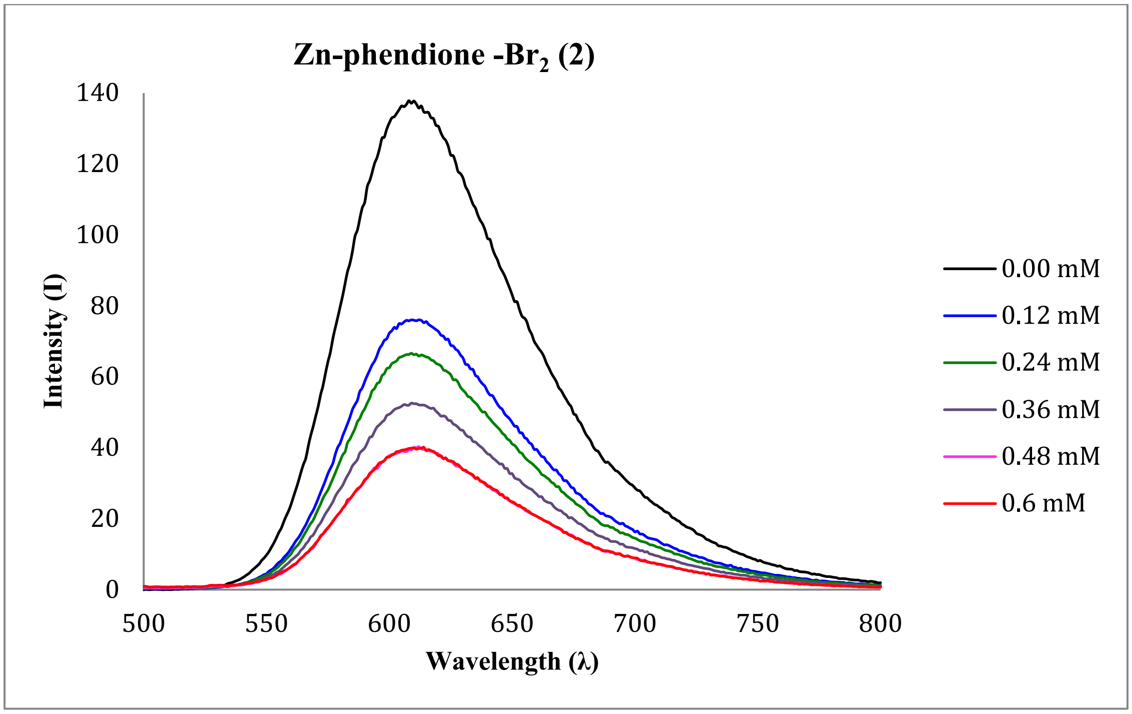

Figure 4.14. Emission-spectra from the quenching experiments with complex Zn-phendione-Br$_2$ (2).

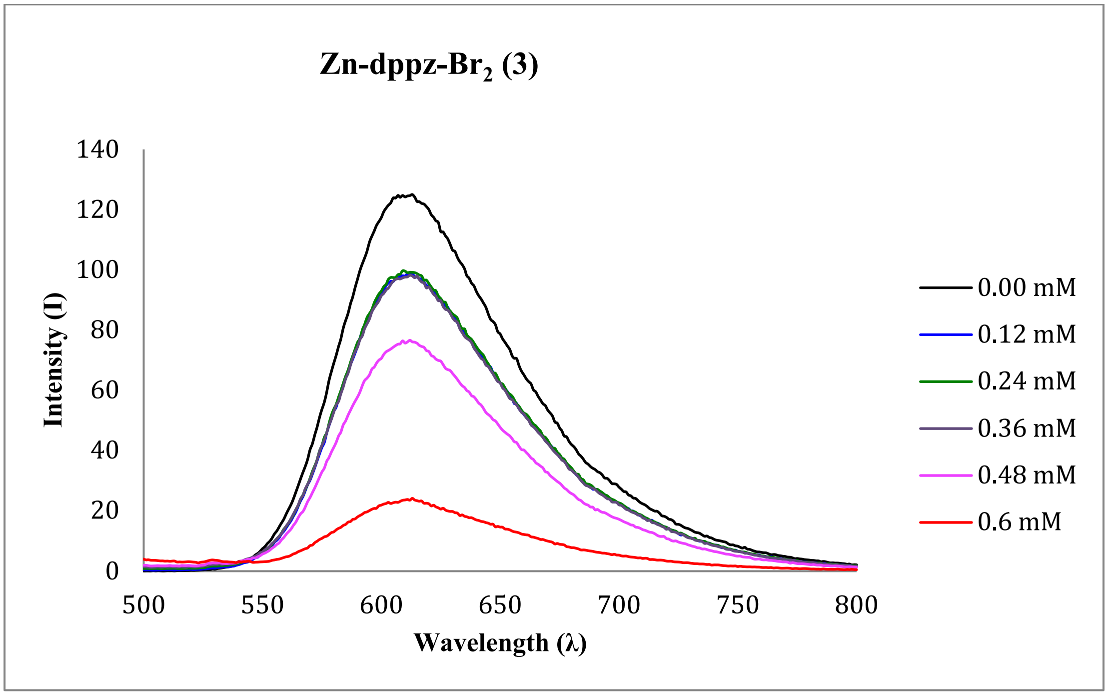

Figure 4.15. Emission-spectra from the quenching experiments with complex Zn-dppz-Br_2 (3).

4.6. The Electrocatalytic CO_2 Reduction

Since the CO_2 photoreduction and in particular the first step for the proposed mechanism involve electron transfer, the electrochemical and electrocatalytic behavior for these catalysts were also examined. The voltammetry studies were performed in CH_3CN (10 mL) solvent containing the catalyst (1.0 mM) and tetrabutylammonium hexafluorophosphate as the supporting electrolyte (100 mM). The standard procedures used for these studies was described in Chapter 1. A standard three-electrode cell was used, with a 3-mm diameter glassy carbon working electrode, a platinum wire counter electrode, and an Ag/AgCl coupled reference electrode. All potentials were referred to the redox potential of ferrocene (Fc)/ferrocenium ion (Fc^+) as an internal standard. The next figures present the results of cyclic voltammetry measurements for reduction of Zn complexes **1-3** under N_2 and CO_2, atmospheres. Also included are results under a CO_2 atmosphere with added H_2O.

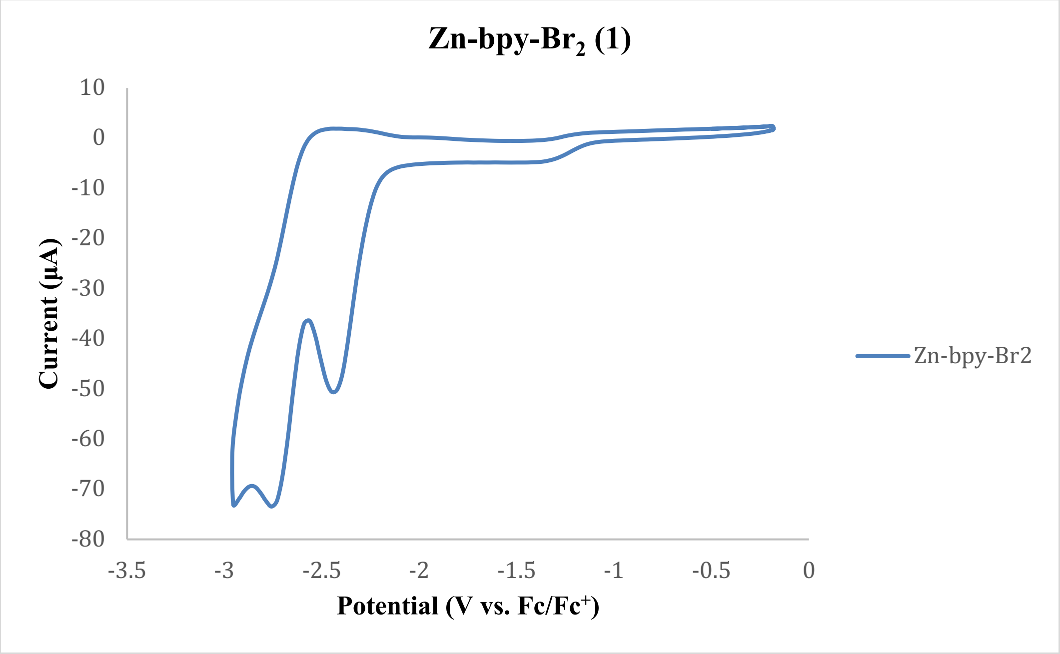

Figure 4.16. Cyclic voltammograms of Zn-bpy-Br$_2$ (1) under N$_2$ (blue) in CH$_3$CN with 0.1M (n-Bu)$_4$NPF$_6$ supporting electrolyte at 100 mV/s.

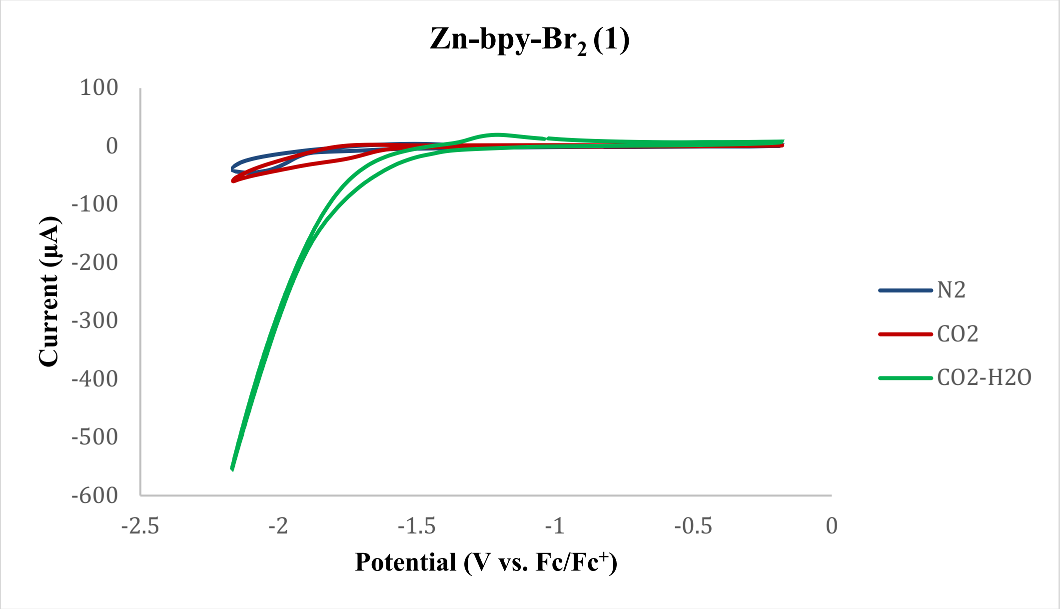

Figure 4.17. Cyclic voltammograms of Zn-bpy-Br$_2$ (1) under N$_2$ (blue), CO$_2$ (red) and Water (green) in CH$_3$CN with 0.1M (n-Bu)$_4$NPF$_6$ supporting electrolyte at 100 mV/s.

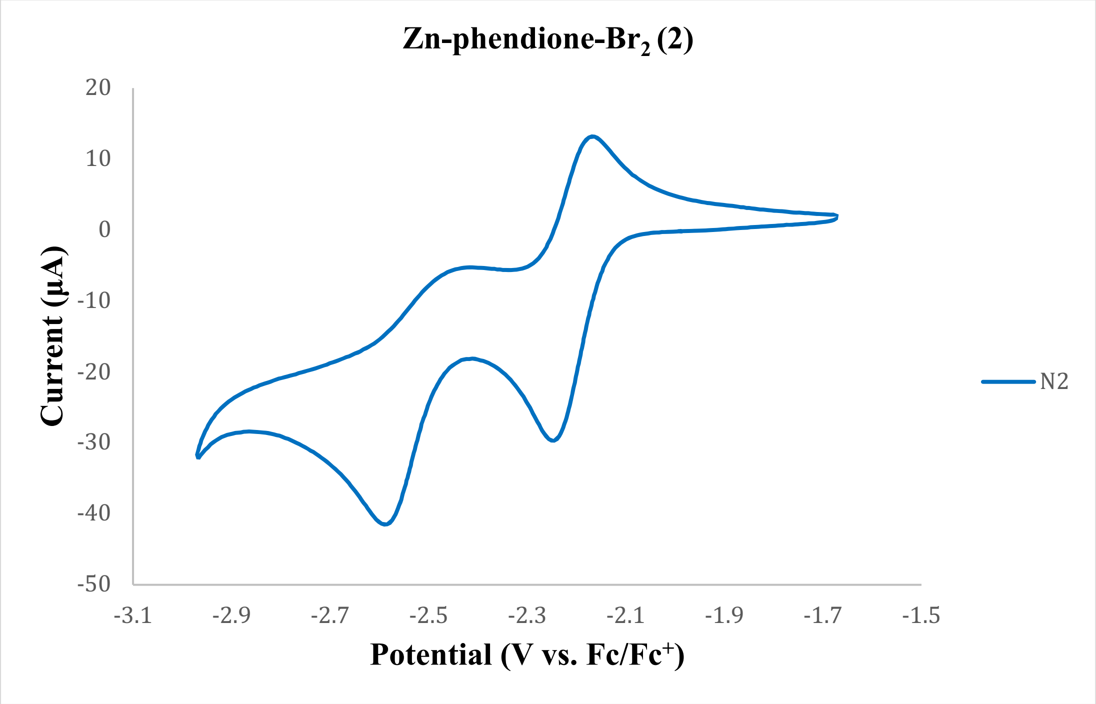

Figure 4.18. Cyclic voltammograms of Zn-phendione-Br$_2$ (2) under N_2 (blue) in CH_3CN with 0.1M (n-Bu)$_4$NPF$_6$ supporting electrolyte at 100 mV/s.

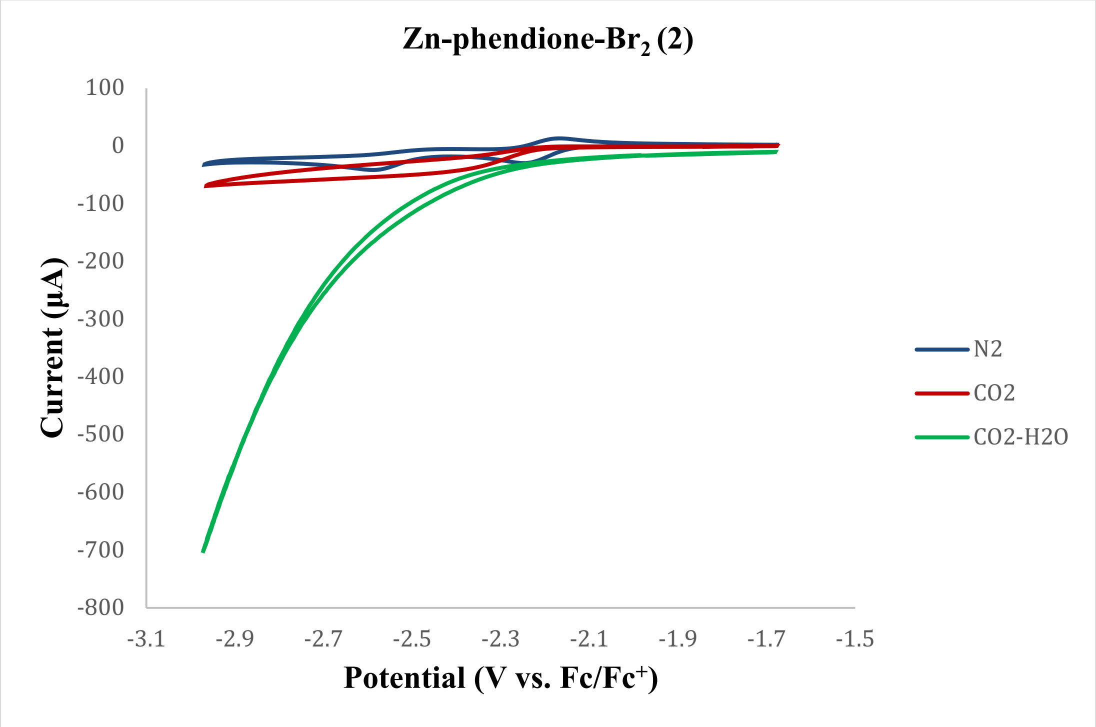

Figure 4.19. Cyclic voltammograms of Zn-phendione-Br$_2$ (2) under N_2 (blue), CO_2 (red) and Water (green) in CH_3CN with 0.1M (n-Bu)$_4$NPF$_6$ supporting electrolyte at 100 mV/s.

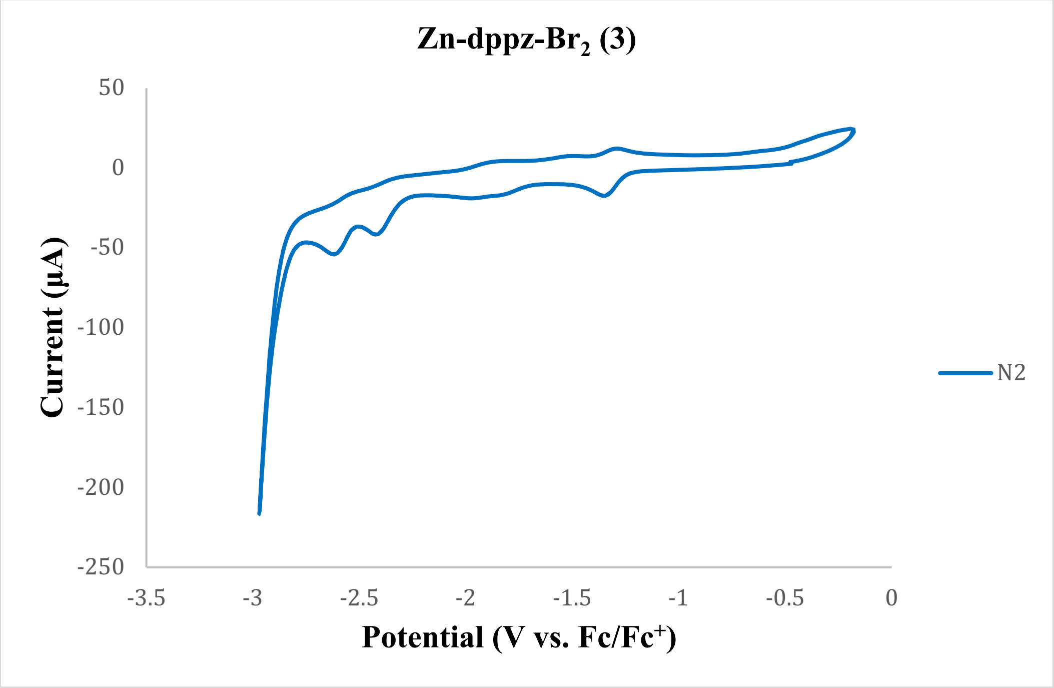

Figure 4.20. Cyclic voltammograms of Zn-dppz-Br$_2$ (3) under N_2 (blue) in CH_3CN with 0.1M $(n\text{-}Bu)_4NPF_6$ supporting electrolyte at 100 mV/s.

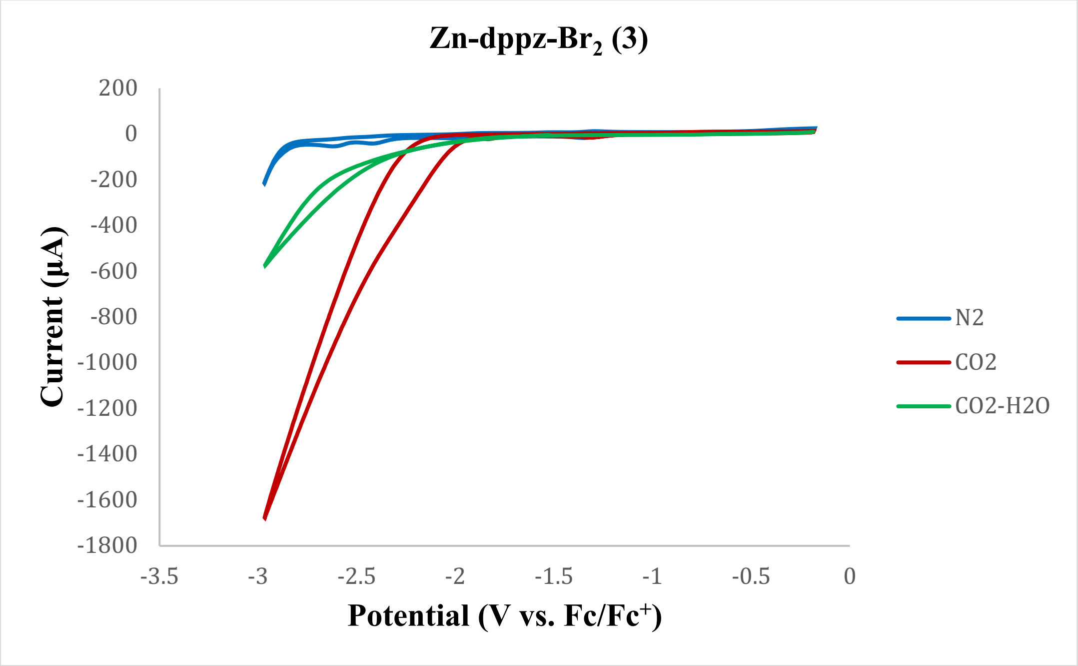

Figure 4.21. Cyclic voltammograms of Zn-dppz-Br$_2$ (3) under N_2 (blue), CO_2 (red) and Water (green) in CH_3CN with 0.1M $(n\text{-}Bu)_4NPF_6$ supporting electrolyte at 100 mV/s.

Some general comments on the cyclic voltammetry data can be made. The most notable is that there was a substantial enhancement of the reduction current for the three Zn catalysts indicating an electrocatalytic process. This is to be expected given the photocatalytic results. A number of additional experiments are required to more carefully and completely uncover the catalytic behaviour that is indicated. For example, bulk electrolysis experiment needs to be done to help understanding more about this electrocatalytic behaviour.

4.7. Conclusion and Future Work

The complexes Zn-bpy-Br_2, Zn-phendione-Br_2, and Zn-dppz-Br_2 are active for photocatalytic CO_2 reduction. The performance parameters of these three species are similar. For the future work, more experiments should be done to investigate more about the mechanism of this photocatalytic cycle. In addition, the electrocatalytic ability should be more carefully investigated.

4.8. References

1 N. Elgrishi, M. B. Chambers, X. Wang and M. Fontecave, *Chem. Soc. Rev.*, 2017, **46**, 761–796.

2 J. Bonin, A. Maurin and M. Robert, *Coord. Chem. Rev.*, 2017, **334**, 184–198.

3 H. Takeda, C. Cometto, O. Ishitani and M. Robert, *ACS Catal.*, 2017, **7**, 70–88.

4 Y. Yamazaki, H. Takeda and O. Ishitani, *J. Photochem. Photobiol. C Photochem. Rev.*, 2015, **25**, 106–137.

5 K. E. Dalle, J. Warnan, J. J. Leung, B. Reuillard, S. Karmel, Isabell and E. Reisner, *Chem. Rev.*, 2019, **119**, 2752–2875.

6 R. Reithmeier, C. Bruckmeier and B. Rieger, *Catalysts*, 2012, **2**, 544–571.

7 S. Kissling, P. T. Altenbuchner, T. Niemi, T. Repo and B. Rieger, in *Zn in Catalysis. Applications in Organic Synthesis*, eds. S. Enthaller and X.-F. Wu, Wiley-VCH Verlag GmbH & Co., Weinheim, Germany, 2015, pp. 179–206.

8 S. Klaus, M. W. Lehenmeier, C. E. Anderson and B. Rieger, *Coord. Chem. Rev.*, 2011, **255**, 1460–1479.

9 R. Dobrovetsky and D. W. Stephan, *Angew. Chemie - Int. Ed.*, 2013, **52**, 2516–2519.

10 Y. Li, K. Junge and M. Beller, in *Zn in Catalysis. Applications in Organic Synthesis*, eds. S. Enthaller and X.-F. Wu, Wiley-VCH Verlag GmbH & Co., Weinheim, Germany, 2015, pp. 5–56.

11 W. Sattler and G. Parkin, *J. Am. Chem. Soc.*, 2012, **134**, 17462–17465.

12 Y. Wu, J. Jiang, Z. Weng, M. Wang, D. L. J. Broere, Y. Zhong, G. W. Brudvig, Z. Feng and H. Wang, *ACS Cent. Sci.*, 2017, **3**, 847–852.

13 E. S. Donovan, B. M. Barry, C. A. Larsen, M. N. Wirtz, W. E. Geiger and R. A. Kemp, *Chem. Commun.*, 2016, **52**, 1685–1688.

14 Y. Kuramochi, M. Kamiya and H. Ishida, *Inorg. Chem.*, 2014, **53**, 3326–3332.

15 D. H. Won, H. Shin, J. Koh, J. Chung, H. S. Lee, H. Kim and S. I. Woo, *Angew. Chemie Int. Ed.*, 2016, **55**, 9297–9300.

Chapter 5: Turning on the Formation of Formic Acid from CO_2 with an Integrated Re Photocatalyst/Sensitizer

The work in this chapter formed a significant component of the submitted publication:

(Y. Hameed, B. Gabidullin, and D. S Richeson, *Chem. Commun.,* 2019)

In this chapter, the goal was to explore homogeneous group 7 CO_2 reduction catalysts with a different ligand array. The reported group 7 catalysts are hugely dominated by the facial α-diimine metal (I) tricarbonyl species with a 2,2′-bipyridine ligand being the most prevalent. This project was conceptualized by Y. Hameed and D. Richeson. The major contribution to the synthesis and characterization of the complexes and the catalytic behavior of the complexes were done by Y. Hameed. The crystallography was carried out by B. Gabidullin., and the DFT calculations of these complexes were carried out by D. Richeson.

5.1. Introduction

The combination of addressing the issues of sustainable energy and the environmental concerns regarding emission of greenhouse gases provides a strong impetus to target the efficient chemical reduction of carbon dioxide. This fundamentally challenging goal, due to the chemical stability of CO_2, requires a significant amount of energy to yield useful products. Photocatalysis is a particularly appealing approach to surmount these barriers since it employs light, a clean and unlimited resource, for this conversion of a waste by-product into a feedstock. In addition to CO, the common two-electron product for CO_2 reduction is formic acid, which is an important commodity chemical and a potential carrier of H_2.[1,2] Identification of catalysts that can convert energy input into chemical transformation is critical for success.[3–5] A general photocatalytic system has three core, integrated components that consist of a photosensitizer (**PS**), for collecting the photon energy, an electron donor (**ED**), that provides electrons for the reduction, and a catalyst (**CAT**) that is a site for the conversion of CO_2.

More than 30 years ago, the pioneering discovery that *fac*-$Re(bpy)(CO)_3X$ (bipy = 2,2'-bipyridine, X = halide) complexes were photocatalysts for the selective reduction of CO_2 to CO using triethanolamine (TEOA) as an electron donor established the ongoing exploration of related *fac*-[Re(α-diimmine)$(CO)_3X$] catalysts and these complexes remain as touchstones for this field.[6,78–1112] The central role of group 7 in this field continued with the report that the manganese analogue *fac*-[$Mn(bpy)(CO)_3Br$] was, with a $Ru(bpy)_3^{2+}$ photosensitizer, competent for photocatalytic CO_2 reduction.[13–16] The *fac*-$Re(bpy)(CO)_3X$ catalysts are particularly unique in their ability to function as amalgamated PS and CAT, thus allowing light absorption and catalysis in one species.[17 6,18–22] These features drive the vigorous search for PS integrated catalysts yet realization remains rather limited. [17,23–25] The expansion of ligand scaffolds have recently revealed Re(I) complexes with N-heterocyclic carbene (NHC) ligands as combined photocatalyst/sensitizer for the reduction of CO_2 to CO.[26,27] and a Ru complex that functions as both PS and CAT.[17] Interestingly other than this Ru complex all of the Re complexes give CO as the reduction product.

With the objectives of discovering new environments for CO_2 photoreduction catalysts, revealing new integrated photosensitizer/catalyst species and uncovering new reaction pathways for this transformation we targeted the preparation of the bis(bipyridine) Re carbonyl, [$Re(bpy)_2(CO)_2$]X, complex. We were encouraged to pursue these targets not only from the known catalytic abilities of [$Re(bpy)(CO)_3X$] but also from the reported observation of the related proficiency of the mono- and bis(α-diimine) Ru species, *cis,trans*-$Ru(N^\wedge N)(CO)_2Cl_2$[28–30] and *cis*-[$Ru(N^\wedge N)_2(CO)_2$]$^{2+}$ in catalysis.[31–34] This report provides the first documentation of this coordination environment as a capable catalyst for the photocatalytic reduction of CO_2 to HCO_2H as well as revealing an entirely new catalyst with integrated photosensitizer ability.

5.2. Experimental Details

5.2.1. Synthetic methods and Characterization

Synthesis of *cis*-$[Re(bpy)_2(CO)_2]^+Otf^-$ (1+Otf-) Complex 1 (according to the reported literature[35])

The cationic complex *cis*-$[Re(CO)_2(bpy)_2](CF_3SO_3)$ was synthesized according to the literature from the *fac*-$Re(bpy)(CO)_3(CF_3SO_3)$ complex **A**.[35] Complex **A** (1.895 g, 3.294 mmol) was mixed with a large excess of bpy (≈ 2.055 g) with a magnetic stir bar in a Schlenk tube, which was capped with a septum and purged with N_2. The reaction mixture was magnetically stirred and heated to melt for 4 h during which time a red solid appeared. The reaction mixture was cooled and then dissolved in CH_2Cl_2 and transferred from the tube to a round bottom flask to remove the solvent under the vacuum. Purification was achieved by column chromatography on acidic alumina with CH_2Cl_2/CH_3CN mixtures. Yield: 1.526 g (83%). The ^1H NMR, UV-visible IR spectra and FAB-MS matched with the reported complex.31 ^1H NMR (δ/ppm, CD_3CN): 9.45 (d, 2H, J = 5.0 Hz), 8.48 (d, 2H, J = 8.6 Hz), 8.40 (d, 2H, J = 8.6 Hz), 8.15 (dt, 2H, J = 1.5, 8.1 Hz), 8.02 (dt, 2H, J = 1.5, 8.1 Hz), 7.63 (m, 2H), 7.41 (dd, 2H, J = 1.0, 5.5 Hz), 7.34 (m, 2H). UV-visible (λ (nm), CH_2Cl_2) (ϵ in M^{-1} cm^{-1}): 288 (47400), 364 (6100), 400 (6590), 492 (5320), 564 (sh, 3660). IR (CH_2Cl_2) (ν(CO), cm^{-1}): 1992, 1852. FAB-MS$^+$: 555.08.[35] ^{13}C -NMR (CD_3CN): δ 117.3, 123.9, 124.8, 127.3, 128.1, 137.6, 139.5, 147.8, 155.8, 200.3. Elemental analysis calcd (%) for $C_{23}H_{16}F_3N_4O_5ReS$ C 39.26, H 2.29, N 7.96, found C 39.34, H 2.13, N 8.0.

5.2.2. X-ray Analysis

The X-ray analysis procedure was described in section 1.7.6 of the introduction chapter (Chapter 1). The crystals of this complex *cis*-$Re(CO)_2(bipy)_2^+OTf^-$ were grown by slow diffusion of saturated CH_2Cl_2 solution in CH_3CN. The structural features of *cis*-$Re(CO)_2(bipy)_2^+OTf^-$ complex were determined by single crystal X-ray analysis as shown in Figure 5.1.

5.2.3. Photocatalytic Experiments

The photoreaction procedure for these experiments is described in section 1.7.1 of the introduction chapter (Chapter 1).

5.3. Result and Discussion

A survey of the literature revealed that the targeted complex with X = OTf^- had been reported.[35] The preparation involved the unusual and severe conditions of using a melt of 2,2'-bipyridine as the solvent at T > 275°C. This reflects the stability of the *fac*-$[Re(bpy)(CO)_3X]$ and consistent with the dominance of this structure in Re(I) chemistry. Our success with the synthesis of *cis*-$[Re(bpy)_2(CO)_2]^+OTf^-$ (**1^+OTf^-**) in 83% yield was demonstrated through the spectroscopic features of our product and microanalysis. In particular, the ^1H and ^{13}C NMR spectra displayed the expected signals for the C_2 symmetric structure. Although some fundamental physical characterization of cis-$[Re(bpy)_2(CO)_2]^+OTf^-$ (**1^+OTf^-**) was reported, no further reactivity was reported.

We were fortunate to obtain crystals of cis-$[Re(bpy)_2(CO)_2]^+OTf^-$ (**1^+OTf^-**) and to apply single crystal X-ray analysis to definitively confirm the metrical parameters of this complex with the results shown in Figure 5.1. As proposed, the cationic complex displayed a Re(I) center in a distorted octahedral geometry with the C_2 symmetry of the cis ligand array and an uncoordinated triflate counter ion. The Re-C distances were identical at

1.883(5) Å and two slightly different Re-N distances of 2.121(3) Å (Re-N1, *trans* to N) and 2.165(3) Å (Re-N12, *trans* to CO) were observed. The largest distortion from orthogonality of the angles around the Re center arise from the restricted bite angle of the bpy with the observed N-Re-N angle of 75.15(13)°. There is only one analogue of this complex that appears in the literature, the bis(1,10-phenanthroline) complex cis-$[Re(phen)_2(CO)_2]^+OTf^-$ and this species displayed very similar metrical features.[35]

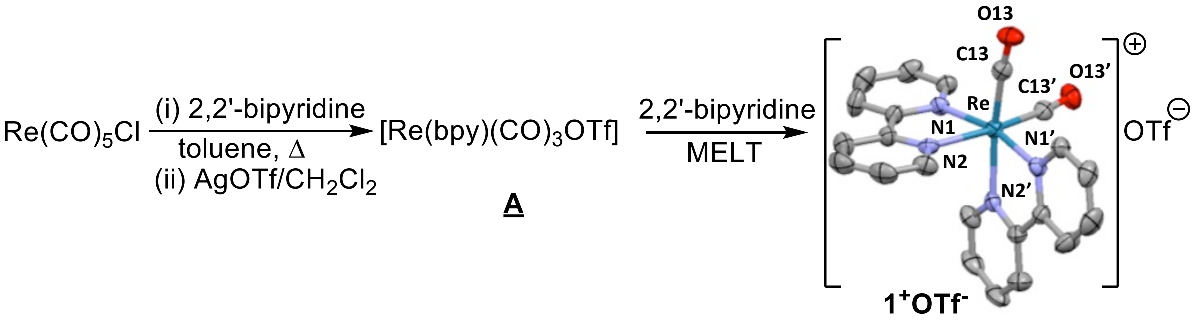

Figure 5.1. The synthetic methods used for preparation of *cis*-$Re(CO)_2(bipy)_2^+OTf^-$ **1**.

Before applying $\mathbf{1^+OTf^-}$ as a photoreduction catalyst, some fundamental physical chemistry characterizations using cyclic voltammetry, DFT optimization and UV-vis electronic spectral characterization were carried out. Under reducing potentials we confirmed that $\mathbf{1^+OTf^-}$ in acetonitrile exhibited reversible one electron reductions at $E_{1/2}$ = -1.67 V and -1.90 V *vs* Fc/Fc^+ (Figure 5.2).[35] Both reduction peaks showed a linear dependence of peak current on the square root of the scan rate ($\nu^{1/2}$) thus indicating freely diffusing species (Figures 5.5-5.6). A nonreversible reduction at a more negative potential of -2.63 V was also observed.

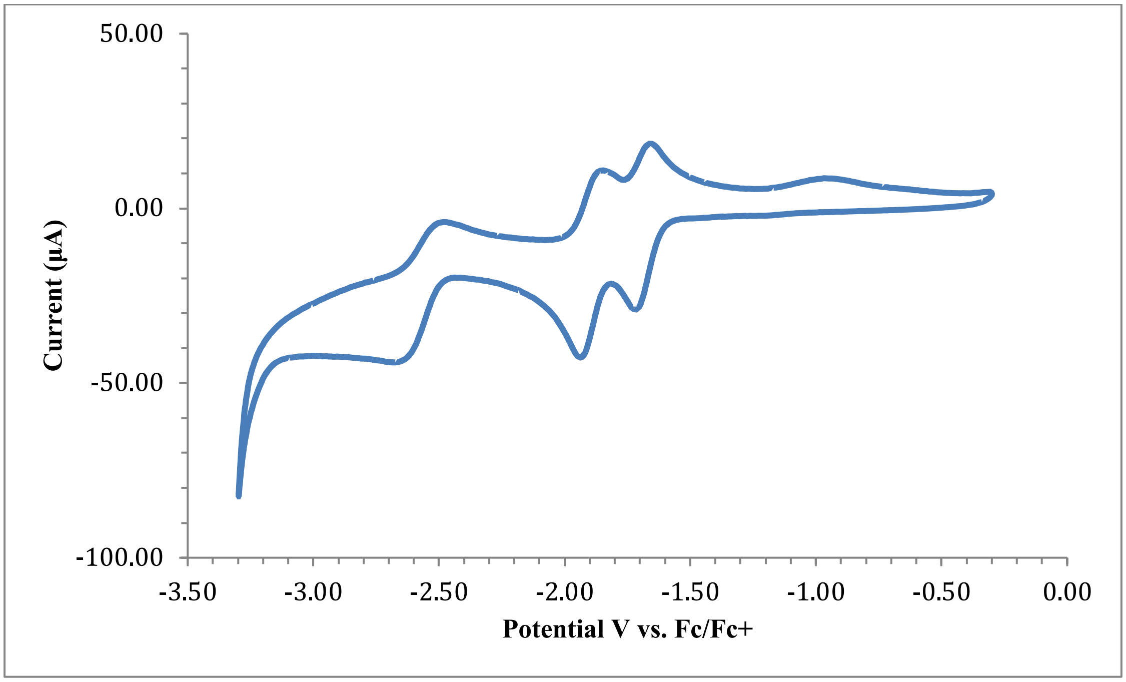

Figure 5.2. The cyclic voltammagram under reducing potentials of *cis*-Re(CO)$_2$(bipy)$_2$$^+OTf^-$ (1.0 mM) under N$_2$ in CH$_3$CN with 0.1Mtetrabutylammoniumhexafluorophosphate (TBAHFP) supporting electrolyte at a scan rate of 100 mV/s. reference to Fc/Fc$^+$.

The electrocatalysis measurements with variable scan rate and isolation of the individual reduction events under N$_2$ was also performed. The first and second reduction waves were shown in Figure 5.3 and 5.4 with different scan rates, and all of these reduction peaks showed a linear dependence of peak current on the square root of the scan rate thus indicating freely diffusing species as shown in Figure 5.5 and 5.6.

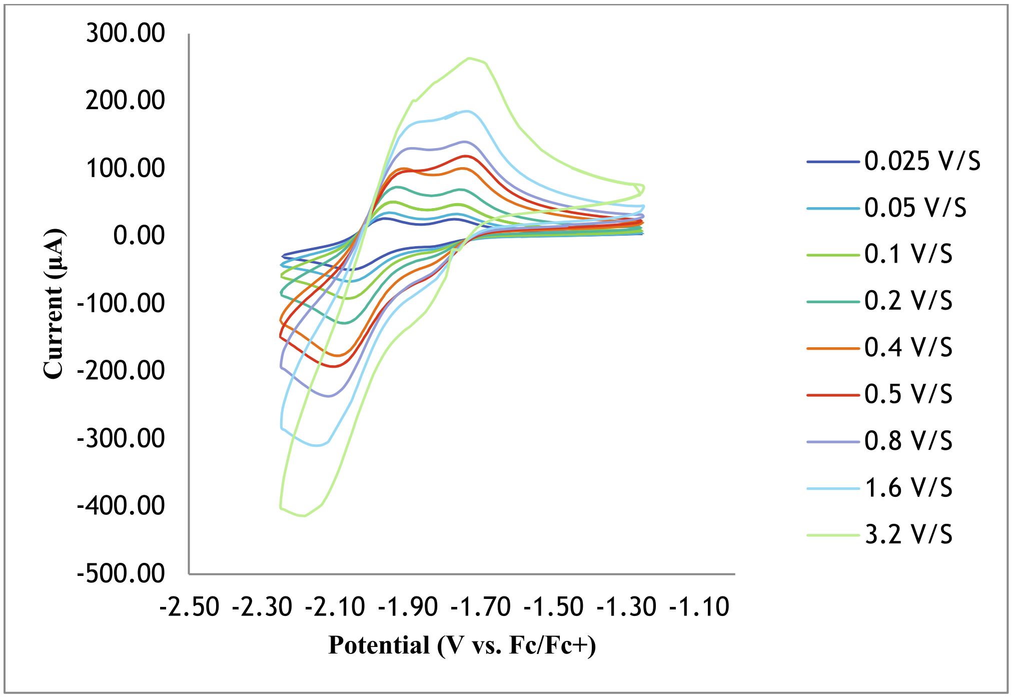

Figure 5.3. Cyclic voltammograms of the first reduction for *cis*-Re(CO)$_2$(bipy)$_2^+$OTf$^-$ (1.0 mM) under N$_2$ in CH$_3$CN with 0.1M tetrabutylammonium hexafluorophosphate (TBAHFP) supporting electrolyte with different scan rates.

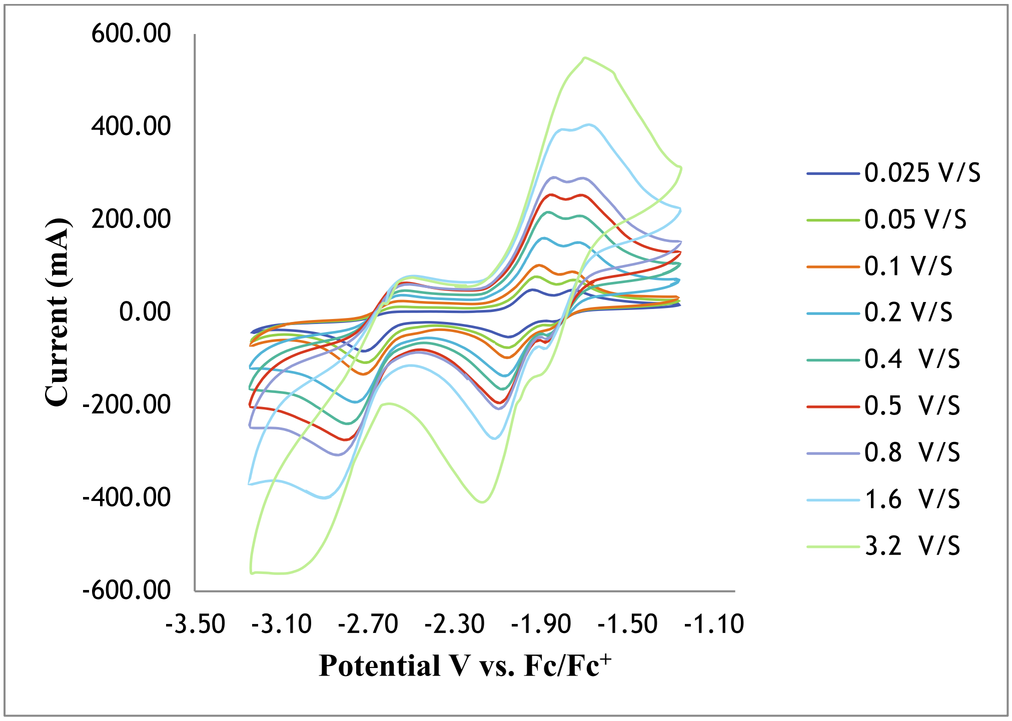

Figure 5.4. Cyclic voltammograms for *cis*-Re(CO)$_2$(bipy)$_2^+$OTf$^-$ (1.0 mM) under N$_2$ in CH$_3$CN with 0.1M tetrabutylammonium hexafluorophosphate (TBAHFP) supporting electrolyte with different scan rates.

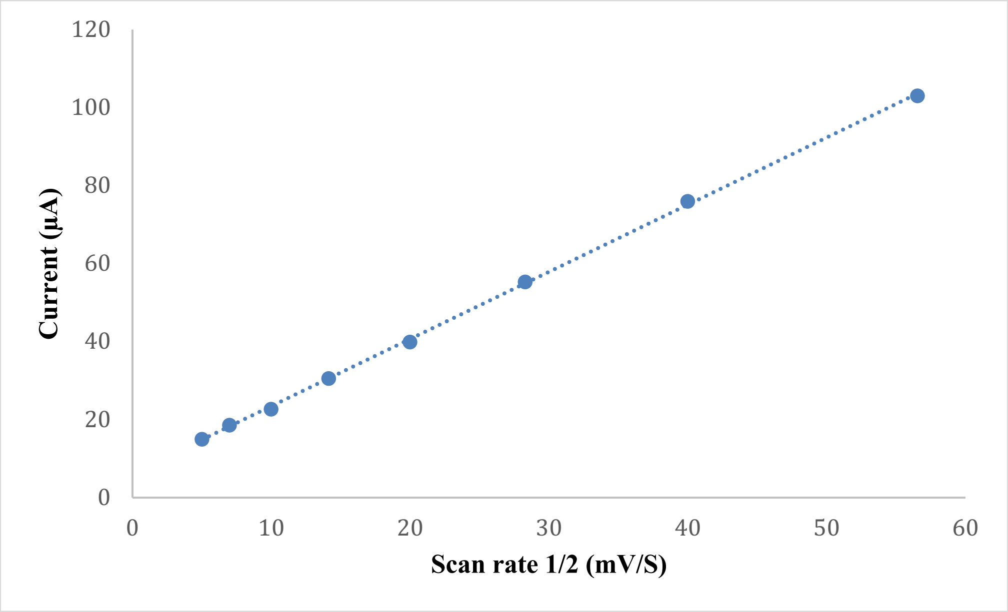

Figure 5.5. Plot of scan rate$^{1/2}$ versus current at first reduction peak at -1.94 V.

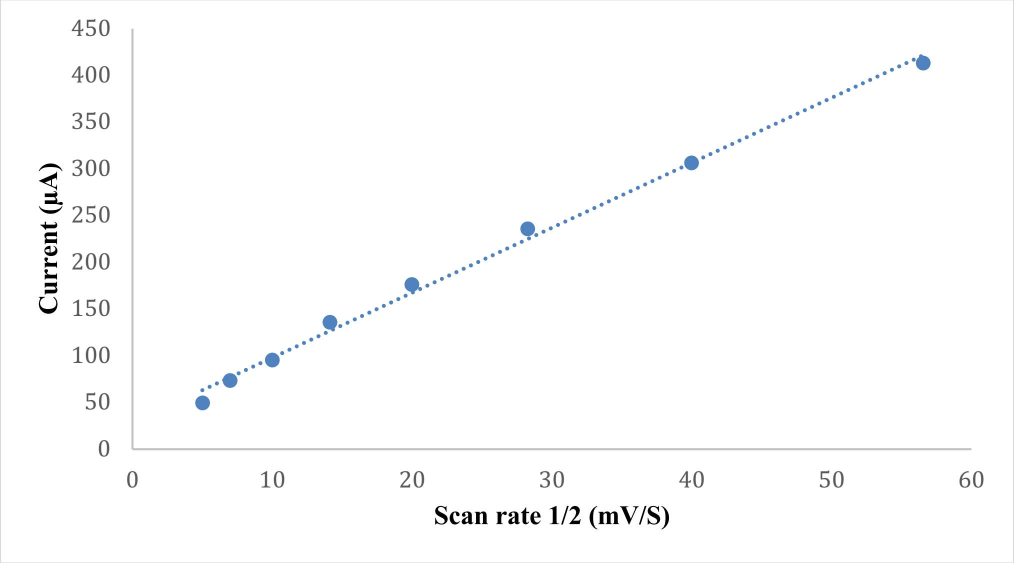

Figure 5.6. Plot of scan rate$^{1/2}$ versus current at second reduction peak at -2.15 V.

DFT optimization (B3LYP functional and def2TZVP basis set) of the cationic complex **1**$^+$ yielded results consistent with the X-ray analysis (Figure 5.7, Table 5.1). A TD-DFT analysis using the integral equation formalism variant of the PCM model (IEFPCM) with CH_2Cl_2 as solvent confirmed MLCT (dπ-π*) absorptions at visible wavelengths of 419, 439, 501, 503, and 544nm. Consistent with these calculations is the appearance of the visible portion (350nm-800nm) of the electronic spectrum of **1$^+$OTf$^-$** in CH_2Cl_2, as shown in Figure 5.8. The **1$^+$OTf$^-$** has an excited state lifetime of 25ns which is similar to that of *fac*-Re(bpy)$(CO)_3$Cl.[19,35]

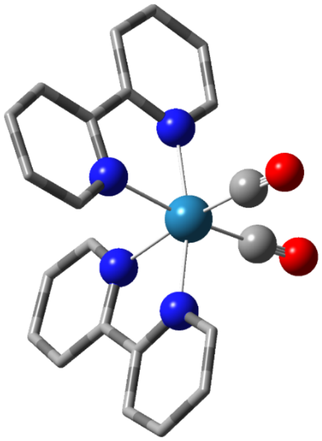

Figure 5.7. A ball and stick structural representation for the computationally optimized [Re{κ^2-bpy}$(CO)_2$]$^+$ compound **1**$^+$. DFT calculations used the B3LYP functional and the def2TZVP basis set. Hydrogen atoms are not shown for clarity. Some carbon atoms have been removed for clarity.

Table 5.1. A comparison of metal–ligand distances and angles from the experimental single crystal X-ray analysis and from the computationally optimized structures (**1**) and and the single electron reduction product [**A**) and the double reduction product (**B**).

Bond/cmpd	[Re{κ^2-bpy}$(CO)_2$]$^+$ (**1**$^+$) Exp[a]	[Re{κ^2-bpy}$(CO)_2$]$^+$ (**1**$^+$) Computed	Reduced complex [Re{κ^2-bpy}$(CO)_2$] Computed
M-N trans CO	2.165(3)	2.215	2.2028
M-N trans N	2.121(3)	2.147	2.1319
M-CO	1.883(5)	1.921	1.9156
N-M-N_{py}	75.15(13	74.67	75.326

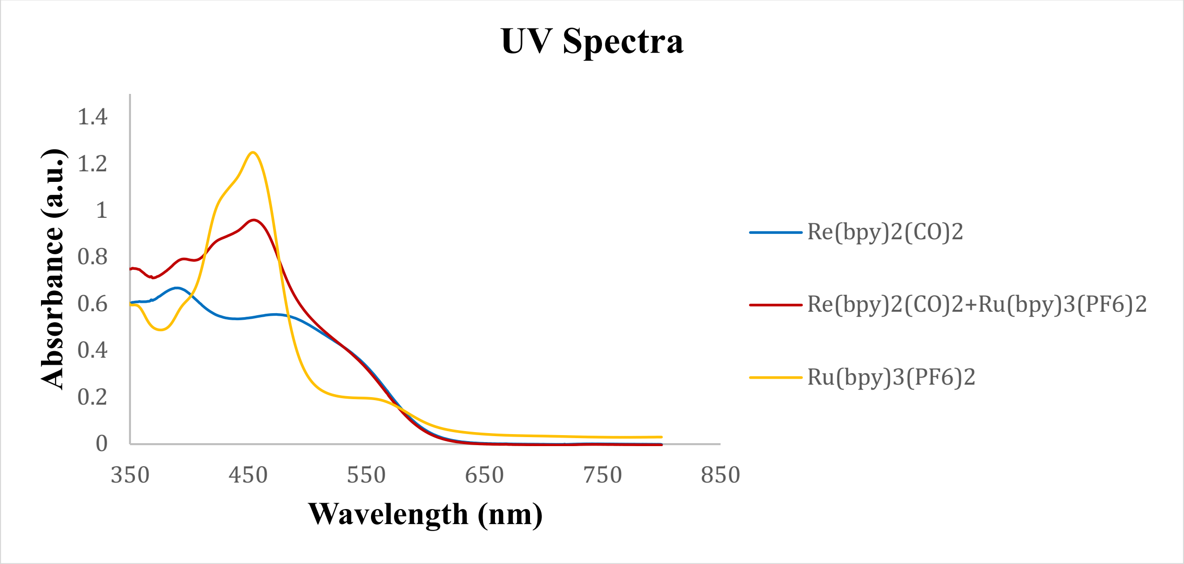

Figure 5.8. Uv-vis spectra in CH_3CN for **1^+OTf^-** (blue), $Ru(bpy)_3(PF_6)_2$ (yellow), and for a solution containing both compounds (red).

5.4. Photocatalytic CO_2 Reduction

The first attempts at photocatalytic reduction of CO_2 were carried out with 4μmol of complex **1^+OTf^-** in dimethylacetamide (DMA) without added photosensitizer using TEOA as the electron donor. Irradiation of this reaction mixture was carried out under an atmosphere of CO_2 with visible light from an LED (405nm, 1050 mW at 700mA, 3.4 x 10^{-8} mol photons/sec) for 24 hr. GC analysis of the reaction headspace revealed no gas phase product formation. The ^1H NMR spectrum of the reaction solution disclosed that the only product was formic acid HCOOH, which was quantified by NMR analysis (Figure 5.9). These observations confirmed that the complex *cis*-$Re(CO)_2(bipy)_2{}^+OTf^-$ was a photoredox catalyst for selective reduction of CO_2 to formic acid. (Table 5.2, Table 5.3). Importantly, blank measurements demonstrated the need of the **ED** (TEOA) and that the unsensitised photocatalytic ability of $Re(CO)_2(bipy)_2{}^+OTf^-$ was very poor in DMF and absent when CH_3CN was used as solvent.

Table 5.2. Summary of results for the photocatalytic CO_2 reduction with the Re complex **1^+OTf^-** in DMF DMA and CH_3CN.
Irradiation with 405 nm light conducted on solution under a CO_2 atmosphere for 24 h. Electron donor used were triethanolamine (TEOA).

Catalyst (µmol)	**$Ru(bpy)_3^{2+}$ (µmol)**	**Solvent**	**e^- donor**	**H_2 (µmol)**	**TON (H_2)**	**HCOOH (µmol)**	**TON (HCOOH)**
4	-	DMA	TEOA	-	-	41	10.25
4	4	DMA	TEOA	6	1.5	208	52
4	-	DMF	TEOA	3	0.75	3	0.75
4	4	DMF	TEOA	11	2.75	202	50
4	-	CH_3CN	TEOA	-		-	
4	4	CH_3CN	TEOA	14	3.5	40	10

Table 5.3. Comparison of the performance parameters for Re complexes that function as combined catalyst and photosensitizer. The top two entries are for the complexes reported in this chapter.

CAT [conc.]	Solvent/ED	PS [conc.]	λ (nm)	Product	TON (time)	Φ%	TOF (hr^{-1})
$[Re(bpy)_2(CO)_2]^+$ [1mM]	**DMA/TEOA**	**-**	**405**	**HCO_2H**	**10 (24h)**	**1.4**	**0.43**
$[Re(bpy)_2(CO)_2]^+$ [0.1mM]	**DMA/TEOA**	**$Ru(bpy)_3^{2+}$ [1mM]**	**405**	**HCO_2H**	**428 (24h)**	**5.8**	**17.8**
$Re(bpy)(CO)_3Cl$ [0.87mM]^{6,18} [0.5mM]^{19}	DMF/TEOA	-	365	CO CO	27 (4h) 15 (25h)	8.7 16	6.75 0.60
$Re(dmb)(CO)_3Cl^{36,(a)}$ [0.05mM]	DMF/TEOA/BNAH	-	365	CO	15 (25h)	-	0.60
$Re(dmb)(CO)_3Cl^{36,(a)}$ [0.05mM]	DMF/TEOA/BNAH	$Ru(dmb)_3^{2+}$ [0.05mM]	480	CO	101 (16h)	6.2	6.3
$Re(Py\text{-}NHC\text{-}PhCF_3)^{26,(b)}$ [0.1mM]	MeCN/TEA/BIH	- $Ir(ppy)_3$	>300	CO	32 (4h) 51 (4h)		8.0 12.8
Re(*N*,*S*-NHC)$^{27,(b)}$ [0.5mM]	DMF/TEOA/BIH	-	≥400 ≥ 480	CO CO	102 (15h) 153 (15h)		6.8 10.2
$[Re(\kappa^2\text{-}PN)(CO)_3Br]^{37,(c)}$ [0.1mM]	DMF/TEOA	$Ru(bpy)_3^{2+}$ [1mM]	405	HCO_2H	343 (24h)	4.7	14.3

(a) dmb = 4,4′-dimethyl-2,2′-bipyridine. (b) structures shown in the indicated references, (c) PN = $(Ph_2P)NH(NC_5H_4)$

Table 5.3 also provides a comparison of selected benchmark Re-based catalysts along with our results for $Re(CO)_2(bipy)_2^+OTf^-$ (**1+OTf-**). It is important to emphasize that care should be taken when comparing the reaction parameters. For example, in Table 1, the turnover frequency (TOF) is provided because it removes the time dependence of the TON and, therefore, allows a more direct comparison of the catalyst activities. since TON is time dependent.

Three key points are notable. First, complex $\mathbf{1^+OTf^-}$ contributes an entirely new geometry to photocatalysis with Re. Second, this compound displayed activity in the absence of an added external photosensitizer which was similar or superior to reported Re(I) catalysts under visible light. Finally, in contrast to all reported Re catalysts, which produce CO as the reduction product, CO_2 reduction with complex $\mathbf{1^+OTf^-}$ led selectively to formic acid productoin.[1138] Clearly, such significant differences in reactivity will have important implications on the catalytic pathway taken by complex $Re(CO)_2(bipy)_2^+$ ($\mathbf{1^+}$).

By adding the common photosensitizer $[Ru(bpy)_3]^{2+}$ to this catalyst system the plan was to take advantage of the longer lived excited state of 1100 ns[39] for this species and to increase the light absorption into the visible region (see Figure 5.8). A similar strategy has been reported using equimolar solutions of $[Ru(dmb)_3]^{2+}$ and $[Re(dmb)(CO)_3Cl]$, (dmb = 4,4′-dimethyl-2,2′-bipyridine).[36] As we anticipated, a significant increase in production of HCO_2H was observed and this was the case across all of the three solvents, DMA, DMF and CH_3CN that were used in this investigation (Tables 5.4 and 5.5). Under these conditions, with added **PS**, other **ED** species were investigate and it was determined that N-benzyl- 1,4-dihydridonicotinamide (BNAH) ascorbic acid and sodium ascorbate and triethylamine gave little or no product.

Table 5.4. Summary of results for the attempted photocatalytic CO_2 reduction using $Re(CO)_2(bipy)^{2+}OTf^-$ (**1^+OTf^-**) examining variation of solvent and electron donor on performance. Irradiation with 405 nm light conducted on a DMF or CH_3CN (5mL) solution under a CO_2 atmosphere for 24 h. Electron donors used were triethanol amine (TEOA), N-benzyl-1,4-dihydridonicotinamide (BNAH), triethylamine (NEt_3), or sodium ascorbate (NaAsc).

Catalyst (mM)	$Ru(bpy)_3^{2+}$ (mM)	Solvent	e^- donor	H_2 (µmol)	HCOOH (µmol)
1	-	DMF	TEOA	3	3
1	1	DMF	-	-	-
1	1	DMF	TEOA	11	202
1	1	DMF	NEt_3	-	-
1	1	DMF	BNAH	-	-
1	1	DMF	AA	-	-
1	1	DMF	NaA	-	-
1	-	CH_3CN	TEOA	-	-
1	1	CH_3CN	TEOA	14	40
1	1	CH_3CN	NEt_3	-	-
1	1	CH_3CN	BNAH	-	-
1	1	CH_3CN	AA	-	-
1	1	CH_3CN	NaA	-	-

Table 5.5. Trends with different concentration of $Re(CO)_2(bipy)^{2+}OTf^-$ (**1^+OTf^-**) for the photocatalytic formation of products. Reaction conditions: **DMA: TEOA** (4:1) 4 mL under CO_2 atmosphere.

Catalyst (mM)	$Ru(bpy)_3^{2+}$ (mM)	H_2 (µmol)	TON (H_2)	HCOOH (µmol)	TON (HCOOH)	Selectivity	HCOOH rate /hr	TOF hr^{-1}
1	-	-	-	41	10.25	1	1.7	0.43
1	1	6	1.5	208	52	0.97	8. 7	2.2
0.5	1	29	14.5	229	114.5	0.89	9.5	4.8
0.2	1	19	23.75	220	275	0.92	9.2	11.5
0.1	1	15	37.5	171	427.5	0.92	7.1	17.8
0.05	1	10	50	107	535	0.91	4.5	22.3
0.02	1	18	225	118	1475	0.87	4.9	61.5
0.01	1	15	375	110	2750	0.88	4.6	114.6

Table 5.5 shows an interesting effect on TON as the concentration of catalyst is varied. A similar effect has been noted in the other systems. For example, in mixed solutions of $[(dmb)Re(CO)_3Cl]$ (CAT) and $[Ru(dmb)_3]^{2+}$ (PS) an increase in the concentration of $[(dmb)Re(CO)_3Cl]$ caused a decrease in TON_{CO}. This effect can be

attributed to the fact that the catalyst cycle depends on the electron transfer cycle to be effective (see Chapter 3, Section 3.3). Essentially, if the concentration of catalyst exceeds the capacity of the electron transfer steps from the reduced PS, the electron transfer cycle limits the TON and reaction rate.

As shown in Figure 5.9, the catalyst reaction rates gave similar behavior to the catalyst reaction rates of Ru catalysts that were presented in Chapter 3. The catalyst reaction rates are increased with the increase of the [cat]. However, this increase is limited as the electron source becomes rate determining.

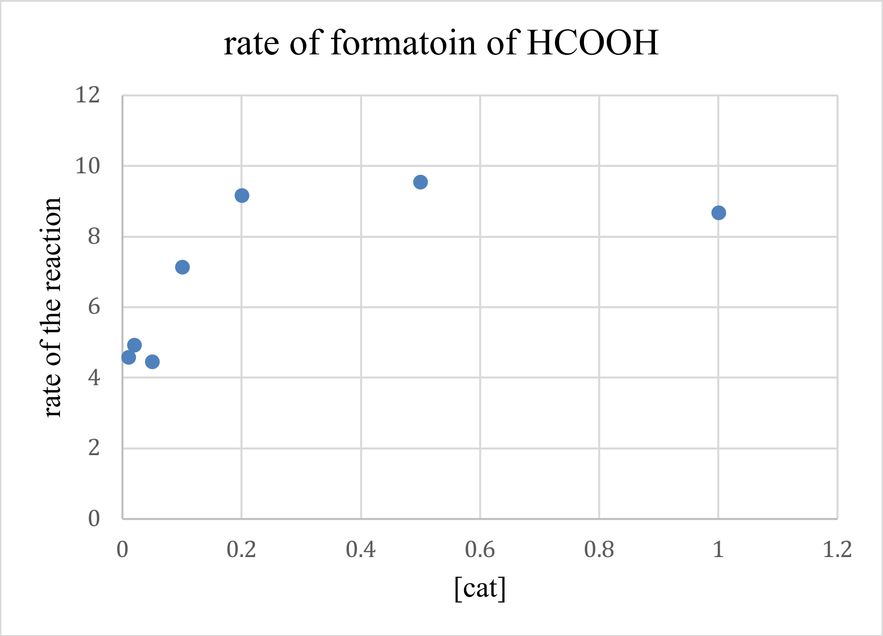

Figure 5.9. A plot of reaction rate for the formation of formic acid versus concentration of catalyst *cis*-$Re(CO)_2(bipy)_2{}^{+}OTf^{-}$. Reaction conditions: DMA: TEOA (4:1) 4 mL; the catalyst *cis*-$Re(CO)_2(bipy)_2{}^{+}OTf^{-}$ and the photosensitizer $[Ru(bpy)_3]^{2+}$ (1 µmol) under CO_2 atmosphere.

In order to confirm that photocatalytic CO_2 reduction is the source of formic acid, a ^{13}C tracer experiment was carried out for the photoreaction with **1^+OTf$^-$**, $Ru(bpy)_3^{2+}$, and TEOA in DMF under a $^{13}CO_2$ atmosphere. HRMS analysis of the reaction headspace clearly documented selective formation of $H^{13}CO_2H$ (Figure 5.10). Furthermore, the NMR data (shown in Figure 5.11 and Figures 5.12) gives conclusive evidence that the formic acid observed in these experiments arose from CO_2 reduction and further highlight the significant switch in product selectivity that contrasts with the reported production of CO from all other Re α-dimmine species. [38,11]

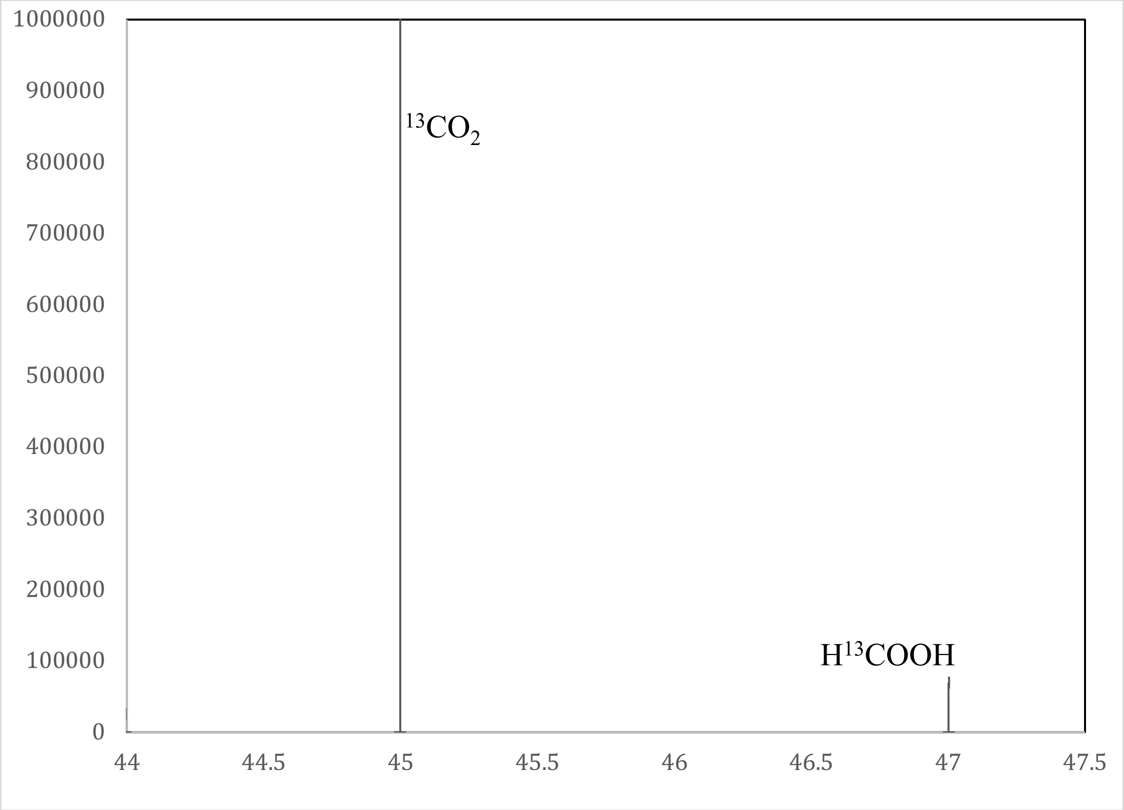

Figure 5.10. High resolution MS of the head space of a photocatalytic reduction experiment in DMF using $^{13}CO_2$ with complex **1, [**$Re(bpy)_2(CO)_2]^+OTf^-$ (**Rubpy**) as photosensitizer and TEOA as the electron donor. Mass peaks for $H^{13}CO_2H$, $^{13}CO_2$ are indicated.

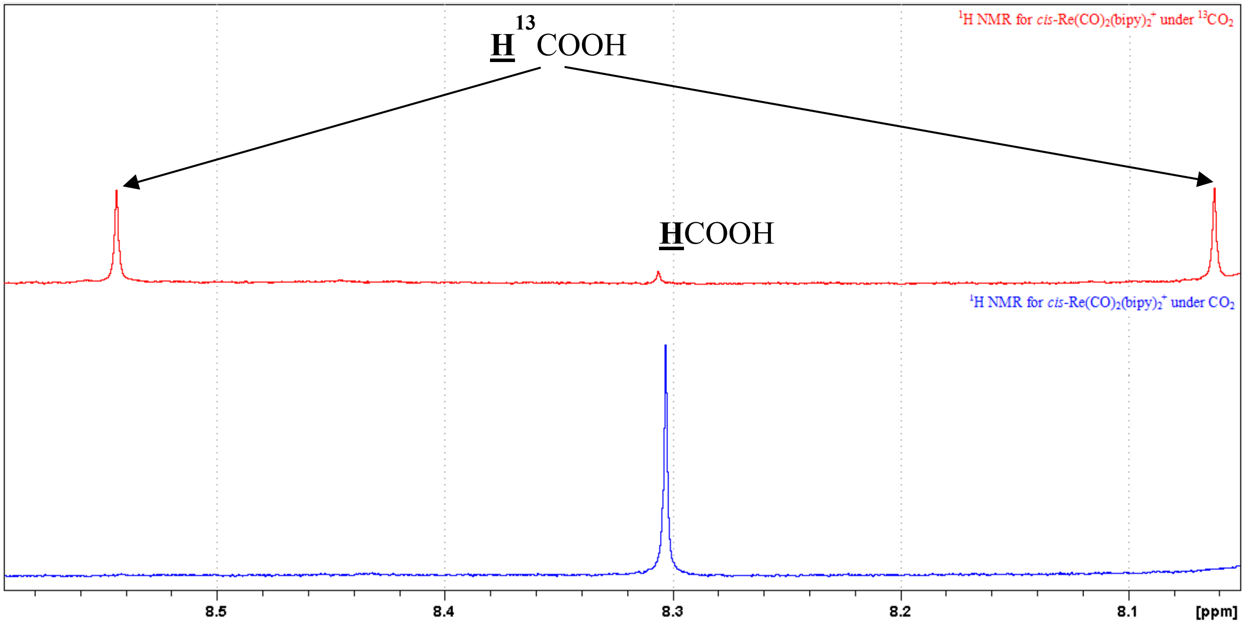

Figure 5.11. ^{1}H NMR spectra for the formyl HOOC-**H** proton of formic acid obtained from photocatalytic reduction of CO_2 using *cis*-Re(CO)$_2$(bipy)$_2^+$OTf$^-$ as the catalyst. The bottom spectrum was from reaction using unlabeled CO_2 and the top spectrum is from a reaction with labeled $^{13}CO_2$.

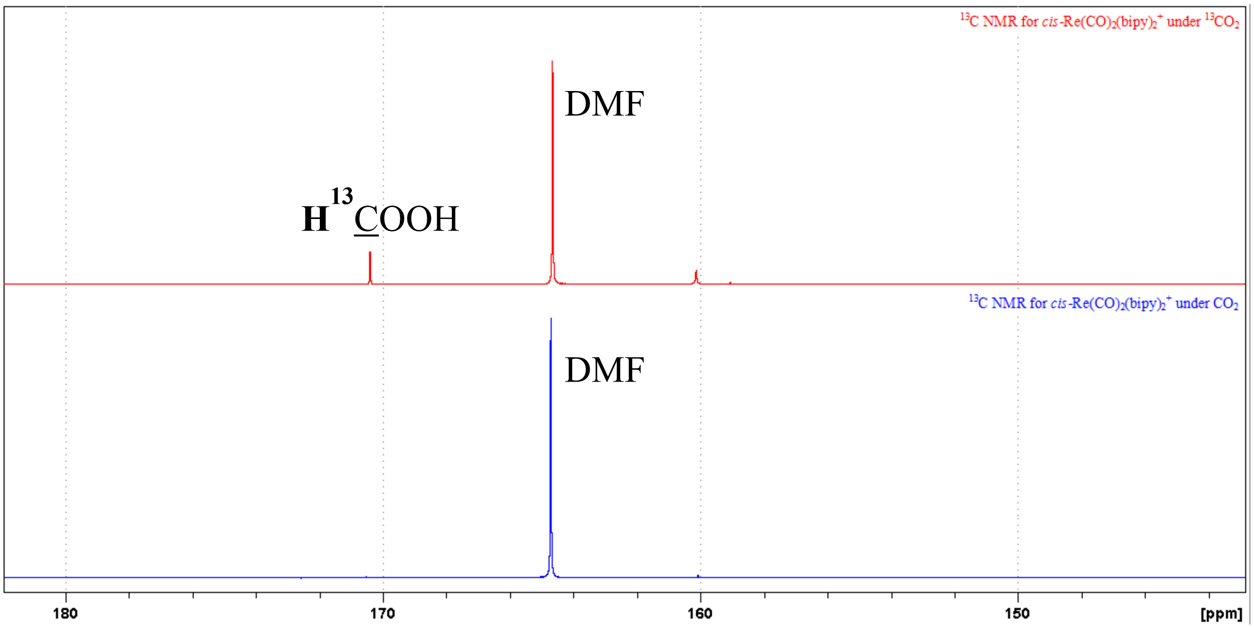

Figure 5.12. ^{13}C NMR spectra in D_2O for the photocatalytic reduction of CO_2 (bottom) and $^{13}CO_2$ (top) to produce formic acid from *cis*-Re(CO)$_2$(bipy)$_2^+$ OTf$^-$ as the catalyst.

The time profiles in Figure 5.13 shows the increase of the HCO_2H formation with the time, and that indicates the stability and the activity of the catalyst during the photocatalytic CO_2 reduction reaction.

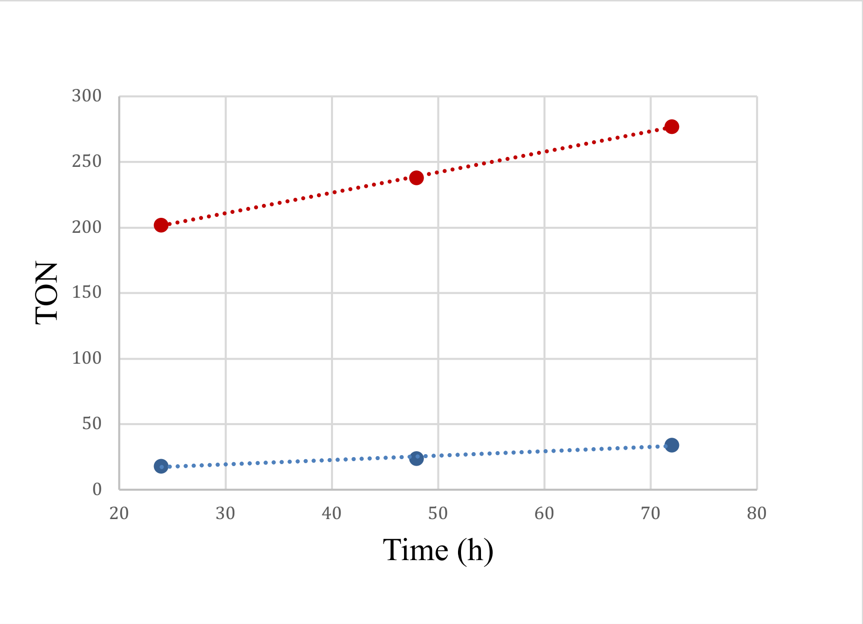

Figure 5.13. Time profile for the photocatalytic formation of the products that are H_2 (blue) and HCOOH (red) with the turnover number (TON). Reaction conditions: DMF: TEOA (4:1) 4 mL; the catalyst *cis*-$Re(CO)_2(bipy)_2^+OTf^-$ (1 µmol); and the photosensitizer $[Ru(bpy)_3]^{2+}$ (1 µmol) under CO_2 atmosphere.

Photoreduction catalysis consists of coupled electron production cycle with a catalysis cycle.[28,30,40] The electron production cycle provides the electrons to the catalyst. In the case of an integrated catalyst/photosensitizer, like 1^+OTf-, the electrons come directly from the ED while in the case of an added photosensitizer, the electrons are generally produced from a reduced photosensitizer (PS^-). The catalytic cycle represents the steps where, in this case, the Re complex, 1^+, catalytically reduces CO_2 using these supplied electrons. The proposed catalytic mechanism for HCO_2H production from the CO_2 photoreduction using complexes 1^+ is presented in Figure 5.14.

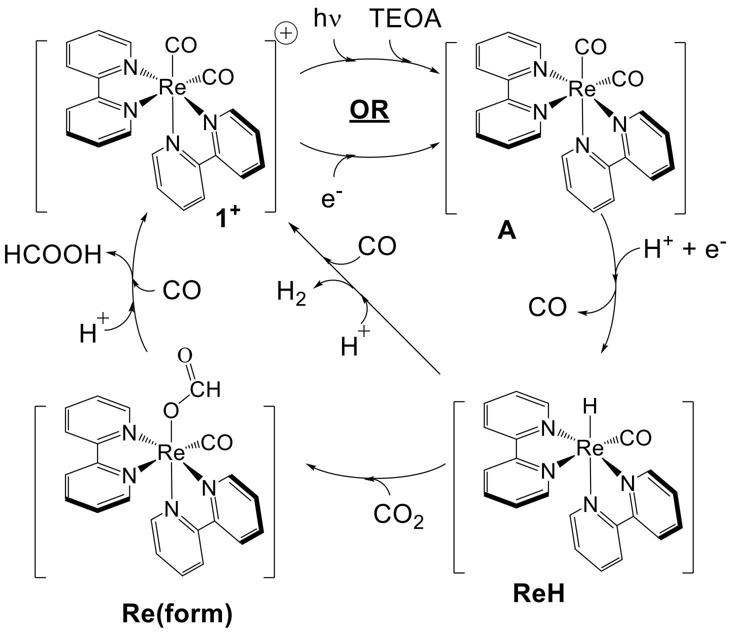

Figure 5.14. The proposed mechanism for the *cis*-Re(CO)$_2$(bipy)$_2^+$ catalyst.

Entry into the catalysis cycle comes from the reduction of **1**$^+$. Addition of a proton and a second electron yields the hydride complex, [Re(bpy)$_2$(CO)H] (**ReH**). Generally, the route to successful transformation of CO$_2$ to formate is envisioned to proceed through a transition metal hydride intermediate that can insert CO$_2$ leading to a metallacarboxylic acid complex.[41,42] The insertion of CO$_2$ into the Re-H complex yielded the metallacarboxylic acid species **Re(form).** The cycle closes with the liberation of formic acid and trapping by CO (or solvent), which through reduction and proton transfer releases formic acid and regenerates **1**$^+$.

The protonation of **ReH** also provides a path for the formation of H$_2$. The protonation of the hydride intermediate, offers an alternate catalytic cycle that bypasses formic acid production. In practice, protonation of the hydride intermediate is a reaction that is difficult to avoid, and this implies that choice of reaction medium (specifically the pKa of any protons available) will influence H_2 formation.

This proposed mechanism using *cis*-$Re(CO)_2(bipy)_2^+$ is reminiscent of the currently accepted mechanism for conversion of CO_2 using the isoelectronic ruthenium (II) complex $[Ru(bpy)_2(CO)_2]^{2+}$. [30] For the structure of the intermediate **ReH**, three different structures were envisioned which are shown in Figure 5.15. Each of these was computationally optimized using DFT with the B3LYP functional and def2TZVP basis set. The energies for the formation of these computed species are shown. The lowest energy option is the one shown in the proposed mechanism.

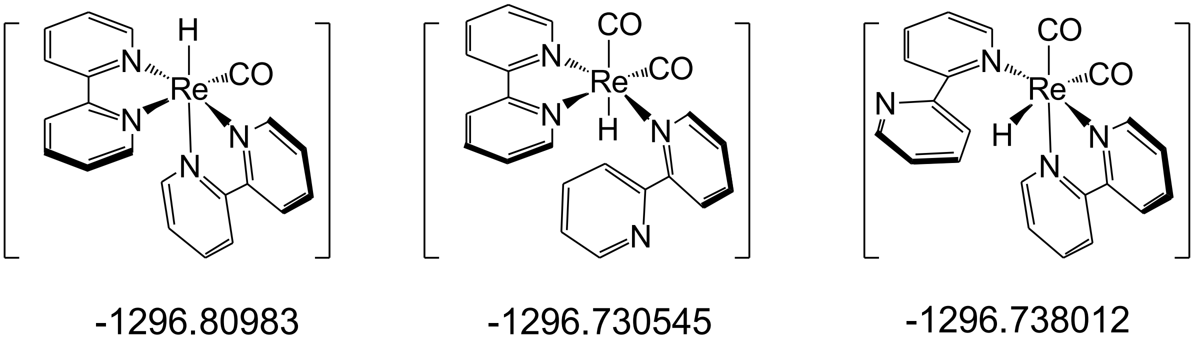

Figure 5.15. The three possible protonation products to yield **ReH**. The energies associated with each of these possibilities is indicated in Hartrees.

Infrared Spectroelectrochemistry (IR-SEC) of the complex *cis*-Re(CO)$_2$(bipy)$_2$$^+OTf^-$ was performed in acetonitrile (CH$_3$CN) with 0.1 M tetrabutylammonium hexafluorophosphate (TBAPF$_6$) under N$_2$ in order to characterize the electroactive species and to observe and monitor the changes in the solution of the complex. At resting potential two IR-active carbonyl stretches were observed for the complex *cis*-Re(CO)$_2$(bipy)$_2$$^+OTf^-$ at 1920 and 1850 cm^{-1}, consistent with the dicarbonyl groups. When voltage was applied at the potential of the one-electron reduction (−1 V), the both peaks had been shifted. One of the peak shifted to about 1880 cm^{-1} and other to about 1820 cm^{-1}, so they both shifted to lower wavenumber. In addition, when the voltage was applied at more negative potential (−1.8 V) in the electrochemistry, these original ν_{CO} stretches at 1920 and 1850 cm^{-1} moved to lower wavenumber. One moved to 1830 cm^{-1}. These results indicate that the pathway of the complex for CO$_2$ reduction is metal center. The metal-carbonyl bands are show below in Figure 5.16.

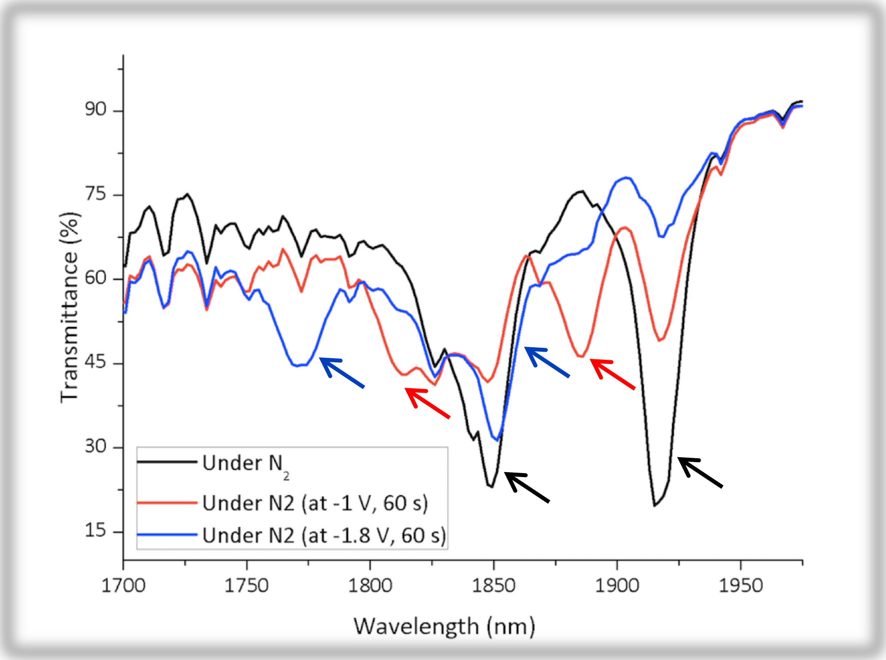

Figure 5.16. IR-SEC spectra under N$_2$ saturation of *cis*-Re(CO)$_2$(bipy)$_2$$^+OTf^-$. Conditions: 0.1 M TBAPF$_6$/CH$_3$CN; glassy carbon working electrode, Pt counter electrode, Ag pseudoreference electrode.

5.5. Conclusions

This chapter has described the successful synthesis of the bis(bpy)dicarbonyl complexes, and their ability for the photocatalytic CO_2 reduction. The Re(I) complex, *cis*-$Re(CO)_2(bipy)_2^+OTf^-$, was synthesized, characterized, and showed promising results in photocatalytic CO_2 reduction applications due to their long-lived excited-state lifetimes. In the future work, different di-carbonyl species with different-ligand coordination spheres can be synthesized, characterized, and examined for the photocatalytic CO_2 reduction applications.

For future work, other ligands should be tried with Re and compared to *cis*-$Re(CO)_2(bipy)_2^+OTf^-$ catalyst. For example, our phendione and dppz ligands should be tried to see if the increasing in the conjugated π system will have a big effect in the ability of the photocatalytic CO_2 reduction. In addition, the Mn analogous to the Re catalyst should be tried and examined for CO_2 reduction.

5.6. Reference

1 K. Sordakis, C. Tang, L. K. Vogt, H. Junge, P. J. Dyson, M. Beller and G. Laurenczy, *Chem. Rev.*, 2018, **118**, 372–433.

2 H. Zhong, M. Iguchi, M. Chatterjee, Y. Himeda, Q. Xu and H. Kawanami, *Adv. Sustain. Syst.*, 2018, **1700161**, 1700161.

3 J. L. Inglis, B. J. MacLean, M. T. Pryce and J. G. Vos, *Coord. Chem. Rev.*, 2012, **256**, 2571–2600.

4 C. Costentin, M. Robert and J.-M. Savéant, *Chem. Soc. Rev.*, 2013, **42**, 2423–36.

5 J. Schneider, H. Jia, J. T. Muckerman and E. Fujita, *Chem. Soc. Rev.*, 2012, **41**, 2036.

6 J. Hawecker, J. Lehn and R. Ziessel, *Helv. Chim. Acta*, 1986, **69**, 1990–2012.

7 J. Hawecker, J.-M. Lehn and R. Ziessel, *J. Chem. Soc. Chem. Commun.*, 1984, **984**, 328.

8 P. L. Cheung, C. W. Machan, A. Y. S. Malkhasian, J. Agarwal and C. P. Kubiak, *Inorg. Chem.*, 2016, **55**, 3192–3198.

9 J. X. Zhang, C. Y. Hu, W. Wang, H. Wang and Z. Y. Bian, *Appl. Catal. A Gen.*, 2016, **522**, 145–151.

10 H. Fei, M. D. Sampson, Y. Lee, C. P. Kubiak and S. M. Cohen, *Inorg. Chem.*, 2015, **54**, 6821–6828.

11 J. Rohacova and O. Ishitani, *Chem. Sci.*, 2016, **7**, 6728–6739.

12 S. Meister, R. O. Reithmeier, M. Tschurl, U. Heiz and B. Rieger, *ChemCatChem*, 2015, **7**, 690–697.

13 M. Bourrez, F. Molton, S. Chardon-Noblat and A. Deronzier, *Angew. Chem. Int. Ed. Engl.*, 2011, **50**, 9903–9906.

14 M. Bourrez, M. Orio, F. Molton, H. Vezin, C. Duboc, A. Deronzier and S. Chardon-

Noblat, *Angew. Chemie - Int. Ed.*, 2014, **53**, 240–243.

15 H. Takeda, H. Koizumi, K. Okamoto and O. Ishitani, *Chem. Commun.*, 2014, **50**, 1491–3.

16 M. D. Sampson and C. P. Kubiak, *J. Am. Chem. Soc.*, 2016, **138**, 1386–1393.

17 S. K. Lee, M. Kondo, M. Okamura, T. Enomoto, G. Nakamura and S. Masaoka, *J. Am. Chem. Soc.*, 2018, **140**, 16899–16903.

18 J. Hawecker, J. Lehn and R. Ziessel, *J. Chem. Soc. Chem. Commun.*, 1983, 536–538.

19 H. Takeda, K. Koike, H. Inoue and O. Ishitani, *J. Am. Chem. Soc.*, 2008, **130**, 2023–2031.

20 P. Kurz, B. Probst, B. Spingler and R. Alberto, *Eur. J. Inorg. Chem.*, 2006, **2006**, 2966–2974.

21 H. Rao, J. Bonin and M. Robert, *Chem. Commun.*, 2017, **53**, 2830–2833.

22 J. Bonin, M. Chaussemier, M. Robert and M. Routier, *ChemCatChem*, 2014, **6**, 3200–3207.

23 D. Behar, T. Dhanasekaran, P. Neta, C. M. Hosten, D. Ejeh, P. Hambright and E. Fujita, *J. Phys. Chem. A*, 1998, **102**, 2870–2877.

24 S. Sato, T. Morikawa, T. Kajino and O. Ishitani, *Angew. Chemie - Int. Ed.*, 2013, **52**, 988–992.

25 Y. J. Yuan, Z. T. Yu, X. Y. Chen, J. Y. Zhang and Z. G. Zou, *Chem. - A Eur. J.*, 2011, **17**, 12891–12895.

26 A. J. Huckaba, E. A. Sharpe and J. H. Delcamp, *Inorg. Chem.*, 2016, **55**, 682–690.

27 A. Maurin, C. Ng, L. Chen, T. Lau, M. Robert and C. Ko, *Dalton Trans.*, 2016, **45**, 14524–14529.

28 Y. Kuramochi, J. Itabashi, K. Fukaya, A. Enomoto, M. Yoshida and H. Ishida, *Chem. Sci.*, 2015, **6**, 3063–3074.

29 K. Sekizawa, K. Maeda, K. Domen, K. Koike and O. Ishitani, *J. Am. Chem. Soc.*, 2013, **135**, 4596–4599.

30 Y. Kuramochi, O. Ishitani and H. Ishida, *Coord. Chem. Rev.*, 2018, **373**, 333–356.

31 H. Ishida, T. Terada, K. Tanaka and T. Tanaka, *Inorg. Chem.*, 1990, **29**, 905–911.

32 J. M. Lehn and R. Ziessel, *J. Organomet. Chem.*, 1990, **382**, 157–173.

33 P. Voyame, K. E. Toghill, M. A. Méndez and H. H. Girault, *Inorg. Chem.*, 2013, **52**, 10949–10957.

34 Y. Kuramochi, M. Kamiya and H. Ishida, *Inorg. Chem.*, 2014, **53**, 3326–3332.

35 J. L. Smithback, J. B. Helms, E. Schutte, S. M. Woessner and B. P. Sullivan, *Inorg. Chem.*, 2006, **45**, 2163–74.

36 B. Gholamkhass, H. Mametsuka, K. Koike, T. Tanabe, M. Furue and O. Ishitani, *Inorg. Chem.*, 2005, **44**, 2326–2336.

37 Y. Hameed, B. Gabidullin and D. Richeson, *Inorg. Chem.*, 2018, **57**, 13092–13096.

38 Y. Yamazaki, H. Takeda and O. Ishitani, *J. Photochem. Photobiol. C Photochem. Rev.*, 2015, **25**, 106–137.

39 C. K. Prier, D. A. Rankic and D. W. C. Macmillan, *Chem. Rev.*, 2013, **113**, 5333–5363.

40 Y. Kuramochi, J. Itabashi, M. Toyama and H. Ishida, *ChemPhotoChem*, 2018, **2**, 314–322.

41 A. Taheri and L. A. Berben, *Chem. Commun.*, 2016, 1768–1777.

42 J. R. Pugh, M. R. M. Bruce, B. P. Sullivan and T. J. Meyer, *Inorg. Chem.*, 1991, **30**, 86–91.

Chapter 6: Dimers, Monomers and Pentacoordination in a Series of Earth-Abundant Transition Metal Dibromido Complexes Supported by a Neutral SNS Ligand Framework and their Applications in the Catalysis.

The work for this chapter formed an important component of the following publication:

(Y. Hameed, S. Ouanounou, T. Jurca, B. Gabidullin, I. Korobkov, and D. S Richeson, Polyhedron, 2018, 154, 252-258. DOI:10.1016/j.poly.2018.07.033.)

Pincer-type architectures represent an important class of ligand frameworks for the design and synthesis of transition metal coordination complexes and catalysts. In this chapter, the first systematic application of bis(thioether)pyridine "SNS" ligands in coordination chemistry of first-row transition-metal bromides and the first structurally characterized "SNS" complexes of Mn and Fe are reported. The complexes were characterized by single crystal X-ray analysis, UV-vis and FTIR spectroscopy, mass-spectrometry, elemental analysis, and where appropriate by Evans method. Analysis of the resulting complexes reveals a set of monomeric and dinuclear species, whose coordination mode is associated with a delicate balance of structural features arising from the metal's d-orbital occupancy and the steric load of the ligand. Dimerization of the solid-state structure appears to be primarily favored through lower steric load from the ligand and lower metal d-electron count. The catalytic behavior of these complexes was examined for the CO_2 reduction and also for H_2 production from H_2O.

The synthesis and characterization of the complexes were performed in approximately equal contributions by Y. Hameed, S. Ouanounou, and T. Jurca. The organization and analysis of the structural trends was done by T. Jurca, Y. Hameed and D. Richeson. The catalytic behavior of the complexes was examined by Y. Hameed. The crystallographic data collection and analyses were carried out by B. Gabidullin. and I. Korobkov.

6.1. Introduction

The advancement of inorganic and organometallic chemistry has been intimately linked with the continued development of supporting ligand chemistry. Among the sizable classes of ligands employed in support of transition metals, pincer-type architectures represent a large category with long-standing importance.[1–6] Such species are characterized by tridentate coordination that bind to metals in a planar, meridional mode. These ligands have been tailored to provide rigidity and stability in their metal complexes and can be rationally designed and constructed to organize the reaction pocket on a metal center thereby enabling enhanced control of the reaction pathways and products upon catalytic application.[7–9] The prototypical pincer ligand has an anionic central group (e.g. aryl ring), that is σ-bonded to the metal, with flanking neutral donors that link to the metal via chelate rings. The most well-developed versions of this framework have been bis(phosphine) and bis(amine) derivatives linked to an aryl core through methylene units. Encompassed within the pincer family are ligands where the central bonding group has been replaced with various neutral donors and the pyridyl function is one of the most common.

The recent reports for the use of "PN_3P" ligands for isolation of novel metal complexes and applications in catalysis prompted our consideration of pincers with other donor arms.[10–13] In particular, we were interested in bis(thioether) ligands displaying an "SNS" coordination array. While the first complexes with these ligands were reported for Cu(II) in 1976,[14] this framework, particularly for earth-abundant metals, has received less and more sporadic attention compared to similar pincer donor arrays. To date, pyridyl-centered, bis(thioether) SNS complexes have been reported for the first row metals from

Fe to Zn[14,15,24,25,16–23] and for some of the heavier congeners of these metals.[26,27,36–44,28–35] A nascent interest in ligands with thioether centers has been stimulated by a report that related thioether ligands form well-defined ethylene trimerization catalysts with Cr(III)[45] as well as the potential for hemilabile bonding,[46] between the coordinated metal center and the hard nitrogen donor and soft sulfur donor atoms.[47,48] For example, a Ni(II) complex bearing a bis(2-pyridylmethyl)-1,2-ethanedithiol ligand was designed as an effective photocatalyst for CO_2 reduction.[49] The application of bis(thioether)pyridine SNS ligands in molecular transformations and catalysis is beginning to be revealed. In addition to stoichiometric reactions,[30–32] there have been investigations of catalytic transformations that have included oxidation reactions,[16] C-S coupling reactions,[18] and catalyzed formation of cyclic carbonates from CO_2 and epoxides.[50] Revealing the fundamental coordination behavior of these ligands with earth-abundant metal complexes provides a broader basis for researchers to more rationally utilize such species. Herein, we report a series of divalent first row transition metal complexes of the simple archetypal neutral SNS pincer, 2,6-$(CH_3SCH_2)_2C_5H_3N$. This series of earth-abundant metals yielded new complexes with the empirical formulae $M(\kappa^3\text{-}2,6\text{-}(CH_3SCH_2)_2C_5H_3N)Br_2$ (M = Mn, Fe, Co, Ni, Cu, Zn) displaying tridentate ligand coordination and a range of five- and six-coordinate species. The purpose was to initiate an exploration of stability of these species and to reveal structural variation in a systematic way that is necessary in order to explore synthetic chemistry and potential in catalysis.

6.2. Results and Discussion

The bis(methylthioether)pyridine ligand, 2,6-$(CH_3SCH_2)_2NC_5H_3$, was synthesized, beginning with bis(chloromethyl)pyridine and NaSMe, according to published procedures.[28] Using a 1:1 stoichiometric ratio of ligand:MBr_2, a direct, heterogeneous, room temperature reaction proceeded in toluene as indicated by color changes to the reaction mixture. Allowing the reactions to continue overnight provided optimal yields. The precipitation of the product solids was facilitated by cooling the reaction mixtures to -20°C and leaving overnight. The solids were then isolated by filtration and washed with hexanes to remove impurities. These reactions proceeded in near quantitative yields for the dibromides of Mn, Fe, Co and Zn, in an excellent, 84% yield in the case of Cu and a slightly lower yield of 64% for the Ni complex as summarized in Scheme 6.1.

SCHEME 1

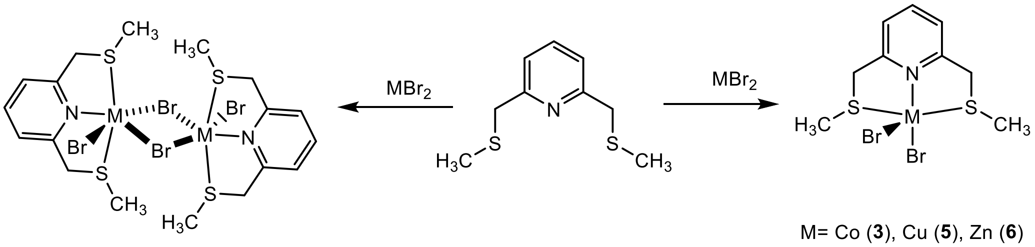

M= Co (**3**), Cu (**5**), Zn (**6**)

M=Mn (**1**), Fe (**2**), Ni (**4**)

Scheme 6.1. Summary of reaction products.

The only diamagnetic complex of this series was the Zn complex **6** and the ^1H and ^{13}C NMR spectra indicated the coordinated ligand. Mass spectrometery was useful to confirm the basic formulae of **1-6** as was the microanalysis of the products **1-6**, which was consistent with the expected formulae of $[M(\kappa^3\text{-}2,6\text{-}\{CH_3SCH_2\}_2NC_5H_3)Br_2]_n$.

Of these compounds only **4** has been previously reported as a green, dinuclear, pseudo-octahedral Ni(II) species assembled through Br bridges as represented in Scheme 6.1.[19] In fact, there are no reported Mn complexes of this SNS family of ligands and the sole related Fe complex, $FeCl_2(2,6\text{-}\{^tBuSCH_2\}_2NC_5H_3)$, was only characterized by IR spectroscopy and microanalysis.[15] Structures of first row transition metal complexes of this family of bis(thioether)pyridine ligands are limited and only scattered examples of divalent Co, Ni, Cu and Zn compounds have been structurally characterized. In order to determine the detailed structures and probe the level of aggregation for the remaining five complexes we carried out single crystal X-ray analyses on complexes **1-3**, **5** and **6**.

The Mn and Fe complexes, **1** and **2**, represent the first reported structures of complexes for either of these metal centers of the general family of bis(thioether)pyridine, $2,6\text{-}\{RSCH_2\}_2NC_5H_3$, ligands. Compounds **1** and **2** crystallized with nearly identical crystallographic parameters as shown in Table 6.1. The structural diagrams of these two compounds are presented in Figures 6.1 and 6.2 with selected bond distances and angles in Table 6.2.

Both complexes **1** and **2** were bimetallic species $[M(\kappa^3\text{-}2,6\text{-}\{CH_3SCH_2\}_2NC_5H_3)Br_2]_2$ (M = Mn or Fe) with the metal centers in pseudo-octahedral coordination environments comprised by a tridentate, meridionally coordinated $2,6\text{-}\{CH_3SCH_2\}_2NC_5H_3$ ligand, two bridging bromo ligands and a third terminal Br group. The largest distortions from ideal octahedral angles were observed for the ligand bite angles for N_{py}-M-S that range from 77.04(15)° to 80.36(5)°. These dinuclear structures are consistent with the observed magnetic moments, which indicated antiferromagnetically coupled high spin metal centers. While there are no reported structures for Mn or Fe complexes of bis(thioether)pyridine there is a single related dinuclear Co(II) complex, $[Co(\kappa^3\text{-}2,6\text{-}\{CH_3SCH_2\}_2NC_5H_3)Cl_2]_2$[16], and only two structurally characterized Ni(II) analogues, $[Ni(\kappa^3\text{-}2,6\text{-}\{^iBuSCH_2\}_2NC_5H_3)Cl_2]_2$[18] and $[Ni(\kappa^3\text{-}2,6\text{-}\{BnSCH_2\}_2NC_5H_3)Br_2]_2$[21], all three of which display parallel structural features to **1** and **2**. In particular the metal coordination environment, the geometry, ligand array, bite angle are analogous of the structure obtained for **1** and **2**. The green Ni complex [Ni(κ^3-2,6-{CH_3SCH_2}$_2NC_5H_3$)Br_2]$_2$ (**4**) has also been reported to have an analogous dinuclear structure with bromo bridged octahedral Ni(II) centers.[19] Interestingly, the reports of these dinuclear Co and Ni complexes also report the observation of related mononuclear five coordinate species whose appearance depends on either changes to the S-R groups of the SNS ligand or on the identity of the metal-halide. For example, in the case of the four reported structures for [Co(κ^3-2,6-{$RSCH_2$}$_2NC_5H_3$)Cl_2]$_2$ only R= Me is dinuclear while the complexes with R = Et, ^{n}Bu or Ph were characterized as mononuclear trigonal bipyramidal species.[16] Similarly, for the reported Ni(II) structures, [Ni(κ^3-2,6-{$RSCH_2$}$_2NC_5H_3$)X_2]$_n$, for X = Cl and R = ^{i}Bu or X = Br and R = Bn the structures are dimeric and the bromo bridged species displayed a magnetic moment of 3.30μ_B consistent with antiferromagnetically coupled high-spin Ni(II) centers.[18,21] In contrast, with X = Cl and R = ^{t}Bu a monomeric trigonal bipyramidal structure was obtained[18] but with X = Br and R = Ph, the mononuclear complex was better classified as square pyramidal. [19]

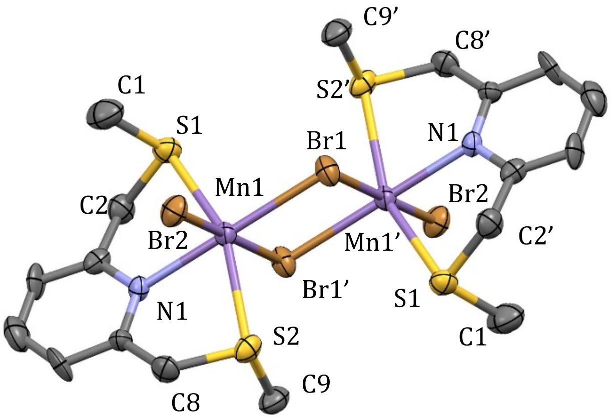

Figure 6.1. Structural representation of [Mn(κ^3-2,6-{CH_3SCH_2}$_2NC_5H_3$)Br_2]$_2$ (**1**) obtained from X-ray analysis. Hydrogen atoms are omitted for clarity. Thermal ellipsoids are shown at 60% probability.

These observations, that rather subtle changes to S-substituents and/or halo ligands can lead to changes from dinuclear to mononuclear species, prompted a closer scrutiny of the structures of **1** and **2**. In fact, this examination supports an alternative structural interpretation of these species as “dimerized” square-based pyramidal (*sp*), five coordinate complexes. Substantiation for this description comes from the M-Br_{bridge} bonding parameters. Specifically in the case of **1**, the Mn1-Br2 and Mn1-Br1 distances are quite similar at 2.6072(13)Å and 2.5983(13)Å (average = 2.602Å) while the Mn-Br1’ distance is considerably longer at 2.7463(13)Å. With this analysis, the structure of the Mn centers in **1** is *sp* with an apical Br2 center and a more weakly coordinated Br1’ in the “open” *trans* position. Satisfyingly, a similar description is consistent with the structure of the Fe complex **2**. Again the Fe1-Br2 and Fe1-Br1 distances are essentially identical at 2.5669(4)Å and 2.5720(4)Å with a longer coordinated Fe-Br1’ interaction at 2.7104(4)Å. Once again, this is consistent with an *sp* Fe(II) center, an apical Br2 ligand and an associated Br1’ donor. Although limited, literature precedent for coordination of an external solvent, in this case isopropanol, to a related Ni complex is provided by the structural report for [Ni{κ^3-2,6-(^{t}BuSCH$_2$)$_2$NC$_5$H$_3$N}Cl$_2$(^{i}PrOH)].[18]

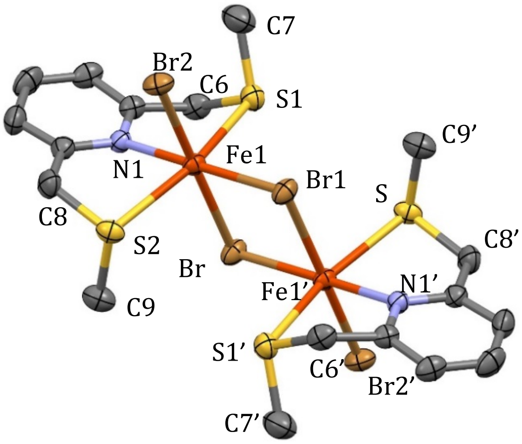

Figure 6.2. Structural representation of [Fe(κ^3-2,6-{CH$_3$SCH$_2$}$_2$NC$_5$H$_3$)Br$_2$]$_2$ (**2**), obtained from X-ray analysis. Hydrogen atoms are omitted for clarity. Thermal ellipsoids are shown at 60% probability.

Table 6.1. Summary of data collection and crystallographic parameters for $[M(\kappa^3\text{-}2,6\text{-}\{CH_3SCH_2\}_2NC_6H_3)Br_2]_2$, compounds **1**, M = Mn, and **2**, M = Fe.

Compound	$[Mn(\kappa^3\text{-}2,6\text{-}\{CH_3SCH_2\}_2NC_6H_3)Br_2]_2$ (**1**)	$[Fe(\kappa^3\text{-}2,6\text{-}\{CH_3SCH_2\}_2NC_6H_3)Br_2]_2$ (**2**)
Empirical formula	$C_{18}H_{26}Br_4Mn_2N_2S_4$	$C_{18}H_{26}Br_4Fe_2N_2S_4$
Formula weight	828.17	829.99
Temperature, K	201(2)	200(2)
λ, Å	0.71073	0.71073
Crystal system	Triclinic	Triclinic
Space group	$P\bar{1}$	$P\bar{1}$
a, Å	7.8407(10)	7.7977(2)
b, Å	8.5380(12)	8.4575(3)
c, Å	11.3830(14)	11.2743(4)
α, °	98.150(7)	98.693(2)
β, °	102.558(7)	102.694(2)
γ, °	110.828(6)	110.110(2)
V, $Å^3$	674.84(16)	659.95(4)
Z	1	1
ρ_{calc}, Mg/m^3	2.038	2.088
μ, mm^{-1}	7.177	7.481
Abs. correction	Semi-empirical from equivalents	
R_1[a]	0.0522	0.0247
wR_2[b]	0.0660	0.0568

[a] $R_1 = \sum||F_o| - |F_c||/\sum|F_o|$, [b] $wR_2 = \{\sum[w(F_o^2 - F_c^2)^2]/\sum[w(F_o^2)^2]\}^{1/2}$

Table 6.2. Selected bond distances (Å) and angles (deg) for compounds **1, 2.**

1		**2**	
Mn(1)-N(1)	2.263(5)	Fe(1)-N(1)	2.1811(19)
Mn(1)-S(1)	2.630(2)	Fe(1)-S(1)	2.5196(7)
Mn(1)-S(2)	2.649(2)	Fe(1)-S(2)	2.5691(7)
Mn(1)-Br(1)	2.6072(13)	Fe(1)-Br(1)	2.5669(4)
Mn(1)-Br(2)	2.5983(13)	Fe(1)-Br(2)	2.5720(4)
Mn(1)-Br(1)’	2.7463(13)	Fe(1)-Br(1)’	2.7104(4)
N(1)-Mn(1)-S(1)	77.04(15)	N(1)-Fe(1)-S(1)	79.11(5)
N(1)-Mn(1)-S(2)	78.35(14)	N(1)-Fe(1)-S(2)	80.36(5)
N(1)-Mn(1)-Br(1)	175.96(13)	N(1)-Fe(1)-Br(1)	176.64(5)
N(1)-Mn(1)-Br(2)	91.08(12)	N(1)-Fe(1)-Br(2)	91.55(5)
N(1)-Mn(1)-Br(1)’	89.88(12)	N(1)-Fe(1)-Br(1)’	90.87(5)
S(1)-Mn(1)-Br(1)	104.65(6)	S(1)-Fe(1)-Br(1)	103.350(19)
S(1)-Mn(1)-Br(1)’	91.32(5)	S(1)-Fe(1)-Br(1)’	91.852(19)
S(1)-Mn(1)-Br(2)	86.96(5)	S(1)-Fe(1)-Br(2)	87.329(19)
S(2)-Mn(1)-Br(1)	99.46(6)	S(2)-Fe(1)-Br(1)	96.88(2)
S(2)-Mn(1)-Br(1)’	81.41(5)	S(2)-Fe(1)-Br(1)’	81.070(19)
S(2)-Mn(1)-Br(2)	100.73(6)	S(2)-Fe(1)-Br(2)	100.62(2)
Br(1)-Mn(1)-Br(2)	92.67(4)	Br(1)-Fe(1)-Br(2)	90.849(13)
Mn(1)-Br(1)-Mn(1)’	93.58(4)	Fe(1)-Br(1)-Fe(1)’	93.211(13)
S(1)-Mn(1)-S(2)	154.32(7)	S(1)-Fe(1)-S(2)	158.17(3)
Br(2)-Mn(1)-Br(1)’	177.79(6)	Br(2)-Fe(1)-Br(1)’	177.254(15)
Br(1)-Mn(1)-Br(1)’	86.42(4)	Br(1)-Fe(1)-Br(1)’	86.789(13)

The UV-visible spectra for the dinuclear complexes **1**, **2** and **4** provide a probe of the electronic structures of these complexes as well as the influence of the pseudo-octahedral metal coordination geometries on the metal-centered *d-d* electronic transition. The spectra for complexes **1-6** are shown in Figure 6.3 and the spectra for **1**, **2** and **4** were consistent with high spin metal centers in pseudo-octahedral geometry. More specifically, the d^5 Mn complex **1** displayed only ligand and charge transfer bands as expected for five half-occupied *d*-orbitals which has no spin allowed *d-d* transitions. In contrast, as seen in the inset to Figure 6.3, the high spin d^6 and d^8 centers in **2** and **4**, respectively, presented absorptions attributed to *d-d* transitions for pseudo-octahedral species. For the discussion of the spectral terms for these complexes the labels for octahedral crystal field will be used. For an octahedral high spin d^6 complex, such as **2,** a single spin allowed transition from a $^5T_{2g}$ ground state to ^5E_g was expected and is in fact observed. Complex **4**, with a d^8 pseudo-octahedral coordination sphere displayed two spin allowed transitions at 480 nm (20,833 cm^{-1}), 770 nm (12,987 cm^{-1}) assigned to $^3A_{2g} \rightarrow ^3T_{1g}$ and $^3A_{2g} \rightarrow ^3T_{1g}(P)$ allowed transitions, respectively.[51]

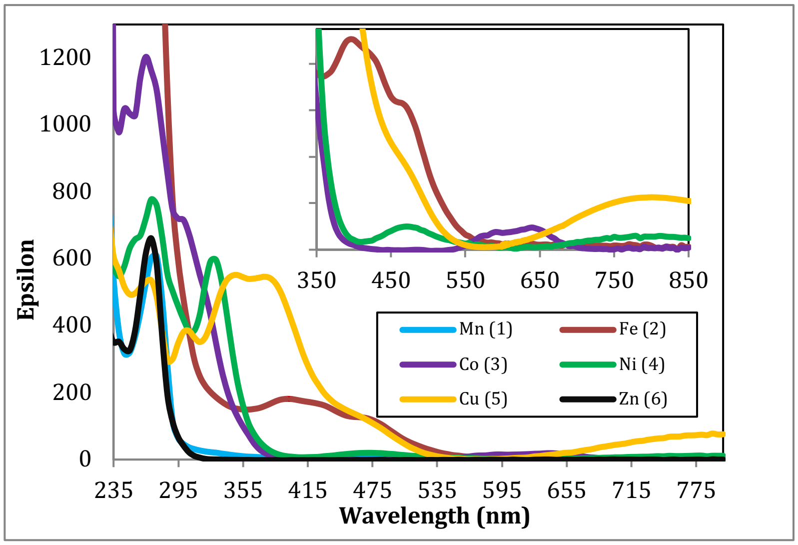

Figure 6.3. UV-vis spectra of complexes **1-6** as indicated. Inset focused on the visible absorptions attributed to the d-d transitions for complexes of Fe (**2**), Co (**3**), Ni (**4**) and Cu (**5**).

In contrast to the dinuclear compounds **1**, **2** and **4**, the X-ray data analysis of compounds **3**, **5** and **6** (Table 6.3.) revealed these complexes to be mononuclear five-coordinate structures as presented in Figures 6.4-6.6. Selected bond distances and angles for these three complexes are provided in Tables 6.4 and 6.5. As seen in Figures 6.4-6.6, compounds **3**, **5** and **6** are all monomeric species with formula given by $M(\kappa^3\text{-}2,6\text{-}\{CH_3SCH_2\}_2NC_5H_3)Br_2$ (M = Co, Cu, Zn). As with complexes **1** and **2**, the metal centers in **3**, **5**, and **6** possess a tridentate planar coordinated SNS ligand that is bonded through the pyridyl N and the two thioether S centers. The coordination environments are completed by two bromo ligands.

In general, the geometric features of five coordinate transition metal structures are influenced by electronic, steric and electrostatic features and provide for a fascinating issue in coordination chemistry. The two common limiting ideal geometries for five coordinate species are trigonal bipyramidal (*tbp*) and square-based pyramidal (*sp*) metal environments. Since complexes **3, 5** and **6** are not homoleptic species**,** deviations from the ideal geometries are expected. Even in such situations it is possible to assign approximate *tbp* or *sp* metal coordination geometry using a quantitative measure derived from simple calculation of structural index parameter, τ.[52,53] Additional geometric deviations can arise due to ligand bite angle restrictions or when the M center is displaced out of the ligand plane. Application of this approach to complexes **3, 5** and **6** yielded the τ parameters in Table 6.6. For complex **5** the value of 0.043 indicated that this Cu(II) complex adopted a coordination geometry that can best be described as distorted square-based pyramidal (*sp*). In contrast the τ values of 0.50 and 0.58 obtained for **3** and **6** respectively are ambiguous in defining a preferred coordination geometry. Utilizing the continuous shape measure program SHAPE2,[54–59] we calculated the comparative shape integrals for the trigonal bipyramid ("TBPY-5") and square pyramid ("SPY-5") cases for the complexes **3**, **5** and **6**. The analysis of these two methods was in agreement with the preferred description of the Cu(II) complex **5** as square pyramidal and the Co (**3**) and Zn (**6**) complexes as trigonal bipyramidal.

Table 6.3. Summary of data collection and crystallographic parameters for compounds $[M(\kappa^3\text{-}2,6\text{-}\{CH_3SCH_2\}_2NC_6H_3)Br_2]$ **3**, M = Co, **5**, M = Cu, and **6**, M = Zn.

Compound	$Co(\kappa^3\text{-}2,6\text{-}\{CH_3SCH_2\}_2NC_6H_3)Br_2]$ (**3**)	$[Cu(\kappa^3\text{-}2,6\text{-}\{CH_3SCH_2\}_2NC_6H_3)Br_2]$ (**5**)	$[Zn(\kappa^3\text{-}2,6\text{-}\{CH_3SCH_2\}_2NC_6H_3)Br_2]$ (**6**)
Empirical formula	$C_9H_{13}Br_2CoNS_2$	$C_9H_{13}Br_2CuNS_2$	$C_9H_{13}Br_2ZnNS_2$
Formula weight	418.07	422.68	424.51
Temperature, K	200(2)	200(2)	200(2)
λ, Å	0.71073	0.71073	0.71073
Crystal system	Triclinic	Monoclinic	Monoclinic
Space group	$P\bar{1}$	$P2_1/c$	$C2/c$
a, Å	10.3494(4)	12.5690(2)	22.6533(7)
b, Å	10.8403(4)	7.3812(2)	8.4765(2)
c, Å	13.4415(5)	14.9067(3)	15.3060(4)
α, °	70.202(2)	90.00	90.00
β, °	77.559(2)	104.2270(10)	101.693(2)
γ, °	85.166(2)	90.00	90.00
V, $Å^3$	1385.45(9)	1340.54(5)	2878.08
Z	4	4	8
ρ_{calc}, Mg/m^3	2.004	2.094	1.959
μ, mm^{-1}	7.277	7.870	7.520
Abs. correction	Semi-empirical from equivalents		
R_1[a]	0.0266	0.0323	0.0345
wR_2[b]	0.0653	0.0742	0.0801

[a] $R_1 = \sum||F_o| - |F_c||/\sum|F_o|$, [b] $wR_2 = \{\sum[w(F_o^2 - F_c^2)^2]/\sum[w(F_o^2)^2]\}^{1/2}$

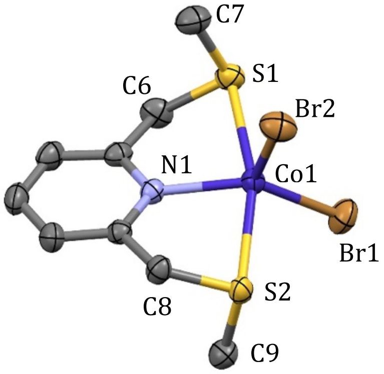

Figure 6.4. Structural representation of one of the two molecules of [Co(κ^3-2,6-{CH_3SCH_2}$_2NC_5H_3$)Br_2] (**3**),obtained from X-ray analysis. Hydrogen atoms are omitted for clarity. Thermal ellipsoids are shown at 60% probability.

Table 6.4. Selected bond distances (Å) and angles (deg) for compounds **3** and **5.**

3		**5**	
Co(1)-N(1)	2.065(2)	Cu(1)-N(1)	2.014(2)
Co(1)-S(1)	2.5028(6)	Cu(1)-S(1)	2.3380(9)
Co(1)-S(2)	2.4945(6)	Cu(1)-S(2)	2.3297(8)
Co(1)-Br(1)	2.3987(4)	Cu(1)-Br(1)	2.3832(5)
Co(1)-Br(2)	2.4100(4)	Cu(1)-Br(2)	2.6741(5)
S(2)-Co(1)-S(1)	163.25(3)	S(2)-Cu(1)-S(1)	165.34(4)
N(1)-Co(1)-S(1)	81.73(5)	N(1)-Cu(1)-S(1)	85.09(7)
N(1)-Co(1)-S(2)	81.56(5)	N(1)-Cu(1)-S(2)	84.42(7)
N(1)-Co(1)-Br(1)	133.28(5)	N(1)-Cu(1)-Br(1)	159.74(7)
N(1)-Co(1)-Br(2)	108.89(5)	N(1)-Cu(1)-Br(2)	94.07(6)
S(1)-Co(1)-Br(1)	95.027(19)	S(1)-Cu(1)-Br(1)	92.87(3)
S(1)-Co(1)-Br(2)	96.521(19)	S(1)-Cu(1)-Br(2)	103.85(3)
S(2)-Co(1)-Br(1)	95.448(18)	S(2)-Cu(1)-Br(1)	93.42(2)
S(2)-Co(1)-Br(2)	90.114(18)	S(2)-Cu(1)-Br(2)	87.10(2)
Br(1)-Co(1)-Br(2)	117.759(17)	Br(1)-Cu(1)-Br(2)	105.965(17)

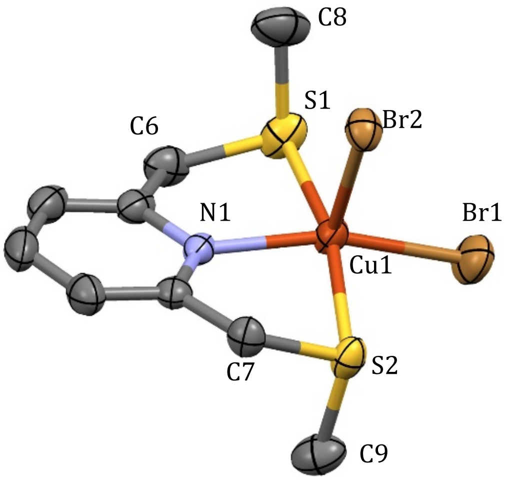

Figure 6.5. Structural representation of [Cu(κ^3-2,6-{CH_3SCH_2}$_2$$NC_5H_3$)$Br_2$] (**5**), obtained from X-ray analysis. Hydrogen atoms are omitted for clarity. Thermal ellipsoids are shown at 60% probability.

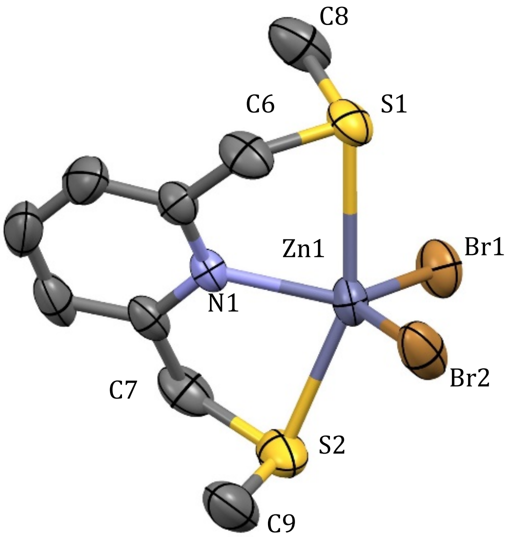

Figure 6.6. Structural representation of [Zn(κ^3-2,6-{CH_3SCH_2}$_2$$NC_5H_3$)$Br_2$] (**6**) obtained from X-ray analysis. Hydrogen atoms are omitted for clarity. Thermal ellipsoids are shown at 60% probability.

Table 6.5. Selected bond distances (Å) and angles (deg) for compound **6**.

Zn(1)-N(1)	2.092(3)	Zn(1)-Br(1)	2.3689(6)
Zn(1)-S(1)	2.751(1)	Zn(1)-Br(2)	2.3635(7)
Zn(1)-S(2)	2.557(1)		
S(2)-Zn(1)-S(1)	157.30(4)	S(1)-Zn(1)-Br(1)	95.53(3)
N(1)-Zn(1)-S(1)	77.08(7)	S(1)-Zn(1)-Br(2)	89.47(3)
N(1)-Zn(1)-S(2)	80.22(8)	S(2)-Zn(1)-Br(1)	96.34(3)
N(1)-Zn(1)-Br(1)	122.58(7)	S(2)-Zn(1)-Br(2)	100.95(3)
N(1)-Zn(1)-Br(2)	116.22(7)	Br(1)-Zn(1)-Br(2)	120.60(2)

Table 6.6. Calculated structural parameters related to metal coordination geometry using either the τ parameter[52,53] or the SHAPE analysis[54–59] as described in the text. All values were derived from the single crystal X-ray analyses.

Compound	**3**	**5**	**6**
τ	0.50	0.043	0.58
TBPY-5	1.726	4.950	2.204
SPY-5	3.581	1.336	4.946

Before discussing the detailed features for the structures of **3**, **5** and **6** it is worthwhile to look at the general bond distance variations for all five of the structures obtained for $[M(\kappa^3\text{-}2,6\text{-}(CH_3SCH_2)_2C_5H_3N)Br_2]_n$ (M = Mn (**1**), Fe (**2**), Co (**3**), Cu (**5**), Zn (**6**)) in this report. A summary of these features is provided in Figure 6.7. Keeping in mind that although these species do not have strictly comparable coordination geometries, it was observed that the trend in $M\text{-}N_{py}$ and $M\text{-}S_{average}$ bond distance displayed a minimum for the Cu complex. These measured bond lengths correlate with the increase in complex stability as expected from the Irving-Williams series Mn(II) < Fe(II)< Co(II) < Ni(II) < Cu(II) > Zn(II).[60,61] The rationalization of this observation involved an increase in both the electrostatic/ionic and covalent interactions that contributed to the stability constants across the series from Mn to Cu. From Cu to Zn there is a decrease in both of these interactions and particularly in the covalency for the d^{10} Zn center.[62] This trend in decreasing bond length across the series also indicates an increasing steric load from the ligands and is consistent with the formation of dinuclear species for **1** and **2** and mononuclear species for **3**, **5**, and **6**. Furthermore, the increasing metal electron count across the M(II) series should also diminish the tendency for the complex to coordinate additional ligands or to dimerize.

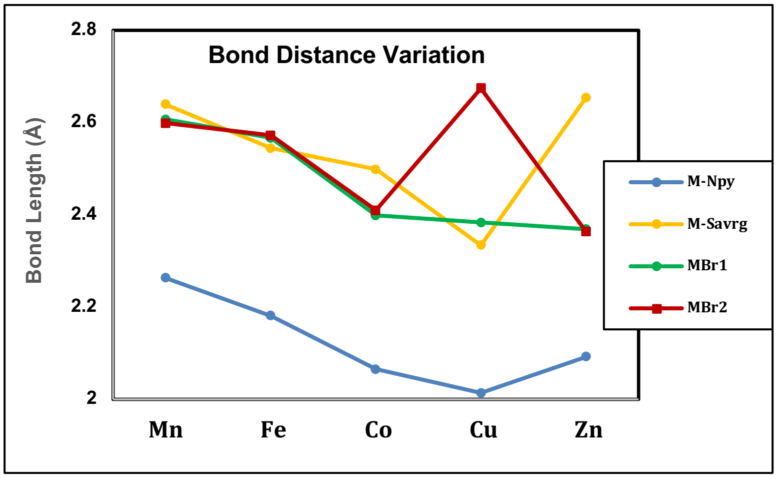

Figure 6.7. Variation of metal-ligand bond distances from the single crystal X-ray structures for $[M(\kappa^3\text{-}2,6\text{-}(CH_3SCH_2)_2C_5H_3N)Br_2]_n$ complexes **1-3**, **5** and **6.**

Coming back to the two *tbp* complexes, $[Co(\kappa^3\text{-}2,6\text{-}\{CH_3SCH_2\}_2NC_5H_3)Br_2]$ (**3**), and$[Zn(\kappa^3\text{-}2,6\text{-}\{CH_3SCH_2\}_2NC_5H_3)Br_2]$ (**6**) the coordination geometries are constituted by an equatorial plane defined by the coordinated pyridyl-N center and the two Br ligands with the pseudo-axial positions defined by two thioether S donors. The UV-visible spectra for these two species are consistent with this formulation. For example, the d^7 Co(II) center in **3** with a pseudo-D_{3h} geometry displayed two overlapping *d-d* transitions at 643 nm

(15,552 cm^{-1}) and 596 nm (16,779 cm^{-1}) that are very reminiscent of reported high spin five coordinate complexes with tridentate "NNN" and "NNS" ligand frameworks.[63–65] These transitions were assigned to $^4A_2'(F) \rightarrow {}^4A_2'(P)$ and $^4A_2'(F) \rightarrow {}^4E''(P)$ respectively. In the case of the d^{10} complex **6** there are no spin allowed *d-d* transitions and only ligand and charge transfer bands were observed (Figure 6.3).

In relation to the structure of [Co(κ^3-2,6-{CH_3SCH_2}$_2$$NC_5H_3$)$Br_2$] (**3**), the literature provides three related dichloro structures, [Co(κ^3-2,6-{$RSCH_2$}$_2$$NC_5H_3$)$Cl_2$] (R = Et, Bu, Ph).[16] Like **3**, the Co(II) coordination geometries for these complexes were identified as *tbp*. The SNS ligands in these four species display very similar Co-N and Co-S distances with the average bond distances for the reported dichloro species being Co-S of 2.50(4)Å and Co-N of 2.08(1)Å *versus* the dibromo complex **3** with average Co-S values equal to 2.499(1)Å and a Co-N of 2.065(2)Å. Furthermore the S-Co-N ligand bite angles are also similar with **3** displaying values of 81.73(5)° and 81.56(5)° compared to the average values for the three dichloro species of 81.6°. Interestingly, the only other structurally reported Co(II) complex of the SNS ligand family is the sterically less demanding dichloro species, [Co(κ^3-2,6-{$MeSCH_2$}$_2$$NC_5H_3$)$Cl_2$]$_2$.[16] This dinuclear species exhibited a structure analogous to those observed for **1** and **2** and this feature provides further support for our analysis of those dinuclear compounds.

There are also three structurally characterized analogues of [Zn(κ^3-2,6-{CH_3SCH_2}$_2$$NC_5H_3$)$Br_2$] (**6**), [Zn(κ^3-2,6-{$RSCH_2$}$_2$$NC_5H_3$)$Br_2$] (R = Et[25] **A**, tBu[15] **B**) and the dichloro species [Zn(κ^3-2,6-{CH_3SCH_2}$_2$$NC_5H_3$)$Cl_2$][17]. These three reported complexes displayed *tbp* coordination geometries. The most direct comparisons are between the three dibromo complexes, **6**, **A** and **B**. Perhaps not surprisingly, the structural parameters for these three species are quite similar. For example, the metal ligand bond distances in **6** for Zn-N (2.092(3)Å) and Zn-Br (2.3689(6)Å, 2.3635(7)Å) compare favorably with the average of Zn-N of 2.09(1)Å and Zn-Br of 2.38(1)Å observed for **A** and **B.** The three complexes display long Zn-S bonds with the average value of 2.65(1)Å in the case of **6** and 2.68(4)Å for **A** and **B**. Finally, the S-Zn-N ligand bite angles average 78.65(10)° in **6** and 78.66(4)° in **A** and **B**. The *tbp* metal coordination geometry and long Zn-S interactions are anticipated for the Zn(II) d^{10} metal center.

A different view of metal coordination environment and M/SNS ligand bonding is provided by the *sp* formulation for Cu compound **5**. In this species, the basal plane was defined by the pyridyl-N center, the two thioether S donors and Br(1). The pseudo-apical position is occupied by the bromo ligand Br(2). Consistent with this assignment is the observation of basal Cu-Br(1) distance of 2.3832(5)Å and a longer Cu-Br(2) distance of 2.6741(5)Å, which correlates with occupation of the Cu-Br(2) σ^* (e.g. d_{z^2}) orbital for a Cu^{2+} d^9 configuration. This interpretation is supported by the UV-visible spectrum observed for **5** (Figure 6.3.). The d^9 configuration displays one low energy *d-d* transition at 797 nm (12,545cm^{-1}) assigned to $d_z{}^2 \rightarrow d_{x}{}^2{}_{-y}{}^2$.

Although there are two reported Cu(II) bis(thioether) pyridine structures, $[Cu(\kappa^3\text{-}2,6\text{-}\{RSCH_2\}_2NC_5H_3)Cl_2]$ (R = 2-(MeOC(O)C_6H_4, Et), the S-(2-methoxycarbonylphenyl) complex yielded a monomeric complex that is distorted *tbp* geometry thus making structural comparison with **6** problematic.[22] On the other hand, similar to **6**, an *sp* structure was observed for $[Cu(\kappa^3\text{-}2,6\text{-}\{EtSCH_2\}_2NC_5H_3)Cl_2]$,[24] and this species gave similar structural parameters to **6**. Specifically, the reported dichloro complex, $[Cu(\kappa^3\text{-}2,6\text{-}\{EtSCH_2\}_2NC_5H_3)Cl_2]$, provided an average Cu-S distance of 2.35Å comparable to the Cu-S distances of 2.3380(9)Å and 2.3297(8)Å observed for **6** and a Cu-N distance of 2.016(10)Å that is nearly identical to the Cu(1)-N(1) distance of 2.014(2)Å obtained for **6**.

In addition, the ligand bite angles (N-Cu-S) for **6** (85.09(7)° and 84.42(7)°) are similar to N-Cu-S bite angles, 85.8(3)° and 84.7(3)° for [Cu(κ^3-2,6-{EtSCH$_2$}$_2$NC$_5$H$_3$)Cl$_2$].[24]

6.3. The Catalytic behavior of the SNS Complexes

6.3.1. The Photocatalytic and Electrocatalytic CO$_2$ Reduction

These SNS complexes have been examined for both photocatalytic and electrocatalytic CO$_2$ reduction. They do not show a good catalytic behavior towards CO$_2$ reduction in both photocatalytic and electrocatalytic processes. In the photocatalytic processes, they show same amount of formic acid as the background, and the electrocatalytic processes did not show any catalytic behavior.

6.3.2. The Photochemical H$_2$ Production from H$_2$O

Since these SNS complexes do not show a good photocatalytic and electrocatalytic behavior towards CO$_2$ reduction, the photocatalytic H$_2$ production from H$_2$O water has been examined for these complexes. These SNS complexes were able to produce H$_2$ from H$_2$O. The next table (Table 6.7.) shows a scan of the ability, under similar photocatalytic conditions, of this series of SNS complexes to generate H$_2$ from water. The best results for the H$_2$ production were with the [Fe{κ^3-2,6-(MeSCH$_2$)$_2$NC$_5$H$_5$}Br$_2$]$_2$ and [Ni{κ^3-2,6-(MeSCH$_2$)$_2$NC$_5$H$_5$}Br$_2$]$_2$.

In addition, the emission-spectra for the both complexes were obtained as shown in Figure 6.8 And 6.10 according to the procedure that is explained in Section 1.7.4. Emission-Quenching Experiment for Chapter 1. The quenching rate constants kq were also calculated from the linear Stern-Volmer plots as shown in Figure 6.9 and 6.11.

Table 6.7. Photochemical H_2 generation from water using complexes 1-6. All reactions were carried out with 1mmol each of complex and photosenstitzer, $[Ru(bpy)_3](PF_6)_2$ in 4mL of reaction solvent (either DMF or CH_3CN) with 0.2mL of added water. Three different electron donors, triethanolamine (TEOA), triethylamine (TEA) and 1-Benzyl-1,4-dihydronicotinamide (BNAH) were employed. Irradiation with 405 nm LED light conducted under an N_2 atmosphere for 24 h.

Complex	**ED**	**H_2 (DMF) (μmol)**	**H_2 (CH_3CN) (μmol)**
$[Mn\{\kappa^3\text{-}2,6\text{-}(MeSCH_2)_2NC_5H_5\}Br_2]_2$ **(1)**	TEOA	**88**	**28**
	TEA	**4**	**53**
	BNAH	**5**	**3**
$[Fe\{\kappa^3\text{-}2,6\text{-}(MeSCH_2)_2NC_5H_5\}Br_2]_2$ **(2)**	TEOA	**133**	**35**
	TEA	**15**	**36**
	BNAH	**28**	**5**
$Co\{\kappa^3\text{-}2,6\text{-}(MeSCH_2)_2NC_5H_5\}Br_2$ **(3)**	TEOA	**58**	**30**
	TEA	**31**	**61**
	BNAH	**16**	**43**
$Ni\{\kappa^3\text{-}2,6\text{-}(MeSCH_2)_2NC_5H_5\}Br_2$ **(4)**	TEOA	**194**	**12**
	TEA	**36**	**80**
	BNAH	**51**	**4**
$Cu\{\kappa^3\text{-}2,6\text{-}(MeSCH_2)_2NC_5H_5\}Br_2$ **(5)**	TEOA	**84**	**56**
	TEA	**6**	**8**
	BNAH	**12**	**3**
$Zn\{\kappa^3\text{-}2,6\text{-}(MeSCH_2)_2NC_5H_5\}Br_2$ **(6)**	TEOA	**4**	**4**
	TEA	**3**	**5**
	BNAH	**4**	**4**
No Catalyst	TEOA	**-**	**-**

6.4. The Emission-Quenching Experiment

The emission-quenching experiment was obtained in order to investigate more about the features for the photocatalytic activity of these complexes (Fe and Ni). The process of this experiment was mentioned in section 1.7.4. Emission-Quenching Experiment in Chapter 1, the emission-spectra and the quenching rate constants kq that were calculated from the linear Stern-Volmer plots for both the both Fe and Ni catalysts are shown below in the next figures.

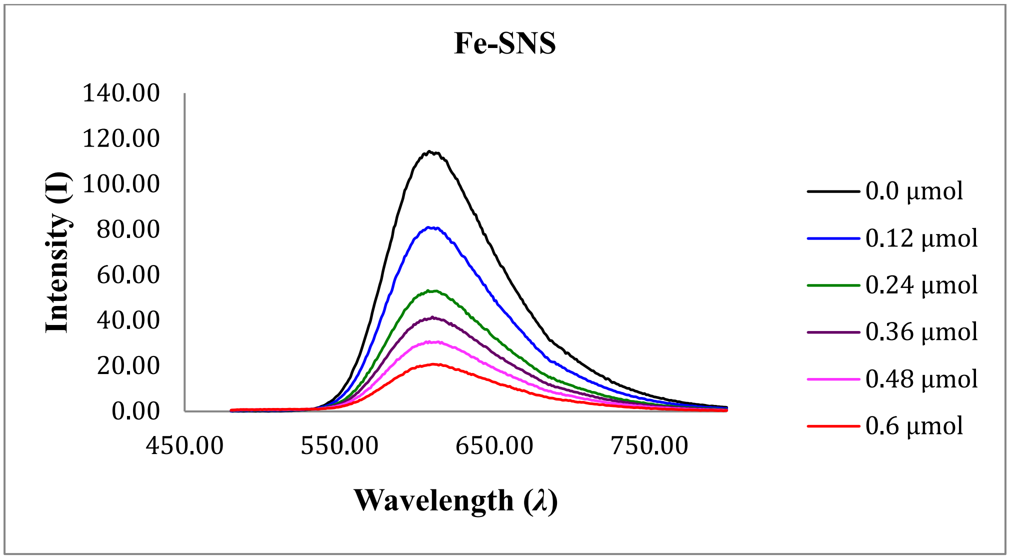

Figure 6.8. Emission-spectra from the quenching experiments with Fe-SNS complex.

Table 6.13. The Emission-spectra data from the quenching experiments with Fe-SNS complex.

concentration (µmol)	Intensity (I)
0	114.4175339
0.12	80.81655884
0.24	52.66041565
0.36	41.56280899
0.48	30.24587822
0.6	20.6122551

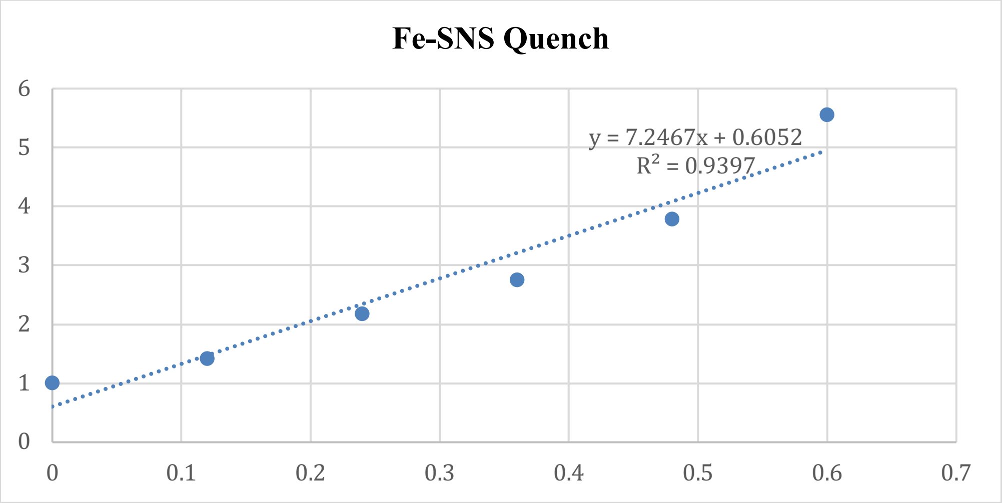

Figure 6.9. Stern-Volmer plot for quenching of the emission of the photosensitizer Ru(bpy)$_3$(PF$_6$)$_2$ with various concentrations of catalyst Fe-SNS complex.

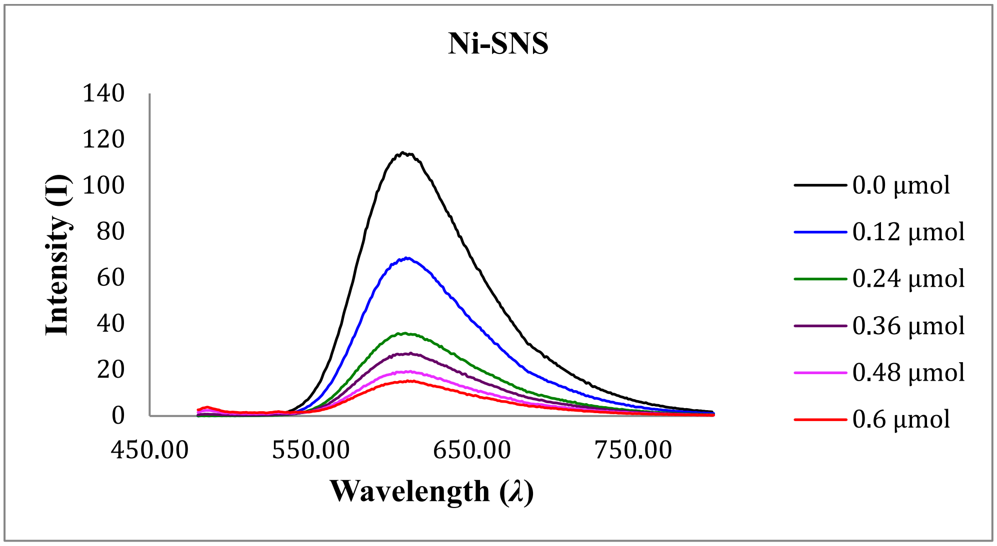

Figure 6.10. Emission-spectra from the quenching experiments with Ni-SNS complex.

Table 6.14. The Emission-spectra data from the quenching experiments with Ni-SNS complex.

concentration (µmol)	Intensity (I)
0	114.4175339
0.12	67.88236237
0.24	35.9315071
0.36	26.96782303
0.48	19.31774712
0.6	14.95480347

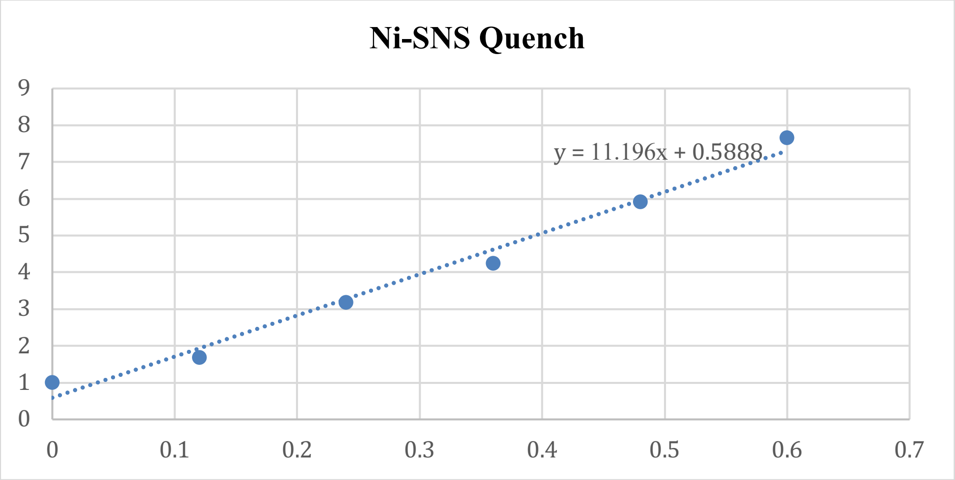

Figure 6.11. Stern-Volmer plot for quenching of the emission of the photosensitizer $Ru(bpy)_3(PF_6)_2$ with various concentrations of catalyst Ni-SNS complex.

6.5. Experimental Section

6.5.1. General Methods

Reactions were performed in a glovebox under a nitrogen atmosphere. All solvents were sparged with nitrogen and then dried by passage through a column of activated alumina using an apparatus purchased from Anhydrous Engineering. Deuterated chloroform was dried using activated molecular sieves. Metal bromides were purchased from Strem Chemicals and used as received. All other chemicals were purchased from Aldrich and used without further purification. The ligand 2,6-$(MeSCH_2)_2NC_5H_5$ was synthesized according to literature procedure.[28]

6.5.2. Some Characterizations

NMR spectra were acquired on a Bruker Avance 300 MHz spectrometer with CD_2Cl_2, and $CDCl_3$ as solvents and internal standards. Mass spectrometry (MS) was obtained at the University of Ottawa using TOF MS ES on a Micromass-Q TOF II. Infrared spectra were measured on powder samples using a Nicolet 6700 FT- IR. UV-Vis spectra were collected using an Agilent Technologies Cary 300 UV-Vis spectrometer. Elemental analyses for 1-6 were performed by Midwest Microlab LLC, Indianapolis IN. Magnetic moments were measured at room temperature using the Evans method.[66,67]

6.5.3. X-ray Crystallography

Crystals were mounted on thin glass fibers using paraffin oil. Prior to data collection crystals were cooled to the collection temperature. Data were collected on Bruker AXS Smart and Kappa single-crystal diffractometers equipped with a sealed Mo tube source (wavelength 0.71073 Å) and APEX II CCD detector. Raw data collection and processing were performed with APEX II software package from BRUKER AXS.[68] Initial unit cell parameters were determined from 60 data frames with 0.3° ω scan each collected at the different sections of the Ewald sphere. Semi-empirical absorption corrections based on equivalent reflections were applied.[69] Systematic absences in the diffraction data-set and unit-cell parameters were consistent with the space groups. The structures were solved by direct methods, completed with difference Fourier synthesis, and refined with full-matrix least-squares procedures based on F^2. For all the compounds all hydrogen atoms positions were calculated based on the geometry of the related non-hydrogen atoms. All hydrogen atoms were treated as idealized contributions during the refinement. All scattering factors are contained in several versions of the SHELXTL program library, with the latest version used being v.6.12.[70]

6.5.4. Experimental Procedure

$[Mn\{\kappa^3\text{-}2,6\text{-}(MeSCH_2)_2NC_5H_5\}Br_2]_2$ (1): $MnBr_2$ powder (32 mg, 0.149 mmol) was added to a clear yellow solution of $2,6\text{-}(MeSCH_2)_2NC_5H_5$ (44.6 mg, 0.224 mmol) in 8 mL of toluene. The reaction mixture was allowed to stir for 14 hours, gradually becoming opaque white. The solution was cooled to -20°C overnight. A pale white precipitate formed which was isolated by filtration and washed with 5 x 2 mL hexanes and then dried under vacuum. A white powder was isolated in 95% yield. Off-white crystals suitable for X-ray analysis were grown by diffusion of hexanes into a saturated THF solution of 1 and storing at -20°C for several days. Elemental analysis calculated (%) for $[C_9H_{13}Br_2MnNS_2]$: C 26.10, H 3.17, N 3.38, found C 26.08, H 3.12, N 3.34. MS m/z: 413.82 M^+. $\mu_{corr}(298K)$ = 5.78 μ_B.

$[Fe\{\kappa^3\text{-}2,6\text{-}(MeSCH_2)_2NC_5H_5\}Br_2]_2$ (2)*:* $FeBr_2$ powder (30 mg, 0.139 mmol) was added to a clear yellow solution of $2,6\text{-}(MeSCH_2)_2NC_5H_5$ (41.5 mg, 0.209 mmol) in 8 mL of toluene. The reaction mixture was allowed to stir for 14 hours, gradually becoming opaque orange. The solution was cooled to -20°C overnight. A brown precipitate formed which was isolated by filtration and washed with 5 x 2 mL hexanes and then dried under vacuum. A fine peach coloured powder was isolated in 96% yield. Peach crystals suitable for X-ray analysis were grown by diffusion of hexanes into a saturated THF solution of 2 and storing at -20°C for several days. Elemental analysis calculated (%) for [$C_9H_{13}Br_2FeNS_2$]: C 26.04, H 3.16, N 3.38, found C 25.93, H 3.11, N 3.08. MS m/z: 414.82 M^+. μ_{corr}(298K) = 4.05 μ_B.

Co{κ^3-2,6-($MeSCH_2)_2NC_5H_5$}Br_2 (3): $CoBr_2$ powder (30 mg, 0.137 mmol) was added to a clear yellow solution of 2,6-($MeSCH_2)_2NC_5H_5$ (41 mg, 0.206 mmol) in 8 mL of toluene. The reaction mixture was allowed to stir for 14 hours, gradually becoming opaque blue. The solution was cooled to -20°C overnight. A dark blue precipitate formed which was isolated by filtration and washed with 5 x 2 mL hexanes and then dried under vacuum. A dark blue powder was isolated in 97% yield. Large pale blue crystals suitable for X-ray analysis were grown diffusion of hexanes into a saturated CH_2Cl_2 solution of 3 and storing at -20°C for several days. Elemental analysis calculated (%) for [$C_9H_{13}Br_2CoNS_2$]: C 25.85, H 3.14, N 3.35, found C 25.74, H 3.11, N 3.37 MS m/z: 417.82 M^+. μ_{corr}(298K) = 4.73μ_B.

[Ni{κ^3-2,6-($MeSCH_2)_2NC_5H_5$}Br_2]$_2$ (4): $NiBr_2$ powder (30 mg, 0.137 mmol) was added to a clear yellow solution of 2,6-($MeSCH_2)_2NC_5H_5$ (41 mg, 0.206 mmol) in 8 mL of toluene. The reaction mixture was allowed to stir for 14 hour, gradually becoming opaque green. The solution was cooled to -20°C overnight. A green precipitate formed which was isolated by filtration and washed with 5 x 2 mL hexanes and then dried under vacuum. A bright green powder was ultimately isolated in 64% yield. Elemental analysis calculated (%) for [$C_9H_{13}Br_2NiNS_2$]: C 25.87, H 3.14, N 3.35, found C 25.89, H 3.17, N 3.38. MS m/z: 416.82 M^+. μ_{corr}(298K) = 3.17μ_B

Cu{κ^3-2,6-($MeSCH_2$)$_2NC_5H_5$}Br_2 (5): $CuBr_2$ powder (32 mg, 0.143 mmol) was added to a clear yellow solution of 2,6-($MeSCH_2$)$_2NC_5H_5$ (43 mg, 0.215 mmol) in 8 mL of toluene. The reaction mixture was allowed to stir for 14 hours, gradually becoming green. The solution was cooled to -20°C overnight. A forest green precipitate formed which was isolated by filtration and washed with 5 x 2 mL hexanes and then dried under vacuum. A bright green powder was isolated in 84% yield. Green crystals suitable for X-ray analysis were grown by diffusion of hexanes into a saturated MeCN solution of 5 and storing at -20°C for several days. Elemental analysis calculated (%) for [$C_9H_{13}Br_2CuNS_2$]: C 25.57, H 3.10, N 3.32, found C 25.64, H 3.09, N 3.22. MS m/z: 421.82 M^+. μ_{corr}(298K) = 2.01μ_B.

Zn{κ^3-2,6-($MeSCH_2$)$_2NC_5H_5$}Br_2 (6): $ZnBr_2$ powder (32 mg, 0.142 mmol) was added to a clear yellow solution of 2,6-($MeSCH_2$)$_2NC_5H_5$ (42 mg, 0.213 mmol) in 8 mL of toluene. The reaction mixture was allowed to stir for 14 hours, gradually becoming opaque white. The solution was cooled to -20°C overnight. A white precipitate formed which was isolated by filtration and washed with 5 x 2 mL hexanes and then dried under vacuum. A white powder was isolated in 93% yield. White crystals suitable for X-ray analysis were grown by diffusion of hexanes into a saturated CH_2Cl_2 solution of 6 and storing at -20°C for several days. Elemental analysis calculated (%) for [$C_9H_{13}Br_2ZnNS_2$]: C 25.46, H 3.09, N 3.30, found C 25.50, H 3.12, N 3.24. MS m/z: 422.81 M^+. ^{1}H NMR (400 MHz, DMSO-d_6): δ 7.68 (t,1H) 7.22 (d, 2H, J = 7.7 Hz), 3.71 (s, 4H, CH_2-py), 1.98 (s, 6H, CH_3). ^{13}C NMR (400 MHz, DMSO-d_6): δ 158.4 (Ar-C), 137.8 (Ar-CH), 121.5 (Ar-CH), 39.36 (Ar-CH_2-S), 15.12 (S-CH_3).

6.6. Conclusions

This report provides the first systematic application of bis(thioether)pyridine SNS ligands, a neutral pincer-type scaffold, in coordination chemistry and the first structurally characterized complexes of this broad ligand family for both Mn and Fe. The importance of such investigations reaches beyond a particular ligand array and addresses fundamental concepts within inorganic chemistry. The analysis of a series of divalent first row transition metal complexes revealed a set of monomeric and dimeric species and presented a delicate balance of structural features arising from the d-orbital occupancy of the metal and the steric load of the ligand. It appears that dimerization of the solid-state structure is primarily favored through lower steric load from the ligand and lower metal d-electron count. Generally, simple ligand field theory suggests that square-based pyramidal metal coordination geometry should be favored for five-coordinate complexes but factors such as d-electron count, effective steric load of ligands and metal-ligand π-bonding are important considerations.[71] These are factors under our scrutiny as we further explore the synthetic/structural chemistry of the SNS framework and the potential of these complexes in chemical transformations and catalysis. These SNS transition metal complexes show a good catalytic behavior towards the hydrogen production. However, a further study of the reactivity of these catalysts should be done.

6.7. References

1 G. van Koten and R. A. Gossage, *The Privileged Platform : Coordination Chemistry & Applications*, Springer, Heidelberg, 2016.

2 D. Morales-Morales, Ed., *Pincer Compounds. Chemistry and Applications*, Elsevier, Amsterdam, 2018.

3 G. van Koten and D. Milstein, *Organometallic Pincer Chemistry, Topics in Organometallic Chemistry 40*, Springer-Verlag, Heidelberg, 2013.

4 H. Valdes, L. Gonzalez-Sebastian and D. Morales-Morales, *J. Organomet. Chem.*, 2017, **845**, 229–257.

5 C. Gunanathan and D. Milstein, *Chem. Rev.*, 2014, **114**, 12024–12087.

6 D. Morales-Morales and C. M. Jensen, *The Chemistry of Pincer Compounds*, Elsevier B.V, Amsterdam, 2007.

7 H. Valdés, M. A. García-Eleno, D. Canseco-Gonzalez and D. Morales-Morales, *ChemCatChem*, 2018, 1–38.

8 K. J. Szabo and O. F. Wendt, *Pincer and Pincer-Type Complexes. Applications in Organic Synthesis and Catalysis*, Wiley-VCH, Weinheim, 2014.

9 M. Asay and D. Morales-Morales, *Dalt. Trans.*, 2015, **44**, 17432–17447.

10 G. K. Rao, S. I. Gorelsky, I. Korobkov and D. Richeson, *Dalton Trans.*, 2015, **44**, 19153–19162.

11 G. K. Rao, W. Pell, I. Korobkov and D. Richeson, *Chem. Commun.*, 2016, **52**, 8010–8013.

12 G. K. Rao, W. Pell, B. Gabidullin, I. Korobkov and D. Richeson, *Chem. - A Eur. J.*, 2017, **23**, 16763–16767.

13 G. K. Rao, I. Korobkov, B. Gabidullin and D. Richeson, *Polyhedron*, 2017, **143**, 62–69.

14 P. S. Bryan and E. Doomes, *J. Coord. Chem.*, 1976, **6**, 97–105.

15 H. F. AbdEl-Halim, G. G. Mohamed, K. Hofmann and B. Albert, *Comptes Rendus Chim.*, 2015, **18**, 619–625.

16 L. Soobramoney, M. D. Bala and H. B. Friedrich, *Dalt. Trans.*, 2014, **43**, 15968–15978.

17 W. Lai, S. M. Berry, D. C. Bebout and R. J. Butcher, *Inorg. Chem.*, 2006, **45**, 571–581.

18 M. Basauri-Molina, S. Hernandez-Ortega and D. Morales-Morales, *Eur. J. Inorg. Chem.*, 2014, **2014**, 4619–4625.

19 R. J. Ball, A. R. J. Genge, A. L. Radford, B. W. Skelton, V.-A. Tolhurst and A. H. White, *J. Chem. Soc. Dalt. Trans.*, 2001, 2807–2812.

20 F. Teixidor, P. Angles, C. Vina, R. Kivekas and R. Sillanpaa, *Inorg. Chem.*, 2001, **40**, 4010–4015.

21 V. E. Marquez, J. R. Anacona, R. J. Hurtado, G. D. de Delgado and E. M. Roque, *Polyhedron*, 1999, **18**, 1903–1908.

22 F. Teixidor, G. Sanchez-Castello, N. Lucena, L. Escriche, R. Kivekas, M. Sundberg and J. Casabo, *Inorg. Chem.*, 1991, **30**, 4931–4935.

23 F. Teixidor, L. Escriche, I. Roderiguez, J. Casabó, J. Ruis, E. Molins, B. Martinez and C. Miravitlles, *J. Chem. Soc. Dalt. Trans.*, 1989, 1381–1384.

24 L. Escriche, M. Sanz, J. Casabo, F. Teixidor, E. Molins and C. Miravitlles, *J. Chem. Soc., Dalt. Trans*, 1989, 1739.

25 F. Teixidor, L. Escriche, J. Casabo, E. Molins and C. Miravitlles, *Inorg. Chem.*, 1986, **25**, 4060–4062.

26 F. López-Saucedo, G. G. Flores-Rojas, L. González-Sebastián, R. Reyes-Martínez,

J. M. German-Acacio, A. Avila-Sorrosa, S. Hernández-Ortega and D. Morales-Morales, *Inorganica Chim. Acta*, 2018, **473**, 83–93.

27 G. Annibale, M. Bortoluzzi, G. Marangoni and B. Pitteri, *Transit. Met. Chem.*, 2005, **30**, 748–750.

28 L. Canovese, G. Chessa, G. Marangoni, B. Pitteri, P. Uguagliati and F. Visentin, *Inorganica Chim. Acta*, 1991, **186**, 79–86.

29 Y. Klerman, E. Ben-Ari, Y. Diskin-Posner, G. Leitus, L. J. W. Shimon, Y. Ben-David and D. Milstein, *Dalt. Trans.*, 2008, **676568**, 3226–3234.

30 L. Canovese, F. Visentin, G. Chessa, P. Uguagliati, C. Levi and A. Dolmella, *Organometallics*, 2005, **24**, 5537–5548.

31 L. Canovese, F. Visentin, G. Chessa, P. Uguagliati, C. Santo, G. Bandoli and L. Maini, *Organometallics*, 2003, **22**, 3230–3238.

32 M. Bassetti, A. Capone, L. Mastrofrancesco and M. Salamone, *Organometallics*, 2003, **22**, 2535–2538.

33 N. Zimmermann, E. Meggers and P. G. Schultz, *J. Am. Chem. Soc.*, 2002, **124**, 13684–13685.

34 L. Canovese, F. Visentin, G. Chessa, G. Gardenal and P. Uguagliati, *J. Organomet. Chem.*, 2001, **622**, 155–165.

35 L. Canovese, F. Visentin, P. Uguagliati, V. Lucchini and G. Bandoli, *Inorganica Chim. Acta*, 1998, **277**, 247–252.

36 L. Canovese, F. Visentin, G. Chessa, A. Niero and P. Uguagliati, *Inorganica Chim. Acta*, 1999, **293**, 44–52.

37 E. W. Abel, E. S. Blackwall, M. L. Creber, P. J. Heard and K. G. Orrell, *J. Organomet. Chem.*, 1995, **490**, 83–88.

38 F. Teixidor, G. Sanchez, N. Lucena, L. Escriche, R. Kivekäs and J. Casabo, *J. Chem. Soc. Chem. Commun.*, 1992, 163–164.

39 D. Parker, J.-M. Lehn and J. Rimmer, *J. Chem. Soc. Dalt. Trans.*, 1985, 1517–1521.

40 M. J. Page, J. Wagler and B. A. Messerle, *Organometallics*, 2010, **29**, 3790–3798.

41 G. Weber, *Inorganica Chim. Acta*, 1982, **58**, 27–33.

42 M. Vetrichelvan, Y. H. Lai and K. F. Mok, *Inorganica Chim. Acta*, 2004, **357**, 1397–1404.

43 S. Y. Shaban, F. W. Heinemann, H. Mansour and D. Sellmann, *J. Coord. Chem.*, 2010, **63**, 2812–2820.

44 S. Ferlay, A. Jouaiti, M. Loï, M. W. Hosseini, A. De Cian and P. Turek, *New J. Chem.*, 2003, **27**, 1801–1805.

45 D. S. McGuinness, P. Wasserscheid, W. Keim, D. Morgan, J. T. Dixon, A. Bollmann, H. Maumela, F. Hess and U. Englert, *J. Am. Chem. Soc.*, 2003, **125**, 5272–5273.

46 P. Braunstein and F. Naud, *Angew. Chemie - Int. Ed.*, 2001, **40**, 680–699.

47 Y. Kawada, Y. Kataoka and Y. Ura, *Dalton Trans.*, 2013, **42**, 14844–55.

48 A. De León, J. A. Ayllón and J. Pons, *J. Organomet. Chem.*, 2012, **696**, 4275–4280.

49 D. Hong, Y. Tsukakoshi, H. Kotani, T. Ishizuka and T. Kojima, *J. Am. Chem. Soc.*, 2017, **139**, 6538–6541.

50 H. G. Sogukomerogullari, E. Aytar, M. Ulusoy, S. Demir, N. Dege, D. S. Richeson and M. Sönmez, *Inorganica Chim. Acta*, 2018, **471**, 290–296.

51 L. Sacconi, F. Mani and A. Bencini, in *Comprehensive Coordination Chemistry, Volume 5*, eds. G. Wilkinson, R. D. Gillard and J. A. McCleverty, Pergamon, Oxford, 1987, pp. 42–55.

52 E. L. Muetterties and L. J. Guggenberger, *J. Am. Chem. Soc.*, 1974, **3021**, 1748–1756.

53 A. W. Addison, T. N. Rao, J. Reedijk, J. van Rijn and G. C. Verschoor, *J. Chem. Soc. Dalt. Trans.*, 1984, 1349.

54 S. Alvarez, P. Alemany, D. Casanova, J. Cirera, M. Llunell and D. Avnir, *Coord. Chem. Rev.*, 2005, **249**, 1693–1708.

55 S. Alvarez, P. Alemany and D. Avnir, *Chem. Soc. Rev.*, 2005, **34**, 313.

56 S. Alvarez, D. Avnir, M. Llunell and M. Pinsky, *New J. Chem.*, 2002, **26**, 996–1009.

57 M. Llunell, D. Casanova, J. Cirera, P. Alemany and S. Alvarez, 2013.

58 S. Alvarez and M. Llunell, *J. Chem. Soc. Dalt. Trans.*, 2000, 3288–3303.

59 J. Cirera, E. Ruiz and S. Alvarez, *Organometallics*, 2005, **24**, 1556–1562.

60 H. Irving and R. J. P. Williams, *Nature*, 1948, **162**, 746.

61 H. Irving and R. J. P. Williams, *J. Chem. Soc.*, 1953, 3192–3210.

62 T. Jurca, S. Ouanounou, W. Shih, T. Ong, G. P. A. Yap, I. Korobkov, S. Gorelsky and D. Richeson, *Dalton Trans.*, 2016, **45**, 14327–14334.

63 L. Sacconi, R. Morassi and S. Midollini, *J. Chem. Soc. A*, 1968, 1510–1515.

64 L. Sacconi and G. P. Speroni, *Inorg. Chem.*, 1968, **7**, 295–299.

65 L. Sacconi, I. Bertini and R. Morassi, *Inorg. Chem.*, 1966, **3**, 1548–1553.

66 E. M. Schubert, *J. Chem. Educ.*, 1992, **69**, 62.

67 D. F. Evans, *J. Chem. Soc.*, 1959, 2003–2005.

68 APEX Softward Suite v 2010 Bruker AXS Inc. Madison Wisconsin USA, 2010.

69 R. H. Blessing, *Acta Crystallogr. Sect. A*, 1995, 33–38.

70 G. M. Sheldrick, *Acta Crystallogr. Sect. A*, 2008, 112–122.

71 A. R. Rossi and R. Hoffmann, *Inorg. Chem.*, 1975, **14**, 365–374.

Chapter 7: Conclusion and Future Study

7.1. Summary of the work

This thesis presents a number of avenues of investigation into the reduction of CO_2. The motivation for this effort was outlined in each chapter and represents an important field of research that continues to attract a great deal of attention due to the valuable and useful molecules that will be produce from this reduction. The increasing levels of CO_2 production provide a strong impetus to discover new catalysts that are able to convert CO_2 into other more valuable compounds. The goals of this thesis work were to design new catalysts that have high efficiency for the reduction of CO_2 and to characterize these catalysts with focus on their photocatalytic properties and their related physical properties. The reduction of CO_2 to the valuable products has many important advantages such as the decrease of the environmental hazards by reducing the CO_2 levels in the atmosphere.

At the heart of these studies has been the preparation of new catalysts. These species have been synthesized, characterized and examined for the CO_2 reduction under photocatalytic and, to a lesser extent, electrocatalytic conditions. Although different levels of success have been observed, most of the catalysts in this thesis show their ability towards the photocatalytic CO_2 reduction. In some cases, these catalysts displayed superior ability towards the electrocatalytic CO_2 reduction. In addition, some of these catalysts actually demonstrated good ability towards the H_2 production from H_2O.

7.2. Recommendations and Future Study

Some of the projects that were presented in Chapters 2-6 have clear directions that require more investigations and that could be explored to improve their catalytic ability towards the reduction of CO_2. In most cases, extensions could be used to improve and elaborate on these results. Importantly, efforts to more clearly define the mechanisms for the catalytic reactions are important. For example, a number of different intermediates were proposed and efforts to establish these species are important additions. In addition, since most of these catalysts give H_2 as by-product from the CO_2 reduction, these catalysts should be examined to H_2O splitting to produce H_2. Finally, there is a vast range of future investigations that have been stimulated by the results of this thesis. In the following sections I will outline directions that seem to be particularly interesting and in many cases I will outline some preliminary results that I was able to obtain.

7.3. Exploring Ligand and Metal Variation

7.3.1. Variation of α-diimine ligands with Group 7 – Re(I) and Mn(I)

- **Mono- and bimetallic Re Complexes with a mono(imino)pyridine ligand**

The tricarbonyl species of Re(I) and Mn(I) have an established and varied history in the field of CO_2 reduction. I have initiated two broad investigations that focus on variation of the supporting ligand. The first employs mono(imino)pyridine ligands for the synthesis of $ReL(CO)_3X$ complexes. The targeted species are represented by X Y, where X is the bimetallic Re complex and Y is the mono Re complex. These complexes were successfully prepared and did display evidence of electrocatalytic CO_2 reduction.

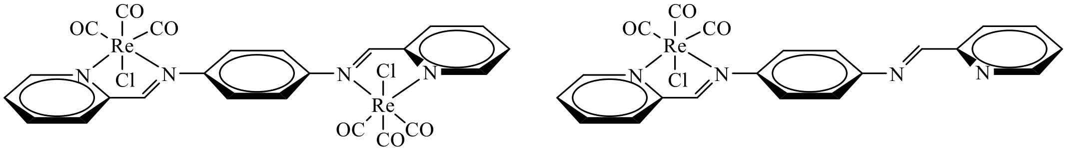

Sceheme 7.1. The mono- and bimetallic Re Complexes with a mono(imino)pyridine ligand.

- **1,10-phenanthroline-5,6-dione (phendione) ligand and 11,12-Dimethyldipyrido[3,2-a:2',3'-c]phenazine (dppz) ligand with Re and Mn**

The idea here is to use the α-diimine ligands used in Chapter 4 and apply them to Re and Mn. These bidentate ligands have an extended π conjunction, which can lead to different reduced intermediates compared with the standard 2,2'-bipyridine and 1,10-phenanthroline complexes. These new ligands phendione and dppz have been synthesized and characterized with Re (I) and Mn(I) metal center, and they also examined for the CO_2 reduction and showed good photocatalytic abilities towards CO_2 reduction.

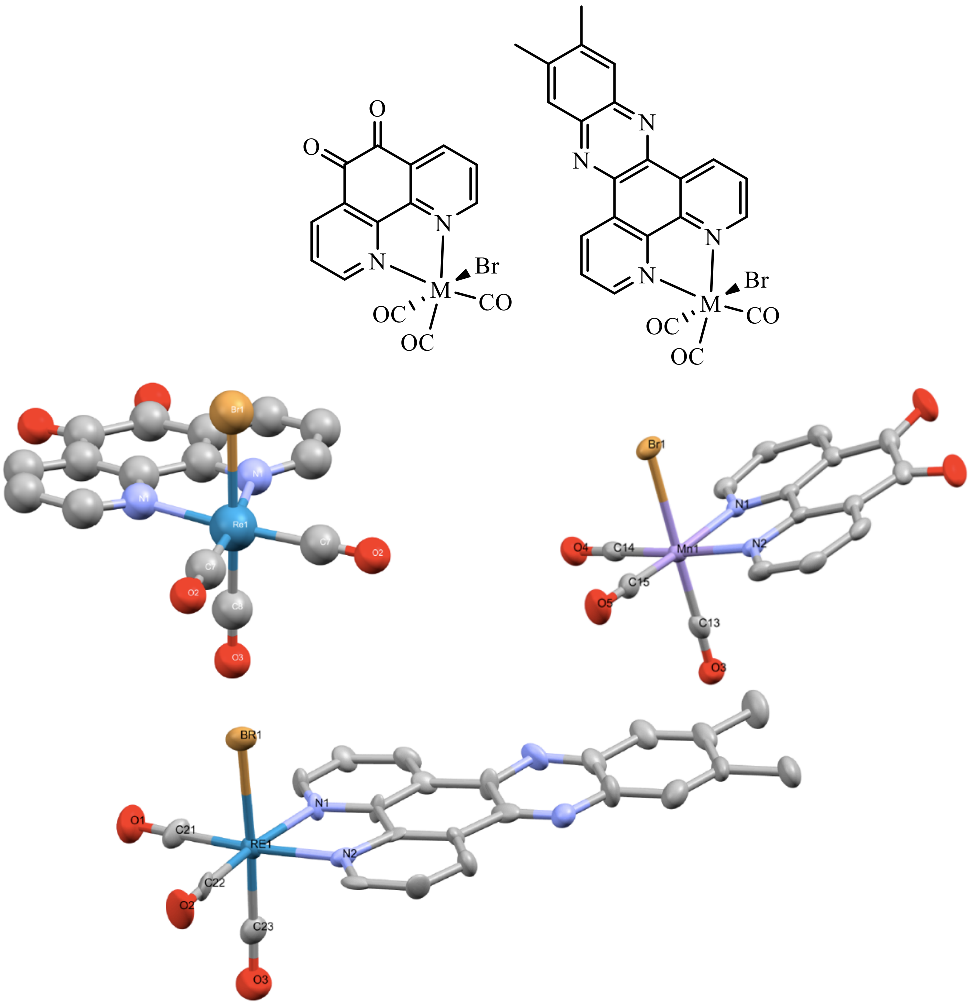

Sceheme 7.2. The Re (I) and Mn(I) complexes with phendione and dppz ligands.

7.3.2. Extending PN Ligation in Group 7 – Re(I) and Mn(I)

- **The Re-PNP-Me and Re-PNP-H Complexes**
- **The Mn-PNP-Me and Mn-PNP-H Complexes**

I have successfully prepared a number of “PNP” complexes of Re(I). For example, Re-PNP-Me and Re-PNP-H have been synthesized and characterized, and these complexes showed ability to reduce CO_2 to HCOOH in photochemical process. More experiments should be done with this project to evaluate the photocatalytic ability of these complexes towards CO_2 reduction. I extended this chemistry to Mn and there are Mn-PNP-Me and Mn-PNP-H that have been synthesized and characterized. These complexes showed a good ability to reduce CO_2 to CO and HCOOH in photochemical process. The Mn-PNP-Me showed higher ability towards photocatalytic CO_2 reduction than the Mn-PNP-H complex. Many conditions were examined for the photocatalytic CO_2 reduction

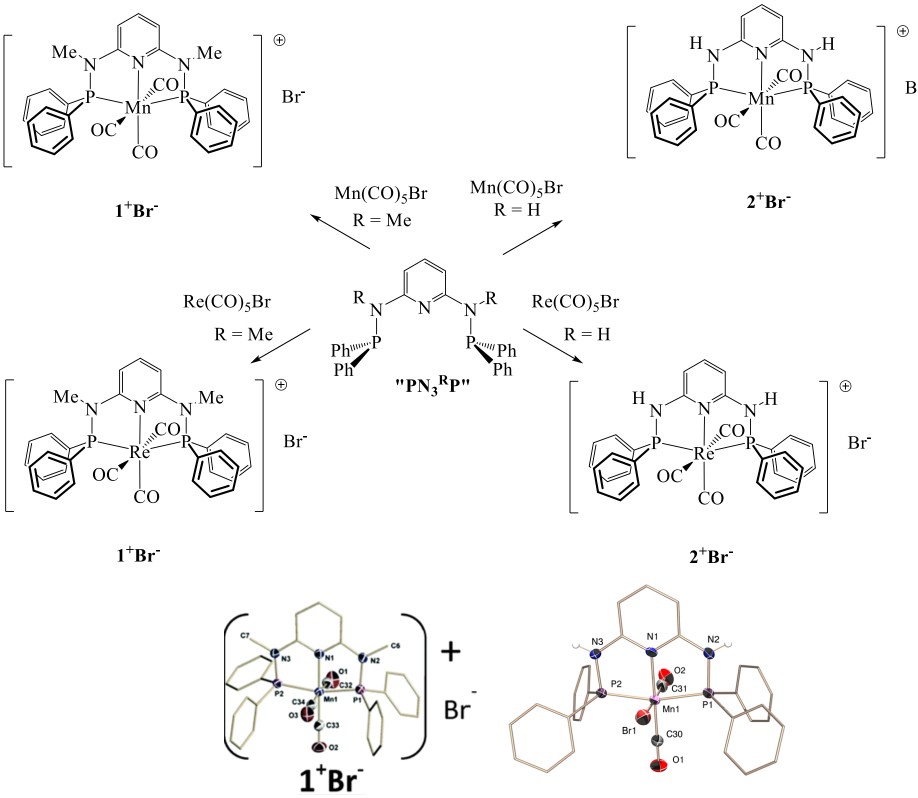

Sceheme 7.3. The Re (I) and Mn(I) complexes with PN-R and PNP-R ligands (R = Me or H).

Table 7.1. The photocatalytic experiments with the Re (I) and Mn(I) complexes with $Ru(bpy)_3(PF_6)_2$ as photosensitizer (**PS**) in DMF (4mL) as solvent and TEOA as electron donors **(ED).**

Complex (1mM)	Ru complex (1mM)	Solvent	e^- donor	Condition	H_2 (µmol)	CO (µmol)	HCOOH (µmol)
Mn-PNP-Me	1	DMF	TEOA	24 h, CO_2	40	22	85
Mn-PNP-Me	1	DMF	NEt_3	24 h, CO_2	5	9	123
Mn-PNP-Me	1	DMF	AA	24 h, CO_2	4	4	-
Mn-PNP-Me	1	DMF	Na.asc	24 h, CO_2	-	2	-
Mn-PNP-H	1	DMF	TEOA	24 h, CO_2	16	-	84
Mn-PNP-H	1	DMF	NEt_3	24 h, CO_2	20	-	85
Mn-PNP-H	1	DMF	AA	24 h, CO_2	-	-	-
Mn-PNP-H	1	DMF	Na.asc	24 h, CO_2	20	-	-
Re-PNP-Me	1	DMF	TEOA	24 h, CO_2	6	2	90
Re-PNP-H	1	DMF	TEOA	24 h, CO_2	8	1	70

7.3.3. Divalent First Row Metal Complexes Fe, Co, Ni

- **The Fe-PN-Me, Fe-PN-H, Fe-PNP-Me and Fe-PNP-H Complexes**
- **The Co-PN-Me, Co-PN-H, Co-PNP-Me and Co-PNP-H Complexes**
- **The Ni-PN-Me, Ni-PN-H, Ni-PNP-Me and Ni-PNP-H Complexes**

Both the PN and PNP ligands have been successfully applied as supporting ligands in CO_2 reduction catalysts. I extended this to include a number of divalent first row transition metals (e.g. Fe, Co and Ni) that are potential CO_2 reduction catalysts. For example, Fe(II) and Ni(II) complexes have been synthesized with both bidentate and tridentate ligands. The Fe-PN-Me, Fe-PN-H, Fe-PNP-Me, Fe-PNP-H, Ni-PN-Me, Ni-PN-H, Ni-PNP-Me, Ni-PNP-H, Co-PNP-Me and Co-PNP-H complexes have been synthesized and characterized. They have been tested for the CO_2 reduction, but still they need more experiments to document their photocatalytic ability towards CO_2 reduction.

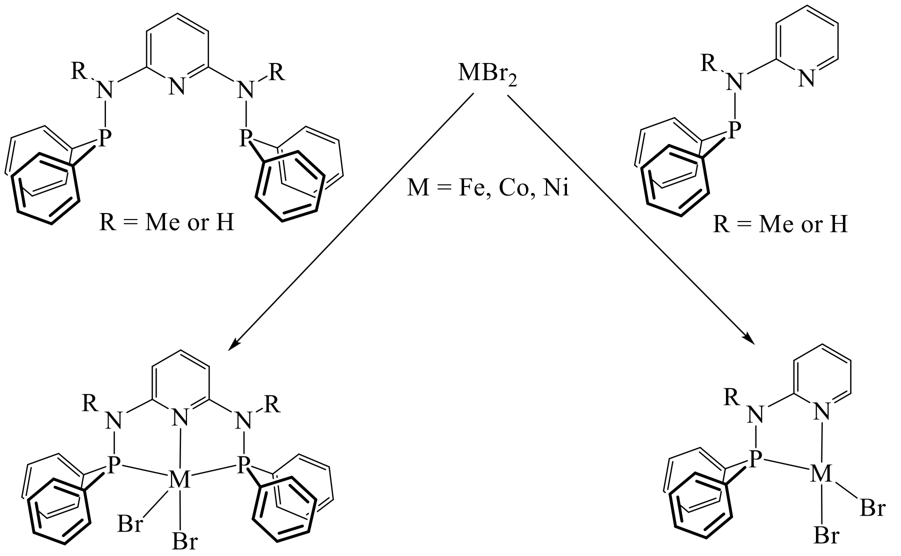

R = Me (1), H (2) **R = Me (3), H (4)**

Sceheme 7.4. The divalent Fe, Co and Ni complexes with PN-R and PNP-R ligands (R = Me or H).

7.3.4. Divalent Zn Complexes with PN-R and PNP-R Ligands

Both the PN and PNP ligands have been successfully applied as supporting ligands in CO_2 reduction catalysts with zinc. Zn(II) complexes Zn-PN-Me, Zn-PN-H, Zn-PNP-Me, and Zn-PNP-H have been synthesized and characterized with both bidentate and tridentate ligands. Preliminary testing for the CO_2 reduction for both photocatalytic and electrocatalytic ability of CO_2 reduction has been performed. They show a good photocatalytic and electrocatalytic ability towards CO_2 reduction.

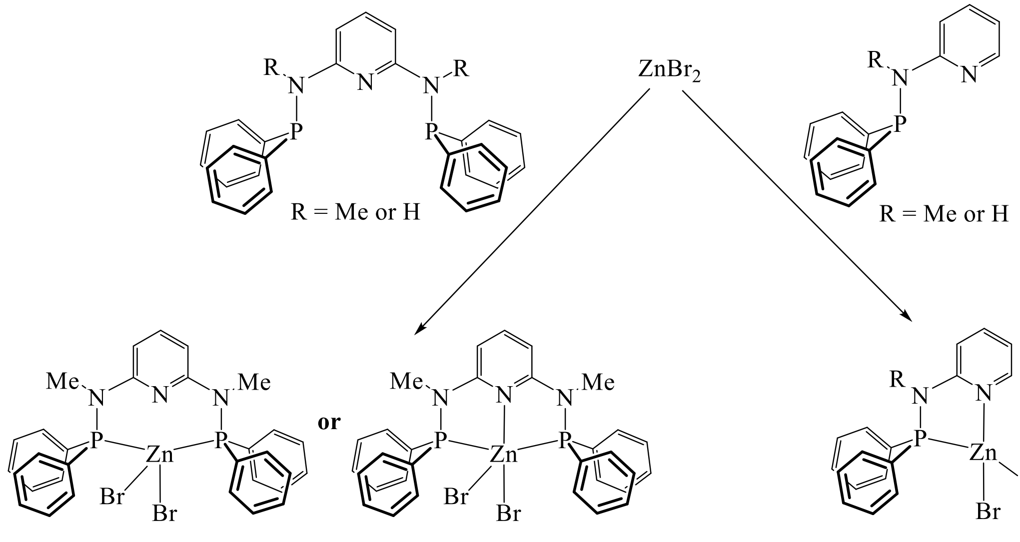

(1) **(2)** **R = Me (3), H (4)**

Sceheme 7.5. The divalent Zn(II) Complexes with both PN-R and PNP-R ligands (R = Me or H).

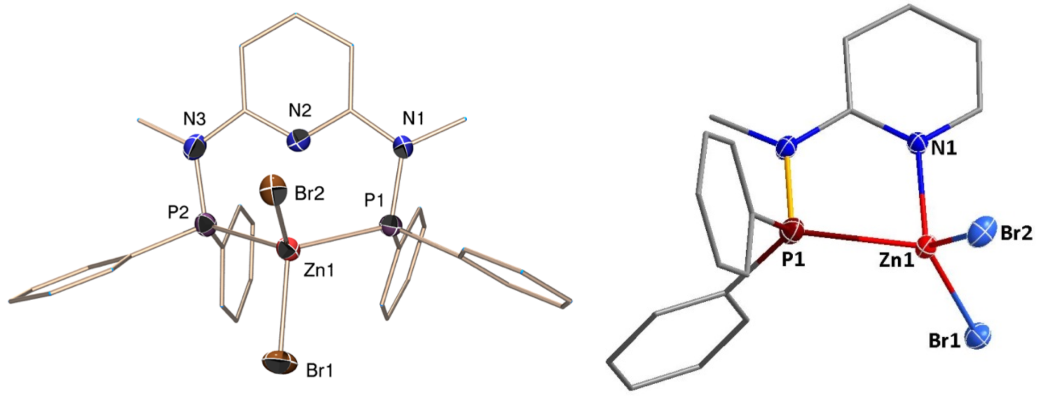

Sceheme 7.6. The X-ray structures of some of the divalent Zn(II) Complexes with both PN-R and PNP-R ligands (R = Me or H).

Table 7.2. The Photocatalytic experiments with the Zn(II) Complexes with Ru(bpy)$_3$(PF$_6$)$_2$ as photosensitizer **(PS)** in DMF (4mL) as solvent and triethanol amine as electron donor **(ED).**

Complex (1mM)	**Ru complex (1mM)**	**Solvent**	**e$^-$ donor**	**Condition**	**H$_2$ (µmol)**	**CO (µmol)**	**HCOOH (µmol)**
Zn-PN-Me	1	DMF	TEOA	24 h, CO$_2$	-	-	46
Zn-PNP-Me	1	DMF	TEOA	24 h, CO$_2$	6	-	82
Zn-PN-H	1	DMF	TEOA	24 h, CO$_2$	4	-	46
Zn-PNP-H	1	DMF	TEOA	24 h, CO$_2$	4	-	41

7.3.5. Changing the Ligand Framework using the First Row Metal Complexes

These NPNPN [N(PN)$_2$] and NPN [N(PN)] ligands have been synthesized and characterized. Both of these N(PN)$_2$ and N(PN) ligands can be applied as supporting ligands to the first row transition metals to make the complexes that can be used as CO$_2$ reduction catalysts. These ligands can be synthesized with the transition metals to make the geometry of ML(CO)$_3$X complexes, and they can be extended to include a number of divalent first row transition metals with the geometry of MLX$_2$. These proposed complexes should be synthesized, characterized, and examined to the CO$_2$ reduction to see their catalytic ability towards the CO$_2$ reduction. Then, they can be compared to our PN and PNP catalysts.

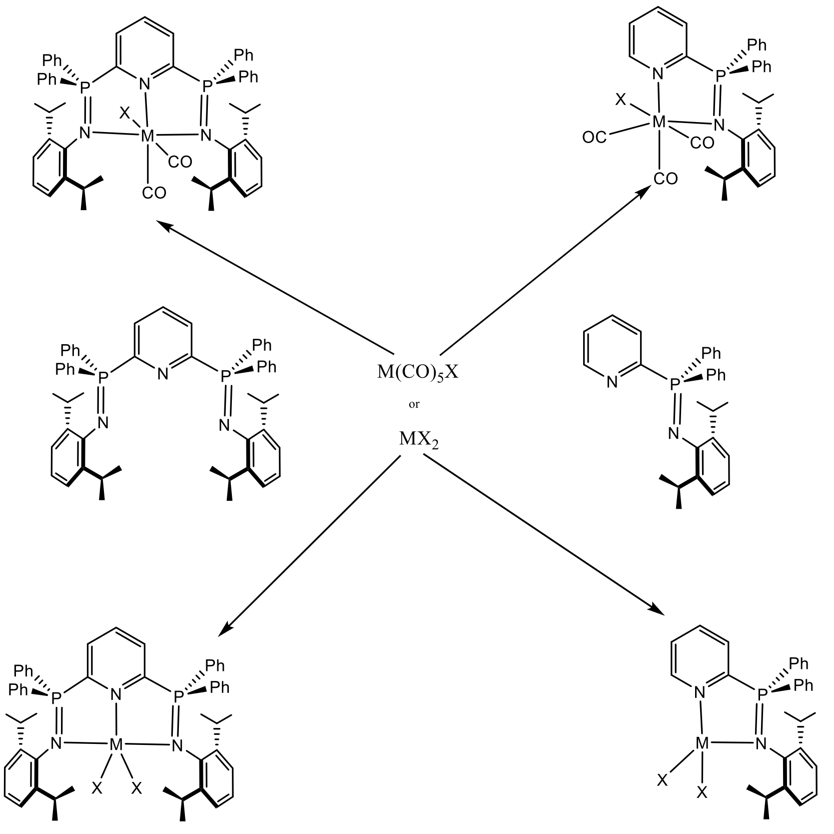

M = Mn, Fe, Co, Ni, Zn
X = Cl, Br

Sceheme 7.7. The proposed transition metal complexes with both N(PN)$_2$ and N(PN) ligands.

In summary, in this chapter I have provided broad outlines and directions for a range of different future directions that extend from the heart of the thesis research presented in Chapters 2-6. I believe that these future avenues will be interesting and noteworthy to try and to be good projects. I am optimistic about the catalyst's behavior of each of these proposed directions since I was able to make a number of the proposed complexes and carry out some preliminary testing of these complexes towards CO_2 reduction. Although I believe there is potential from each of these ideas, I am particularly attracted to investigate the chemistry shown in Scheme 7.7. These species represent a new ligand framework. These ligands have been successfully synthesized and characterized. They are primed to form metal complexes, which could then be examined towards the CO_2 reduction. I am very excited to see the results of this work and to compare it with the PN and PNP ligand frameworks presented in this document.